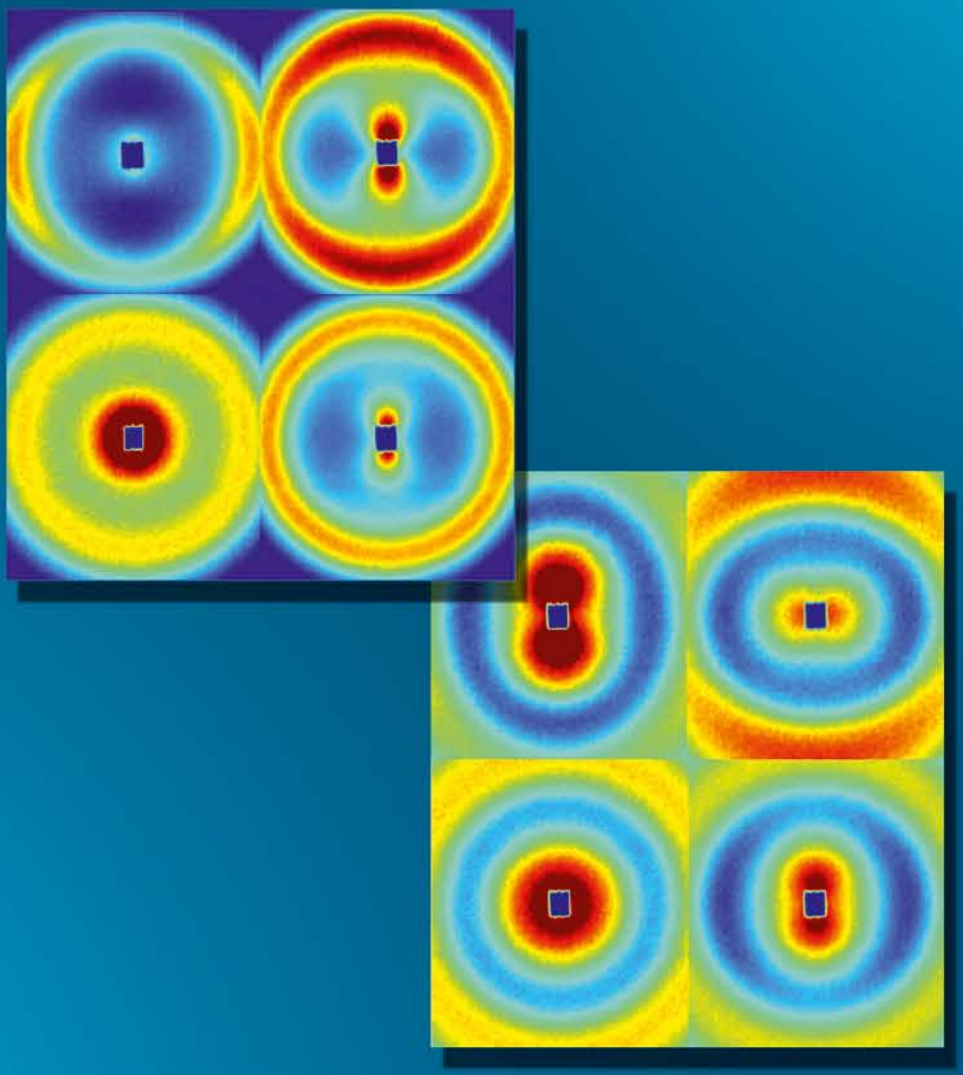

The spin structure of magnetic nanoparticles and in magnetic nanostructures

Sabrina Disch

Mitglied der Helmholtz-Gemeinschaft

JÜLICH
FORSCHUNGSZENTRUM

Schriften des Forschungszentrums Jülich
Reihe Schlüsseltechnologien / Key Technologies Band / Volume 21

Forschungszentrum Jülich GmbH
Jülich Centre for Neutron Science (JCNS)
Streumethoden (JCNS-2)

The spin structure of magnetic nanoparticles and in magnetic nanostructures

Sabrina Disch

Schriften des Forschungszentrums Jülich
Reihe Schlüsseltechnologien / Key Technologies Band / Volume 21

ISSN 1866-1807 ISBN 978-3-89336-704-7

Bibliographic information published by the Deutsche Nationalbibliothek.
The Deutsche Nationalbibliothek lists this publication in the Deutsche Nationalbibliografie; detailed bibliographic data are available in the Internet at http://dnb.d-nb.de.

Publisher and Distributor:	Forschungszentrum Jülich GmbH Zentralbibliothek 52425 Jülich Phone +49 (0) 24 61 61-53 68 · Fax +49 (0) 24 61 61-61 03 e-mail: zb-publikation@fz-juelich.de Internet: http://www.fz-juelich.de/zb
Cover Design:	Grafische Medien, Forschungszentrum Jülich GmbH
Printer:	Grafische Medien, Forschungszentrum Jülich GmbH
Copyright:	Forschungszentrum Jülich 2011

Schriften des Forschungszentrums Jülich
Reihe Schlüsseltechnologien / Key Technologies Band / Volume 21

D 82 (Diss.,RWTH Aachen University, 2010)

ISSN 1866-1807
ISBN 978-3-89336-704-7

The complete volume ist freely available on the Internet on the Jülicher Open Access Server (JUWEL) at http://www.fz-juelich.de/zb/juwel

Neither this book nor any part of it may be reproduced or transmitted in any form or by any means, electronic or mechanical, including photocopying, microfilming, and recording, or by any information storage and retrieval system, without permission in writing from the publisher.

Meiner Familie

Abstract

The present thesis provides an extensive and original contribution to the investigation of magnetic nanoparticles regarding synthesis and structural characterization using advanced scattering methods in all length scales between the atomic and mesoscopic size range. Particular emphasis is on determination of the magnetic structure of single nanoparticles as well as preparation and characterization of higher dimensional assemblies thereof.

The unique physical properties arising from the finite size of magnetic nanoparticles are pronounced for very small particle sizes. With the aim of preparing magnetic nanoparticles suitable for investigation of such properties, a micellar synthesis route for very small cobalt nanoparticles is explored. Cobalt nanoparticles with diameters of less than 3 nm are prepared and characterized, and routes for variation of the particle size are developed. The needs and limitations of primary characterization and handling of such small and oxidation-sensitive nanoparticles are highlighted and discussed in detail.

Comprehensive structural and magnetic characterization is performed on iron oxide nanoparticles of ~ 10 nm in diameter. Particle size and narrow size distribution are determined with high precision. Investigation of the long range and local atomic structure reveals a particle size dependent magnetite - maghemite structure type with lattice distortions induced at the particle surface. The spatial magnetization distribution within these nanoparticles is determined to be constant in the particle core with a decrease towards the particle surface, thus indicating a magnetic dead layer or spin canting close to the surface.

Magnetically induced arrangements of such nanoparticles into higher dimensional assemblies are investigated in solution and by deposition of long range ordered mesocrystals. Both cases reveal a strong dependence of the found structures on the nanoparticle shape (spheres, cubes, and heavily truncated cubes). Nanospheres and nanocubes form closed packed mesocrystals and a short range ordered hard spheres interaction potential in dispersion. In addition, the arrangements of the cuboidal nanoparticles exhibit a strong tendency of face to face oriented attachment, which may result from van der Waals interaction of the cubic facets. Mesocrystals of aged nanocubes with higher de-

gree of truncation reveal a structural transition between the structures of nanocubes and nanospheres.

Kurzzusammenfassung

Die vorliegende Arbeit leistet einen umfassenden und originären Beitrag zur Erforschung magnetischer Nanoteilchen in den Bereichen der Synthese und der strukturellen Charakterisierung mittels fortgeschrittener Streumethoden auf allen Größenordnungen zwischen atomarer und mesoskopischer Skala. Ein besonderer Schwerpunkt liegt auf der Bestimmung der magnetischen Struktur einzelner Nanoteilchen sowie der Präparation und Charakterisierung höherdimensionaler Anordnungen von Nanoteilchen.

Die aus der endlichen Größe magnetischer Nanoteilchen hervorgehenden einzigartigen physikalischen Eigenschaften sind für sehr kleine Nanoteilchen besonders ausgeprägt. Mit dem Ziel der Darstellung geeigneter Nanoteilchen zur Erforschung solcher Eigenschaften wurde eine mizellare Synthesemethode sehr kleiner Cobaltnanoteilchen untersucht. Cobaltnanoteilchen mit Durchmessern von unter 3 nm wurden dargestellt und charakterisiert, und Wege zur Variation der Partikelgröße wurden entwickelt. Die Anforderungen und Grenzen bezüglich Primärcharakterisierung und Handhabung solch kleiner und oxidationsempfindlicher Nanoteilchen werden aufgezeigt und im Detail diskutiert.

Eine umfassende strukturelle und magnetische Charakterisierung wurde an Eisenoxidnanoteilchen mit Durchmessern von ~ 10 nm durchgeführt. Die Partikelgrößen und geringe Größenverteilung wurden mit hoher Genauigkeit bestimmt. Untersuchungen der langreichweitigen und lokalen atomaren Struktur offenbaren einen partikelgrößenabhängigen Magnetit - Maghemit Strukturtyp mit in der Partikeloberfläche induzierten Gitterverzerrungen. Die ortsaufgelöst bestimmte Magnetisierungsverteilung in diesen Nanoteilchen ist im Partikelzentrum konstant und nimmt zur Oberfläche hin ab, was auf Demagnetisierung oder Verkantung der Spins nahe der Oberfläche hinweist.

Magnetisch induzierte Anordnungen solcher Nanoteilchen in höherdimensionalen Strukturen wurden in Lösung sowie mittels Deposition langreichweitig geordneter Mesokristalle untersucht. Beide Fälle zeigen eine starke Abhängigkeit der gefundenen Struktur von der Morphologie der Nanoteilchen (Kugeln, Würfel und stark trunkierte Würfel). Nanokugeln sowie -würfel bilden dichtgepackte Mesokristallstrukturen und zeigen in Lösung kurzreichweitige Wechselwirkung harter Kugeln. Die Anordnung der würfelartigen Nanoteilchen weist darüber hinaus eine starke Tendenz der parallelen Aus-

richtung der Partikelflächen auf, was aus van der Waals Wechselwirkungen der kubischen Oberflächen resultieren kann. Mesokristalle gealterter Nanowürfel mit stärkerem Trunkierungsgrad weisen einen strukturellen Übergang zwischen den Strukturen kubischer und kugelförmiger Nanoteilchen auf.

Contents

1. Introduction

The phenomenon of magnetism has fascinated mankind for thousands of years, since the discovery of loadstone by the ancient Greeks and also the early Chinese civilization. Since then, research on magnetism has been driven by both the desire for discovery and understanding and the desire for invention and optimization of practical products [1].

Among the important historical cornerstones in understanding and applying magnetism are the navigational magnetic compass and the discovery of the earth magnetic field. A rapid progress in development of magnetic applications occurred during the last two centuries, starting with the discovery of the relationship between electricity and magnetism by Oersted in 1819. Electromagnetism related applications have had a fundamental impact to everyday life until today, *i. e.* by enabling wireless communication at the speed of light. The control of coercivity achieved in the 20th century allows furthermore for generation of specific hysteresis loop shapes demanded by technological applications [1].

In the past decades, magnetism related research progressed towards nanometer sized objects, leading to fundamentally new magnetic properties and applications. The recently most prominent effect is certainly the giant magnetoresistance (GMR), observed simultaneously by P. Grünberg and A. Fert in 1988 and honored with the Nobel Prize in Physics in 2007 [2, 3]. The GMR effect is based on a significant change of resistance in a stack of two ferromagnetic layers separated by a sub-nm nonmagnetic layer, depending on the parallel or antiparallel magnetization direction in the ferromagnetic layers. Paving the way to Gigabyte capacity hard disk drives, this discovery led to a breakthrough in data storage technology and generated tremendous developments in spintronics research.

Superparamagnetism is a further technologically relevant property related to nanomagnetism. It is observed exclusively in magnetic nanoparticles with particle sizes in the single magnetic domain range and may either impede or enhance technological applications, depending on the desired property. For example, the progress towards higher density magnetic data storage requires increasingly smaller magnetic entities, ultimately down to the molecular size range. However, the effect of superparamagnetism limits the smallest possible size of magnetic objects that retain their magnetization state in the required relaxation time range at a given temperature. In order to approach a larger storage density, higher magnetic anisotropies thus need to be achieved to overcome the superparamagnetic limit.

On the other hand, approaches exist which take advantage of superparamagnetism. Magnetic hyperthermia is investigated intensely for cancer treatment and is based upon local heat generation by electromagnetically induced Brownian motion and Néel relaxation of magnetic nanoparticles [4]. Superparamagnetic relaxation is moreover impor-

tant for application of magnetic nanoparticles as contrast agents in nuclear magnetic imaging [4–6]. Further possible applications, *e. g.* in electronic devices and mechanical engineering, take advantage of the collective magnetic behavior observed in ferrofluids.

A challenge for the future is to understand and control magnetism and magnetic phenomena on very small length and time scales and in reduced dimensions. Fundamental questions concern the origin of enhanced magnetization and magnetic anisotropies. As the observed nanomagnetic phenomena are related to surfaces and interfaces, magnetic nanoparticles serve as an interesting case due to their surface to volume ratio which varies linearly with particle size.

This thesis aims at contributing to the understanding of magnetic nanoparticles by giving insight into their electronic and spin structure. In particular, the variation of the magnetization density within magnetic nanoparticles is investigated. Furthermore, suitable model systems for investigation of magnetic interparticle interactions will be given.

Concept

The scope of this work is an interdisciplinary study of magnetic nanoparticles, comprising synthesis, characterization, and the determination of fundamental properties of suitable model systems. In particular, information on the magnetization distribution within nanoparticles as well as possible interparticle interactions are desired.

The first objective is the optimization of a chemical synthesis route for preparation of magnetic nanoparticles in a range of different particle sizes and with a narrow distribution. In particular, a water-free synthesis technique for cobalt nanoparticles from micellar solutions as developed by Feygenson *et al.* [7] is further optimized (see chapter 4). Primary characterization of the prepared nanoparticles will be discussed in detail.

The second objective is an investigation of the structure and magnetization distribution within magnetic nanoparticles as well as of interparticle interactions. Scattering methods are best suited for investigating both intra-particle phenomena, such as the magnetization distribution or the spin structure of individual magnetic nanoparticles, and inter-particle interactions of such nanoparticles in higher dimensional mesostructures. However, before addressing the problems of magnetization distributions or magnetic interactions between magnetic nanoparticles, the availability and the precise structural characterization of highly monodisperse nanoparticles and highly ordered nanos-

tructures is required. Owing to the time limitations for the realization for this thesis, a consecutive realization of both nanoparticle synthesis development and detailed investigation of the physical properties is not feasible. For this reason, investigations on the chemical and magnetic structure (chapter 5) of iron oxide nanoparticles received through collaborations are pursued in parallel with the synthesis development of cobalt nanoparticles.

A precise structural characterization including size and size distribution is required before determination of magnetization densities and will be given in section 5.1. Furthermore, information on the long range structure and particularly the local structural correlations on atomic length scales as given in section 5.2 is needed because it may be correlated with deviations in the magnetization density. Investigations on the magnetization distribution within nanoparticles are presented in section 5.3.3.1.

Magnetic interparticle interactions may be investigated either in dispersion or in highly ordered assemblies. Shape dependent conformations of nanoparticles in concentrated dispersions as induced by an applied magnetic field are investigated by small-angle neutron scattering in section 5.3.3.2. The preparation and structural characterization of long range ordered superlattices of spherical and cubic nanoparticles will be presented in section 5.4. Both systems will serve as a prerequisite for determination of magnetic interparticle interactions by polarized neutron scattering.

Polarization analysis is an important technique for determination of the purely magnetic neutron scattering contributions. For investigations on very small nanoparticles with diameters below 5 nm, the gap in accessible momentum range between small-angle neutron scattering and conventional neutron diffraction with polarization analysis has to be bridged. Chapter 6 will focus on first experiments and development of polarized small-angle scattering in this intermediate Q range.

2. Theoretical Background

2.1. Superparamagnetism

Formation of domain walls in ferromagnetic materials is governed by the competition between the energy cost for domain wall formation and the energy gain from the magnetostatic self energy density. The latter is often denoted as demagnetizing energy density and is given by

$$E_D = -\frac{1}{2}\mu_0 \vec{M} \cdot \overleftrightarrow{N} \cdot \vec{M} \tag{2.1.1}$$

with the magnetization $\vec{M}$ and the shape dependent demagnetization tensor $\overleftrightarrow{N}$. With decreasing grain size, surface and interface energies (such as the domain wall energy) become more important as compared with volume energies (such as the demagnetizing energy). Hence, there exists a critical particle diameter, below which ferromagnetic nanoparticles become single-domain and behave as small permanent magnets. This critical diameter can be estimated as

$$d_c \approx 18\frac{\sqrt{AK_{eff}}}{\mu_0 M^2} \tag{2.1.2}$$

with A the exchange, K_{eff} the effective magnetic anisotropy, and M the saturation magnetization. Typical values for the critical diameter, assuming typical values for exchange and magnetic anisotropy, are in the range of 10 - 1000 nm [8].

The magnetization in such a single-domain nanoparticle is preferably oriented along an easy axis, and an energy barrier of $\Delta E = KV$ (with K the anisotropy constant and V the particle volume) has to be overcome for magnetization reversal. If the thermal energy $k_B T$ is large compared to the energy barrier, the magnetization will be easily flipped by thermal fluctuations [9]. If the nanoparticles are separated enough to prevent any interparticle interactions and $k_B T \gg KV$, the system will behave as a paramagnet. Due to the large independent magnetic moments of the individual nanoparticles in the range of some $10^4 \mu_B$, this magnetic state is called superparamagnetism. The magnetization curve of a superparamagnetic system follows the classical Langevin behavior

$$M(H,T) = N\mu\left[\coth\left(\frac{\mu H}{k_B T}\right) - \frac{k_B T}{\mu H}\right] = N\mu L\left(\frac{\mu H}{k_B T}\right) \tag{2.1.3}$$

with N the number of particles, μ the integral particle moment, and $L(x)$ the Langevin function.

The field dependent magnetization curve for a single-domain particle for $k_B T < KV$ can be calculated according to the Stoner Wohlfarth model. In a single-domain par-

ticle, magnetization reversal occurs by coherent domain rotation rather than domain wall movement. With a magnetic field H applied at an angle θ to the easy axis of the nanoparticle and the magnetization at an angle ϕ to the applied magnetic field, the energy density of the system is given by

$$E = K\sin^2(\theta - \phi) - \mu_0 H M_s \cos\phi \tag{2.1.4}$$

The magnetization curve for a particular orientation θ of the particle in the applied magnetic field can be obtained by evaluating the minima in the energy surface given by equation (2.1.4) depending on ϕ and h with

$$h = \frac{\mu_0 M_s H}{2K} \tag{2.1.5}$$

The obtained energy surfaces for $\theta = 90°$ and $30°$ are presented in Figure 2.1.1. Magne-

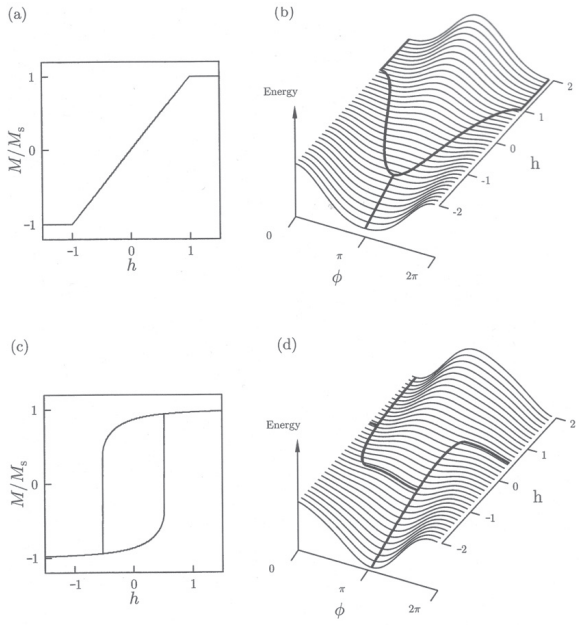

Figure 2.1.1.: Hysteresis loops in the Stoner-Wohlfarth model for (a) $\theta = 90°$ and (c) $\theta = 30°$ as obtained by finding the minimum energy points on the energy surfaces as a function of h and ϕ, which are shown for (b) $\theta = 90°$ and (d) $\theta = 30°$ [9].

tization curves for a larger variety of nanoparticle orientations θ are presented in Figure

2.1.2 along with the magnetization curve obtained for a polycrystalline average of orientations.

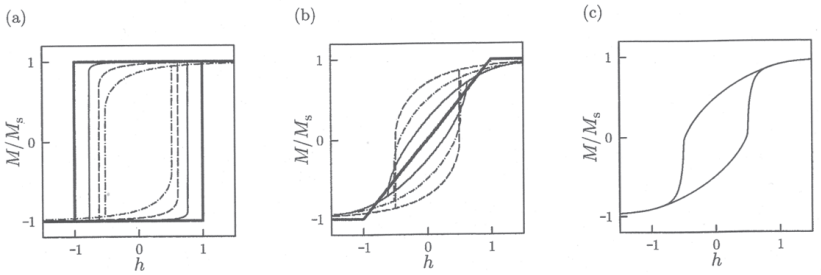

Figure 2.1.2.: Hysteresis loops in the Stoner-Wohlfarth model for (a) $\theta = 0°$ (bold), 5°, 15°, 30°, (b) $\theta = 45°$, 60°, 75° and 90° (bold). (c) A calculated hysteresis loop for polycrystalline average [9].

The single-domain nanoparticle moments fluctuate with a temperature and particle volume dependent relaxation time τ

$$\tau = \tau_0 \exp\left(\frac{KV}{k_B T}\right) \tag{2.1.6}$$

where the inverse attempt frequency τ_0 is typically 10^{-9} s. The system appears superparamagnetic, when the relaxation time is faster than the characteristic timescale of the applied measurement technique. When the relaxation time is longer than the characteristic timescale, the system appears blocked. The temperature of equal relaxation and measurement times is therefore called the blocking temperature T_B. As the characteristic timescale varies depending on the probe, the measured blocking temperature is not an absolute parameter. However, due to the logarithmic dependence on $\frac{\tau}{\tau_0}$ even large variations in the characteristic time scale induce relatively small changes in the observed blocking temperature as can be seen in Figure 2.1.3. Typical timescales are 10^{-12} - 10^{-10} s for neutron scattering, 10^{-10} - 10^{-7} s for Mössbauer spectroscopy, 10^{-10} - 10^{-5} s for muon spin relaxation, and 10^{0} - 10^{-5} s for magnetic susceptibility measurements. While the blocking temperatures determined by different probes are not directly related, a combination of blocking temperatures obtained in different time windows allows for determination of the effective magnetic anisotropy

$$K_{eff} = \frac{k_B}{V}\left(\frac{1}{T_{B,1}} - \frac{1}{T_{B,2}}\right)^{-1} \ln\left(\frac{\tau_1}{\tau_2}\right). \tag{2.1.7}$$

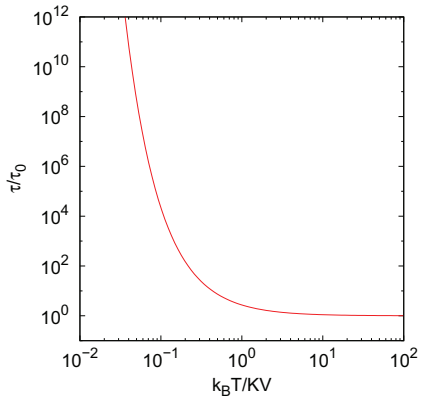

Figure 2.1.3.: Superparamagnetic relaxation time τ as a function of the temperature T (scaled by $\frac{k_B}{KV}$) according to eq. (2.1.6). The fluctuations therefore slow down (τ increases) as the temperature is reduced [9].

2.2. Scattering methods applied to magnetic nanoparticles

Magnetic nanoparticles and assemblies thereof exhibit correlations in a wide size (and time) range that can be investigated by various scattering techniques. The nanoparticle morphology, including particle size and size distribution is in the lower nm size range and can thus be investigated by small-angle scattering methods. Interparticle interactions, ranging from disordered nanoparticle aggregates up to the crystalline order in nanoparticle mesocrystals, result in a structure factor that is also studied by small-angle scattering. The grazing incidence geometry is advantageous for the study of ordered assemblies on a substrate because at least one preferred orientation (the substrate normal) and a good illumination of a large part of the sample are provided. Moreover, dynamical scattering effects close to the condition of total reflection can be exploited in this geometry in order to enhance the scattered intensity. On a much lower scale, atomic correlations ranging from local to long range order within the individual nanoparticles are investigated by wide angle scattering techniques. Conventional powder diffraction gives insight into a possible long-range order of the atomic structure. Whereas Bragg diffraction gives information on the averaged long range atomic order, the atomic Pair Distribution Function (PDF) provides insight into the local structure in real space and is complementary to X-ray absorption techniques, which probe mainly the first coordination sphere of a chosen element. The structural correlations examined in the framework

of this thesis range over five orders of magnitude, *i. e.* from the pm accuracy of atomic distances in the local order of the nanoparticles up to about 180 nm, which is the correlation length in the superstructure of iron oxide nanocubes.

The neutron spin can be employed to investigate magnetic scattering contributions using polarized neutron scattering techniques. Information on the magnetization distribution can be gained on both atomic and nanoparticulate length scales, depending on the measurement geometry. Furthermore, polarization analysis allows for separation of the pure magnetic scattering contribution as well as elimination of parasitic incoherent scattering background.

In this section, the scattering techniques applicable for investigation of magnetic nanoparticles will be introduced. Due to the wide range of scientific cases connected to nanomaterials, this compilation does not claim to be exhaustive. Focus is on a qualitative introduction into those scattering techniques applied throughout this thesis. For further techniques and a more detailed derivation of the physical background, refer to the literature [10–12].

2.2.1. Structural correlations on the atomic scale

The atomic structure of materials is generally investigated by analysis of the Bragg scattering, giving a precise description of the average periodic structure. However, Bragg scattering relies on the long range periodicity of the investigated material, which breaks down rapidly in nanomaterials. The most obvious effect of finite size on Bragg scattering is the significant Debye-Scherrer reflection broadening. Apart from the inaccuracy of determination of a long range periodic structure in finite size nanomaterials, the periodic structure itself is also insufficient, because it does not take into account the short range order. Local deviations from the average crystal structure are more pronounced in nanomaterials because they often originate in disorder at interfaces and surfaces. Examples include lattice strain induced by surface disorder and atomic dislocations. Although some deviations from the average structure may technically be described by analysis of the Debye-Waller factors, a precise determination of the local structure requires consideration of the diffuse scattering. The total scattering structure function includes scattering from the Bragg peaks (the global structure), elastic diffuse scattering (the static local structure), and inelastic scattering from moving atoms (atom dynamics) [13]. Analysis of the total scattering structure function can be performed in either reciprocal or real space and gives the opportunity of a precise description of atomic order in all length scales.

In this section, the methods of crystallography for determination of structural correlations on the atomic scale will be introduced. First, evaluation of Bragg scattering by Rietveld analysis will be covered. Secondly, analysis of the atomic pair distribution function (PDF) as obtained by Fourier transformation of the total scattering structure function into real space will be introduced. A complementary approach to obtain a PDF is the EXAFS method. For this reason, X-ray absorption techniques will be presented, which provide element-specific information on the oxidation state (XANES) and local environment (EXAFS) of the probed atom.

2.2.1.1. Bragg scattering

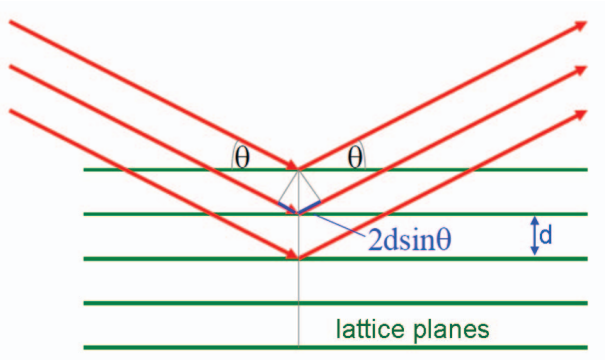

Figure 2.2.1.: Schematic of the Bragg scattering condition. Picture taken from [11]

Bragg scattering occurs when a crystalline arrangement of atoms is irradiated with an X-ray or neutron beam of wavelengths comparable to the atomic distances. When the incident beam is scattered from a set of lattice planes with a distance d_{hkl}, the scattered beams interfere constructively for a difference in path lengths of $n\lambda$. The difference in path length depends on the scattering angle and the distance of the lattice planes as shown in Figure 2.2.1. Bragg reflections are observed for constructive interference of the scattered beams at scattering angles 2θ according to Bragg's law

$$2d_{hkl} \sin\theta = n\lambda \tag{2.2.1}$$

The Ewald construction as presented in Figure 2.2.2 is a geometric representation of the relationship between the wavelength of the incident and scattered beams, the scat-

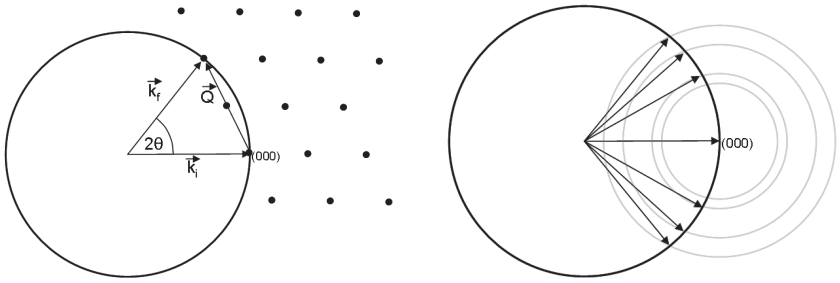

(a) Single crystal. Bragg reflections are observed at intersections of a reciprocal lattice point and the Ewald sphere surface.

(b) Crystalline powder. The reciprocal lattice consisting of spherical reciprocal lattice shells around (000) is represented in grey. Bragg reflections are observed at intersections of reciprocal lattice shells and the Ewald sphere surface (Debye-Scherrer rings).

Figure 2.2.2.: Ewald construction. The Ewald sphere has a radius of $|\vec{k_i}| = |\vec{k_f}| = \frac{2\pi}{\lambda}$.

tering angle of a given reflection, and the reciprocal lattice of a crystalline sample. For elastic scattering the energy of incident and scattered waves is identical

$$|\vec{k_i}| = |\vec{k_f}| = \frac{2\pi}{\lambda} \tag{2.2.2}$$

The scattering vector $\vec{Q}$ is defined as the difference vector between wave vectors of the incident and scattered beams

$$\vec{Q} = \vec{k_f} - \vec{k_i} \tag{2.2.3}$$

with a magnitude of

$$|\vec{Q}| = Q = \frac{4\pi}{\lambda} \sin\theta \tag{2.2.4}$$

and is thus visualized in the Ewald construction as any vector starting and ending at the surface of the so called Ewald sphere with radius $|\vec{k_i}|$. Bragg reflections are observed if $\vec{Q}$ coincides with a reciprocal lattice vector of the studied sample with

$$Q = \frac{2\pi}{d_{hkl}} \tag{2.2.5}$$

As the Bragg condition is only fulfilled for reciprocal lattice points coinciding with the surface of the Ewald sphere, a single crystalline sample needs to be rotated in order to observe more Bragg reflections. In contrast, the reciprocal lattice of an orientationally averaged powder sample consists of spherical reciprocal lattice shells rather than recip-

rocal lattice points. As presented in Figure 2.2.2b, these shells intersect with the Ewald sphere without rotation of the sample. The resulting Bragg reflections appear as Debye Scherrer rings on a 2D detector.

The lattice plane distance d_{hkl} is directly related to the lattice parameters as given for the higher symmetric crystal classes in Table 2.2.1. The lattice parameters of an unknown sample can thus be deduced from the positions of a set of Bragg reflections.

Table 2.2.1.: Lattice plane distances.

crystal class	$\left(\frac{1}{d_{hkl}}\right)^2$
cubic	$\frac{h^2+k^2+l^2}{a^2}$
hexagonal	$\frac{4}{3}\frac{h^2+k^2+hk}{a^2}+\frac{l^2}{c^2}$
tetragonal	$\frac{h^2+k^2}{a^2}+\frac{l^2}{c^2}$
orthorhombic	$\frac{h^2}{a^2}+\frac{k^2}{b^2}+\frac{l^2}{c^2}$

While the reflection position gives information on the unit cell symmetry and dimensions, the intensity of the individual Bragg reflections depends on the unit cell contents. The measured intensity is the square modulus of the structure amplitude, which is comprised of element specific atomic form factors (or scattering lengths in case of neutron scattering) with the phase relation depending on the position of each atom in the unit cell and the Debye-Waller factor attributed to thermal atomic displacements.

$$I(\vec{Q}) = |F(\vec{Q})|^2 = \sum_j f_j \cdot e^{i\vec{Q}\vec{r}} \cdot e^{-\frac{1}{3}\vec{Q^2}\vec{|u_j|^2}} \tag{2.2.6}$$

As the measured intensity is related to the scattering probability and thus to the square modulus of the structure factor amplitude, the phase information of the amplitude is lost. The structural information is thus not directly accessible by measurement of the scattering intensity, which is known as the phase problem in crystallography. For this reason, the observed scattering intensities are modelled according to a structure model instead of a direct determination of the crystal structure from measured intensities.

The Rietveld method is mostly used for refinement of powder diffraction data. Instead of evaluating single reflection intensities, an entire diffraction intensity profile for

the proposed structure model is calculated and refined, an approach that allows for correct modelling of overlapping reflections. The calculated diffraction profile is comprised of contributions from the sample, *i. e.* the average crystal structure, reflection broadening effects due to finite particle size and strain, as well as instrumental contributions such as the peak shape, absorption, polarization correction, sample geometry, and the background [13].

As a criterion for the quality of a refinement, several R-factors (residuals functions) are defined. An important one to judge the overall fit of the entire diffraction pattern is the weighted profile R-factor

$$R_{wp} = \frac{\sum w(I_o - I_c)^2}{\sum w I_o^2} \tag{2.2.7}$$

with I_o and I_c the observed and calculated intensities, respectively, and w a weighting factor for the estimated random error on each data point [14]. For estimation of the validity of the structural model and comparison to single crystal structure refinements, R(F^2) is defined as

$$R(F^2) = \frac{\sum |F_o^2 - SF_c^2|}{\sum F_o^2} \tag{2.2.8}$$

with F_o and F_c the observed and calculated structure amplitudes, respectively, and S the scale factor of the studied data set [14].

2.2.1.2. Total scattering and the Pair Distribution Function [13]

Whereas Bragg scattering as described in the previous section is a useful tool for investigation of long range, average crystal structures, it does not give sufficient information on the local structure for a complete description of nanoparticle structures. Local atomic correlations appear as diffuse scattering in diffraction intensity profiles. In Rietveld refinements this information is lost, as the diffuse scattering and other background contributions are treated phenomenologically.

The total scattering structure function S(Q) is the radial Fourier transform of the reduced pair density function

$$S(Q) = 1 + 4\pi\rho_0 \int_0^\infty (g(r) - 1)\frac{\sin(Qr)}{Qr} r^2 dr \tag{2.2.9}$$

with the average number density ρ_0 and the pair distribution function $g(r)$. The total scattering structure function contains thus information on both the long range structure from the Bragg reflections and the local structure from the diffuse scattering. In order

to obtain S(Q), normalization and correction of the measured diffraction data have to be performed carefully. In particular the instrumental background intensity has to be measured with equally good statistics as the sample measurement. After background subtraction, corrections for sample absorption, multiple scattering, Compton scattering, and polarization effects are made. The obtained corrected scattering intensity I(Q) is normalized to the average atomic scattering power to obtain S(Q). With S(Q) approaching 1 at high Q, the reduced total scattering structure function

$$F(Q) = Q(S(Q) - 1) \tag{2.2.10}$$

is derived, which oscillates around zero at high Q. Examples for I(Q) and F(Q) of nickel powder are presented in Figure 2.2.3. Significant diffuse scattering is found at

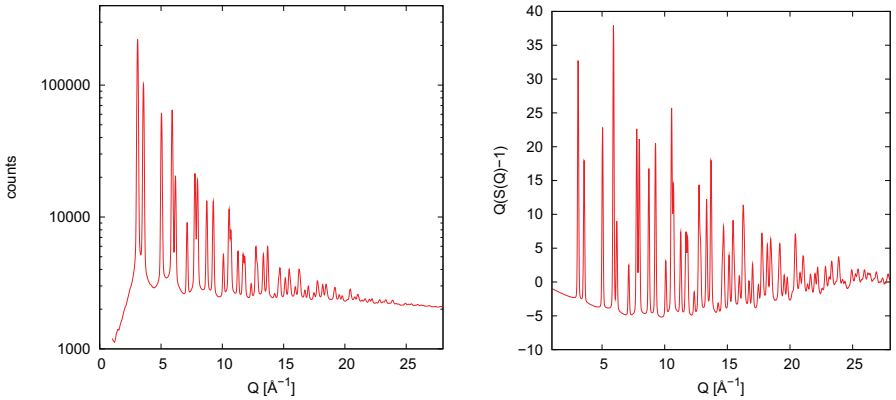

(a) Corrected scattering intensity I(Q).

(b) Reduced total scattering structure function F(Q).

Figure 2.2.3.: Correction and normalization of total scattering data of nickel powder.

high Q in the reduced total scattering structure function in Figure 2.2.3b, which was not apparent in Figure 2.2.3a. The reduced total scattering function is converted into the PDF by a Fourier transform

$$G(r) = 4\pi r\rho_0(g(r) - 1) = \frac{2}{\pi}\int_0^\infty Q[S(Q) - 1]\sin(Qr)dQ \tag{2.2.11}$$

Several distribution functions need to be distinguished. First, the original pair distribution function is given as $g(r)$ and approaches 1 for large r and zero for small r. Then, the pair density function is derived by multiplication with the average number density ρ_0

$$\rho(r) = \rho_0 g(r) \tag{2.2.12}$$

and approaches ρ_0 at large r and zero at the low r limit. Finally, G(r) is the reduced pair distribution function

$$G(r) = 4\pi r \rho_0 (g(r) - 1) \tag{2.2.13}$$

G(r) oscillates around zero for large r and approaches $-4\pi r\rho_0$ in the low r range. The obtained G(r) for the nickel powder data presented in Figure 2.2.3 is given in Figure 2.2.4. These three distribution functions contain generally the same information, pro-

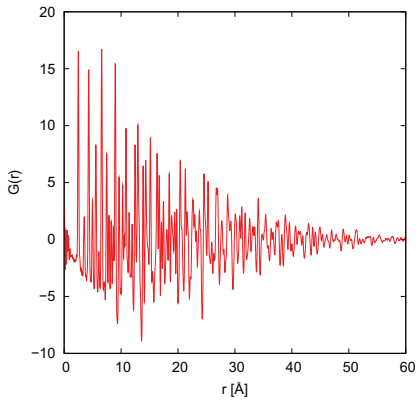

Figure 2.2.4.: Reduced pair distribution function of nickel powder. The decay of the PDF at large r originates in the instrumental resolution.

viding a direct distribution of atomic pair distances in real space. However, for PDF refinement, G(r) is preferably used. The main reason for this is that G(r) is directly obtained by Fourier transformation of the reduced total scattering function (eq. (2.2.11)) without any assumption of the average number density ρ_0. In contrast, the number density can experimentally be derived by analysis of the slope of G(r) at low r. Furthermore, after Fourier transform the uncertainties of G(r) are constant in r, which facilitates refinement of a structure model and comparison to the obtained PDF.

Since S(Q) is obtained from real measured data, only a finite Q range can be probed. The termination of the S(Q) at a suitable Q_{max} is important for generation of a reliable G(r) because termination ripples will occur depending on the chosen Q_{max} as a result of the Fourier transform. Termination ripples will be less pronounced and the resolution obtained in the PDF will be better for a higher Q_{max}. On the other hand, if a large Q_{max}

is chosen, low statistics in the high Q range will result in noise ripples in the obtained PDF. Whereas termination ripples can be modelled during refinement of the PDF, noise ripples are purely statistical and cannot be modelled. For this reason, a high Q_{max} is desired for generation of the PDF, but good statistics in the high Q range is as important. For the study of nanomaterials, a good Q resolution is furthermore required in order to achieve a large r range in the obtained PDF. This is important for determination of the particle size or space resolved local structure deviations within the nanoparticle.

2.2.1.3. X-ray absorption techniques

X-ray absorption spectroscopy is an element specific local probe of the electronic and geometric structure of materials. As a spectroscopy technique, it is strictly speaking not related to scattering methods. However, due to backscattering of emitted photoelectrons the local structure is probed, and for this reason X-ray absorption techniques will be introduced in this section.

Figure 2.2.5a presents exemplarily the absorption spectrum of copper metal in the vicinity of the L and K edges. Absorption of the studied material changes drastically, when the incident X-ray energy is close to the absorption edge of one of the constituent elements. At the absorption edge, the energy is sufficient to excite a core electron to an energy level above the Fermi level. The created hole can then decay by X-ray emission and transfer of an electron from a higher occupied level into the hole. The absorption edge and the energy range up to about 30 eV beyond are called the X-ray Absorption Near Edge Structure (XANES). XANES and the pre-edge range provide information on the electronic structure of the probed atom [10]. In particular the valence state scales linearly with the absorption edge position.

About 30 eV beyond the absorption edge, the Extended X-ray Absorption Fine Structure (EXAFS) region begins [10, 16]. The minima and maxima in the EXAFS spectrum are interpreted as a quantum-interference phenomenon. The outgoing photoelectron can be viewed as a quantum wave that is scattered at the neighboring atoms, leading to constructive and destructive interference of the scattered waves. Because this interference pattern changes with the energy of the virtual photoelectron, the absorption cross section exhibits similar oscillations as presented in Figure 2.2.5b [16]. After normalization and background subtraction, the EXAFS range is converted into a wave number scale of the photoelectron by

$$k = \sqrt{\frac{2m}{\hbar^2}(E - E_0)} \tag{2.2.14}$$

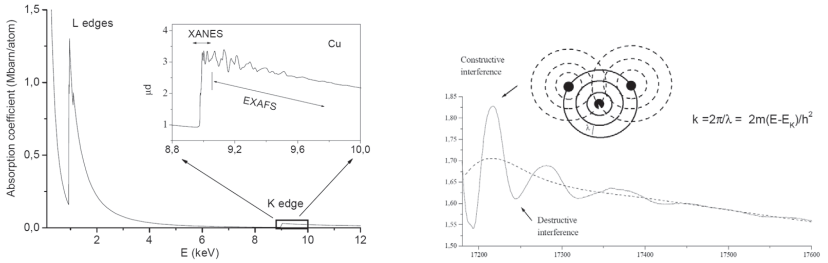

(a) X-ray absorption of copper. The inset presents an expansion of the K edge with assignment of the XANES and EXAFS ranges [15].

(b) Constructive and destructive interference of outgoing and backscattered electron waves [15].

Figure 2.2.5.: X-ray absorption spectroscopy.

with m the electron mass, E the energy of the absorbed photon, and E_0 the energy of the absorption edge. The obtained EXAFS spectrum $\chi(k)$ can be either analyzed in k space or Fourier transformed in order to obtain the real space atomic pair distribution function. The Fourier transform of the EXAFS is generally comparable with the PDF obtained by diffraction, whereas EXAFS probes exclusively the first few coordination shells up to $r \sim 10$ Å. However, the positions of the maxima in both PDFs are not directly comparable due to the different phase shifts measured by EXAFS and diffraction. Whereas the maxima in the diffraction PDF are direct real space distances, the correct distances in the EXAFS can only be obtained by modelling.

The EXAFS can be modelled by computing the contributions from each individual scattering path Γ between absorber and backscattering atom(s) and summing up the individual contributions [17]. As there is an infinite number of possible scattering paths even in a small cluster, it is useful to choose the most important paths contributing to the EXAFS and model those. Important paths are usually single scattering and short double scattering paths as well as collinear multiple scattering paths with a half path length in the evaluated r range. The EXAFS equation used for modelling of the individual scattering paths is given as

$$\chi(k,\Gamma) = \mathrm{Im}\left(\frac{(N_\Gamma S_0^2) F_\Gamma(k)}{kR_\Gamma^2} e^{i(2kR_\Gamma + \Phi_\Gamma(k))} e^{-2\sigma_\Gamma^2 k^2} e^{-2R_\Gamma \lambda(k)}\right) \tag{2.2.15}$$

with

$$R_\Gamma = R_0 + \Delta R_\Gamma \tag{2.2.16}$$

Input parameters generated from a structure model by the FEFF program [16] are the

scattering amplitude $F_\Gamma(k)$, a net phase shift $\Phi_\Gamma(k)$, the mean free path $\lambda(k)$, and the path length R_0. Parameters which can be refined during modelling are the coordination (or degeneracy) N_Γ, the amplitude reduction S_0^2, a change in path length ΔR_Γ, the mean square displacement σ_Γ and an energy shift E_0. The full EXAFS is obtained by the sum over all included path contributions

$$\chi(k) = \sum_\Gamma \chi(k, \Gamma) \tag{2.2.17}$$

2.2.2. Nanoparticle Morphology: Small-Angle Scattering

Small-angle scattering allows for the characterization of density fluctuations in the nanometer size range. With typical small-angle instruments, the magnitude of the wave vector Q can be probed in a range of 10^{-3} to 0.6 $Å^{-1}$, corresponding to real space distances of 1 nm up to several 100 nm. This leads to a wide range of applications in soft matter research, biology, and solid state physics, for investigation of a variety of materials such as polymers, biological samples, microemulsions, colloids, and superconductors. Although both static and dynamic density fluctuations can be probed, this section will be confined to static density fluctuations as investigated throughout this thesis.

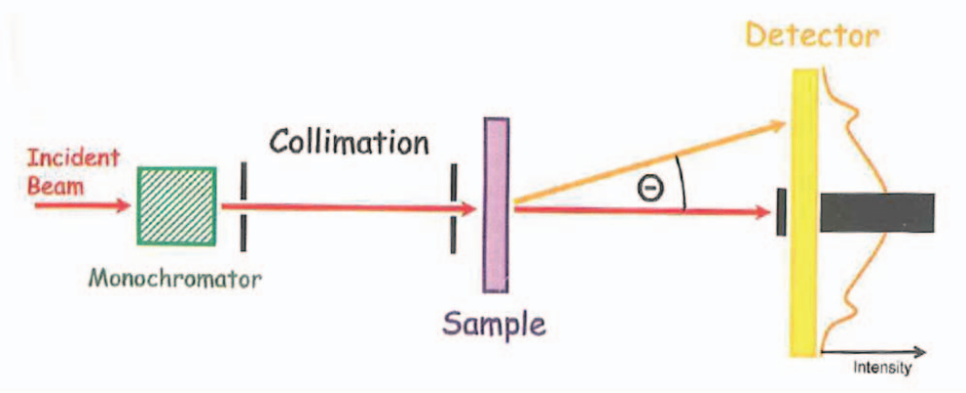

Figure 2.2.6.: Schematic of a small-angle scattering instrument. Figure from [10].

The schematic of a small-angle scattering instrument is given in Figure 2.2.6. A monochromator or wavelength selector determines the wavelength of the incoming photons or neutrons, respectively. In order to measure the scattered intensity at very low angles, the angular divergence of the beam has to be minimized, which is achieved by collimation of the incoming beam. Optimal conditions in terms of resolution and intensity

are achieved when collimation and detector distances are in an equal size range. For this reason, small-angle instruments have a long flight path, with detector and collimation distances up to 20 m for many SANS instruments. In order to achieve a large momentum transfer range, measurements are usually performed at several detector distances [10].

The measured small-angle scattering intensity scales with the respective spatial density difference, the so called contrast. Depending on the probe, different information can be obtained for one and the same sample. X-rays probe fluctuations of the electron density, which is determined by

$$\rho_{el} = \frac{r_e \sum_j Z_j}{V_m} \tag{2.2.18}$$

with the classical electron radius $r_e = 2.81 \cdot 10^{-15}$m, Z_j the electron number of the atom j, and V_m the molecular volume of the formula unit. The nuclear scattering length density, which is probed by neutrons, is determined by the respective nuclear scattering lengths b_j [12]

$$\rho_n = \frac{\sum_j b_j}{V_m} \tag{2.2.19}$$

With polarized neutrons magnetization density fluctuations can be investigated, which will be subject of section 2.2.4. Scattering length density profiles for SAXS and SANS by iron oxide nanoparticles as investigated in section 5.1 are given in Figure 2.2.7. For

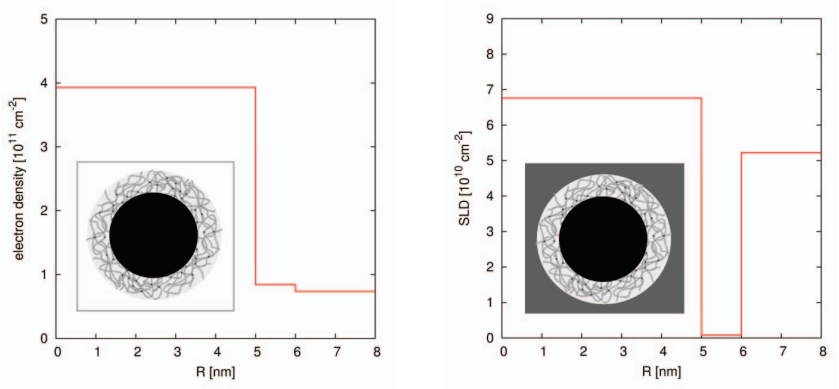

Figure 2.2.7.: Scattering length density profiles for iron oxide nanoparticles with particle radius of 5 nm and oleic acid shell thickness of 1 nm for X-rays (left) and neutrons (right). The insets illustrate the respective contrasts by the shading of particle, shell, and matrix.

X-ray scattering, the contrast between particle core and shell is largest, while for neu-

tron scattering considerable contrasts between all the three components are observed. Consequently, SAXS gives information on the particle core, and SANS gives additional information on the thickness and scattering length density of the particle shell.

Because the scattering length density is in general different for each isotope, contrast variation can be achieved for neutron scattering by a defined variation of the isotopic composition of the different phases. Due to the large difference in scattering length densities of hydrogen and deuterium, (partial) deuteration of the matrix is the most common approach for contrast variation. Thus, the pure shell scattering can be obtained by matching the scattering length densities of solvent and particle core, and an exclusive core contrast can be achieved by matching the scattering length densities of solvent and shell.

The scattering cross section for small-angle scattering by monodisperse particle dispersions can be written as [18]

$$\frac{d\sigma(Q)}{d\Omega} = n\Delta\rho^2 P(Q)S(Q) \tag{2.2.20}$$

where n is the number density of particles, $\Delta\rho$ the scattering contrast between the particles and the solvent, P(Q) the particle form factor, and S(Q) the structure factor. The particle form factor describes the morphology of the individual particles and fulfills the condition of $P(0) = V$ with V the particle volume. The structure factor gives information on the interaction between the particles and the resulting interference of scattering from different particles. For very dilute dispersions of non-interacting particles, the structure factor approaches 1 and can be neglected.

The scattering cross section $\frac{d\sigma(Q)}{d\Omega}$ has the unit of area per solid angle and is measured as the number of scattering events per second with a momentum transfer of Q into the solid angle $d\Omega$. By normalization of measured scattering intensities with the sample volume and calibration with a reference material the absolute scattering intensity μ is obtained in units of cm^{-1}. In what follows, μ [cm^{-1}] will be used for presentation and discussion of small-angle scattering data which have been normalized to absolute units, and $\frac{d\sigma}{d\Omega}$ will be used otherwise.

2.2.2.1. Form factors

The form factor of a given particle is the square of its scattering amplitude which can generally be derived by the Fourier transform of the radial density distribution.

$$P(\vec{Q}) = F(\vec{Q})^2 = \left| \int \rho(\vec{r}) e^{-i\vec{Q}\vec{r}} d\vec{r} \right|^2 \tag{2.2.21}$$

For a centrosymmetric object, this expression reduces to

$$F(Q) = 4\pi \int \rho(r) \frac{\sin(Qr)}{Qr} r^2 dr \tag{2.2.22}$$

There are basic particle shapes for which the integral in equation (2.2.21) can be solved analytically. For a homogeneous spherical particle with constant density ρ for $r \leq R$, the scattering amplitude is given by

$$F_{sphere}(Q,R) = 4\pi \int_0^R \frac{\sin(Qr)}{Q} r dr = \frac{4}{3}\pi R^3 \frac{3[\sin(QR) - QR\cos(QR)]}{(QR)^3} \tag{2.2.23}$$

while for a linearly increasing radial density distribution with $\rho(r) = mr$ the scattering amplitude is given by [19]

$$F_{lin}(Q,R) = 4\pi m \int_0^R \frac{\sin(Qr)}{Q} r^2 dr = 4\pi m R^4 \frac{2\cos(QR) + 2QR\sin(QR) - (QR)^2\cos(QR)}{(QR)^4} \tag{2.2.24}$$

For an oriented cube with edge length a the scattering amplitude results in

$$F_{cube}(Q_x, Q_y, Q_z, a) = \frac{8}{a^3 Q_x Q_y Q_z} \cdot \sin\frac{a}{2}Q_x \sin\frac{a}{2}Q_y \sin\frac{a}{2}Q_z \tag{2.2.25}$$

A comprehensive list of these and further frequently used form factors has been given by Pedersen [18].

Core shell form factors A wide variety of more complex form factors can be generated analytically by linear combination of the amplitudes of underlying basic form factors. As an example, the core shell form factor of a sphere with a uniform shell thickness will be derived.

The scattering length density (SLD) profile of the particles under discussion is presented in Figure 2.2.8. It can be separated into the SLD profiles of two individual spheres with the radii R_{core} and (R_{core} + d_{shell}) and contrasts of $\Delta\rho_{core} = \rho_{core} - \rho_{shell}$ and $\Delta\rho_{shell} = \rho_{shell} - \rho_{matrix}$, respectively. Same as the scattering length density profile of the core shell particle can be derived by linear combination of these more simple SLD profiles, the scattering amplitude is derived by linear combination of the amplitudes of the two spherical form factors weighted by the respective scattering contrasts and volumina.

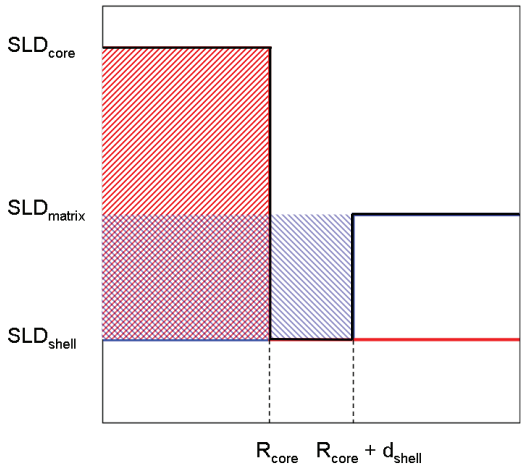

Figure 2.2.8.: SLD profile of a core shell particle (black line). SLD profiles of spherical particles with R = R_{core} and R = (R_{core} + d_{shell}) are shown in red and blue, respectively.

$$\begin{aligned} F_{core-shell}(Q) = (\rho_{core} - \rho_{shell})F_{sphere}(Q, R_{core}) \\ +(\rho_{shell} - \rho_{matrix})F_{sphere}(Q, R_{core+shell}) \end{aligned} \tag{2.2.26}$$

As in equation (2.2.21), the square of the obtained scattering amplitude gives the scattering intensity measured by small-angle scattering. By this approach, various core and shell geometries can be employed to derive core shell form factors, such as the truncated cubic form factor with different shell geometries derived in section 5.1.2.3 or the linear shell model for the magnetic form factor derived in section 5.3.2.2.

2.2.2.2. Structure factors

Interparticle interactions give rise to additional or reduced scattering contributions in the lower Q range, depending on the interaction potential. The resulting structure factor is related to the respective interaction potential.

For a repulsive interaction potential, the scattering at low Q is reduced. In case of short range ordered correlations such as the Percus Yevick hard spheres interaction [21] or the sticky hard spheres potential [22], the scattering exhibits a correlation peak. The structure factor of liquid ^{36}Ar is shown exemplarily in Figure 2.2.9a [20]. The Q posi-

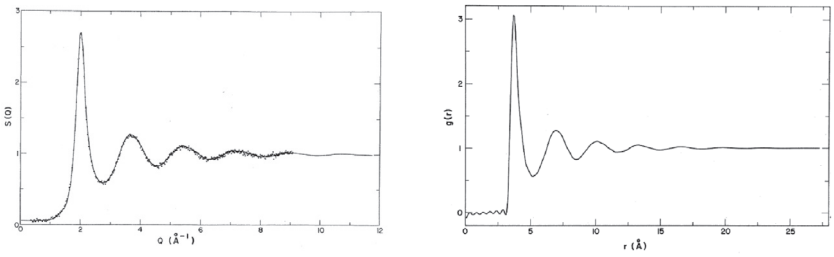

(a) Structure factor or liquid ^{36}Ar as obtained by neutron scattering. The line is obtained from a molecular dynamics calculation.

(b) Radial distribution function obtained from S(Q).

Figure 2.2.9.: Hard spheres structure factor obtained for liquid ^{36}Ar [20].

tion of this first order correlation peak corresponds to the mean distance of the particle centers

$$d = 2(R + dR) = \frac{2\pi}{Q} \tag{2.2.27}$$

where R denotes the particle radius and dR the thickness of a possible ligand shell of nanoparticles. By a Fourier transform the full structure factor can be converted into the pair correlation function as shown in Figure 2.2.9b, giving real space information on the local order [23].

In case of attractive interparticle interactions, an increase in intensity at low Q is observed as a result of a mass fractal [24]. The exhibited power law determines the fractal dimension. Thus, a Q^{-1} power law points to a rigid linear arrangement, while a Q^{-2} behavior is observed for a flexible and more dense arrangement such as a polymer coil.

2.2.2.3. Size distribution

The expression for the scattering cross section given in equation (2.2.20) is based on the assumption of monodisperse objects. However, because real samples always exhibit a varying degree of size dispersion, the particle size distribution has to be taken into account. This is achieved by weighting the scattering cross section of non-interacting nanoparticles with a size distribution function $D(R, R_0, \sigma)$

$$\frac{d\sigma(Q)}{d\Omega} = n\Delta\rho^2 \int P(Q,R)D(R,R_0,\sigma)dR \tag{2.2.28}$$

Throughout this thesis, a lognormal distribution was implemented to model the particle size distributions.

$$D(R, R_0, \sigma) = \frac{1}{\sqrt{2\pi}\sigma R} \cdot \exp\left(-\frac{\ln(\frac{2R}{R_0})}{2\sigma^2}\right) \tag{2.2.29}$$

The advantage of this distribution function over a standard Gaussian distribution is the logarithmic weighting that ensures that even for small particle sizes and wide size distributions no negative particle size is assumed.

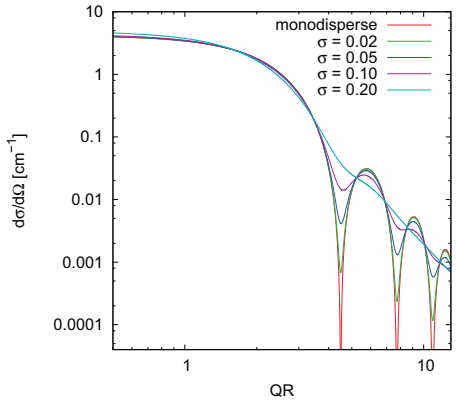

Figure 2.2.10.: Effect of particle size distribution on small-angle scattering.

The effect of different size distributions on the scattering cross section is illustrated in Figure 2.2.10. The largest effect of increasing size distribution is observed for the form factor minima. For a lognormal size distribution of 20 %, the minima are entirely smeared out. Thus, the measurement of one or several form factor minima is crucial for a precise determination of the particle size distribution.

If a structure factor is observed, implementation of the size distribution requires partial structure factors that account for interparticle interactions of particles with different particle sizes [18]. For narrow size distributions, a decoupling approach can be applied under the assumption of interparticle interactions independent on the particle size [25]. A further approach is the local monodisperse approximation, which is based on the assumption that a particle of a certain size is always surrounded by particles of the same size [26]. A comparison of these approaches is given in [18].

2.2.2.4. Instrumental resolution

Next to the particle size distribution, the instrumental Q resolution is another parameter resulting in smearing of the form factor minima. In order to get reliable information on particle size and size distribution, the instrumental resolution thus has to be determined carefully and implemented into the scattering cross section model.

An expression for the Q resolution of small-angle scattering experiments is obtained by differentiation of equation (2.2.3)

$$dQ = \sqrt{\left(\frac{4\pi}{\lambda}\right)^2 d\theta^2 + Q^2\left(\frac{d\lambda}{\lambda}\right)^2} \tag{2.2.30}$$

Thus, the instrumental uncertainty of the scattering vector ΔQ originates in two independent conributions:

$$\left(\frac{\Delta Q}{Q}\right)^2 = \left(\frac{\Delta\theta}{\theta}\right)^2 + \left(\frac{\Delta\lambda}{\lambda}\right)^2 \tag{2.2.31}$$

where $\Delta\theta$ denotes all angular uncertainties which originate from the collimation apertures and the finite size of the detector elements, and $\frac{\Delta\lambda}{\lambda}$ is the wavelength spread arising from the wavelength distribution of the velocity selector or the monochromator.

Q resolution can be implemented into a scattering model by smearing the scattering intensity with a Gaussian function representing instrumental resolution.

$$\frac{d\sigma(Q)}{d\Omega} = n\Delta\rho^2 \int P(Q,R)Q_{res}(Q,Q_0,\sigma_Q)dQ \tag{2.2.32}$$

with

$$Q_{res}(Q,Q_0,\sigma_Q) = \frac{1}{\sqrt{2\pi}\sigma_Q}\cdot\exp\left(-\frac{(Q-Q_0)^2}{2\sigma_Q^2}\right) \tag{2.2.33}$$

The standard deviation σ_Q of the Gaussian is connected to the FWHM dQ of the resolution function by

$$\sigma_Q^2 = \frac{1}{8ln2}dQ^2 \tag{2.2.34}$$

Taking into account all instrumental resolution parameters, the angular uncertainty results in [27]

$$\sigma_Q^2 = \frac{1}{8ln2}k^2\left((\Delta\beta)^2 + \left(\frac{d_D}{L_D}\right)^2 + \theta^2\left(\frac{\Delta\lambda}{\lambda}\right)^2\right) \tag{2.2.35}$$

with:

$$\Delta\beta = \frac{d_E}{L_C} - \frac{1}{4}\frac{d_S^2}{d_E}\frac{(L_C + L_D)^2}{L_C L_D^2} \tag{2.2.36}$$

with d_E and d_S the collimation and sample apertures, respectively, d_D the detector pixel size, and L_C and L_D the collimation length and detector distance, respectively. The pure angular divergence term in equation (2.2.30) including the detector resolution results in

$$d\theta = \sqrt{(\Delta\beta)^2 + \left(\frac{d_D}{L_D}\right)^2} \tag{2.2.37}$$

2.2.2.5. Asymptotic behavior

Depending on the sample size, size distribution, and possible byproduct scattering contributions, there may not be any obvious minima visible in the small-angle scattering pattern. Consequently, the particle morphology, size and size distribution can not be determined with high precision. However, some information can be drawn from the asymptotic behavior of the scattering slope. For non-interacting particles and in the limit of very low Q (R_GQ < 1), the scattering intensity follows the Guinier approximation [28]

$$I(Q) = I(Q = 0) \cdot \exp\left(-\frac{(QR_G)^2}{3}\right) \tag{2.2.38}$$

where R_G denotes the radius of gyration of the particle or the weighted average of the radii of gyration of a mixture of particles. The radius of gyration is not equal to the spherical nanoparticle radius, but can be calculated for many simple bodies as given in Table 2.2.2 [29].

The asymptotic scattering behavior at higher Q can give information on the particle surface. For dense spherical particles with a smooth surface, the scattering density follows a so-called Porod law of I(Q) $\propto Q^{-4}$. For particles with a more rough surface, the scattering intensity may decrease even faster, while for flexible objects such as polymer coils, a Porod law of I(Q) $\propto Q^{-2}$ is observed [23].

Beaucage has combined the characteristics of several Guinier and Porod laws into a unified power law that allows for interpretation of multiple hierarchical levels of structure [30].

Table 2.2.2.: Radii of gyration of simple triaxial bodies.

body		R_G^2
sphere	radius R	$\frac{3}{5}R^2$
hollow sphere	radii R_1 and R_2	$\frac{3}{5}\frac{(R_2^5-R_1^5)}{(R_2^3-R_1^3)}$
ellipsoid	semi-axes a, b, c	$\frac{(a^2+b^2+c^2)}{5}$
parallelepiped	edge lengths A, B, C	$\frac{(A^2+B^2+C^2)}{12}$
elliptic cylinder	semi-axes a,b; height h	$\frac{(a^2+b^2)}{4}+\frac{h^2}{12}=R_c^2+\frac{h^2}{12}$

R_c is the cross-sectional radius of gyration.

2.2.2.6. Anomalous Small-Angle Scattering

Contrast variation is a versatile tool in small-angle scattering for differentiation between different nanostructure components. In case of neutron scattering, isotope substitution is commonly performed, *e. g.* by use of fully or partially deuterated compounds. For X-ray scattering, the Anomalous Small-Angle X-ray Scattering (ASAXS) technique allows for separation of element-specific scattering contributions from the total scattering.

Contrast variation by ASAXS is based on the variation of the atomic form factor with the X-ray energy in vicinity of an absorption edge.

$$f(Q,E) \simeq f(Q) + f'(E) + if''(E) \tag{2.2.39}$$

The anomalous dispersion correction terms f′ and f″ change drastically with energy when the incident energy is close to the absorption edge of the respective element. Thus, two measurements of the same sample at different incident energies much lower and close to the absorption edge of a particular element will differ in scattering intensity. This difference will be due to the scattering contribution of the respective element, which is diminished when approaching the absorption edge. This anomalous scattering effect is often very small, in the range of 10^{-2} – 10^{-3} of the total scattering cross section. Thus, precise measurements of the differential scattering cross section at different incident energies are required.

The measured scattering intensity is the square modulus of the total scattering amplitude, and consists thus of a non-resonant, a mixed-resonant, and a pure-resonant term.

$$I(Q,E) = |F_{\text{total}}(Q)|^2 = |F_{\text{non-res}}(Q)|^2 + |F_{\text{mix}}(Q,E)|^2 + |F_{\text{res}}(Q,E)|^2 \tag{2.2.40}$$

Subtraction of two scattering curves $\Delta I(Q, E_1, E_2) = I(Q, E_1) - I(Q, E_2)$ thus leads to a combination of both mixed and pure-resonant scattering contributions. In order to separate the pure-resonant scattering contribution, the scattering cross section has to be measured at three different energies below the absorption edge. Separation is then performed by subtraction of two separated scattering curves $\Delta I(Q, E_1, E_2)$ and $\Delta I(Q, E_1, E_3)$ with normalization to the energy-dependent anomalous dispersion corrections [31].

$$|F_{\text{res}}(Q, E)|^2 = \left[\frac{\Delta I(Q, E_1, E_2)}{f'(E_1) - f'(E_2)} - \frac{\Delta I(Q, E_1, E_3)}{f'(E_1) - f'(E_3)} \right] \cdot \frac{1}{K(E_1, E_2, E_3)} \tag{2.2.41}$$

with

$$K(E_1, E_2, E_3) = f'(E_2) - f'(E_3) + \frac{f''^2(E_1) - f''^2(E_2)}{f'(E_1) - f'(E_2)} - \frac{f''^2(E_1) - f''^2(E_3)}{f'(E_1) - f'(E_3)} \tag{2.2.42}$$

Due to the normalization to the anomalous dispersion corrections, E_1, E_2, and E_3 are interchangeable. However, the three different incident energies need to be chosen carefully in order to maximize the anomalous scattering contrast.

2.2.3. Nanoparticle assemblies: Scattering under grazing incidence

For investigation of nanoparticle assemblies in two or three dimensions, the grazing incidence geometry has several advantages. First, if the incident angle of the incoming X-ray or neutron beam is small, the large footprint of the beam allows for investigation of a large sample volume. This is important because the sample thickness for transmission scattering experiments has to be kept rather small, *e. g.* in the range of 1 - 2 mm for small-angle neutron scattering. Secondly, substrate absorption is not problematic because grazing incidence scattering is in general measured in the reflection hemisphere (whereas for GISANS the transmission hemisphere can give complementary information). Furthermore, intensity enhancements due to dynamical diffraction effects close to the condition of total reflection can be exploited. Finally, because the sample is confined to the two dimensional substrate, density correlations can be probed in different correlation lengths and directions, depending on the scattering method, as will be shown in this section.

The scattering geometry for grazing incidence scattering is presented in Figure 2.2.11. The sample coordinate system is defined with z perpendicular to the substrate. The incoming beam enters the sample under a shallow angle α_i, and the scattered beam is

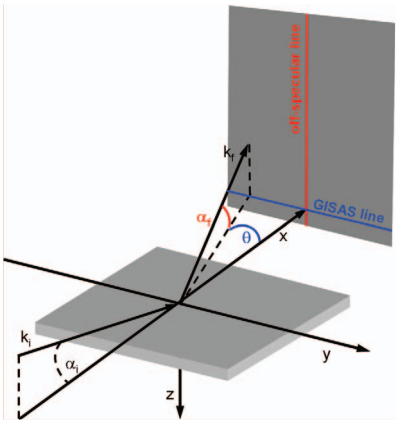

Figure 2.2.11.: Grazing incidence scattering geometry.

determined by specifying two angles for the in plane component $2\theta_f$ and the out of plane component α_f[1]. The components of the scattering vector $\vec{Q}$ are thus given by

$$Q_x = \frac{2\pi}{\lambda}(\cos(\alpha_f)\cos(2\theta_f) - \cos(\alpha_i)) \tag{2.2.43}$$

$$Q_y = \frac{2\pi}{\lambda}\cos(\alpha_f)\sin(2\theta_f) \tag{2.2.44}$$

$$Q_z = -\frac{2\pi}{\lambda}(\sin(\alpha_f) + \sin(\alpha_i)) \tag{2.2.45}$$

There are three different approaches of grazing incidence scattering that give different information: specular reflectivity, off-specular reflectivity, and grazing incidence small-angle scattering (GISAS).

2.2.3.1. Specular reflectivity

The specular reflection is observed at $\alpha_f = \alpha_i$ and $2\theta_f = 0$. Following equations (2.2.43) - (2.2.45), the scattering vector reduces to $Q_z = -\frac{4\pi}{\lambda}\sin(\alpha)$ without any x or y contributions. Accordingly, specular reflectivity gives exclusively information on the sample profile perpendicular to the substrate, such as the layer thickness, roughness, or layer sequence. For a typical specular reflectivity measurement, α_i and $\alpha_f = \alpha_i$ are varied simultaneously, and the intensity of the specular reflection is measured, *e. g.* with a point detector, in dependence of the incident angle. At incident angles below the critical angle,

[1]The coordinate system is defined such that $\theta_i = 0$.

total reflection occurs and the detected intensity remains constant[2]. At higher incident angles, the scattered intensity decreases with Q^{-4} (for a single interface) with a slope depending on the critical angle. The critical angle of total reflection is defined via Snell's law

$$\frac{\cos(\alpha_i)}{\cos(\alpha_t)} = \frac{k_t}{k_i} = n_1 \tag{2.2.46}$$

where k_i and k_t are the wave vectors of the incident and transmitted beam, respectively. The index of refraction of the material n_1 is given by the ratio $\frac{k_t}{k_i}$ and relates to the scattering length density ρ by

$$n = 1 - \delta \tag{2.2.47}$$

with

$$\delta = \frac{\lambda^2}{2\pi}\rho \tag{2.2.48}$$

and the electron and scattering length densities ρ_{el} and ρ_n as given for X-ray and neutron scattering by equations (2.2.18) and (2.2.19), respectively. Absorption of X-rays or neutrons can be taken into account by addition of an imaginary part to the refractive index

$$n = 1 - \delta + i\beta \tag{2.2.49}$$

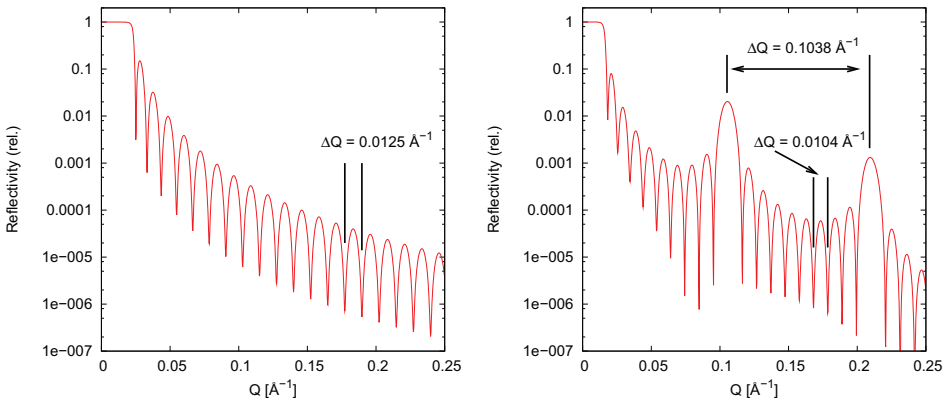

(a) A nickel monolayer of 500 Å thickness.

(b) A nickel - silicon multilayer of 60 Å with 10 repetitions.

Figure 2.2.12.: Theoretical specular reflectivity curves [32].

[2]In a real measurement, the scattered intensity is not observed as a plateau due to the shadowing effect of the sample. This effect is corrected by division of the data by $\sin(\alpha_i)$.

In case of a rough surface, a larger part of the beam is scattered off-specularly, resulting in an even faster decrease of the scattered intensity with incident angle. If a homogeneous monolayer is probed, *e. g.* a thin layer of nickel (Figure 2.2.12a), the beam can be reflected at either the surface of the sample or the interface between nickel and the substrate, whereas refraction at the surface has to be taken into account as well. As a result of the interference of the two differently reflected beams, so called Kiessig fringes are observed in the measured reflectivity curve. The distance between the individual fringes at higher angles (where refraction can be neglected) contains the information of the layer thickness

$$d_{monolayer} = \frac{2\pi}{\Delta Q_{Kiessig}} \tag{2.2.50}$$

For a precise determination of the layer thickness, a significant contrast of critical angles of sample and substrate is required, because this enhances the relative intensity of the fringes. Furthermore, a homogeneous surface and interface is important, because the Kiessig fringes are smeared out by interface roughness.

If a multilayer sample is probed, Bragg reflections are observed as additional feature as presented in Figure 2.2.12b. These multilayer peaks scale with the contrast between the individual layers and give information on the thickness of a single multilayer repetition by

$$d_{multilayer} = \frac{2\pi}{\Delta Q_{Bragg}} \tag{2.2.51}$$

Depending on the contrast to the substrate, additional Kiessig fringes may be observed in between the multilayer Bragg reflections. These Kiessig fringes contain the information on the number of multilayer repetitions by

$$d_{sample} = N \cdot d_{multilayer} = \frac{2\pi}{\Delta Q_{Kiessig}} \tag{2.2.52}$$

Consequently, a number of N repetitions of the multilayer unit leads to N-2 Kiessig fringes in between two Bragg reflections. An analytic derivation of the reflectivities of thin layers and multilayers is given in [33, 34]

2.2.3.2. Off-specular reflectivity

For off-specular reflectivity, the entire off-specular scattering line in Figure 2.2.11 is measured in dependence of the incident angle. With $\alpha_i \neq \alpha_f$ and $2\theta_f = 0$, the scattering vector

according to equations (2.2.43) - (2.2.45) has contributions in x and z directions:

$$Q_x = \frac{2\pi}{\lambda}(\cos(\alpha_f) - \cos(\alpha_i)) \tag{2.2.53}$$

$$Q_z = -\frac{2\pi}{\lambda}(\sin(\alpha_f) + \sin(\alpha_i)) \tag{2.2.54}$$

For small incident and scattered angles, the Q_x contribution is much smaller than the Q_z contribution. Consequently, the accessible lateral correlation lengths are typically in the range of 100 nm and much larger than correlation lengths perpendicular to the substrate. Thus, different length scales are probed simultaneously in one experiment. In a typical off-specular measurement, α_f is scanned in dependence of α_i or vice versa. The data can be illustrated in a 3D plot of scattering intensity versus α_i and α_f. The specular intensity of exclusively out of plane scattering is then visible at the diagonal with $\alpha_i = \alpha_f$. Along perpendicular diagonals with $\alpha_i + \alpha_f = const$, pure lateral scattering contributions are measured for the respective constant Q_z. Thus, off-specular scattering can give depth-resolved information on lateral structures [10].

Related to the samples of nanoparticle mesocrystals investigated throughout this thesis, lateral correlations were investigated on much smaller lengths scales than achievable with off-specular reflectivity. Instead, single off-specular scattering scans were measured for particular incident angles in order to complement and support the performed Grazing Incidence Small-Angle X-ray Scattering (GISAXS) studies. This is necessary because during a synchrotron radiation GISAXS experiment the off-specular line is usually blocked by a beam stop to avoid saturation of the detector.

2.2.3.3. Grazing Incidence Small-Angle Scattering

By grazing incidence small-angle scattering (GISAS), a third dimension of the scattering vector is investigated as for each defined incident angle, a full 2D GISAS pattern is measured with $\alpha_i \neq \alpha_f$ and $2\theta_f \neq 0$. In order to achieve a good resolution in all directions, an incident beam collimated in two dimensions is required. For measurement of a full 2D pattern, also a position sensitive 2D detector is useful. For these reasons GISAS experiments are usually performed on small-angle scattering instruments.

The 2D GISAS pattern can be described by the $2\theta_f$ and α_f contributions measured in direction of the x and y axis of the detector image, respectively. The specular reflection is detected at $\alpha_i = \alpha_f$ and $2\theta_f = 0$, and in case of neutron scattering, the transmission is often large enough to allow for detection of the transmitted beam, which is located below the sample horizon. Both reflections are located on the off-specular scattering line

at $2\theta_f = 0$ and can thus also be determined by a single off-specular scan. This is useful because in many GISAXS measurements a beam stop is located at this high intensity line, in order to allow for longer exposure times and thus better statistics in the lower intensity regions.

The so called Yoneda line [35], is located at $\alpha_f = \alpha_c$ (α_c: critical angle of total reflection) and contains exclusively lateral scattering contributions. Because the Q_y component of the scattering vector does not contain any out of plane scattering, the Bragg equation can be applied to reflections in the Yoneda line without any refraction correction.

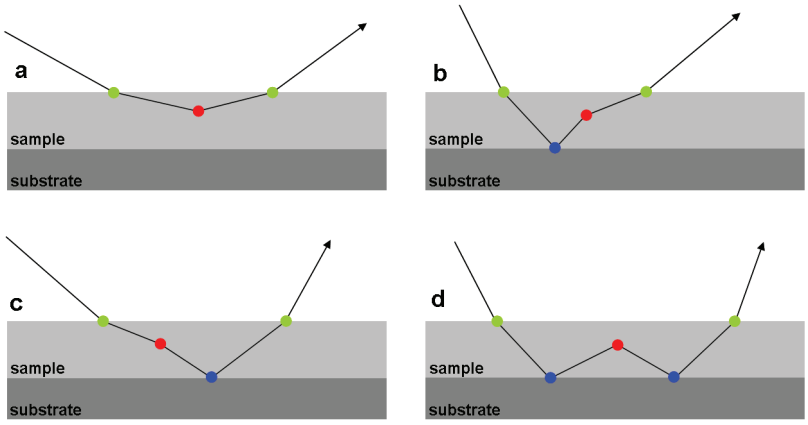

Figure 2.2.13.: Possible X-ray scattering paths under grazing incidence. Refraction, reflection, and scattering events are marked by green, blue, and red points, respectively. For neutron scattering, transmission by the substrate has to be considered additionally. Reproduced after [34].

In order to study the scattering contributions perpendicular to the substrate, appearing above (and for neutron scattering also below) the sample horizon, refraction of the beam at the air-sample interface has to be taken into account. Four cases of possible scattering paths have to be considered as illustrated in Figure 2.2.13: reflection of the incoming beam at the respective lattice plane a) without any reflection at the substrate, with reflection at the substrate b) before or c) after the scattering event, and d) with reflection before and after the scattering event. Because each reflection at the substrate extends the scattering path within the material and thus results in a loss in intensity, the latter case is not observed in GISAXS. For the same reason, signals resulting from a single reflection at the substrate are usually much lower in intensity and also broader as compared to non-reflected signals. The b) and c) cases can not be distinguished by

GISAXS, resulting with a) in a set of two signals emanating from each lattice plane. For a quantitative evaluation of the GISAXS intensities, the distorted wave Born approximation (DWBA) has to be applied. However, as for the present study a qualitative evaluation of the reflection positions was sufficient, a combination of Bragg's and Snell's laws [36] was applied as described in section 5.4.2.3. An introduction into DWBA is given in [10, 34].

2.2.4. Nanoparticle magnetization: polarized neutron scattering

Polarized neutron scattering is required in order to separate individual scattering contributions, such as nuclear coherent and spin-incoherent scattering or magnetic scattering.

A polarized neutron beam can be obtained by either total reflection from magnetic multilayers, Bragg reflection of polarizing single-crystals (Heusler crystals), or absorption by polarized ^{3}He filters. Both total reflection at magnetic thin layers and reflection of polarizing single-crystals take advantage of different scattering cross sections depending on the neutron polarization. In a magnetic supermirror, neutrons with a defined polarization direction are reflected, while neutrons with opposite polarization direction are transmitted or absorbed. The critical angle is seemingly increased by Bragg reflection from alternating layers of a ferromagnetic and a non magnetic material of varying thickness. ^{3}He filter cells take advantage of a different absorption cross section depending on the polarization. Neutrons with polarization parallel to the He polarization pass the filter cell, while neutrons with an antiparallel polarization are absorbed.

The polarized neutron beam has to be kept in a weak magnetic guide field in order to maintain the polarization. The guide field has to be weak enough not to affect the sample magnetization, but strong enough to overcome the earth magnetic field as well as any surrounding stray fields.

Spin flippers are used in order to change the polarization direction of the beam. In so-called Mezei flippers, this is achieved by Larmor precession of the neutron spin induced by a magnetic field perpendicular to the polarization. The flipper itself is a rectangular coil providing a homogeneous field. Field strength and flight path of the neutrons through the flipper are tuned to achieve the desired degree of precession, *e. g.* for a π flipper, the neutron polarization precesses exactly by an angle π before leaving the flipper. Thus, a π flipper is used to invert the neutron polarization. A $\frac{\pi}{2}$ flipper can be used to rotate the polarization by 90° and induce Larmor precession in the guide field. This is required for *e. g.* Neutron Spin Echo Spectroscopy or spherical polarization analysis.

In order to perform polarization analysis, an analyzer is placed between the sample and the detector to allow for detection of a specific directional component of the neutron

polarization. Technically, the analyzer has the same function as a polarizer, with the same functional principle, *i. e.* a supermirror (as used at DNS), a Heusler crystal (IN12), or a ^{3}He filter cell (D22, intended for KWS 1 and MARIA).

2.2.4.1. Scattering cross sections

Nuclear scattering results from interaction of the neutron with the scattering nucleus. The nuclear interaction is isotope-specific and also spin-dependent, if the scattering nuclei have a non-zero spin. Three contributions of nuclear scattering are distinguished, namely nuclear coherent scattering, isotope-incoherent scattering, and spin-incoherent scattering

$$\begin{aligned} \sigma^N_{\vec{Q}} &= \mid N_{\vec{Q}} \mid^2 \\ &= \sigma^N_{\vec{Q},coh} + \sigma^N_{isotope-inc} + \sigma^N_{spin-inc} \end{aligned} \tag{2.2.55}$$

with $N_{\vec{Q}}$ the nuclear term of the total scattering amplitude

$$N_{\vec{Q}} = \sum_j b_j e^{i\vec{Q}\vec{r}_j} \tag{2.2.56}$$

The isotopic-incoherent scattering results from the variation of scattering lengths among the different isotopes, while spin-incoherent scattering results from interaction of the neutron spin with randomly oriented nuclear spins. Coherent and isotope-incoherent scattering do not affect the polarization of the scattered neutron. In contrast, the neutron polarization is flipped by the component of the nuclear spin perpendicular to the neutron polarization. Because the nuclear spins are oriented randomly, two thirds of the spin-incoherent scattering are spin-flip scattering.

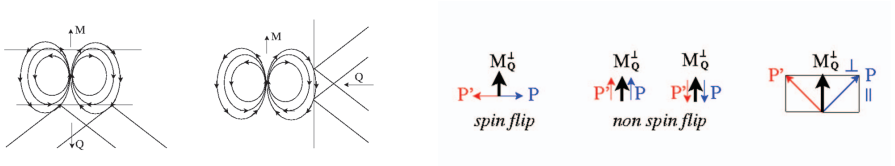

(a) Magnetic field amplitudes of the dipole field show destructive interference for $\vec{M} \parallel \vec{Q}$ (left) and constructive interference for $\vec{M} \perp \vec{Q}$ (right).

(b) Only the polarization component perpendicular to $\vec{M}_{\vec{Q}}^{\perp}$ is flipped.

Figure 2.2.14.: Magnetic scattering with respect to scattering vector and polarization. Pictures from [10].

Magnetic scattering results from interaction of the neutron spin with the magnetic dipole field of the sample. Interference of the scattered waves can be constructive or destructive, depending on the relative orientation of the magnetic dipole field and the scattering vector. As illustrated in Figure 2.2.14a, the interference is constructive for $\vec{M} \perp \vec{Q}$, where $\vec{M}$ denotes the Fourier transform of the microscopic magnetization density. Consequently, only contributions of the magnetization perpendicular to the scattering vector are detected. The magnetic scattering length density is thus given by

$$SLD_m = 0.27 \cdot 10^{-12} cm \frac{\Sigma M_j^{\perp}}{V_m} \tag{2.2.57}$$

Upon scattering at a magnetic dipole, the neutron polarization component perpendicular to the magnetic field amplitude is flipped, as illustrated in Figure 2.2.14b. As a consequence, if the vector of the neutron polarization $\vec{P} \parallel \vec{Q}$ and $\vec{P}, \vec{Q} \perp \vec{M}$, then all magnetic scattering will be spin flip scattering.

There are two equations that describe the scattering process for the scattering cross section σ (equation (2.2.58)) and for $\vec{P'}\sigma$ (equation (2.2.59)), where $\vec{P'}$ denotes the polarization after the scattering process [37–40]

$$\begin{aligned} \sigma_{\vec{Q}} \;=\; & \sigma^N_{\vec{Q},coh} + \sigma^N_{isotope-inc} + \sigma^N_{spin-inc} \\ & + \mid \vec{M}^{\perp}_{\vec{Q}} \mid^2 + \vec{P}\,(N_{-\vec{Q}} \vec{M}^{\perp}_{\vec{Q}} + \vec{M}^{\perp}_{-\vec{Q}} N_{\vec{Q}}) + i\,\vec{P}\,(\vec{M}^{\perp}_{-\vec{Q}} \times \vec{M}^{\perp}_{\vec{Q}}) \end{aligned} \tag{2.2.58}$$

$$\begin{aligned} \vec{P}'\sigma_{\vec{Q}} \;=\; & \vec{P}\,\sigma^N_{\vec{Q},coh} + \vec{P}\,\sigma^N_{isotope-inc} - \frac{1}{3}\vec{P}\,\sigma^N_{spin-inc} \\ & + \vec{M}^{\perp}_{\vec{Q}}(\vec{P}\,\vec{M}^{\perp}_{-\vec{Q}}) + \vec{M}^{\perp}_{-\vec{Q}}(\vec{P}\,\vec{M}^{\perp}_{\vec{Q}}) - \vec{P}\,\vec{M}^{\perp}_{\vec{Q}}\vec{M}^{\perp}_{-\vec{Q}} \\ & + \vec{M}^{\perp}_{\vec{Q}} N_{-\vec{Q}} + \vec{M}^{\perp}_{-\vec{Q}} N_{\vec{Q}} + i\vec{M}^{\perp}_{\vec{Q}} \times \vec{M}^{\perp}_{-\vec{Q}} + i(\vec{M}^{\perp}_{\vec{Q}} N_{-\vec{Q}} - \vec{M}^{\perp}_{-\vec{Q}} N_{\vec{Q}}) \times \vec{P} \end{aligned} \tag{2.2.59}$$

Equation 2.2.58 shows that the scattering cross section is composed of the polarization independent contributions $N^2_{\vec{Q}}$ and $\mid \vec{M}^{\perp}_{\vec{Q}} \mid^2$, a polarization dependent cross term of $N_{\vec{Q}}$ and $\vec{M}^{\perp}_{\vec{Q}}$, and an imaginary polarization dependent cross product of $\vec{M}^{\perp}_{\vec{Q}}$. The cross product accounts for chiral correlations which can be found in complex magnetic materials and can result in the creation of polarization from an unpolarized incident beam. Because the materials investigated in this theses do not exhibit any chiral contributions, this term will be neglected for subsequent calculations.

2.2.4.2. Polarization analysis

The aim of polarization analysis is the determination of the 3 x 3 polarization matrix $\overrightarrow{P}_{ij}$, that describes the rotation of the initial polarization during scattering

$$\overrightarrow{P}'_i = \overrightarrow{P}_{ij}\overrightarrow{P}_j + \overrightarrow{P}''_i \tag{2.2.60}$$

Here, $\overrightarrow{P}''_i$ denotes the polarization created during scattering which can be determined experimentally but may be neglected for the case of magnetic nanoparticles, in case of small-angle scattering and if the particles are not magnetically oriented.

In order to identify all magnetic scattering contributions including scattering with chirality and magnetic-nuclear interference, a determination of all matrix elements is required. However, the determination of the trace of the (3 x 3) polarization matrix allows for separation of paramagnetic scattering from nuclear scattering. The standard technique developed by Moon, Riste, and Koehler is called longitudinal polarization analysis (LPA) [41], and is performed both with polarization parallel and perpendicular to $\overrightarrow{Q}$. The difference gives the pure magnetic scattering contribution [42]. Because $\overrightarrow{P} \parallel \overrightarrow{Q}$ can not be performed in a single measurement with today's multi-detector instruments, xyz polarization analysis is performed. The z direction is defined perpendicular to the scattering plane, *i. e.* $\overrightarrow{P} \parallel z$ equals $\overrightarrow{P} \perp \overrightarrow{Q}$. The x and y directions are perpendicular to each other and perpendicular to z, *i. e.* in the scattering plane. The sum of measurements with $\overrightarrow{P}$ along x and y directions thus equals the sum of measurements with $\overrightarrow{P}$ parallel and perpendicular to $\overrightarrow{Q}$. Consequently, the pure paramagnetic scattering contribution can be derived by [43, 44]

$$\frac{d\sigma}{d\Omega_{pm}} = 2\left(\frac{d\sigma}{d\Omega_x}^{SF} + \frac{d\sigma}{d\Omega_y}^{SF} - 2\frac{d\sigma}{d\Omega_z}^{SF}\right) = -2\left(\frac{d\sigma}{d\Omega_x}^{NSF} + \frac{d\sigma}{d\Omega_y}^{NSF} - 2\frac{d\sigma}{d\Omega_z}^{NSF}\right) \tag{2.2.61}$$

The coherent and spin-incoherent scattering contributions are derived accordingly by

$$\frac{d\sigma}{d\Omega_{coh}} = \frac{d\sigma}{d\Omega_z}^{NSF} - \frac{1}{3}\frac{d\sigma}{d\Omega_{spin-inc}} - \frac{1}{2}\frac{d\sigma}{d\Omega_{para}} \tag{2.2.62}$$

$$\frac{d\sigma}{d\Omega_{spin-inc}} = \frac{3}{2}\cdot\left(\frac{d\sigma}{d\Omega_z}^{SF} - \frac{1}{2}\frac{d\sigma}{d\Omega_{para}}\right) \tag{2.2.63}$$

If magnetic scattering contributions can be excluded, the coherent and spin-incoherent scattering cross sections can be derived by longitudinal polarization analysis in any x, y or z direction.

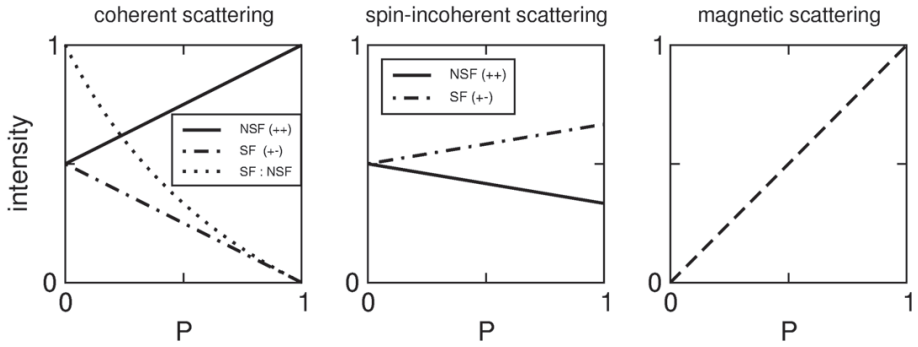

Figure 2.2.15.: Polarization dependence of coherent, spin-incoherent, and magnetic scattering contributions. Picture from [10].

While the above relations are valid under the assumption of perfect polarization (P = 1), for a real experiment corrections to non-perfect polarization have to be performed. Figure 2.2.15 illustrates the spin flip and non spin flip contributions of coherent, spin-incoherent, and magnetic scattering cross sections in dependence of the neutron polarization.

2.2.4.3. SANSPOL

While polarization analysis is required in order to detect the magnetic dipole field in all directions, magnetization densities can be determined in a stronger magnetic field without polarization analysis. Applied to small-angle scattering, this experiment is called SANSPOL [45, 46].

For the SANSPOL experiment, a saturating magnetic field is applied perpendicular to the incoming beam at the sample position in order to align the nanoparticle moments. The SANS is measured on a 2 dimensional detector in dependence of the incoming neutron polarization , denoted as (+) for a parallel and (-) for an antiparallel polarization of the neutrons with respect to the applied magnetic field. Analysis of the neutron polarization after the scattering event is not performed.

The scattering intensities depend on the polarization state of the incident neutrons, the applied magnetic field, and the azimuthal angle α between the wave vector Q and the magnetic field [47]

$$I^{\pm}(Q,\alpha) = \left\{F_N^2(Q) + \left[F_M^2(Q)L^2(x) \mp 2F_N(Q)F_M(Q)L(x)\right]\sin^2\alpha\right\} * S(Q,\alpha) + B \cdot F_M^2(Q) \tag{2.2.64}$$

with

$$B = \left\{ 2\frac{L(x)}{x} - \left[L^2(x) - 1 + 3\frac{L(x)}{x} \right] \sin^2 \alpha \right\} \tag{2.2.65}$$

The first term of equation (2.2.64) describes the interference of the nuclear and magnetic particle form factor aligned in the applied magnetic field as well as possible interparticle interactions defined by the structure factor $S(Q,\alpha)$. The form factor equals equation (2.2.58), after implementation of the nuclear and magnetic particle form factor amplitudes for $N_{\vec{Q}}$ and $\vec{M}^{\perp}_{\vec{Q}}$, respectively. The magnetic particle form factor is weighted by a Langevin term in order to account for the superparamagnetic behavior of the magnetic nanoparticles

$$L(x) = \coth(x) - \frac{1}{x} \tag{2.2.66}$$

with

$$x = \frac{M(R)H_{eff}}{k_B T} \tag{2.2.67}$$

where $M(R)$ denotes the total magnetic moment of the nanoparticle, H_{eff} the effective magnetic field, and k_B the Boltzmann constant.

The second term in equation (2.2.64) accounts for scattering due to misalignment of individual particles. In a saturating magnetic field, where $L(x) = 1$ and $\frac{L(x)}{x} = 0$, this term vanishes, whereas in a vanishing magnetic field, where $L(x) = 0$ and $\frac{L(x)}{x} = \frac{1}{3}$, $B = \frac{2}{3}$ of the magnetic scattering contribution is scattered isotropically and $\frac{1}{3}$ of it interferes with the nuclear scattering contribution.

If the difference between both polarization directions is studied for a sample of non-interacting magnetic nanoparticles ($S(Q,\alpha) = 1$), the contribution due to misalignment of the particle moments in equation (2.2.64) cancels out. The scattering intensity is reduced to the nuclear magnetic cross term

$$I^+(Q,\alpha) - I^-(Q,\alpha) = -4F_N(Q)F_M(Q)L(x)sin^2\alpha \tag{2.2.68}$$

According to equation (2.2.68), the nuclear-magnetic cross term is linear in both the magnetic and the nuclear form factor amplitudes. Thus, the magnetic form factor may be determined if the nuclear amplitude is determined in advance.

3. Instruments

Experiments performed for this thesis have been carried out on a large number of synchrotron beamlines and neutron scattering instruments at large scale facilities. Many of these instruments are uniquely dedicated to specific experiments. For this reason, the characteristics of all instruments used for investigations in the framework of this thesis are compiled in this chapter. All the information presented here is taken from the referenced websites and publications.

3.1. Small-angle Scattering

3.1.1. B1 - JUSIFA [48]

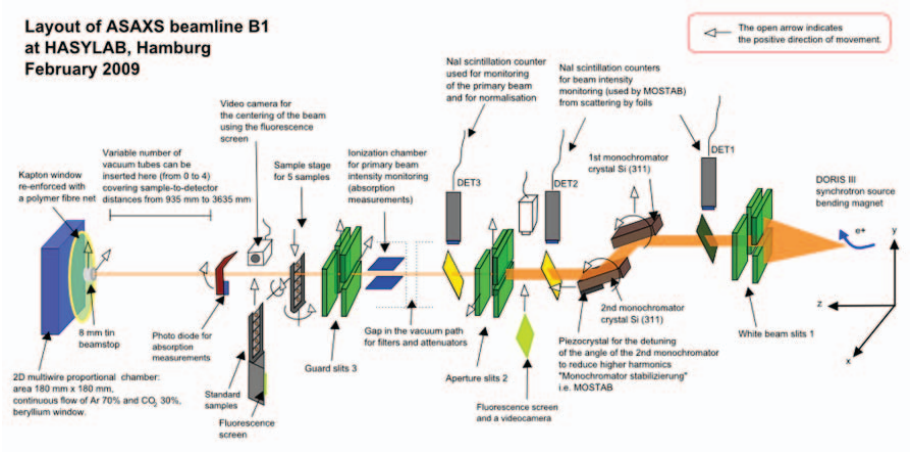

Figure 3.1.1.: Schematic view of B1. Taken from [48].

A schematic representation of the B1 beamline at HASYLAB, formerly called JUSIFA, is given in Figure 3.1.1. Beamline B1 is specifically designed for anomalous small-angle x-ray scattering measurements (ASAXS) of materials with length scales of interest in the range D = $2\pi/Q$ = 0.5 - 100 nm.

Measurements at B1 are made with nonfocusing pinhole collimation with photon energies from 4.9 to 35 keV. The variation in the energy of the monochromatic radiation is obtained using a fixed exit monochromator with two flat asymmetrically cut Si (311) crystals. The higher harmonics in the synchrotron radiation are suppressed by detuning of the second monochromator crystal using a MOSTAB unit. Absorption scans (XANES) can be made at B1 from samples and standard foils are used to calibrate the energy scale.

Samples are mounted into a vacuum chamber in order to reduce air scattering. The sample stage in the chamber can be moved in y-direction in and out of the beam and rotated around the y- and x-axes. The normal sample holder fits five samples. Standard samples to calibrate the absolute intensity scale and the beam center position are located in a sample holder downstream of the sample and these can be measured separately before or after the sample measurement. The standard samples are essential for the analysis of the ASAXS data. The beam size on the sample is typically about 1 mm x 1 mm.

The scattered photons are detected with a two-dimensional position sensitive detector, which can be situated at five distances from the sample, ranging from 935 to 3635 mm. To cover an as large Q-range as possible with good resolution, measurements are typically made for the same sample with the shortest and the longest distances. The change of the sample-to-detector distance is automated so that the samples can stay in the sample holder while changing distances.

Two detectors are available for measurements at B1. First, a multiwire proportional chamber gas detector (Gabriel type). The active area of the detector is 180 x 180 mm^2. The detector image is divided in 256 x 256 pixels of 0.8 x 0.8 mm^2 pixel size. The filling gas of the detector is 70% Argon and 30% CO_2. This detector should not be used with count rates above 60 000 cps so if samples scatter more than that, it is suggested to either use a smaller beam size or to use attenuators.

The second available detector is a 2D PILATUS 300k detector, borrowed from the MINAXS beamline at PETRA III. This detector can count up to about a million counts per pixel. The pixel size of this detector is 172 μm. The active area of the detector is 83.8 x 106.5 mm^2, and the detector is placed off-center to maximize the Q range. A semitransparent beam stop is used to define the beam center accurately.

3.1.2. SWING [49]

The experimental set up of the SWING beamline at Synchrotron Soleil, St. Aubin, allows for simultaneous small-angle X-ray scattering (SAXS) and wide-angle X-ray scattering experiments (WAXS) as well as grazing incidence small angle scattering (GISAXS). Variation in photon energy in the 5-17 keV range is performed by a double Si (111) fixed exit monochromator achieving an energy resolution of ~2 eV and a source divergence of 14.5 $\times$ 4.6 μrad^2. The sample position can be equipped with an automatic sample changer for up to 50 SAXS samples or a GISAXS chamber which holds up to four GISAXS samples. An important feature of SWING is the dynamic vacuum in the entire beamline, which allows for windowless operation.

The detector is a combination of 4 Aviex CCD detectors with 2048 x 2048 pixels each. Software binning of 4x4 pixels each results in a 1024 x 1024 detector with a final pixel size of 164 x 164 μm^2. The detector can be positioned inside the detection chamber with a distance to the sample of 1 - 6.5 m and can be offset both horizontally and vertically.

3.1.3. ID01 [50]

ID01 beamline at ESRF, Grenoble, is mainly dedicated to diffuse scattering experiments near an element's absorption edge using small and/or wide-angle techniques (SAXS and/or WAXS). It is designed to achieve a combination of SAXS and WAXS experiments on a single experimental stage in a large tunable energy-range i.e. 2.1 keV < E < 35 keV with an extension up to 42 keV at the expense of flux. A very good energy resolution (i.e. $\Delta E/E < 10^{-4}$) is provided to scan an element's absorption edge with a high rate of harmonic rejection ($< 10^{-4}$). A low background can be reached by an optional complete vacuum environment (p = 5 x 10^{-3} Torr) in windowless operation. The beam size at the sample is 100 x 100 microns (6 - 16 keV energy range) with a flux of 10^{13} photons/s in the focused beam. Two insertion devices (IDs), an undulator and a wiggler, have been installed in a low β straight section. The energy range 5 keV < E < 42 keV is covered by the different harmonics of the undulator, whereas the wiggler is dedicated to energies lower than 5 keV.

A heavy load 2+4-circle diffractometer + 2 circle analyzer stage is set up in a big vacuum vessel to perform scattering experiments (bulk or surface) either in the vertical or horizontal scattering planes. Working in the reciprocal space (hkl mode) is also possible. The diffractometer is ideal for GID, GISAXS and reflectivity measurements. The sample is held on a flat plate by a suction hole in the center of the holder. A laser is used to orient the surface of the sample perpendicular to the axis of the phi rotation.

The second part of the instrument is a tube for SAXS experiments with a diameter of 1 m which hosts a vacuum compatible CCD camera (Princeton). The detector is placed between 1 and 4.5 meters downstream from the sample inside the vacuum vessel and provides a pixel size of 60 μm. The detector tube can be closed and operated under vacuum, while the diffractometer chamber remains at atmospheric pressure. Moreover, a SAXS conical nose can be mounted close to the sample, reducing the air-scattering path to a few centimeters only, and still allowing for fast change of the sample. The sample can be in air or in a small He-flow cell.

3.1.4. KWS2 [51]

The JCNS KWS2 instrument at FRM II is a classical 2 x 20 m long pinhole small-angle neutron scattering instrument. Nano- and mesoscopic structures in solids and liquids in the order of magnitude of 1 to 100 nm can be investigated. Dedicated sample environment allows for measurements of polymers and surfactant systems over a large range of temperatures.

An incoming wavelength in the range of 4.5 Å $\leq \lambda \leq$ 20 Å is selected by a velocity selector with a wavelength spread of $\frac{\Delta\lambda}{\lambda} = 0.2$. A neutron flux in the range of $4.5 \cdot 10^6$ to $3 \cdot 10^8$ n/cm^{2}s is obtained at the sample position. A fixed primary collimation length of 8 m is available at the moment, whereas the sample detector distance can be varied from 2 to 8 m. Both distances will be extended up to 20 m in the near future. The detector has an active area of 60 x 60 cm^2 with a spatial resolution of 5.25 x 5.25 mm^2. With these characteristics, a momentum transfer range of $2 \cdot 10^{-3} \leq Q \leq 0.2$ Å^{-1} is achieved for an incident wavelength of 7 Å.

3.1.5. D22 [52]

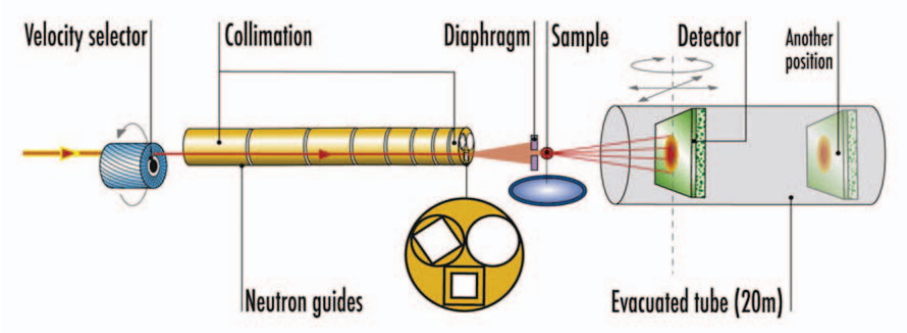

Figure 3.1.2.: Schematic view of D22. Taken from [52].

A schematic representation of the D22 beamline at ILL, Grenoble, is presented in Figure 3.1.2. A relatively narrow wavelength band of 10% is chosen by a velocity selector from the horizontal cold source neutrons. Other wavelength resolutions (from 8 to 20%) can be obtained by manually rotating the selector. The selector has a 25 cm long rotating drum with helical lamellae shaped in a three dimensional mould. The maximal speed is 28300 rpm filtering a wavelength of about 4.5 Å.

The virtual source-to-sample distance is chosen by a collimation system consisting of eight sections. Each section comprises three tubes, any one of which can be positioned on the beam axis. One tube contains a neutron guide with 40 x 55 mm cross section; the second is equipped with an antiparasitic aperture.

A removable transmission polarizer mirror has been installed in the selector bunker, and a radio-frequency spin flipper close to the sample zone. A ^{3}He polarizer cell is available to allow for polarization analysis. The solid angle of the ^{3}He spin analyzer cell, however, restricts the detector to distances greater than 10m, resulting in a reduced Q range that can be probed with polarization analysis.

The sample equipment consists of a remotely controlled XYZ and rotation table and a Eulerian cradle for mounting devices (*e. g.* sample changer, shear and stopped-flow apparatus, electro-magnets) for working in air or in vacuum.

D22 possesses the largest area multidetector (^{3}He) of all small-angle instruments (active area 1 m^2), with a pixel size of 7.5 x 7.5 mm. It moves inside a 2.5 m wide and 20 m long vacuum tube providing sample-to-detector distances of 1.1 m to 17.6 m. D22 thus covers a total Q range of 4 x 10^{-4} to 0.44 Å^{-1} (no detector offset) or 0.85 Å^{-1} (with detector offset in standard conditions.

3.2. Reflectivity

3.2.1. TREFF

The JCNS neutron reflectometer TREFF at FRM II is the reinstallation of the reflectometer HADAS, which was operated in Jülich until the reactor shut down in 2006.

TREFF has been designed for polarized neutron reflectometry on layered samples in specular and off-specular scattering geometries. A double monochromator of pyrolytic graphite crystals is used for wavelength selection, along with a Be filter for removal of the higher harmonics. Within the collimation distance, a supermirror is installed for optional generation of a polarized incident beam. The sample is mounted vertically, and the horizontal scattering plane is scanned by rotation of the scattering arm with the detector around the sample position. A spin flipper and a polarization analyzer are mounted inside the scattering arm. Finally, the 2D position sensitive detector allows for simultaneous measurement of specular and off-specular intensities.

3.3. Wide angle scattering

3.3.1. 6-ID-D

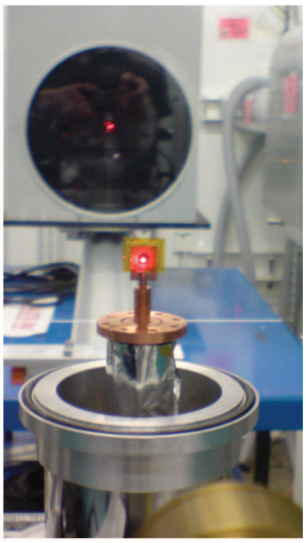

Figure 3.3.1.: Sample position and view of the Mar345 image plate detector at 6-ID-D. The trace of a laser used for alignment of the sample is visible at both sample and beam stop.

The 6-ID-D instrument, property of Forschungszentrum Jülich GmbH, is located in a side station operated in the MUCAT [53] sector at APS, which uses the white beam of an undulator insertion device. This instruments provides high incident energies between 28 and 136 keV, which are particularly useful for diffraction experiments aiming at a wide momentum transfer range as required for PDF analysis.

The side station uses a Bragg double monochromator in horizontal geometry. Three different cuts of annealed silicon crystals give access to a wide energy range from 28 keV to 136 keV. The four circle diffractometer placed at the sample position can be equipped with a cryostat.

A Mar345 image plate detector with a diameter of 345 mm can be placed in a variable distance of 0.25 to 1.6 m to the sample position in order to reach either a wide Q range as required for PDF analysis or a good Q resolution as desired for Rietveld refinements.

3.4. Absorption Spectroscopy

3.4.1. SAMBA [54]

SAMBA is a hard X-ray absorption spectroscopy (XAS) beamline at synchrotron SOLEIL, St. Aubin. Aiming at large and varied scientific communities from physics to chemistry and biology, SAMBA combines a variety of techniques with XAS, such as Differential Scanning Calorimetry, Raman Spectroscopy and UV-Visible Spectroscopy.

SAMBA covers the 4-40 keV energy range with a high photon flux and a good energy resolution. Measurements of the absorption coefficients can be done either in the step by step mode or in a quick mode.

A wide energy range can be scanned owing to the use of a bending magnet and a silicon monochromator reaching an energy resolution of $\frac{\Delta E}{E} = 1.2 \cdot 10^{-4}$ at 5 keV.

A set of ion chambers as well as a fluorescence detector are available for data collection. The ion chambers are installed consecutively, with the sample position between the first two chambers and a reference sample between the last two chambers. The sample absorption is measured simultaneously with the reference absorption. A Rontec fluorescence detector installed at 90° in the horizontal plane next to the sample position allows for simultaneous measurement of the sample fluorescence, which is particularly useful for strongly absorbing samples.

3.5. Polarization Analysis

3.5.1. DNS [55]

The JCNS Diffuse Neutron Spectrometer DNS at FRM-II is a high flux time-of-flight spectrometer with polarization analysis. Its main scientific applications cover magnetic, lattice and polaronic correlations in various length and time scales. Single crystal and powder TOF spectroscopy can be performed for investigation of single-particle excitations, magnons, and phonons. Uniaxial, longitudinal, and vector polarization analysis can be performed with applications ranging from magnetism to soft condensed matter.

A schematic representation of the DNS instrument is given in Figure 3.5.1. The incoming neutron wavelength is selected by a PG(002) double focussing monochromator in the range of 2.4 Å $\leq \lambda \leq$ 6.0 Å. A double-chopper system is installed between monochromator and sample position in order to provide the short neutron pulses required for time-of-flight spectroscopy. Polarized neutrons are generated by a polarizer placed in

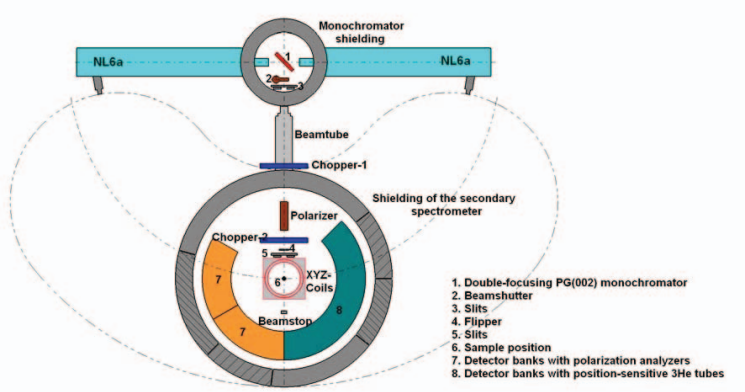

Figure 3.5.1.: Schematic view of DNS. Taken from [55].

between of the two choppers, and spin reversal is performed by a π-flipper in front of the sample aperture.

The sample position is equipped with xyz Helmholtz coils providing a magnetic field in any direction as required for xyz and vector polarization analysis.

The scattering intensity is recorded by multidetector arrays. 128 position sensitive ^{3}He detector tubes are available for detection of non-polarized neutrons, covering a scattering angle of $0° \leq 2\theta \leq 135°$. For detection of polarized neutrons, 24 ^{3}He detector tubes covering a scattering angle of $0° \leq 2\theta \leq 120°$ are equipped with m=3 supermirror polarization analyzers. The achieved maximum momentum transfer Q_{max} ranges from 1.93 Å^{-1} to 4.84 Å^{-1} for an incoming wavelength of 6 and 2.4 Å, respectively. The expected energy resolution for these configuration ranges from 0.1 meV to 1 meV.

3.5.2. J-NSE [56]

The JCNS spin echo spectrometer J-NSE at FRM II is especially suited for the investigation of slow (~101 ns) relaxation processes in soft matter, glasses, magnetic materials, and biological systems at high energy resolution. The neutron spin echo technique uses the neutron spin as an indicator of the individual velocity change of the neutron upon

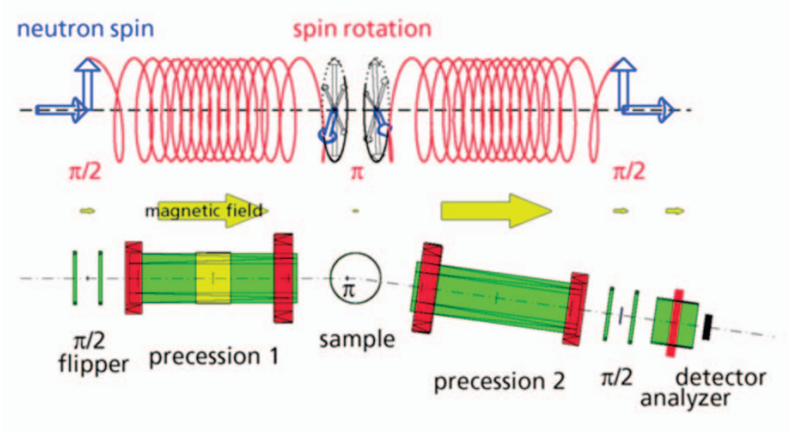

Figure 3.5.2.: Schematic view of J-NSE. Taken from [56].

scattering by the sample. With this trick the instrument accepts a broad wavelength band and at the same time is sensitive to velocity changes down to 10^{-5}s.

The instrument as depicted in Figure 3.5.2 consists mainly of two large water-cooled copper solenoids that generate the precession field. Polarized neutrons are produced by a bent section of the neutron guide with FeSi m=3 remanent supermirror coating and precession is induced by the first $\pi/2$-flipper. The precession tracks are limited by the $\pi/2$-flippers and the π-flipper near the sample position. The embedding fields for the flippers are generated by Helmholtz-type coil pairs around the flipper locations. After leaving the last flipper the neutrons enter an analyzer containing 60 (30 x 30 cm^2) CoTi supermirrors located in a solenoid set. These mirrors reflect only neutrons of one spin direction into the multidetector. By the addition of compensating loops the main coils and the analyzer coil are designed such that the mutual influence of the different spectrometer components is minimized.

The achievable momentum transfer range of 0.02 Å^{-1} $\leq Q \leq$ 1.5 Å^{-1} depends on the chosen incoming wavelength in the range of 4.5 Å $\leq \lambda \leq$ 18 Å. Due to the intrinsic Fourier transform property of the NSE instrument it is especially suited for the investigation of relaxation-type motions that contribute to at least several percent to the entire scattering intensity at the momentum transfer of interest. In those cases the Fourier transform property yields the desired relaxation function directly in time domain without numerical transformation and resolution deconvolution. For a given wavelength the Fourier time range is limited to short times (about 1 ps for the FRM II-setup) by spin depolarization due to vanishing guide field and to long times by the maximum achievable field

integral J. The spin echo time is proportional to J x λ^3, where J denotes the field integral in the solenoids. The J-NSE may achieve a J = 0.5 Tm corresponding to τ = 48 ns at λ = 8 Å.

3.5.3. IN12 [57]

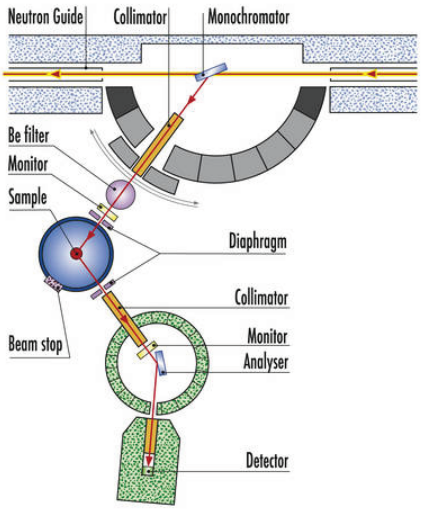

Figure 3.5.3.: Schematic view of IN 12. Taken from [57].

The JCNS cold neutron triple axis spectrometer IN12 at ILL is dedicated to the investigation of dynamics in the low energy range, including low energy magnetic excitations and lattice dynamics at low frequency.

The monochromator of IN12 is a set of vertically focussing pyrolytic graphite (002) crystals, which can select an incoming wavelength of 2.3 Å $\leq \lambda \leq$ 6.0 Å, corresponding to an incoming energy of 2.3 meV $\leq E_i \leq$ 14 meV. Due to the double curvature of the neutron guide there is little $\lambda/2$ contamination for wavelengths shorter than 4 Å. At longer wavelengths a liquid nitrogen cooled beryllium filter of 10 cm length is used. The sample is mounted on a motorized, non-magnetic goniometer which may achieve tilts of ± 20°.

For use with polarized neutrons a supermirror bender is mounted after the first collimator to polarize the incident beam. A curved Heusler (111) analyzer replaces the usual

PG(002) analyzer. A small field (< 150 mT) may be imposed at the sample position using a system of coils. Alternatively, a superconducting magnet is used for larger magnetic fields.

4. Cobalt Nanoparticles

4.1. Nanoparticle Synthesis

The controlled synthesis of nanoparticulate materials is significantly more complex than the synthesis of the respective bulk materials, due to the additional requirements arising from the reduction of the crystal dimensionality. Whenever the statistical average of a large amount of nanoparticles is probed, *i. e.* for investigation of long range ordered nanoparticle arrays or for investigations involving statistical methods such as scattering techniques, a narrow size distribution and a uniform particle shape are desired. Fine control over the kinetics of nucleation and growth processes is thus required. In turn, non interacting nanoparticle dispersions are needed for the investigation of single particle properties such as the magnetization density, which additionally involves control of the surface chemistry.

A large variety of synthesis methods has been developed in order to fulfill the requirements mentioned above and to prepare nanoparticles with tunable particle size, shape, and surface properties [58, 59]. Metal nanoparticles can in principle be prepared by either reduction of metal salts, performed in microemulsions or by coprecipitation, or thermal decomposition of single precursors. For all synthesis methods the presence of stabilizers, *e. g.* donor ligands, polymers, and surfactants, is crucial to stabilize the particle size and to prevent agglomeration.

In the synthesis of metal nanoparticles by the reduction method, a variety of reducing agents has been studied in order to influence the reduction time and thus control the nucleation and growth kinetics. Commonly used reducing agents include complex hydrides (mainly B and Al hydrides) as strong reducing agents and hydrazine (N_2H_4), which reacts more slowly and at a higher temperature, as compared to the hydroborates [60]. Alcohols and carboxylic acids present much weaker reduction properties. They rather form solvates and chelate complexes, which are thermally unstable and decompose easily yielding metal nanoparticles. An example for the application of carboxylic acids is the synthesis of colloidal gold particles by reduction with citrate [61]. The particle size can be controlled by various additional parameters such as the molar ratio of metal salt, stabilizer, and reducing agent, reaction time, applied temperature and pressure [59]. A combination of weakly (trialkyl phosphine and phosphine oxide) and strongly (carboxylic acid) bound ligands together with a variation of their ratio and chain length has also been reported to allow for particle size tuning [62].

Thermolysis synthesis routes involve thermal decomposition of single molecule precursors. Such precursors can be metal carbonyls, which contain the metal atom in a nonvalent state and do thus not require any reducing agent. Upon decomposition the pure metal and carbon monoxide are formed. Further precursors include metal

alkene and arene complexes composed of a low-valent metal with ligands such as 1,5-cyclooctadiene (COD), 1,3,5-cyclooctatriene (COT), and cyclopentadienyl anion (Cp^-) [63].

By variation of the reaction temperature, heating rate, and stabilizer type the kinetics of the particle nucleation and growth are controlled. Besides preventing agglomeration, the capping ligand can also influence the nanocrystal symmetry, *e. g.* by formation of the kinetically stable ε-Co instead of fcc Co [64]. By combination of several ligands that interact differently with the metal, crystal growth can be controlled resulting in a variation of the nanoparticle shape [65, 66].

For the long-term objective of investigations of the spin structure and magnetization density of magnetic nanoparticles, cobalt has been chosen as the material under study because its specific magnetic properties are likely to yield the largest observable effect upon nanostructuration. A variation of the spin structure or magnetization distribution within nanoparticles as compared to bulk material is expected to be most pronounced for compounds with a large magnetic anisotropy. A comparison of the first magnetocrystalline anisotropy constant for several magnetic materials given in Table 4.1.1 [67] shows that cobalt possesses by far the largest anisotropy constant.

Table 4.1.1.: Magnetic parameters for several recording materials. Comparison of saturation magnetization and first magnetocrystalline anisotropy constant as reproduced from [68].

	M_S [emu/cm^3]	K_1 [10^4 erg/cm^3]
Fe	1710	45
Co	1430	430
Ni	483	-4.5
Fe_3O_4	480	-11
γ-Fe_2O_3	350	-4.6

Due to our experience with microemulsion templating techniques and the resulting small size regime of the obtained nanoparticles, it was decided to develop a new colloidal synthesis route for the preparation of cobalt nanoparticles [7, 69]. This synthesis route was originally based on the reduction of $Co(AOT)_2$ in water-in-oil microemulsions [70]. Within this section the principles of nanoparticle preparation by microemulsion techniques will be introduced [71]. Furthermore, the status of the development of colloidal synthesis technique for the preparation of cobalt nanoparticles will be given.

Microemulsions are formed as isotropic dispersions of two immiscible solvents stabilized with a surface active agent, a so called surfactant. Surfactants are amphiphilic molecules consisting of a hydrophilic head group (sulphates, carboxylates, amines, or ethylene oxide) and a lipophilic tail (long-chain hydrocarbon). The addition of alcohols and amines as cosurfactants may further enhance stabilization of the microemulsion. In contrast to macroscopic emulsions, microemulsions are thermodynamically stable dispersions. A large variety of stable phases can be formed by tuning the relative concentrations of surfactant, polar, and nonpolar solvent, thus offering a wide range of applications for microemulsion templating [71, 72]. The Gibbs phase triangle presented in Figure 4.1.1 visualizes the existence regions of the different phases and gives examples for solid phases of different morphologies prepared by microemulsion templating.

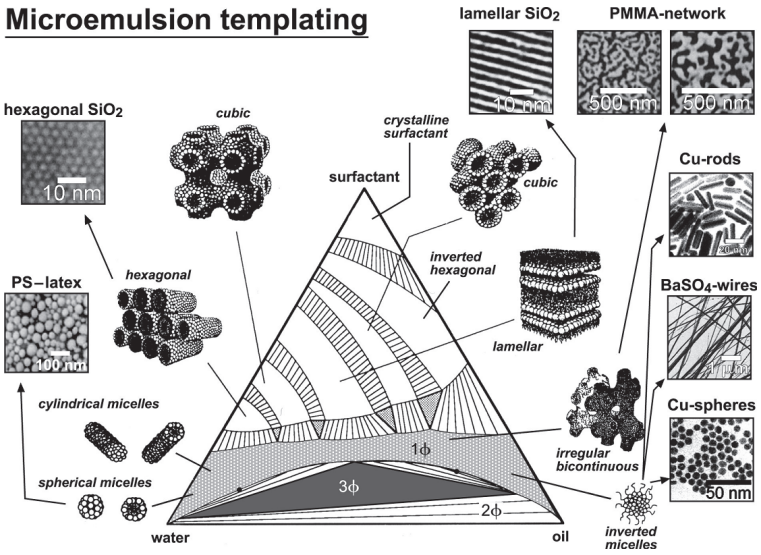

Figure 4.1.1.: Schematic Gibbs triangle (central part) displaying self-assembling structure formation in binary and ternary surfactant systems. The outer part shows examples for solid phases of different morphologies that have been prepared from the indicated self-assembled surfactant phases [71] (and references therein) .

Synthesis of nanoparticles using microemulsions involves employing spherical micellar phases of oil-in-water or water-in-oil microemulsions, whereas the latter are commonly denoted as reverse micelles [72]. Due to their small size, micelles are subject to Brownian motion and undergo frequent collisions. Some of these micelle collisions create short-lived dimers that provide a fast exchange of their contents [58]. Nanoparticle synthesis in microemulsions takes advantage of a constant size and number of the

micelles in time as well as of an equilibrium distribution of all micelle contents that is provided by the fast intermicellar exchange kinetics. This allows for preparation of nanoparticles with a narrow size distribution.

The formation of metal nanoparticles in microemulsions can in principle be performed by two different approaches. First, both the metal ions and the reducing agent are solubilized in the interior of two different microemulsions. Upon mixing, the contents of the reverse micelles are exchanged via intermicellar collisions, and the metal cations are reduced to metal atoms. For the second possible approach, either the reducing agent or the metal source is dissolved in the continuous phase and can enter the micelles to initiate reduction. If the critical aggregation number of free metal atoms inside the micelles is exceeded, nucleation occurs. Due to further intermicellar exchange, the formed metal seeds grow until all free metal atoms are used up. This basic principle of nucleation and growth is illustrated in Figure 4.1.2.

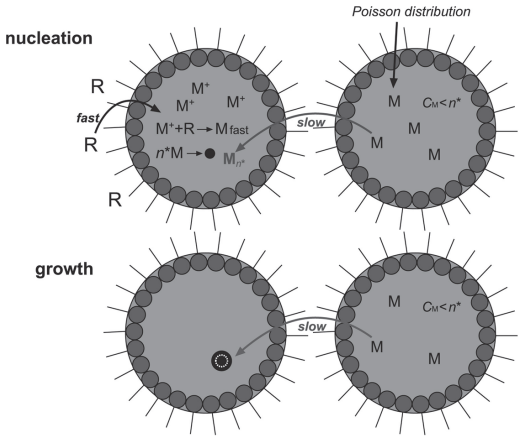

Figure 4.1.2.: Schematic presentation of nucleation and growth processes occurring in the reduction of metal ions in water-in-oil microemulsions. Metal ions M^+ solubilized in the aqueous core become reduced when, as in this case, the reducing agent R enters the droplet interior from the continuous phase. If the number of metal atoms is higher than the critical aggregation number $n^\star$, a metal cluster nucleus forms that grows due to the exchange of metal ions with other droplets. Reproduced from [71].

The initial synthesis procedure for cobalt nanoparticles is based on the mixing of two different microemulsions [70] and employs water in *iso*-octane microemulsions stabilized by the anionic surfactant bis(2-ethylhexyl) sulfosuccinate (AOT[1]). One microemulsion contains the cobalt cation in the form of $Co(AOT)_2$ added to the NaAOT reverse

[1] the abbreviation AOT relates to the trade name of its sodium salt, Aerosol OT.

micelles. The second microemulsion contains the dispersed reducing agent $NaBH_4$ instead of the cobalt source.

A higher yield of cobalt nanoparticles is achieved by reduction of a microemulsion stabilized exclusively by $Co(AOT)_2$ [73]. The reducing agent $NaBH_4$ is then directly added to the microemulsion, thus following the second approach mentioned above. Particle size and size distribution are tuned by variation of the water:AOT as well as $NaBH_4$:$Co(AOT)_2$ ratio, respectively, whereas a narrow size distribution requires a high amount of reducing agent. However, if $NaBH_4$ is added as aqueous solution directly to the $Co(AOT)_2$ microemulsion, the aqueous solution needs first to be solubilized into the interior of the microemulsion droplets leading to an additional parameter that needs to be controlled to avoid irreproducibility. If more aqueous phase is necessary to reduce the Co^{2+} ions than can be solubilized in the microemulsion droplets, phase separation occurs additionally. In this case an oil-continuous phase containing most of the AOT reverse micelles and the Co nanoparticles forms, together with an almost pure water phase. The latter needs to be removed as fast as possible in order to avoid particle oxidation.

In the further development of this colloidal synthesis technique, a water-in-oil microemulsion was prepared with the nonionic surfactants $C_{12}E_5$ or Igepal CO 520 as stabilizers, which contained $NaBH_4$ in the water droplets. Cobalt nanoparticles were then prepared by addition of a $Co(AOT)_2$ solution in hexane or toluene [7]. It was found that even the small amount of water inside the micelles lead to an oxidation of the formed cobalt nanoparticles. For this reason, an entirely water-free synthesis route was explored by reducing $Co(AOT)_2$ micellar solutions with the organic and thus oil-soluble borohydride $NaEt_3BH$. The prepared nanoparticle dispersions were found to be stable against oxidation if stored in the N_2 atmosphere of a glove box. A superparamagnetic blocking temperature of 10 K and a particle diameter of about 4 nm were determined by SQUID magnetization measurements and small-angle scattering, respectively.

The objectives of the work described in this chapter are the reproduction of cobalt nanoparticles by the water-free synthesis route described above and their detailed structural characterization concerning particle size and size distribution as well as magnetic properties. Further development of the synthesis method regarding nanoparticle dispersions suitable for neutron scattering experiments as well as a variation of the nanoparticle size are also explored.

4.2. Methods

4.2.1. Sample preparation

In this section, the details for the preparation of all samples mentioned in this chapter will be given. This includes a description of the standard synthesis procedure and investigated variations thereof, as well as a reference of the sample compositions. All samples prepared by the standard synthesis procedure are labelled as 'Co A' samples, while samples belonging to different experimental series performed for synthesis optimization are labelled by different letters. A list of all used chemicals can be found in Table B.0.1 in Appendix B.

For samples investigated by (A)SAXS at the JUSIFA beamline, different experimental configurations are distinguished as (07), (08), and (09), corresponding to the different beamtime sessions. The technical details of these measurements will be given in section 4.2.2.

4.2.1.1. $Co(AOT)_2$

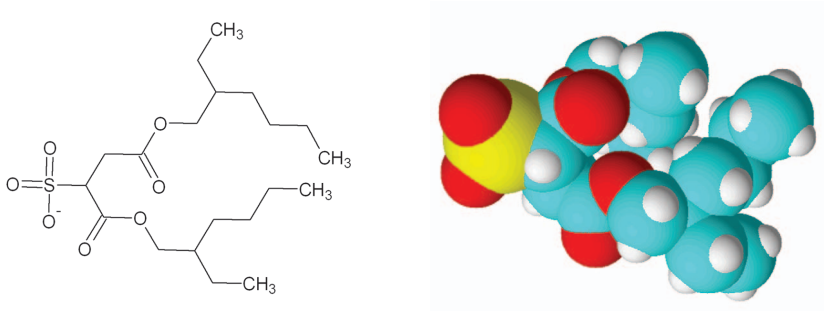

(a) Molecular formula of the AOT anion.

(b) Geometric representation of the AOT molecule. Carbon, hydrogen, oxygen, and sulfur atoms are represented as spheres in cyan, white, red, and yellow, respectively.

Figure 4.2.1.: The AOT anion.

Cobalt bis(2-ethylhexyl) sulfosuccinate ($Co(AOT)_2$) was prepared according to a method described earlier [74]. In a first step, sodium bis(2-ethylhexyl) sulfosuccinate (NaAOT) is ion exchanged to its acidic form by ion exchange on a strong cationic resin.

$$NaAOT + HCl \longrightarrow NaCl + HAOT \tag{4.2.1}$$

An ion exchange column filled with ~ 50 g Dowex 50 W ion exchange resin is charged with 300 ml of 1 M HCl and afterwards rinsed with dest. H_2O until the effluent pH is neutral. The resin is then washed water-free by rinsing with ethanol until the effluent has the mass density of pure ethanol (ϱ = 0.79 g/ml). The such prepared ion exchange column is loaded with a solution of ~ 6 g (13.5 mmol) NaAOT in 300 ml abs. ethanol (0.045 M) and rinsed with further 200 ml of abs. ethanol. The effluent containing the acidic HAOT is collected and concentrated to ~ 200 ml using a rotary evaporator. The obtained solution of HAOT in ethanol is then converted to $Co(AOT)_2$ by a second ion exchange process.

$$2\,HAOT + Co(OAc)_2 \longrightarrow 2\,HOAc + Co(AOT)_2 \tag{4.2.2}$$

An ion exchange column filled with ~ 30 g of the weakly acidic cation exchange resin Amberlit IRC-76 is loaded with ~ 12.5 g (50 mmol) cobalt acetate tetrahydrate ($Co(OAc)_2.4\,H_2O$) in ~ 100 ml H_2O and rinsed until the effluent is free of cobalt. The resin is washed water-free with ethanol until the effluent has the mass density of pure ethanol. The previously formed acidic HAOT solution is passed through the cobalt-loaded ion exchange column for exchange into $Co(AOT)_2$. The effluent is collected and concentrated under vacuum using a rotary evaporator down to a pressure of ~ 7 mbar. The residual paste of $Co(AOT)_2$ is further dried in an oil pump generated vacuum over 2-3 days. A pink solid is obtained, which is further characterized.

Characterization of the obtained $Co(AOT)_2$ was performed by thin layer chromatography and NMR spectroscopy. Elementary analysis was carried out by the central division of analytical chemistry (ZCH). For thin layer chromatography, ~ 30 mg of the prepared $Co(AOT)_2$ were dissolved in ethanol. Silica plates of 0.25 mm thickness were used as stationary phase, and a mixture of 1:1 cyclohexane and n-propanol was used as mobile phase. For chemical development, 2,7-dichlorofluorescein was sprayed onto the plate and dried immediately in N_2. The prepared $Co(AOT)_2$ resulted in a single spot with a retention factor of R_f = 0.05 as observed for the NaAOT reference. In case of a decomposition of the AOT anion, such as by hydrolysis of the ester groups, at least two different spots are expected.

^{1}H–NMR spectroscopy of the prepared $Co(AOT)_2$ in CD_3Cl yielded extremely broad peaks that can only roughly be assigned to the expected chemical shifts. ^{13}C–NMR spectra of the prepared compound exhibit sharper signals, which can, despite the very low intensity of the carbonyl C atoms, be attributed to the AOT anion [75]. However, small impurities were found as observed by minor peaks in the spectra. According to their chemical shifts, these impurities can be assumed to consist of aliphatic hydrocarbons.

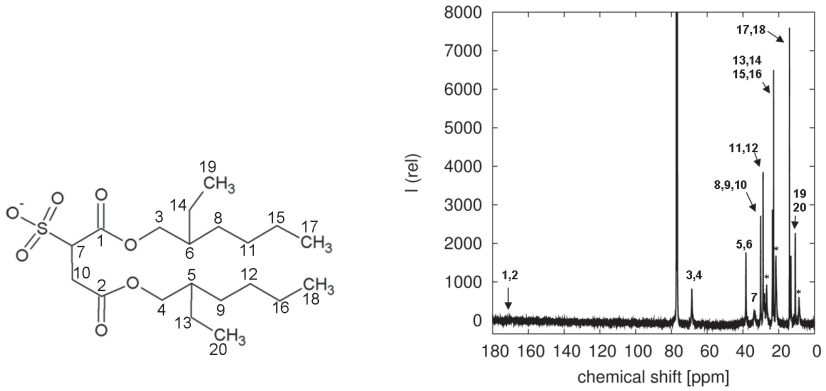

(a) Molecular formula of the AOT anion.

(b) ^{13}C-NMR of the prepared Co(AOT)$_2$. Peaks are assigned to C atoms as labelled in (a). Peaks due to impurities are labelled by (∗). The peak at ~ 78 ppm originates in the solvent CD_3Cl.

Figure 4.2.2.: ^{13}C-NMR by Co(AOT)$_2$.

Inductively Coupled Plasma with Optical Emission Spectroscopy (ICP-OES) was applied for a quantitative determination of the cobalt and sodium contents. The found mass fractions of cobalt and sodium in the prepared Co(AOT)$_2$ sample are 4.0(1) % and 0.15(2) %, respectively. For pure Co(AOT)$_2$, a mass fraction of 6.53 % of cobalt is expected. Thus, only 61.3 % of the prepared sample can be attributed to Co(AOT)$_2$ according to the ICP-OES result. The found sodium mass fraction, however, can account for a NaAOT fraction of the sample of maximal 2.9 %. The remaining ~ 35 % of the sample may consist of organic side products, such as decomposition products of AOT, or residual ethanol which has not been dried off completely. Considering the somewhat pasty appearance of the product, some ethanol traces seem realistic. However, the thin layer chromatography and NMR spectroscopy results do not indicate impurities in an extent as large as 35 mass-%. Considering that for ICP-OES the sample is dissolved in water and nebulized into an inductively generated argon plasma, a systematic deviation of the quantitative results can be speculated for colloidal solutions such as the micellar solution of Co(AOT)$_2$ in water. A similar observation is discussed in section 4.3.1.6. Further elemental analysis is thus suggested to verify the cobalt content of the prepared Co(AOT)$_2$.

For the following experiments on the preparation of cobalt nanoparticles, the prepared Co(AOT)$_2$ was implemented as if 100% pure. This leads to a systematic error on

the equivalents of reducing agent used, which has to be kept in mind during experiments on a variation of the reducing agent. However, the experimental series investigated in this study are still internally comparable.

4.2.1.2. Cobalt nanoparticles standard synthesis route

$$Co(AOT)_2 + 2\,NaEt_3BH \longrightarrow Co + 2\,NaAOT + 2\,Et_3B + H_2 \tag{4.2.3}$$

For preparation of cobalt nanoparticles, 45 mg (50 μmol) of $Co(AOT)_2$ are dissolved in 1 ml of toluene (0.05 M) and reduced by 105 μl (105 μmol, 1.05 eq) of a 1 M $NaEt_3BH$ solution in toluene. A sudden change of the dispersion color from pink to black upon reduction indicates the formation of cobalt nanoparticles. This standard synthesis route was used as a reference sample for most of the experimental series. The exact amounts of starting materials used for all samples presented in section 4.3.1 are given in Table 4.2.1. Note that samples investigated by SANS (A02, A18, A19) were prepared with deuterated toluene (C_7D_8), whereas the used reducing agent is dissolved in non-deuterated toluene (C_7H_8). In order to avoid nanoparticle oxidation, the nanoparticle synthesis as well as preparation of the samples for characterization was performed inside the inert N_2 atmosphere of an MBraun glove box. For deliberate oxidation, the indicated samples were exposed to air over night.

Table 4.2.1.: Composition of cobalt nanoparticle dispersions prepared by the standard synthesis route.

Co #	$Co(AOT)_2$		Toluene	$NaEt_3BH$ (1 M)		[Co]	method	instrument
	[mg]	[μmol]	[ml]	[μl]	[eq]	[mM]		(config.)
A01	44.9	49.8	1.0	102	1.02	45.2	VSM	PPMS
A02	90.8	100.7	2.0	200	0.99	45.8	SAXS	JUSIFA (07)
							ASAXS	JUSIFA (07)
							SANS	KWS2
								TREFF
A03	45.8	50.8	1.0	100	0.99	46.2	VSM	PPMS
							XAS	SAMBA
A04[1]	45.8	50.8	1.0	100	0.99	46.2	VSM	PPMS
							XAS	SAMBA
A05	46.7	51.8	0.9	100	0.97	51.8	VSM	PPMS

Continued on next page

Table 4.2.1 – continued from previous page

Co #	$Co(AOT)_2$		Toluene	$NaEt_3BH$ (1 M)		[Co]	method	instrument
	[mg]	[μmol]	[ml]	[μl]	[eq]	[mM]		(config.)
A06	45.7	50.7	0.9	102	1.01	50.6	VSM	PPMS
A07	44.9	49.8	1.0	100	1.00	45.3	VSM	PPMS
							SAXS	JUSIFA (08)
							ASAXS	JUSIFA (08)
A08	45.0	49.9	0.9	100	1.00	49.9	VSM	PPMS
							XAS	SAMBA
A09	(see sample # Co N01 in section 4.2.1.9.)						XAS	SAMBA
A10	45.5	50.4	0.9	100	0.99	50.4	SAXS	in house
A11	27.4	30.4	0.6	62	1.02	45.9	SAXS	JUSIFA (09)
A12[1]	27.4	30.4	0.6	62	1.02	45.9	SAXS	JUSIFA (09)
A13	22.8	25.3	0.5	51	1.01	45.9	SAXS	JUSIFA (09)
A14	22.5	24.9	0.5	50	1.00	45.4	SAXS	JUSIFA (09)
A15[2]	11.5	12.7	1.0	22	1.18	12.5	SAXS	SWING
								ID01
A16[3]	22.5	24.9	0.95	55	1.10	24.8	SAXS	SWING
								ID01
A17[3]	11.3	12.5	0.975	28	1.12	12.5	SAXS	SWING
								ID01
A18	315.8	350.0	6.3	700	1.00	50.0	SANS	DNS
A19	899.0	996.6	1.0	2000	1.00	332.2	SANS	IN12

[1] This sample has been oxidized deliberately.
[2] An additional amount of $C_{12}E_5$ was added as given in section 4.2.1.6.2.
[3] An additional amount of Igepal CO 520 was added as given in section 4.2.1.6.1.

4.2.1.3. Particle extraction

For separation of the prepared cobalt nanoparticles from organic byproducts such as excess surfactant, varied amounts of the nonpolar ligand trioctyl phosphine ($P(oct)_3$) were added to the reverse micellar $Co(AOT)_2$ solution before reduction. After reduction, each sample was shaken with ~ 1 ml formamide. After phase separation, a large fraction of the cobalt nanoparticles was expected to remain in the upper toluene phase, while those byproducts soluble in the polar solvent, such as excess AOT, were supposed

to have transferred to the lower formamide phase. The toluene phase was characterized by magnetization measurements, and the cobalt content in this phase was determined by elementary analysis (ICP-OES). The composition of all investigated samples before solvent extraction is given in Table 4.2.2.

Table 4.2.2.: Composition of the cobalt nanoparticle dispersions prepared for extraction with $P(oct)_3$.

Co #	$Co(AOT)_2$ [μmol]	$P(oct)_3$ [μmol]	Toluene [ml]	$NaEt_3BH$ (1 M) [μl]	[eq]	[Co] [mM]	Co:$P(oct)_3$
B01	49.9	0.25	1.0	100	1.00	49.9	1:0.005
B02	49.6	0.5	1.0	100	1.01	49.6	1:0.010
B03	49.4	1.0	1.0	100	1.01	49.4	1:0.020
B04	50.5	2.5	1.0	100	0.99	50.5	1:0.049
B05	50.8	4.0	1.0	100	0.98	50.8	1:0.079
B06	50.0	5.0	1.0	100	1.00	50.0	1:0.100

4.2.1.4. Concentration variation

Experiments regarding synthesis optimization and particle size variation were performed by variation of reaction parameters such as cobalt concentration and reaction temperature, and by variation of the different reaction components such as surfactants, polar phase, and reducing agent.

For variation of the cobalt concentration a stock solution of 547.6 mg (0.607 mmol) $Co(AOT)_2$ in 12 ml toluene (0.051 M) was diluted with toluene to different cobalt concentrations and subsequently reduced with 1 M $NaEt_3BH$. For comparison, a reference sample of the stock solution was first reduced with $NaEt_3BH$ and then diluted to obtain the same cobalt concentrations. The compositions of the samples are listed in Table 4.2.3. These samples were investigated by SAXS at the JUSIFA beamline (09).

4.2.1.5. Temperature variation

The influence of the reaction temperature was studied on cobalt nanoparticle samples prepared according to the standard synthesis procedure. For each experimental series, a stock solution of 0.05 M $Co(AOT)_2$ in toluene was prepared in order to ensure comparability of the cobalt concentration. Samples were reduced at either room temperature or elevated temperatures. After reduction all samples were heated to elevated temperatures, and the temperature was held for ~ 1 hour. The compositions and reaction

Table 4.2.3.: Composition of the cobalt nanoparticle dispersions prepared in different concentrations.

Co #		$Co(AOT)_2$ [mg]	$Co(AOT)_2$ [μmol]	Toluene [ml]	$NaEt_3BH$ (1 M) [μl]	$NaEt_3BH$ (1 M) [eq]	[Co] [mM]
A10		27.4	30.4	0.6	62	1.02	45.9
C01	first diluted	9.1	10.1	0.3	21	1.04	31.5
C02	first diluted	4.6	5.1	0.3	11	1.09	16.3
C03	first reduced	8.3	9.2	0.3	19	1.02	30.6
C04	first reduced	4.1	4.6	0.3	9	1.02	15.3

temperatures of all samples are given in Table 4.2.4. The samples were characterized by magnetization measurements and SAXS either in house or at the JUSIFA beamline as indicated in Table 4.2.4.

Table 4.2.4.: Composition of the cobalt nanoparticle dispersions prepared at different temperatures.

Co #	$Co(AOT)_2$ [μmol]	Toluene [ml]	$NaEt_3BH$ (1 M) [μl]	$NaEt_3BH$ (1 M) [eq]	[Co] [mM]	red. temp.	heat. temp.	meth.	instr. (config.)
A01	49.8	1.0	102	1.02	45.2	RT	-	VSM	PPMS
								SAXS	in house
D01	49.8	1.0	102	1.02	45.2	75°C	75°C	VSM	PPMS
								SAXS	in house
A12	25.3	0.5	51	1.01	45.9	RT	-	SAXS	JUSIFA (09)
D02	25.3	0.5	51	1.01	45.9	40°C	40°C	SAXS	JUSIFA (09)
D03	25.3	0.5	51	1.01	45.9	RT	40°C	SAXS	JUSIFA (09)
D04	25.3	0.5	51	1.01	45.9	75°C	75°C	SAXS	JUSIFA (09)
D05	25.3	0.5	51	1.01	45.9	RT	75°C	SAXS	JUSIFA (09)
D06	25.3	0.5	51	1.01	45.9	95°C	95°C	SAXS	JUSIFA (09)
D07	25.3	0.5	51	1.01	45.9	RT	95°C	SAXS	JUSIFA (09)

4.2.1.6. Addition of nonionic and anionic surfactants

4.2.1.6.1. Igepal CO 520 Cobalt nanoparticle dispersions were prepared with Igepal CO 520 as additional surfactant with varying surfactant ratios. Both $Co(AOT)_2$ and Igepal were dispersed in toluene and subsequently reduced with $NaEt_3BH$. The total surfactant concentration was maintained constant throughout the different experimental series. Consequently, the cobalt concentration decreases with increasing Igepal

content. The compositions of the samples are given in Table 4.2.5. Samples were characterized by magnetization measurements and SAXS at either the JUSIFA beamline (07) (A02, E01-E05) or the SWING beamline (E09-E12). A reference series of mixed micellar solutions of $Co(AOT)_2$ and Igepal was characterized with SAXS at the SWING beamline (E06-E08).

Table 4.2.5.: Composition of the cobalt nanoparticle dispersions prepared with Igepal CO 520.

Co #	$Co(AOT)_2$ [μmol]	Igepal [μmol]	Toluene [ml]	$NaEt_3BH$ (1 M) [μl]	[eq]	[Co] [mM]	AOT:Igepal
A02	100.7	-	2.0	200	0.99	45.8	1:0.0
E01	50.5	101.1	2.0	100	0.99	24.1	1:1.00
E02	25.3	149.3	2.0	50	0.99	12.3	1:2.95
E03	16.9	165.7	2.0	33	0.98	8.3	1:4.92
E04	12.4	176.8	2.0	25	1.01	6.1	1:7.12
E05	9.8	180.2	2.0	20	1.03	4.8	1:9.24
E06	24.9	50.0	0.95	-	-	26.3	1:1.00
E07	24.9	150.0	0.95	-	-	26.3	1:3.01
E08	24.9	250.0	0.95	-	-	26.3	1:5.01
E09	24.9	50.0	0.95	55	1.10	24.8	1:1.00
E10	12.5	75.0	0.98	28	1.12	12.4	1:3.01
E11	6.2	87.5	0.99	14	1.12	6.2	1:7.02
E12	5.0	90.0	0.99	11	1.10	5.0	1:9.01

4.2.1.6.2. $C_{12}E_5$ For the preparation of cobalt nanoparticles with the nonionic surfactant $C_{12}E_5$, both $Co(AOT)_2$ and $C_{12}E_5$ were dissolved in toluene. While the cobalt concentration was constant, the ratio of $C_{12}E_5$: AOT was varied. Samples were reduced with 1.1 eq of $NaEt_3BH$, whereas reference samples of the same composition were prepared without reduction. The samples were characterized with SAXS at the SWING beamline. The compositions of all samples are given in Table 4.2.6.

4.2.1.6.3. NaAOT For the preparation of cobalt nanoparticles with addition of the anionic surfactant NaAOT, different amounts of $Co(AOT)_2$ and NaAOT were dissolved in toluene. The cobalt concentration was maintained constant for all samples, whereas the AOT(Co):AOT(Na) ratio was varied. Samples were reduced with 1.1 eq of $NaEt_3BH$. Reference samples of the same compositions were prepared without reduction. All samples were characterized with SAXS at the SWING beamline. The compositions of the samples are given in Table 4.2.7.

Table 4.2.6.: Composition of the cobalt nanoparticle dispersions prepared with $C_{12}E_5$.

Co #	$Co(AOT)_2$ [μmol]	$C_{12}E_5$ [μmol]	Toluene [ml]	$NaEt_3BH$ (1 M) [μl]	[eq]	[Co] [mM]	AOT:$C_{12}E_5$
F01	25.2	49.7	0.95	-	-	26.5	1:0.99
F02	25.2	149.0	0.95	-	-	26.5	1:2.96
F03	25.2	248.3	0.95	-	-	26.5	1:4.94
F04	25.2	49.7	0.95	55	1.09	25.0	1:0.99
F05	25.2	149.0	0.95	55	1.09	25.0	1:2.96
F06	25.2	248.3	0.95	55	1.09	25.0	1:4.94

Table 4.2.7.: Composition of the cobalt nanoparticle dispersions prepared with NaAOT.

Co #	$Co(AOT)_2$ [μmol]	NaAOT [μmol]	Toluene [ml]	$NaEt_3BH$ (1 M) [μl]	[eq]	[Co] [mM]	AOT(Co):AOT(Na)
G01	25.2	51.6	0.95	-	-	26.5	1:1.03
G02	24.9	100.3	0.95	-	-	26.2	1:2.01
G03	24.9	150.4	0.95	-	-	26.2	1:3.02
G04	25.2	154.7	0.95	-	-	26.5	1:3.08
G05	24.9	200.6	0.95	-	-	26.2	1:4.02
G06	25.2	257.9	0.95	-	-	26.5	1:5.13
G07	25.2	51.6	0.95	55	1.09	25.0	1:1.03
G08	24.9	100.3	0.95	55	1.10	24.8	1:2.01
G09	24.9	150.4	0.95	55	1.10	24.8	1:3.02
G10	25.2	154.7	0.95	55	1.09	25.0	1:3.08
G11	24.9	200.6	0.95	55	1.10	24.8	1:4.02
G12	25.2	257.9	0.95	55	1.09	25.0	1:5.13

4.2.1.6.4. NaAOT and Igepal CO 520 For the preparation of cobalt nanoparticles with a combination of NaAOT and Igepal CO 520 surfactants, $Co(AOT)_2$ and the respective surfactants were dissolved in toluene and reduced with $NaEt_3BH$. The molar ratio of $Co(AOT)_2$:NaAOT was maintained constant at 1:2 throughout the experimental series, and the dependence of the particle size on a varied AOT:Igepal ratio was investigated. Samples were characterized with SAXS at the SWING beamline. The compositions of all samples are given in Table 4.2.8.

Table 4.2.8.: Composition of the cobalt nanoparticle dispersions prepared with a combination of NaAOT and Igepal CO 520.

Co #	$Co(AOT)_2$ [μmol]	NaAOT [μmol]	Igepal [μmol]	Toluene [ml]	$NaEt_3BH$ (1 M) [μl]	[eq]	[Co] [mM]	AOT:Igepal
H01	24.9	50.6	105.9	2.0	50	1.00	12.1	1:1.05
H02	12.5	25.3	150.7	2.0	25	1.00	6.1	1:3.00
H03	8.3	16.8	166.6	2.0	17	1.00	4.1	1:5.00
H04	6.2	12.7	175.9	2.0	13	1.00	3.1	1:7.01
H05	5.0	10.1	181.6	2.0	10	1.00	2.5	1:9.04

4.2.1.7. Microemulsion

4.2.1.7.1. Formamide Before the preparation of the cobalt nanoparticles from formamide-in-oil microemulsions, the phase diagram of the system toluene/$Co(AOT)_2$/formamide was determined in the temperature range of 16 - 46°C in dependence of the formamide-to-surfactant mass ratio. The starting solution of 223.3 mg (0.248 mmol) $Co(AOT)_2$ in 2.4 ml toluene (0.103 M) was mixed with 92 μl (104 mg) of formamide. The resulting sample with a formamide:surfactant mass ratio of F/S = 0.466 separated into two phases at temperatures up to ~ 50°C. Small volumes (typically 20 - 40 μl) of a 0.1 M $Co(AOT)_2$ stock solution were added stepwise, and the transition temperature between the low temperature two-phase system and the high temperature single phase microemulsion was determined for each step using a thermostatic bath.

Cobalt nanoparticles were prepared at room temperature from microemulsions with a constant cobalt concentration of 0.05 M and a varying formamide:surfactant mass ratio, which was kept in the single phase region of the determined phase diagram. The compositions of the investigated samples are given in Table 4.2.9. Samples were characterized by either magnetization measurements and in house SAXS (I01-I04) or synchrotron SAXS at the ID01 beamline (I08-I10). Reference samples of the microemulsions

were prepared without reduction and characterized with SAXS at the ID01 beamline (I05-I07).

Table 4.2.9.: Composition of the cobalt nanoparticle dispersions prepared from formamide microemulsions.

Co #	$Co(AOT)_2$		Toluene	Formamide		$NaEt_3BH$ (1 M)		[Co]	F/S
	[mg]	[μmol]	[ml]	[μl]	[mg]	[μl]	[eq]	[mM]	mass-%
I01	45.7	50.7	0.9	6.0	6.8	100	0.99	50.7	0.148
I02	45.1	50.0	0.9	10.0	11.3	100	1.00	50.0	0.251
I03	45.4	50.3	0.9	12.0	13.6	100	0.99	50.3	0.299
I04	45.4	50.3	0.9	16.0	18.1	100	0.99	50.3	0.398
I05	22.8	25.3	0.5	7.0	7.9	-	-	50.6	0.347
I06	22.8	25.3	0.5	3.5	4.0	-	-	50.6	0.173
I07	22.8	25.3	0.5	7.8	2.0	-	-	50.6	0.087
I08	22.8	25.3	0.5	7.0	7.9	50	0.99	46.0	0.347
I09	22.8	25.3	0.5	3.5	4.0	50	0.99	46.0	0.173
I10	22.8	25.3	0.5	7.8	2.0	50	0.99	46.0	0.087

4.2.1.7.2. EAN The ionic liquid ethyl ammonium nitrate (EAN) was obtained through collaboration with Prof. W. Kunz, Universität Regensburg, and was used as polar phase in microemulsions without prior determination of the phase diagram. Similar to the microemulsions with formamide, the cobalt concentration was maintained constant throughout the experimental series, while the EAN:surfactant mass ratio E/S was varied between 0.06 and 0.24. The E/S ratios are calculated with an EAN mass density of ϱ = 1.2 g/ml as determined from the molar density of ϱ_m = 11.1 mol/ml [76] and its molar mass of M = 108.1 g/mol. The prepared microemulsions as well as the reduced nanoparticle dispersions were investigated with SAXS at the ID01 beamline. The compositions of the samples are given in Table 4.2.10.

4.2.1.8. Variation of the reducing agent

4.2.1.8.1. Hydrazine For a variation of the reducing agent, $NaEt_3BH$ was partially substituted by hydrazine (N_2H_4). The reduction of Co^{2+} to cobalt metal with hydrazine occurs according to

$$2\,Co^{2+} + N_2H_4 \longrightarrow N_2 + 2\,Co + 4\,H^+ \tag{4.2.4}$$

Table 4.2.10.: Composition of the cobalt nanoparticle dispersions prepared from EAN microemulsions.

Co #	$Co(AOT)_2$		Toluene	EAN		$NaEt_3BH$ (1 M)		[Co]	E/S
	[mg]	[μmol]	[ml]	[μl]	[mg]	[μl]	[eq]	[mM]	mass-%
J01	22.8	25.3	0.5	4.5	5.4	-	-	50.6	0.237
J02	22.8	25.3	0.5	1.1	1.4	-	-	50.6	0.059
J03	22.8	25.3	0.5	4.5	5.4	50	0.99	46.0	0.237
J04	22.8	25.3	0.5	1.1	1.4	50	0.99	46.0	0.059

Cobalt nanoparticle dispersions were prepared from 0.05 M $Co(AOT)_2$ micellar solutions with a combination of $NaEt_3BH$ and N_2H_4 of varying equivalent ratio. The obtained nanoparticle dispersions were characterized by magnetization measurements, UV-VIS spectroscopy, and SAXS at the JUSIFA beamline (07) (K01-K05) and (09) (A13, K06, K07). The compositions of the investigated samples are given in Table 4.2.11.

Table 4.2.11.: Composition of the cobalt nanoparticle dispersions prepared with a combination of $NaEt_3BH$ and N_2H_4.

Co #	$Co(AOT)_2$	Toluene	$NaEt_3BH$ (1 M)		N_2H_4 (1 M)		[Co]
	[μmol]	[ml]	[μl]	[eq]	[μl]	[eq]	[mM]
K01	49.1	0.9	100	1.02	-	-	49.1
K02	50.1	0.92	75	0.75	6.3	0.25	50.0
K03	50.6	0.94	50	0.49	12.5	0.49	50.5
K04	50.2	0.96	25	0.25	18.8	0.75	50.0
K05	49.9	0.975	-	-	25	1.00	49.9
A13	24.9	0.5	50	1.00	-	-	45.4
K06	24.9	0.5	37.5	0.75	3	0.24	46.1
K07	24.9	0.5	25	0.50	6.25	0.50	47.0

4.2.1.8.2. Reducing agent deficiency For cobalt nanoparticle synthesis with a deficient reduction, a 0.05 M $Co(AOT)_2$ reverse micellar solution in toluene was reduced with varied amounts of the reducing agent $NaEt_3BH$. The compositions of the investigated samples are given in Table 4.2.12. Note that the calculation of the reducing agent equivalents is based on the assumption of a 100% pure $Co(AOT)_2$ starting material. As this purity was not found by elementary analysis, as mentioned in section 4.2.1.1, the equivalents given in Table 4.2.12 are tainted with a systematic error. However, this does not affect the relative comparison of the entire experimental series.

Table 4.2.12.: Composition of the cobalt nanoparticle dispersions prepared with a deficient reduction.

Co #	$Co(AOT)_2$ [μmol]	Toluene [ml]	$NaEt_3BH$ (1 M) [μl]	[eq]	[Co] [mM]
L01	50.9	0.93	70	0.687	50.9
L02	50.9	0.95	50	0.491	50.9
L03	49.9	0.962	38	0.381	49.9
L04	24.9	0.5	20	0.401	48.0
L05	24.9	0.5	15	0.301	48.4
L06	24.9	0.5	10	0.200	48.9

4.2.1.8.3. Stepwise nanoparticle reduction Based on the size variation observed for a deficient reduction of the $Co(AOT)_2$ micellar solution, a stepwise reduction was investigated. 0.05 M $Co(AOT)_2$ solutions in toluene were reduced by different deficient initial amounts of $NaEt_3BH$. The remaining reducing agent needed for a full reduction was added within few days with either a constant reduction rate or a constant reduction period. For the experimental series of a constant reduction rate (M01-M04), a stock solution of 0.1333 M $NaEt_3BH$ in toluene was prepared, and 100 μl of this stock solution were added three times a day until 1 eq was reached for each sample. For the experimental series of a constant reduction period (M05-M07), a stock solution of 0.1 M $NaEt_3BH$ in toluene was prepared, and the required amounts were added three times a day during four days finally leading to 1 eq. The compositions of the prepared samples are given in Table 4.2.13.

Table 4.2.13.: Composition of the cobalt nanoparticle dispersions prepared by stepwise reduction. The amount of reducing agent is differentiated into initial reduction and reducing agent added over a given period.

Co #	$Co(AOT)_2$	Toluene	initial R.		added R.		time	[Co]
	[μmol]	[ml]	[μl]	[eq]	[μl]	[eq]	[d]	[mM]
M01	50.1	1.0	10	0.100	675	0.898	5	29.7
M02	50.2	1.0	20	0.199	600	0.796	4	31.0
M03	49.3	1.0	40	0.405	450	0.608	3	33.1
M04	50.0	1.0	60	0.600	300	0.400	2	36.8
M05	50.1	1.09	10	0.100	900	0.898	4	25.1
M06	50.8	1.18	20	0.197	800	0.788	4	25.4
M07	50.2	1.36	40	0.398	600	0.597	4	25.1

4.2.1.9. Decomposition of dicobalt octacarbonyl

Experiments on cobalt nanoparticles were performed by thermolysis of dicobalt octacarbonyl ($Co_2(CO)_8$) in the presence of cobalt nanoparticle seeds prepared by the standard synthesis route. Solid $Co_2(CO)_8$ was dissolved in a dilute cobalt nanoparticle seed dispersion in toluene. The mixture was heated under stirring in the inert atmosphere of a Schlenk line up to 100°C with a heating rate of ~30 K/h. The temperature was held constant at 100°C for one hour and the sample was cooled to room temperature over night. The resulting samples were characterized by SAXS in house. The final sample compositions are given in Table 4.2.14.

Table 4.2.14.: Composition of the cobalt nanoparticle dispersions grown by thermolysis of $Co_2(CO)_8$.

Co #	$Co(AOT)_2$ [μmol]	Toluene [ml]	$Co_2(CO)_8$ [mg]	$Co_2(CO)_8$ [μmol]	[Co] [mM]	Co(AOT):$Co_2(CO)_8$
N01	59.3	5.5	60	175.5	74.6	1:2.960
N02	13.6	3.0	30	87.7	63.0	1:6.449

4.2.2. Characterization and data treatment

4.2.2.1. Magnetization measurements

All magnetization measurements discussed in this chapter were performed using the VSM option of a Quantum Design PPMS. For measurements of liquid nanoparticle dispersions performed in an evacuated sample chamber, a new air-tight sample holder was developed. Vespel® polyimide was chosen as the sample holder material because this polymer is resistant to toluene, thus not likely to swell in contact with the nanoparticle dispersion and to incorporate traces of cobalt. The material has furthermore a low diamagnetic contribution. The magnetic sample is placed inside a hollow cylinder and held in position by two thin walls that are screwed in from both sides (see Figure 4.2.3). The sample cavity has a cylindric volume of 3.5 mm in diameter and 4 mm in height. In a VSM, the magnetic moment is detected by the electromotive force it induces while vibrating in between two coils. In order to minimize the influence of magnetic contributions from the sample holder, the sample holder should ideally be as homogeneous as possible in between these coils. For this reason, all parts of the sample holder are hollow and the assembled sample holder has the appearance of a hollow tube, aside from the two thin walls holding the sample. Note that the upper part of the sample holder

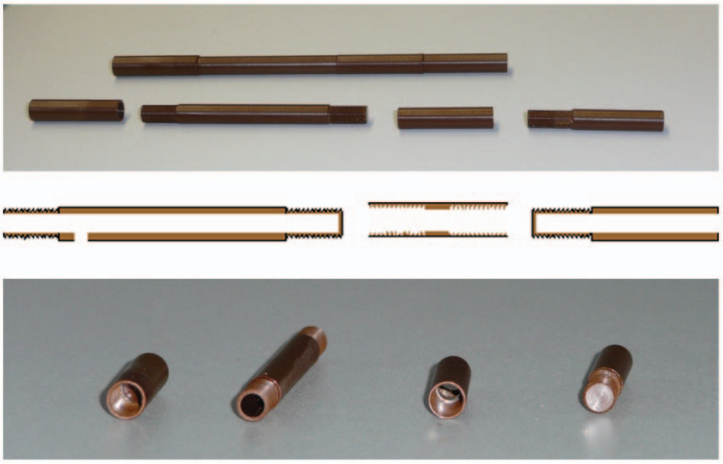

Figure 4.2.3.: Sample holder designed for measurements of liquid samples using the VSM option of the PPMS. The drawing in the center represents a cut through the sample holder. A technical drawing including all measures can be found in the Appendix C.1.

that is attached to the sample rod of the instrument has a small hole which provides the required exchange of atmosphere.

Figure 4.2.4 presents a temperature dependent magnetization measurement of the developed sample holder filled with toluene. The measurement was performed in an applied magnetic field of 100 Oe, and the maximal background contribution to the magnetic susceptibility is thus $2 \cdot 10^{-8}$ emu/Oe. Measured susceptibilities for cobalt nanoparticle sample were generally 1-2 orders of magnitude larger. A correction of this minor background contribution was thus neglected.

In order to tighten the sample holder, the threads are greased with vacuum grease and small pieces of teflon ribbon are wrapped around the screws before closing the sample cavity. Such a sample holder filled with toluene lost less than 1% of the toluene when heated to 50°C for several hours under the low pressure of a vacuum oven. Such a small loss can be neglected, considering that all magnetization measurements were performed at temperatures below the melting point of toluene (180 K).

Cobalt nanoparticle dispersions were filled into the developed sample holder inside the glove box and transported to the PPMS instrument inside a compartment filled with N_2 in order to minimize air exposure even for the sealed sample holder. For zero field cooled measurements, the sample was cooled to a base temperature of 2 K before application of a magnetic field of few mT. The temperature dependent magnetization was measured with heating rates of 0.5 K/min up to 20 K and 2 K/min up to 100 K. For field

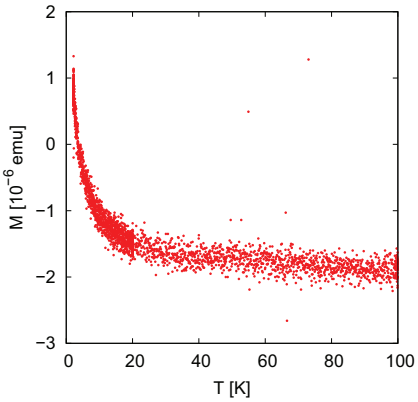

Figure 4.2.4.: Temperature dependent magnetization measurement of the PPMS sample holder filled with toluene in an applied magnetic field of 10 mT.

cooled magnetization measurements, the same conditions were applied except for the magnetic field that was applied to the sample during cooling prior to the measurement. Field dependent magnetization curves were measured with a magnetic field sweep rate of 20 mT/s with a maximum field of up to 8.5 T at low temperatures.

For conversion of the measured magnetization data into SI units, the cobalt volume was determined from its mass fraction as calculated for each sample, the sample weight, and the cobalt density of $\varrho_{Co} = 8.9\ \mathrm{g/cm^3}$. The magnetic moment measured in emu was then converted into the volume magnetization via

$$M[\mathrm{A/m}] = \frac{M[\mathrm{Am^2}]}{V_{Co}[\mathrm{m^3}]} = \frac{M[\mathrm{emu}] \cdot 10^{-3}}{V_{Co}[\mathrm{m^3}]} \tag{4.2.5}$$

Due to the imprecise determination of the mass fraction of cobalt in the prepared $Co(AOT)_2$, the absolute magnetization values are subject to a considerable systematic error. Nonetheless, the sample magnetization can be discussed qualitatively by comparison of several measurements of the same sample.

4.2.2.2. SAXS

For SAXS measurements, the nanoparticle dispersions were filled into Hilgenberg quartz capillaries with an inner diameter of 1.5 mm and a wall thickness of 0.01 mm. The capillaries were sealed with PMMA stoppers using Loctite 408 glue.

In house SAXS SAXS measurements were performed with a fixed incoming wavelength of Cu Kα with λ = 1.54 Å and a fixed sample to detector distance of 106 cm, yielding a maximal accessible Q range of 0.007 to 0.2 Å^{-1}. Measurements were performed in vacuum, and typical exposure times were 8h per sample. Data were reduced and normalized to absolute units using the program Reduce [77].

JUSIFA SAXS measurements at the JUSIFA beamline were performed during three different beamtimes with slightly different configurations. All measurements were performed in vacuum. Two different sample detector distances were chosen, with a beam size of 0.8 x 0.8 mm for the 935 mm detector distance, and 0.8 x 0.5 mm for the 3635 mm detector distance. The data was recorded on one of two available detectors. The first detector is a multiwire proportional chamber gas detector (Gabriel detector) with 256 x 256 pixels of 0.8 mm pixel size. As alternative detector, a PILATUS 300k detector with 487 x 619 pixels of 0.172 mm pixel size was used.

During beamtime **(07)** an incident energy of 7.420 keV (below the Co K edge) was used, and the scattered intensity was recorded on the Gabriel detector. All samples investigated during this beamtime were diluted to a cobalt concentration of 0.01 M. Configuration **(08)** used an incident energy of 12.00 keV along with the Gabriel detector. SAXS measurements during beamtime **(09)** were performed with an incident energy of 12.02 keV and two different detector distances using the PILATUS detector. The beam size was set to 0.8 x 0.8 mm for the 935 mm detector distance, and 0.8 x 0.5 mm for the 3635 mm detector distance.

The data were radially averaged and normalized to absolute units by use of glassy carbon with a thickness of 1 mm as a reference material.

SWING SAXS measurements at the SWING beamline were performed in vacuum using an incident energy of 11.000 keV and a sample detector distance of 1030 mm, resulting in a maximal momentum transfer range of 0.45 Å^{-1}. The scattering was recorded on an Aviex CCD detector of 4096 x 4096 pixels with a software binning to 1024 x 1024 pixels with a pixel size of 164 μm. Data reduction was performed using the Actionjava 1.4 software [78], and normalization to absolute units was not performed.

ID01 SAXS measurements at the ID01 beamline were performed using an incident energy of 7.665 keV. Two detector positions of 520 and 1400 mm distance to the sample were measured, resulting in a wide investigated momentum transfer range of 0.009 - 0.5 Å^{-1}. Data reduction and normalization was performed using the ID01 data reduction software.

4.2.2.3. ASAXS

ASAXS measurements were performed at the JUSIFA beamline on the same samples as prepared for SAXS. Three different incident energies below the Co K edge were chosen in order to separate the pure resonant cobalt scattering.

For determination of the anomalous scattering factors f′ and f″, X-ray absorption was measured around the K edge. The program Chooch was used for normalization of the absorption data and determination of f″ as well as f′ by Kramers-Kronig transformation [79]. The resulting f′ and f″ in dependence of the incident energy are presented in Figure 4.2.5. For determination of the anomalous scattering factors far from the Co K edge, X-

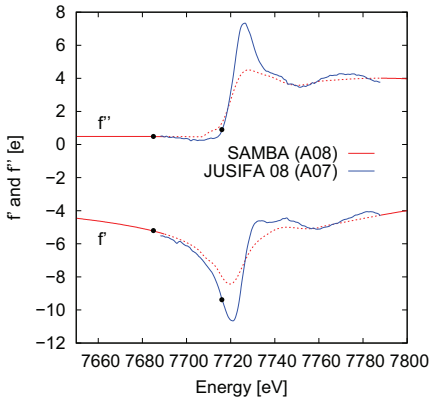

Figure 4.2.5.: Anomalous scattering factors as determined by X-ray absorption spectroscopy. The f′ and f″ values for incident energies chosen during the JUSIFA 08 beamtime are indicated as black points.

ray absorption data of a cobalt nanoparticle sample measured at the SAMBA beamline in a much wider energy range was used. The finally obtained f′ and f″ values for the chosen incident X-ray energies are given in Table 4.2.15. Separation of the pure resonant scattering was performed according to the relations given in section 2.2.2.6. In order to account for cobalt fluorescence close to the absorption edge, a constant contribution was subtracted from the SAXS data measured at highest incident X-ray energy.

4.2.2.4. SANS

SANS measurements at KWS 2 were performed using Hellma quartz cuvettes with a sample thickness of 1 mm as sample holders. The sample holders were filled in the inert argon atmosphere of a glove box in order to avoid oxidation, and the samples were

Table 4.2.15.: Anomalous scattering factors determined for ASAXS experiments. The incident energies chosen for the (08) beamtime are indicated in Figure 4.2.5.

ASAXS beamtime	cobalt sample	Energy [eV]	f′ [e]	f″ [e]
(07)	A02	7420	-2.99	0.507
		7693	-5.99	0.475
		7709	-11.57	3.94
(08)	A07	7458	-3.01	0.50
		7685	-5.20	0.49
		7716	-9.38	0.90

measured within a closed compartment with argon atmosphere. A wavelength of 5 Å was chosen, and SANS was measured at 2 m and 8 m detector distances with a collimation distance of 8 m for both detector distances. Collimation and sample apertures were set to 30 x 30 mm and 9 x 9 mm, respectively. The detector has a pixel size of 5.25 mm. The measured data was circularly averaged and normalized to absolute units using the data reduction program qtiKWS [80].

Polarized SANS measurements with polarization analysis were performed at the DNS, J-NSE, and IN12 instruments. Aluminum flat plate sample holders with a sample thickness of 1 mm were used. A detailed description of instrument configuration, data reduction, and separation of coherent and incoherent scattering contributions can be found in chapter 6.

4.2.2.5. XAS

For XAS measurements on the Co K edge, cobalt nanoparticle dispersions were sealed in quartz capillaries as for SAXS measurements. As reference materials, a thin cobalt foil and a pellet consisting of 5 mg CoO and 60 mg cellulose were measured. The experiments were performed at the SAMBA beamline at the Synchrotron Soleil. All the samples were measured at room temperature. XAS data of the cobalt dispersions were obtained by detecting the cobalt fluorescence using a Rontec detector. Simultaneously, three ionization chambers were used in order to detect the incident flux (I_0), the transmission of the sample (I_1/I_0), and the transmission of a standard Co foil (I_2/I_1).

Data analysis was performed using the program Athena [81]. Data correction was performed by a polynomial fit of the pre-edge range and a spline fit of the normalization range. The radial distribution function in real space was obtained by Fourier transformation of the processed EXAFS in k space weighted by a factor of k^3.

4.2.2.6. UV-VIS spectroscopy

Absorption spectra in the UV-VIS spectral range were measured using a Varian Cary 50 Bio spectrophotometer. Samples were filled into Hellma precision cuvettes with a sample thickness of 1 cm. Absorption was measured in a wavelength range of 200 - 800 nm with a scan rate of 300 nm/min. A baseline of pure toluene was measured as a reference.

4.3. Results and Discussion

Many different routes have been investigated in order to develop nanoparticle dispersions suitable for investigation of their spin structure by neutron scattering techniques as well as to prepare nanoparticle samples of a varied particle size and defined size distribution. In order to give a clear overview of the obtained results, the focus will be first on the standard synthesis route and characterization of cobalt nanoparticles (section 4.3.1) and then on investigated routes to particle size variation (section 4.3.2).

Section 4.3.1.1 will cover the standard synthesis procedure and give a first estimation of the properties of the as-synthesized nanoparticles. Sections 4.3.1.2 - 4.3.1.7 will give insight to the applied characterization methods such as magnetization measurements and small-angle X-ray scattering (SAXS). Observed obstacles for synthesis optimization such as nanoparticle oxidation, synthesis byproducts, and reproducibility will be addressed. A statement on the applicability of the available primary characterization methods to the studied nanoparticle system will be given, which is a prerequisite for assessment of the results of the size variation experiments discussed in section 4.3.2.

4.3.1. Preparation and Characterization of Cobalt nanoparticles

4.3.1.1. Nanoparticle preparation

The general synthesis route explored in this chapter for the preparation of cobalt nanoparticles involves the reduction of $Co(AOT)_2$ in toluene and is originally based on a nanoparticle synthesis route from water-in-oil microemulsions [73]. Since it was found that even small amounts of water, which are necessary to dissolve the reducing agent $NaBH_4$, lead to a nearly complete oxidation of the formed cobalt nanoparticles, an organic borohydride was successfully employed as reducing agent for a water-free synthesis route yielding cobalt nanoparticles [7].

A schematic representation of the synthesis procedure studied in this chapter is given in Figure 4.3.1. The starting material $Co(AOT)_2$ serves thus both as cobalt source and

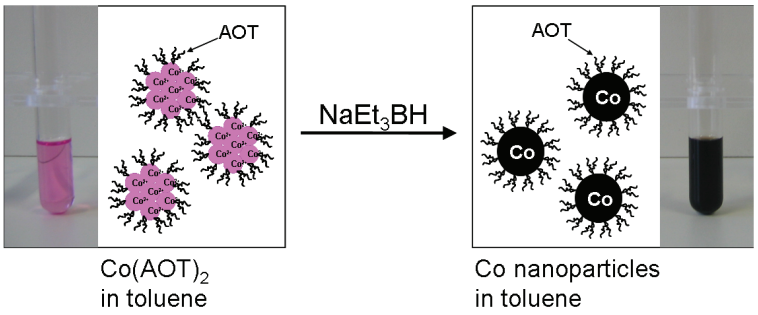

Figure 4.3.1.: Schematic of cobalt nanoparticle synthesis from $Co(AOT)_2$ reverse micelles.

as ligand forming the nanoparticle shell preventing particle agglomeration. Combining the cobalt cation with the surfactant anion results in a lower amount of byproducts as compared to *e. g.* the use of Co^{2+} salts and the more common surfactant NaAOT. Furthermore using $Co(AOT)_2$ allows for bringing in more Co^{2+} ions into the microemulsions. If Co^{2+} would be incorporated as inorganic salt, high concentrations of the ions in the aqueous phase would be necessary, which in turn would also lead to drastic changes in the phase behavior and the structure of the water-in-oil microemulsions [82, 83]. $Co(AOT)_2$ is prepared by ion exchange of NaAOT via HAOT (see section 4.2.1.1 for the experimental details of the preparation). $Co(AOT)_2$ forms reverse micelles if dissolved in nonpolar solvents such as hexane or toluene, which were used as a solvent for this study. The reverse micellar solution has a pink color as commonly observed for Co^{2+} cations (see Figure 4.3.1). The reducing agent sodium triethylborohydride ($NaEt_3BH$) was chosen as a replacement for $NaBH_4$, which was previously used in the microemulsion synthesis route [70]. $NaBH_4$ needs to be solubilized in the polar phase of water-in-oil microemulsions, whereas $NaEt_3BH$ is soluble in organic solvents and can thus be added directly to a reverse micellar solution of $Co(AOT)_2$ in toluene. In this way the cobalt nanoparticles can be synthesized free of water and this route is more stable against oxidation. The immediate change of the dispersion color from pink into black results from the fast reduction of Co^{2+} cations to Co atoms, which nucleate to cobalt nanoparticles and grow via intermicellar exchange. In order to prevent oxidation of the nanoparticles, the samples were prepared and stored in an inert N_2 atmosphere. The standard synthesis procedure referred to in what follows, consists of using a 0.05 M reverse micellar solution of $Co(AOT)_2$ in toluene, which is then reduced by 1 equivalent of $NaEt_3BH$.

In order to give a first estimation of the properties of the synthesized nanoparticles,

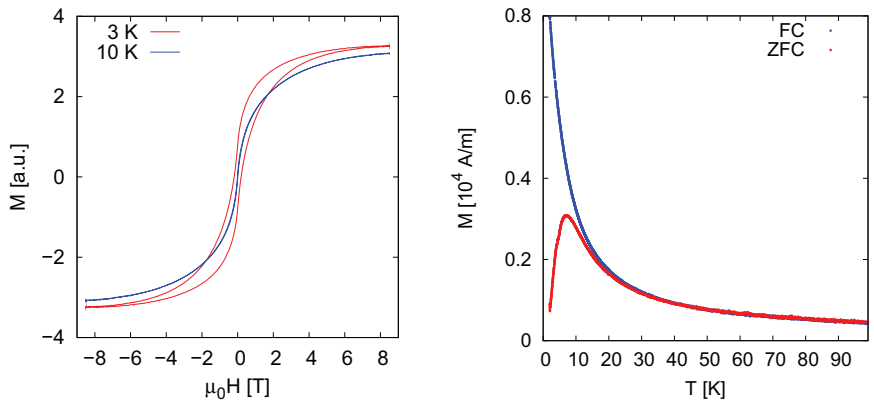

(a) Field dependent magnetization.

(b) Temperature dependent magnetization.

Figure 4.3.2.: Magnetization measurements on cobalt nanoparticles (Co A01). Field dependent measurements were performed at 3 and 10K. Temperature dependent magnetization measurements were performed in a magnetic field of 5 mT after zero field cooling (ZFC) and field cooling (FC).

selected magnetization and small-angle scattering measurements have been performed and will be discussed in this section. Magnetization measurements on a sample displaying the required quality are presented in Figure 4.3.2. The temperature dependent magnetization measurements reveal a superparamagnetic blocking temperature, which is observed below 10 K for all investigated cobalt nanoparticle samples. The narrow slope of the ZFC measurements indicates a relatively narrow size distribution. Field dependent measurements performed at temperatures below the blocking temperature reveal hysteresis as expected for single domain nanoparticles. However, the shape of the hysteresis curve is somewhat different from the expected Stoner Wohlfarth behavior. It is remarkable that saturation was not reached at the highest applied magnetic field of 8.5 T.

A typical small angle X-ray scattering curve as obtained by the as-prepared cobalt nanoparticles at the JUSIFA beamline, HASYLAB, is presented in Figure 4.3.3. Guinier behavior is observed in the lower Q range, and an approximate spherical particle radius of 16.0(2) Å is determined by refinement of the radius of gyration within the Guinier regime ($QR_G < 1$). Typical particle diameters of 3 nm correspond to very small nanoparticles comprised of ~ 1300 atoms. The refinement of a spherical form factor and thus determination of the particle size distribution is not possible because a form factor minimum is not observed in the investigated momentum transfer range, which is due to the small particle size.

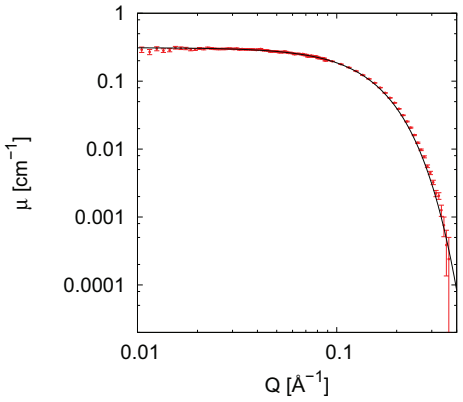

Figure 4.3.3.: SAXS by cobalt nanoparticles (Co A02). The black line represents a Guinier fit.

Note that the SAXS and magnetization measurements presented here have not been performed on the same sample, but on two samples prepared by the standard synthesis method. A variation of particle size (SAXS) and also much lower blocking temperatures (magnetization measurements) were observed for further samples prepared by the exact same method and will be discussed in later sections. However, the presented measurements show that the proposed synthesis route produces magnetic nanoparticles with particle diameters in the order of 3 nm. The sample investigated by SAXS is furthermore well dispersed as deduced from the absence of a structure factor, which would result from agglomeration.

In order to prepare nanoparticle dispersions that are suitable for the investigation of the nanoparticle spin structure by neutron scattering techniques, several requirements have to be fulfilled. The nanoparticles should be magnetic (*i. e.* non-oxidized) and have a defined (*i. e.* reproducible) particle size along with a narrow size distribution. Furthermore, the availability of different particle sizes is desired for size dependent investigations. Thus, a precise monitoring of the particle size, the size distribution, and the magnetic properties is required for cobalt nanoparticles prepared by the standard synthesis recipe presented here as well as during further synthesis optimization.

In the following sections, the pre-characterization of the prepared cobalt nanoparticles is presented. Magnetic characterization by magnetization measurements as well as structural characterization by small-angle scattering will be discussed with respect to the applicability of the studied synthesis procedures. Furthermore, obstacles in synthesis optimization such as oxidation and low reproducibility are taken into account. As a result, the frontiers of synthesis optimization for the given synthesis procedure and

primary characterization methods will be identified.

4.3.1.2. Magnetization measurements

Magnetization measurements are performed for two purposes. First, the magnetic nature of the sample can be confirmed, thus clarifying that the particles are not oxidized. Secondly, if determination of the superparamagnetic blocking temperature is possible, information on the particle size relative to another sample can be deduced because the blocking temperature is in a first approximation proportional to the particle volume (in case of a size-independent magnetic anisotropy, see equation (2.1.6)).

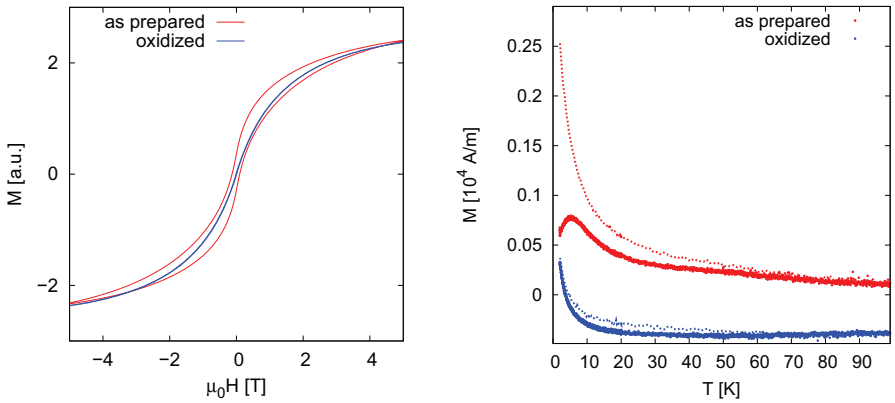

(a) Field dependent magnetization measured at 3 K. Data were scaled in order to match at high field.

(b) Temperature dependent magnetization.

Figure 4.3.4.: Magnetization measurements on nanoparticles as prepared (Co A03) and fully oxidized by exposition to air (Co A04). Temperature dependent magnetization measurements were performed in a magnetic field of 5 mT after zero field cooling (points) and field cooling (dashed line).

In order to perform magnetization measurements on liquid nanoparticle dispersions that are air-sensitive, air-tight sample holders were developed for the VSM option of the PPMS which were filled with the cobalt nanoparticle dispersion inside the inert atmosphere of a glove box (see section 4.2.2.1 for more details on the sample holder). Figure 4.3.4 compares magnetization measurements performed on a cobalt nanoparticle sample as prepared by the standard synthesis procedure and a deliberately oxidized sample. The magnetic properties of partially and fully oxidized cobalt nanoparticles were studied in detail by Tracy *et al.* [84]. In agreement with their results, the field dependent magnetization of the oxidized nanoparticle sample at 3 K does not exhibit hys-

teresis (H_C = 0), and no blocking temperature is observed in the temperature dependent magnetization measurement. The non-oxidized sample, however, exhibits a blocking temperature of 5.2(1) K as well as hysteresis of the field dependent magnetization measurement. The observed blocking temperature is slightly lower than the blocking temperature observed in Figure 4.3.2b. Despite the observation of a blocking temperature, which is indicative of magnetic cobalt particles, the peculiar curve of the hysteresis in Figure 4.3.4a can be attributed to a partial oxidation. Noticeable criteria therefore are the suppressed coercive field with respect to the large splitting at higher magnetization as well as a small positive shift of the curve along the magnetization axis [84]. For the exchange bias contribution of a larger degree of oxidation, an asymmetric hysteresis may furthermore be expected [84]. The blocking temperature exhibited by a partially oxidized sample is reported to be higher than for non-oxidized nanoparticles. Taking into account the hysteresis shape of the samples presented in both Figures 4.3.2 and 4.3.4, the blocking temperature of perfectly non-oxidized cobalt nanoparticles is expected to be even lower than observed in the corresponding temperature dependent magnetization measurements. As a result, the correct blocking temperature can only be determined if the field dependent magnetization reveals a Stoner Wohlfarth behavior as expected for single domain nanoparticles. For size variation experiments, however, a slight degree of oxidation can be accommodated. If the hysteresis curves in an experimental series are similar in shape, the impact on the blocking temperature should be systematic, and a variation of the blocking temperature within the experimental series can be explained by a variation of the particle volume.

Thus, the differentiation between fully or partially oxidized and non-oxidized cobalt nanoparticles can be achieved with good reliability by field dependent magnetization measurements. For the relative size determination, *e. g.* during size variation experiments, reliability of the sample preparation, with a comparable degree of oxidation on a whole experimental series, is required.

An additional important requirement is the reliability of the zero field cooled (ZFC) magnetization measurement. The ZFC experiment relies on the compensation of any residual magnetic field during cooling of the sample. Furthermore, the ZFC magnetization measurement is an irreversible process that requires a monotonic temperature increase. In particular the sample temperature was many times observed to be unstable below 10 K and to increase suddenly to temperatures exceeding the expected blocking temperature. The typical run time for FC, ZFC, and two field dependent magnetization measurements of one sample adds up to 7 hours. Along with the typically limited availability of measurement time at a highly frequented instrument, a sporadical failure of the ZFC measurement may result in time periods of weeks between measurements of

samples belonging to the same experimental series (which typically includes 4-6 samples). Because particle oxidation and further ageing effects may not be excluded, an experimental series has to be measured within a short time frame to ensure comparability. Thus, such a delay certainly impacts the determination of the size variation. As a consequence, it is often unclear whether a deviation in results of magnetization measurements results from poor reproducibility of the synthesis method or low reliability of the measurement.

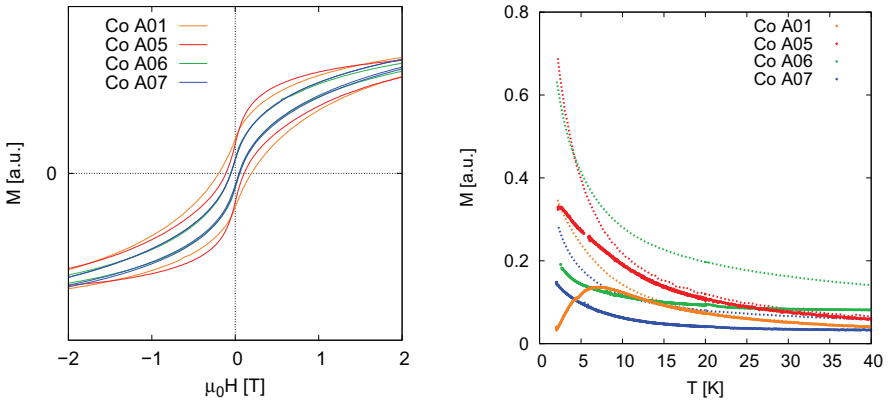

(a) Field dependent magnetization measured at 3 K.

(b) Temperature dependent magnetization.

Figure 4.3.5.: Magnetization measurements on several cobalt nanoparticle samples prepared by the same method. Temperature dependent magnetization measurements were performed in a magnetic field of 5 mT (Co A01 and A07) or 10 mT (Co A05 and A06) after zero field cooling (lines) and field cooling (points). Data are scaled for display.

As an example, Figure 4.3.5 presents a comparison of magnetization results for several samples that were all prepared by the same standard synthesis route described above. While the different hysteresis curves can certainly be attributed to a different degree of partial oxidation of the samples, the absence of a blocking temperature for some samples in Figure 4.3.5b can not be explained by a full oxidation due to the observation of a coercive field at 3K. In this case, instrumental reasons such as a non-zero field during cooling may be speculated.

This differentiation is not as obvious if an experimental series intending size variation is studied, because the deviation between the measured samples may also result from different particle sizes. Therefore, an insufficient reliability of the characterization method heavily impedes synthesis optimization regarding reproducibility.

4.3.1.3. Partial and full oxidation

The issue of oxidation of cobalt nanoparticles has been addressed in several reports. The cobalt nanoparticles prepared from microemulsions by Pileni *et al.* are reported to be 6 nm in diameter and air-stable after a surface treatment with trioctyl phosphine ($P(oct)_3$) [70]. This is in contrast to the observation that even the small amount of water inside the reverse micelles leads to a complete oxidation of the formed nanoparticles [7]. Bönnemann *et al.* produced cobalt nanoparticles of 10 nm in diameter that are reported to be air-stable after passivation by mild oxidation and subsequent peptization [85]. Both examples refer to considerably larger nanoparticles than those studied here. The larger the particle, the lower the surface to volume ratio, and the influence of a thin and possibly passivating oxide layer on the spin structure may be smaller. In contrast, very small nanoparticles are likely to oxidize completely once exposed to air. Furthermore, for investigation of their spin structure entirely oxide-free nanoparticles are required in order to minimize effects not resulting from the finite size. Chaudret *et al.* showed that small cobalt nanoparticles in a size range of 1 - 1.5 nm in diameter can be produced oxide-free inside a polymer matrix with excess of reducing agent in an entirely inert atmosphere [63, 86].

Despite the entirely water-free synthesis technique and the inert conditions maintained during synthesis, magnetization measurements of the cobalt nanoparticles prepared in this study reveal a varying degree of oxidation. The origin of the oxidation is expected to be either an imperfect inert atmosphere inside the glove box, contamination of the used starting materials, or oxygen contamination inside the sample holders used for magnetization measurements. Due to the varying performance of the magnetization measurements this origin could not be clarified. In this section, a more detailed investigation of partially and fully oxidized cobalt nanoparticles is given.

Additionally to the minimization of the coercive field observed for most samples due to a partial oxidation [84], a considerable positive shift of the hysteresis curve along the magnetization axis was observed occasionally. Examples for this magnetization shift are presented in Figure 4.3.6. The magnetization is scaled to 1 at the highest applied magnetic field $\mu_0 H_{max}$. For both samples, the modulus of the magnetization at an applied field of -$\mu_0 H_{max}$ is considerably lower, leading to a shift of the hysteresis curve of 1.52 % and 10.5 % of M_{max} for sample Co A03 and A08, respectively. Additional exchange bias fields of 3.4 and 3.6 mT resulting in a small shift in direction of the field axis are observed for sample Co A03 and A08, respectively, but are considered a minor effect as compared to the large magnetization shifts. Large magnetization shifts have been observed for partially oxidized cobalt nanoparticles along with an asymmetric hysteresis shape as a

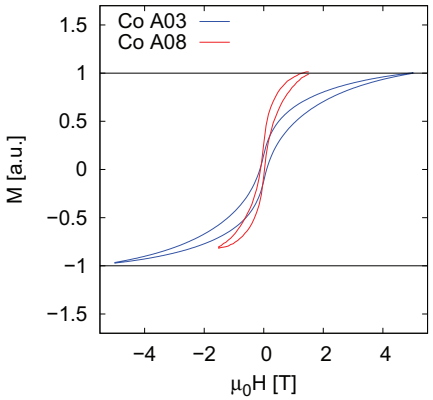

Figure 4.3.6.: Magnetization shift observed by partially oxidized cobalt nanoparticles. Measurements were performed at 3 K.

result of a combination of exchange bias and an additional superparamagnetic component [84]. Such a magnetization shift, which in this case can not be explained by a large exchange bias field, has to the best of our knowledge not been reported yet.

X-ray absorption spectroscopy measurements were performed at the SAMBA beamline of the Synchrotron Soleil in order to determine the local structure of the prepared cobalt nanoparticles. Normalized spectra of the Cobalt K edge are presented in Figure 4.3.7. All samples seem to consist of mixtures of Co and CoO as suggested by comparison of the intensity of the white line and the multiple scattering oscillations beyond the edge with Co and CoO reference measurements. Magnification of the XANES region in Figure 4.3.7b reveals low-intensity pre-edge features for all samples, corresponding to 1s 3d electronic transitions. Transition metals generally exhibit a pre-edge step which is not observed for oxidized transition metals. In contrast, transition metal oxides may exhibit a small pre-edge peak if the excited atom site has a lack of centrosymmetry [87]. Such a pronounced pre-edge peak is observed for the sample A04, which is the deliberately oxidized sample discussed before (with magnetization measurements presented in Figure 4.3.4). Because the cobalt site in CoO has a centrosymmetric local symmetry of O_h, the peak can be attributed to either Co_3O_4, where $\frac{1}{3}$ of the cobalt atoms has a T_d local symmetry, or a reduction of centrosymmetry at the cobalt-cobalt oxide interface or the particle surface, which is an important contribution for nanoparticles of such small particle size.

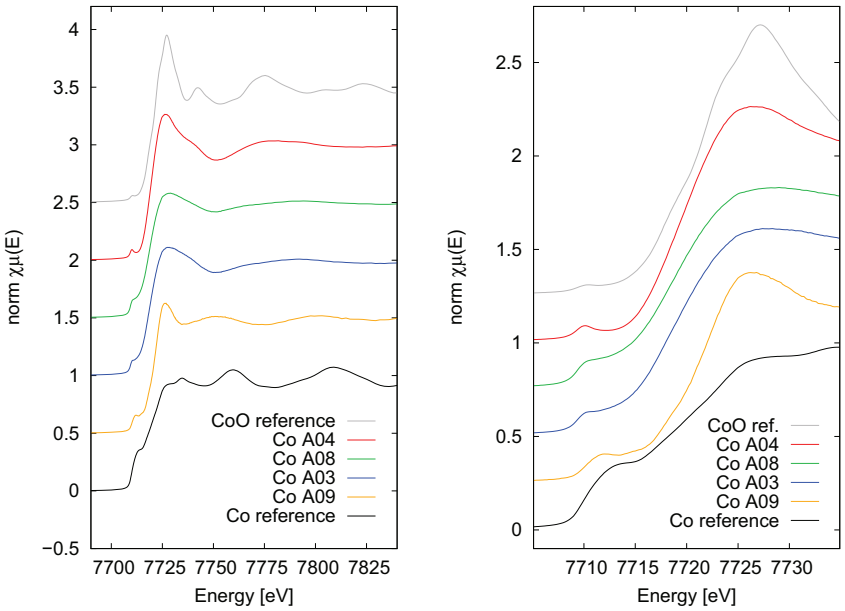

(a) Cobalt K edge.

(b) XANES of the cobalt K edge.

Figure 4.3.7.: X-ray absorption spectroscopy of cobalt nanoparticles.

A higher intensity of the pre-edge step and a more gradual slope of the main absorption edge indicate a larger proportion of metallic cobalt in the sample. Particularly the samples A03 and A08 exhibit a larger pre-edge step and a lower main absorption edge slope suggesting a lower degree of oxidation. The sample A09 has a more complicated near edge structure, with a sharp absorption peak indicative of oxidized cobalt, but a peak around 30 meV beyond the main absorption edge, which is similar to the shape resonance observed for cobalt metal.

As XANES is sensitive to the electronic configuration of the probed atom, comparison of the measured spectra with bulk references may in general be an indication of the valence state. However, for small nanoparticles the electronic configuration for atoms at the particle surface may be different and not directly comparable to bulk references. Here, EXAFS analysis will provide more precise information by giving insight into the type and distance of the nearest neighbor correlations.

The EXAFS and its Fourier transform into real space are presented in Figure 4.3.8. The normalized and background subtracted EXAFS presented in Figure 4.3.8a exhibits comparable features for the samples A03, A04, and A08. For the sample A09, a significantly higher frequency of the oscillations is observed. The Fourier transformed

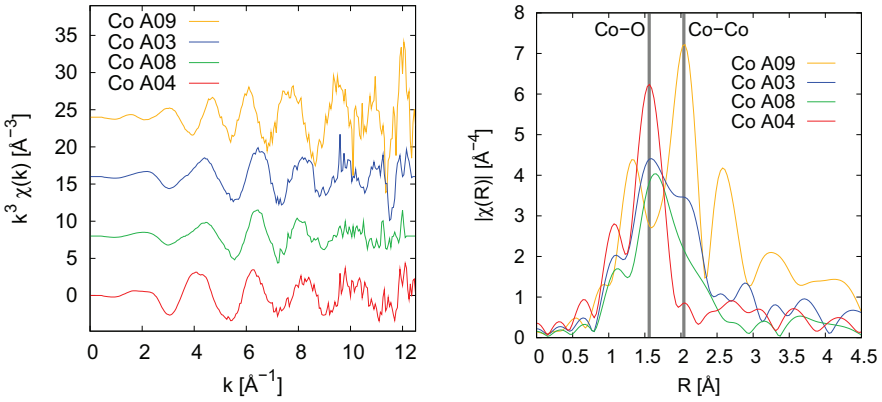

(a) EXAFS spectra weighted by k^3.

(b) Fourier transform of the EXAFS spectra weighted by k^3.

Figure 4.3.8.: EXAFS of cobalt nanoparticles.

EXAFS data presented in Figure 4.3.8b clearly exhibits Co-O as well as Co-Co nearest neighbor correlations at real space distances of 1.6 and 2.0 Å, respectively. The intensity of the Co-Co correlation decreases with A09, A03, A08, A04, while the intensity of the Co-O correlation increases. A09 is the only sample with a dominating Co-Co correlation, which explains the different oscillation frequency observed in the reciprocal space. While the deliberately oxidized sample does not exhibit any Co-Co correlations, minor Co-Co contributions are observed for A03 and A08, which are the samples exhibiting shifted hysteresis curves as presented in Figure 4.3.6. Thus, the prepared cobalt nanoparticles consist of cobalt metal as well as oxidized cobalt, which is supposed to form a shell around the metallic nanoparticle core.

In order to explain the large intensity of the Co-O correlations, a quantitative analysis of the EXAFS is required along with a precise information on the particle size. Unfortunately, the particle size of these specific samples could not be determined by SAXS. As the samples A03, A04, and A08 were prepared according to the standard synthesis route given above, an average particle diameter of 3 nm can be assumed. A09 was prepared via particle growth by decomposition of dicobalt octacarbonyl ($Co_2(CO)_8$) and is discussed more detailed in section 4.3.2.6. Its particle size is supposedly larger than for the other samples, but a precise value can not be determined from SAXS.

An estimate of the amount of Co-O correlations can be given assuming purely metallic cobalt nanoparticles with a diameter of 3 nm. The typical Co-Co distance is 2.5 Å. Thus, cobalt atoms within a core of 1.25 nm radius will have a full coordination sphere of cobalt atoms. Cobalt atoms at the particle surface (of 0.25 nm thickness) will have a

mixed Co and O coordination sphere because the nanoparticle surface is coordinated by AOT sulfonate groups. In a particle as small as 3 nm in diameter, the pure cobalt core amounts to 58 % of the total particle volume. According to the surface area ratio of spheres with R_{core} = 1.25 nm and R_{shell} = 1.5 nm, the coordination sphere of cobalt atoms at the particle surface is estimated to consist of 41% Co-Co correlations and 59% Co-O correlations. Thus, further assuming a constant coordination number in particle core and surface, ~ 75% of the nearest neighbor correlations are estimated Co-Co, and 25% are estimated Co-O correlations in a non-oxidized cobalt nanoparticle of 3 nm in diameter. A size dependent EXAFS study by Cheng *et al.* illustrates the higher reactivity of smaller cobalt nanoparticles resulting in a larger fraction of Co-O correlations [88].

By a visual inspection of the local structure presented in Figure 4.3.8b no defined Co-O correlation is found for A09. Because this sample is expected to have a larger particle size, the fraction of Co-Co correlations may certainly be larger than 75%. All the other samples exhibit a fraction of Co-O correlations larger than 50%, indicating either a particle diameter much smaller than 3 nm or a significant degree of oxidation. For an equal amount of Co-Co and Co-O correlations in a non-oxidized cobalt nanoparticle, a particle diameter of 1.5 nm is estimated by the same relations, which is probably below the real particle radius. Furthermore, the observation of shifted hysteresis curves for A03 and A08 indicates the coexistence of metallic cobalt and cobalt oxide. Such a defined cobalt core and cobalt oxide shell structure with a gradual variation of the cobalt oxide fraction has not been observed before for nanoparticles as small as 3 nm in diameter.

4.3.1.4. Small-angle X-ray scattering

Small-angle scattering is the method of choice for a precise determination of the nanoparticle morphology, including particle size and size distribution. This structural analysis is a prerequisite for further investigation of the magnetic structure and magnetization density, which can be probed by polarized small-angle neutron scattering. Because the determination of the particle size by magnetization measurements was not found to be sufficiently reliable for synthesis optimization experiments, small-angle X-ray scattering was applied as an additional primary characterization method for experiments aiming at a variation of the particle size. However, information on the degree of oxidation is not obtained by SAXS. This section will focus on the applicability of SAXS as a primary characterization method for the cobalt nanoparticle samples under study as well as experiments aiming at suitable samples for a precise structural characterization.

The in house SAXS instrument covers a typical momentum transfer range of 0.007 to 0.2 $Å^{-1}$. A comparison of the momentum transfer ranges of the in house SAXS in-

strument and the JUSIFA beamline at HASYLAB is given in Figure 4.3.9. The first form

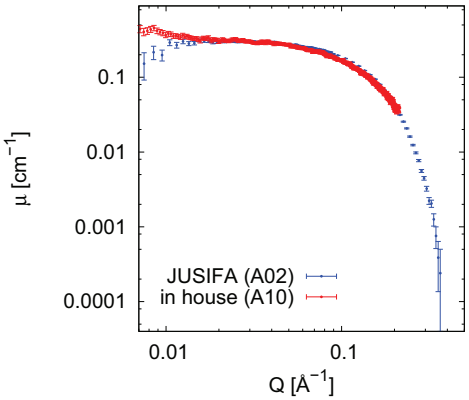

Figure 4.3.9.: Comparison of momentum transfer ranges at JUSIFA and in house. The SAXS already presented in Figure 4.3.3 is compared to in house SAXS by a sample prepared by the same synthesis route. The in house measurement is scaled to match the normalized JUSIFA measurement.

factor minimum, which is the best indication for determination of the particle size and size distribution, is expected at ~0.4 Å, which is not in the measured Q range for neither instrument. While with synchrotron radiation a wider Q range can be achieved by selection of a larger incident energy, the energy of the in house instrument is fixed by the X-ray source. The scattering curve measured in house does not reach the Q^{-4} Porod regime, and an intensity range of only one order of magnitude is covered. Thus, determination of the particle size by refinement of a spherical form factor will not be possible for the in house measurement. Instead, an estimation of the particle size can be obtained by Guinier approximation because the sample presented in Figure 4.3.9 does not exhibit a pronounced structure factor in the lower Q range. For these reasons, a particle size determination can generally be performed using in house SAXS if the measured sample is either free of interparticle interactions or is comprised of substantially larger particles, exhibiting a form factor minimum at $Q < 0.2$ Å.

Synchrotron SAXS measurements were performed at the JUSIFA beamline at HASYLAB, ID 01 at ESRF, and SWING at Soleil. The use of synchrotron radiation leads to shorter exposure times due to the much higher photon flux as compared to in house X-ray tubes. Furthermore, the measured momentum transfer range can be controlled by choice of both sample-detector distance and incident photon energy. However, a pronounced form factor minimum is generally not observed in the SAXS curves of the prepared cobalt nanoparticles. Instead, the first form factor minimum of the cobalt

nanoparticles is expected to be superposed by the small-angle scattering of smaller aggregates resulting from the reaction byproducts. It is supposed that the NaAOT formed as byproduct of the reaction exceeds the amount necessary to cover the nanoparticle surface and as a result forms excess reverse micelles. These NaAOT micelles are smaller than the formed nanoparticles and the initial $Co(AOT)_2$ reverse micelles.

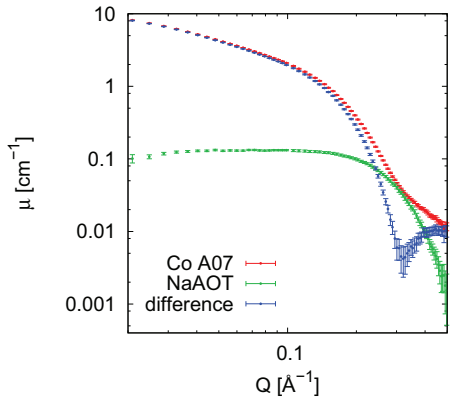

Figure 4.3.10.: Comparison of SAXS by cobalt nanoparticles and NaAOT reverse micelles.

Figure 4.3.10 presents SAXS by cobalt nanoparticles as well as NaAOT reverse micelles as measured at the JUSIFA beamline. While for the cobalt nanoparticle sample an edge is observed rather than a pronounced form factor minimum, the difference curve after subtraction of a scaled SAXS curve of NaAOT reverse micelles clearly exhibits an intensity minimum. The position of the intensity minimum at 0.31(1) $Å^{-1}$ indicates a particle diameter of 20.3(7) Å. In contrast to the position of the intensity minimum, its smearing depends on the scattering intensity of the excess NaAOT micelles that is subtracted. Because the exact amount of excess NaAOT micelles is not known, the particle size distribution can not be reliably determined. For the example presented in Figure 4.3.10, a 0.098 M solution of NaAOT in toluene was arbitrarily scaled by 0.85 and subtracted from a cobalt nanoparticle dispersion prepared from a 0.045 M $Co(AOT)_2$ solution. Thus, the scattering by NaAOT micelles corresponding to 92 % of the entire amount of AOT in the dispersion has been subtracted, which likely overestimates the real amount of free NaAOT in the dispersion.

In order to determine both particle size and size distribution reliably, either the pure cobalt scattering intensity has to be separated or the cobalt nanoparticles have to be extracted from the synthesis dispersion and redispersed to prepare a nanoparticle dispersion free of excess micelles. ASAXS experiments aiming at the separation of the

pure cobalt scattering contribution and experiments regarding the extraction of cobalt nanoparticles will be presented in sections 4.3.1.5 and 4.3.1.6, respectively.

If the refinement of a particle form factor is not possible in the measured SAXS data, which is the case for in house as well as many of the synchrotron SAXS measurements, the Guinier approximation may provide an estimation of the particle size. However, the applicability of the Guinier approximation is restricted to non-interacting nanoparticle dispersions, exhibiting a Guinier plateau in the low Q range.

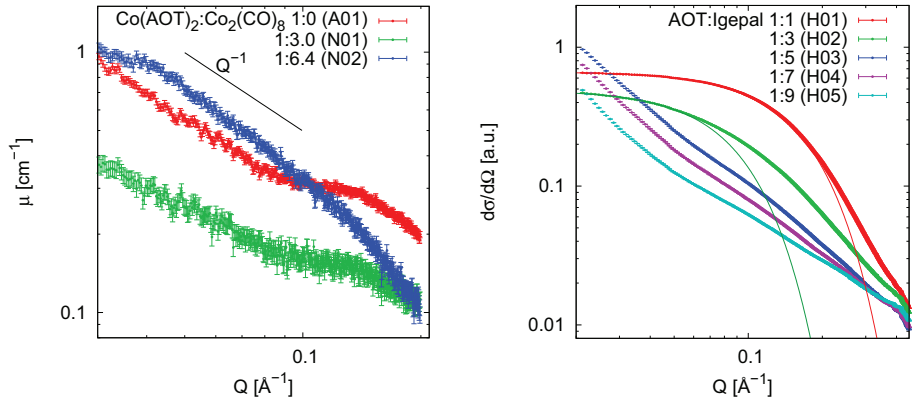

(a) SAXS by interacting cobalt nanoparticles measured in house. Discussion of the presented samples is given in section 4.3.2.6.

(b) SAXS by interacting cobalt nanoparticles measured at the SWING beamline. Guinier fits are presented as thin green and red lines. Discussion of the presented samples is given in section 4.3.2.3.4.

Figure 4.3.11.: Examples for SAXS by interacting cobalt nanoparticles.

In Figure 4.3.11 examples for SAXS by different cobalt nanoparticle dispersions are presented. Discussion of the preparation and characterization of the samples is given in sections 4.3.2.6 and 4.3.2.3.4. For two samples in Figure 4.3.11b, the Guinier approximation is applicable and the particle size was determined. The remaining samples presented in Figure 4.3.11 exhibit different degrees of interparticle interaction, thus impeding particle size determination by the Guinier approximation. For interacting magnetic nanoparticles, the formation of linear aggregates is commonly observed [89–93]. A linear aggregate corresponds to a fractal dimension of 1 leading to a Q^{-1} power law in the lower Q range of SAXS measurements as illustrated in Figure 4.3.11a. However, many cobalt nanoparticle samples investigated throughout this thesis exhibit fractal dimensions between 1 and 2, or even higher. It is not clear whether mass fractals observed by SAXS originate in pure cobalt agglomeration or agglomeration of the excess NaAOT

micelles or even mixtures of both. The observation of linear aggregates of magnetic nanoparticles certainly changes if the nanoparticles are oxidized. In Figure 4.3.12 the

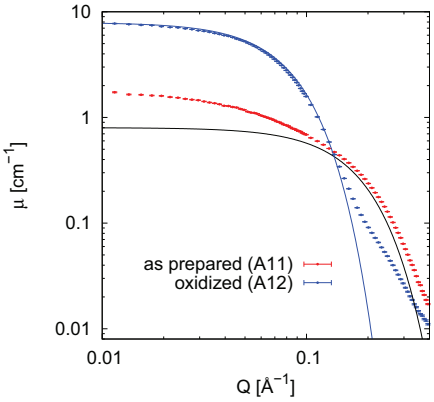

Figure 4.3.12.: SAXS by oxidized cobalt nanoparticles. The black Guinier law is given as a guide to the eye.

SAXS by cobalt nanoparticles prepared by the standard synthesis route is compared with the same sample which was deliberately oxidized. The particle size of the as prepared sample can not be determined by Guinier approximation because in the Guinier regime ($R_G Q < 1$) the scattering is superposed by a structure factor due to agglomeration of the nanoparticles. In contrast, the oxidized sample exhibits a pure Guinier behavior in the lower Q range, allowing for determination of a particle radius of 28.7(3) Å. This illustrates the different interparticle interaction of cobalt nanoparticles depending on the degree of oxidation. Furthermore, the particle size of the oxidized sample is much larger compared to the as prepared sample (the Guinier law displayed as a guide to the eye in Figure 4.3.12 is related to a particle radius of 13 Å). Thus, as long as the sample composition including particle size, degree of oxidation, and the possible excess surfactant micelles is not known, appearing interparticle interactions in the lower Q range cannot be modelled. Consequently, the particle size determination is only possible if either a form factor minimum or a flat Guinier plateau is observed.

Both reproducibility of the nanoparticle synthesis and reliability of the characterization method are important for particle size determination as was observed for magnetization measurements. Figure 4.3.13a compares SAXS measurements performed during the same beamtime at the JUSIFA beamline of samples prepared by the exact same standard synthesis route discussed before. The SAXS curves of these samples (Co A11, A13,

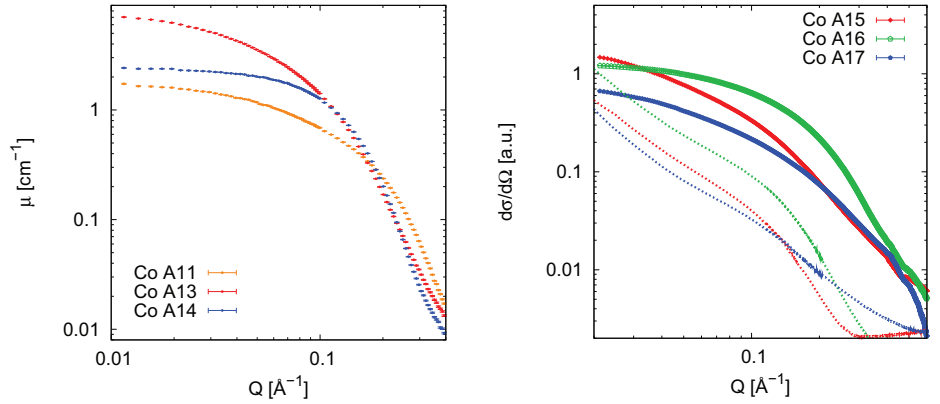

(a) SAXS by cobalt nanoparticles prepared by the same method.

(b) SAXS by cobalt nanoparticle samples measured at both SWING (points) and ID01 (dotted lines) beamlines.

Figure 4.3.13.: Reproducibility of SAXS results.

A14) differ by both the expected position of the first form factor minimum, indicating the particle size, and the asymptotic behavior in the lower Q range, indicating nanoparticle agglomeration. By matching the Q^{-4} asymptotic behavior with a spherical form factor, particle sizes between ~ 11 Å (A11) and ~ 17 Å (A14) are estimated. Because oxidation of the nanoparticles can not be excluded, it is unclear whether the different SAXS results are due to a poor reproducibility of the synthesis route itself or a different degree of oxidation of the samples. Oxidation may have occurred after synthesis, *e. g.* during sample storage or filling of the SAXS samples. Figure 4.3.13b compares the SAXS results for three different samples measured at different instruments. The exactly same sealed capillaries were measured at both the SWING and the ID01 instruments. Although the underlying particle form factor seems to be independent on the instrument, the SAXS curves measured at ID01 seem to be shifted to lower Q, indicating larger particle sizes which may result from particle ageing. Furthermore, the asymptotic behavior in the lower Q range exhibits a different structure factor for both instruments.

Thus neither sample reproducibility nor comparability of SAXS measurements performed at different instruments is confirmed. Consequently, the applicability of this method for primary characterization of synthesis optimization experiments is restricted to the relative comparison of whole experimental sample series.

4.3.1.5. Anomalous small-angle X-ray scattering

At incident energies close to the absorption edge of a particular element, its atomic form factor changes drastically with energy due to anomalous dispersion. By combination of the SAXS measurements performed at different energies below the absorption edge, the pure, element specific anomalous scattering can be extracted from the total scattering containing also energy independent contributions of other elements. In order to separate the purely resonant cobalt scattering, SAXS measurements were performed at three different incident energies below the Co K edge. The separation procedure itself is described more detailed in section 2.2.2.6.

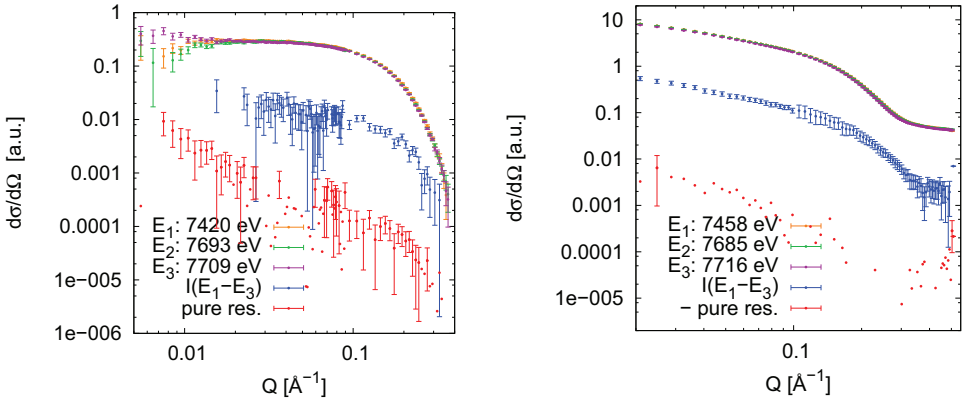

(a) Lower cobalt concentration (0.01 M, Co A02).

(b) Higher cobalt concentration (0.045 M, Co A07). The pure resonant scattering intensity after separation is negative and was inverted for display.

Figure 4.3.14.: ASAXS by cobalt nanoparticles. The total scattering measured at three different incident energies is presented along with one curve of mixed-resonant scattering and pure resonant cobalt scattering each. Intensity values smaller than their error bars are omitted. For the purely resonant scattering contributions, these intensity values are displayed without error bars.

Figure 4.3.14 presents two ASAXS experiments performed at the JUSIFA beamline on cobalt nanoparticles prepared according to the standard synthesis route. The first experiment (Figure 4.3.14a) was performed on a dilute dispersion with a cobalt concentration of 0.01 mol/l (Co A02). The pure resonant cobalt scattering extracted from this data exhibits large error bars arising from the repeated subtraction of scattering curves. A rise in intensity in the low Q range indicates the formation of aggregates, which is not visible in the total scattering. In the higher Q range ($Q > 0.1$) the slope of the pure resonant cobalt scattering is not significantly different from the total scattering slope. A

first form factor minimum is expected beyond the investigated Q range and is thus not observed in this experiment. A further experiment was performed in a larger Q range on a nanoparticle dispersion displaying a higher cobalt concentration of 0.045 mol/l (Co A07) in order to improve statistics. Although the error bars on the total scattering data are similar and the mixed-resonant scattering exhibits improved statistics compared to the first experiment, the error bars of the separated pure resonant scattering are much larger. Note that the separated pure resonant scattering contribution is negative in intensity and was inverted for display. These observations indicate that either the incident energies changed in a way that the order of increasing energy was changed or the highest energy was chosen too close or even beyond to the cobalt K edge with the result that the correct f' would be larger than that of the second highest incident energy. However, the anomalous dispersion correction values f' and f'' were determined in high accuracy from XANES measurements performed on the same sample and also on a different cobalt sample in a much wider energy range at the SAMBA beamline at Soleil. Details of the determination of the anomalous dispersion correction are given in section 4.2.2.3.

The same observation of a negative separated pure resonant scattering contribution was made on a whole series of ASAXS measurements performed at the ID01 beamline at ESRF. Because this issue could not be resolved, these measurements can not be evaluated reliably.

4.3.1.6. Particle extraction

In order to extract the prepared cobalt nanoparticles from the as-synthesized dispersion, application of a ligand exchange technique was investigated. For this purpose, a nonpolar ligand is added to the $Co(AOT)_2$ reverse micellar solution before reduction. If this nonpolar ligand coordinates to the nanoparticle surface, the nanoparticles will remain in the toluene phase, while excess surfactant can be extracted by elution with a polar solvent such as formamide.

The nonpolar ligand investigated here is trioctylphosphine ($P(oct)_3$). Cobalt nanoparticle samples extracted with a varying amount of $P(oct)_3$ are presented in Figure 4.3.15. With increasing amount of $P(oct)_3$ an increasing amount of cobalt nanoparticles is maintained in the toluene phase after elution with formamide as visible by the darker color of the upper phase. The formamide phase is supposed to contain the amphiphilic AOT surfactant. As visible by its pink color, a significant amount of Co^{2+} is transferred to the formamide phase as well. However, the Co^{2+} concentration in the lower phase is likely constant as observed by the same color of all samples. Due to a systematic overestimation of the cobalt content in the prepared $Co(AOT)_2$, the reducing agent is used in large

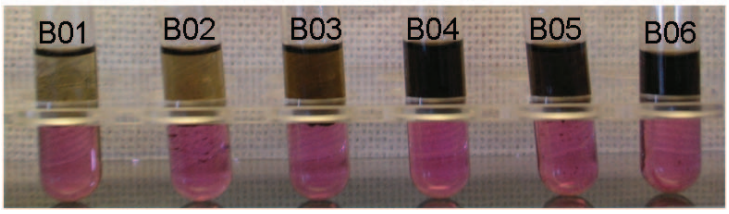

Figure 4.3.15.: Cobalt nanoparticle dispersions as extracted with $P(oct)_3$ and elution with formamide. Equivalent ratios of $P(oct)_3$:$Co(AOT)_2$ are 0.005:1.0, 0.01:1.0, 0.02:1.0, 0.05:1.0, 0.08:1.0 and 0.1:1.0 (from left to right).

excess (see section 4.2.1.1 for a detailed description of the prepared $Co(AOT)_2$). The presence of Co^{2+} cations after reduction and elution is thus unlikely to result from insufficient reducing agent. Oxidation of cobalt nanoparticles will not result in a magenta colored solution because this bright color is only exhibited by molecularly coordinated cobalt centers. The origin of the Co^{2+} cations thus remains unclear.

A large fraction of the cobalt nanoparticles agglomerates at the toluene-formamide interphase as shown for a $P(oct)_3$:Co ratio of 0.02 (B03) in Figure 4.3.16a. With an increasing amount of $P(oct)_3$ a smaller agglomeration fraction is observed at the interface.

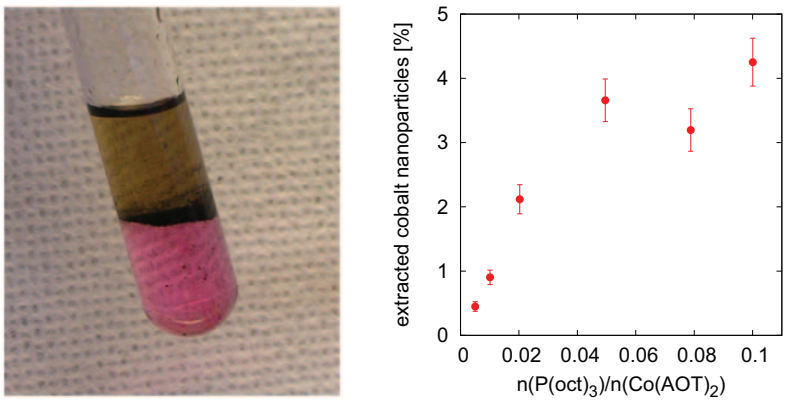

(a) Agglomeration of cobalt nanoparticles at the toluene - formamide interface.

(b) Fraction of extracted cobalt nanoparticles as function of $[P(oct)_3]$.

Figure 4.3.16.: Extraction of cobalt nanoparticles with $P(oct)_3$.

The cobalt content in the respective toluene phases was determined by elementary analysis (ICP-OES). The determined cobalt concentration relative to the initial cobalt

concentration is presented in dependence of the added amount of $P(oct)_3$ in Figure 4.3.16b. The amount of cobalt nanoparticles maintained in the toluene phase increases with increasing $P(oct)_3$ content up to 3.6 % for $P(oct)_3$:Co ratio of 0.05. A further increase of the extracted amount of nanoparticles may be expected with a higher amount of $P(oct)_3$. This is not evident from the investigated range of $P(oct)_3$ concentrations, but seems reasonable because of the large surface to volume ratio of the nanoparticles as mentioned in section 4.3.1.3. In order to coordinate the entire surface of nanoparticles as small as 3 nm in diameter ~ 40 mol% of ligand is required.

However, the determined absolute cobalt concentration appears to be too low. Visual comparison of the samples presented in Figure 4.3.16a with diluted cobalt nanoparticle dispersions prepared by addition of nonionic surfactants in Figure 4.3.26 suggests a cobalt concentration of 25 % of the initial concentration for the sample prepared with a $P(oct)_3$:Co ratio of 0.02 (B03). Even taking into account the $Co(AOT)_2$ content of 60 % as determined by ICP-OES for the starting material (see section 4.2.1.1), the determined amount of extracted Co in this sample adds up to no more than 3.5 %, which is too low considering the dark dispersion color. For this reason, a systematic error in the elementary analysis may be assumed. The relative increase of the extracted amount of nanoparticles with $P(oct)_3$ content is nonetheless reasonable.

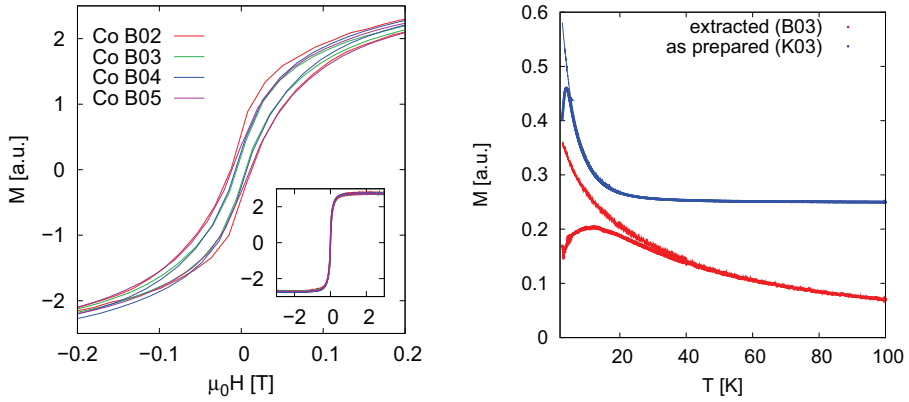

(a) Field dependent magnetization measured at 10 K. Data have been corrected for diamagnetic contributions and scaled to match in high magnetic fields.

(b) Temperature dependent magnetization. Data have been scaled and offset for display.

Figure 4.3.17.: Magnetization measurements on nanoparticles extracted by ligand exchange. Temperature dependent magnetization measurements were performed in a magnetic field of 10 mT after zero field cooling (points) and field cooling (lines).

Magnetization measurements on extracted cobalt nanoparticles dispersed in the toluene

phase are presented in Figure 4.3.17. The field dependent magnetization measurements are comparable for all samples, exhibiting the same behavior after subtraction of all linear susceptibility contributions (such as diamagnetic contributions), which indicates a similar particle size and size distribution. All samples reveal a small coercivity at 10 K, indicating a superparamagnetic blocking temperature around this temperature. Indeed, the temperature dependent magnetization of the nanoparticle sample extracted with a $P(oct)_3$:Co ratio of 0.02 and presented in Figure 4.3.17b reveals a blocking temperature of ~ 10 K. However, the peak in the ZFC measurement is much broader than observed for samples which were not extracted as compared in Figure 4.3.17b. The much higher blocking temperature along with a broadened ZFC peak indicates agglomeration of the nanoparticles to larger clusters with a wide size distribution. It is suggested that the added amount of $P(oct)_3$ is not sufficient for a full surface coverage of the nanoparticles, and that elution with formamide also removes those AOT surfactant molecules coordinated to the cobalt nanoparticle surface. As a result, the nanoparticles agglomerate heavily and the size distribution increases. Thus, a much higher amount of $P(oct)_3$ would be required in order to cover the entire nanoparticle surface and separate most of the nanoparticles from excess AOT. However, a much larger amount of added ligands may as well result in excess of these ligands instead of excess AOT, which does thus not improve the sample quality.

Precipitation A further approach for separation of the prepared cobalt nanoparticles from excess surfactant, but without addition of any further compounds, is the use of an antisolvent in order to precipitate the nanoparticles. Pileni *et al.* used ethanol for precipitation of their cobalt nanoparticles [73]. However, even large amounts of ethanol failed to precipitate the studied nanoparticles, probably due to the small particle size of ~ 3 nm in diameter.

A further antisolvent which has been applied successfully for precipitation of Ag nanoparticles is compressed CO_2 [94]. Compressed CO_2 is soluble in many organic solvents such as toluene, and the fraction of dissolved CO_2 can be tuned by pressure adjustment. The surfactant AOT precipitates if the CO_2 pressure exceeds the so called cloud point. Because nanoparticles precipitate at a lower CO_2 concentration than excess AOT micelles, the nanoparticles are precipitated at a pressure below the cloud point, and decantation of the organic solvent/CO_2 solution with excess reverse micelles is performed while maintaining the high pressure, thus leaving the pure nanoparticle precipitate.

A high pressure cell allowing for compression of CO_2 to pressures of ~ 70 bar and decantation of the nanoparticle dispersion under high pressure was built and is illustrated

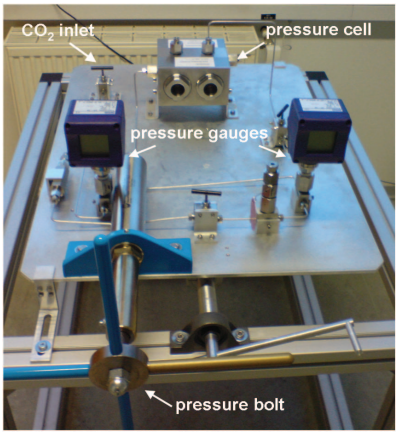

Figure 4.3.18.: CO_2 pressure cell.

in Figure 4.3.18. The cell consists of two connected chambers. The prepared nanoparticle dispersion is filled into the first chamber. CO_2 is filled into the pressure cell and compressed by a screw press. After precipitation of the nanoparticles, the whole pressure cell can be tilted while maintaining the high pressure in order to decant the toluene/CO_2 solution containing the reaction byproducts and excess AOT micelles into the second chamber. After release of the CO_2 pressure the precipitated cobalt nanoparticles can be redispersed in toluene and removed from the pressure cell.

The commissioning of this pressure cell is ongoing, and first microemulsion samples have been precipitated at high pressure [69]. Because this pressure cell does not fit inside a glove box, the construction was equipped with a glove bag in order to provide a relatively air-free transfer of air-sensitive samples into and out of the chamber. However, the atmosphere in a glove bag will certainly not reach the level of inertness achieved by a glove box. Thus, as oxidation has been observed even for cobalt nanoparticles prepared and handled inside the glove box, precipitation using this CO_2 pressure cell is unlikely to yield any nonoxidized cobalt nanoparticles. However, for nanoparticles that are insensitive to oxidation, this approach promises well dispersed and byproduct free nanoparticle dispersions suitable for further characterization.

4.3.1.7. Small-angle neutron scattering

Whereas small-angle X-ray scattering is used for determination of particle size and size distribution of dispersed nanoparticles, small-angle neutron scattering gives additional information on the ligand shell thickness due to the different scattering contrasts of

inorganic core and organic shell for X-ray and neutron scattering. Furthermore, the neutron spin interacts with the spins of magnetic nanoparticles which provides additional opportunities for contrast variation in order to determine the magnetization density of magnetic nanoparticles (see section 2.2.4.3). In this section, SANS investigations on cobalt nanoparticles with the aim of further structural characterization will be discussed.

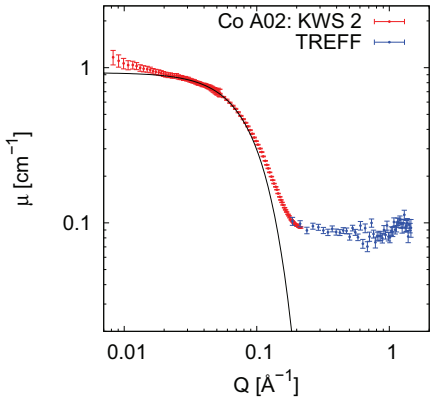

Figure 4.3.19.: SANS by cobalt nanoparticles measured at KWS 2 and TREFF. The TREFF data has been scaled to overlap with the normalized KWS 2 data. The Guinier curve was refined in a Q range of 0.025 to 0.05 Å^{-1}.

SANS measurements performed at KWS 2, JCNS, are presented in Figure 4.3.19. The cobalt nanoparticle sample was prepared by the standard synthesis procedure using d_8-toluene. Due to the small onset of a structure factor at low Q, the particle radius was estimated as 23.9(2) Å by Guinier approximation in a narrow Q range of 0.025 to 0.05 Å^{-1}. Nonetheless, the obtained radius is in good agreement with the particle radius of 16.0(2) Å as determined from SAXS (Figure 4.3.3), if a typical shell thickness of the AOT ligand of 7.9 Å is considered. The first form factor minimum is expected beyond the high Q limit of the KWS 2 instrument. However, SANS by the same sample in an extended Q range, measured at the TREFF instrument, reveals a flat background which is attributed to incoherent scattering. While the solvent of this sample was fully deuterated in order to minimize incoherent scattering, neither the surfactant AOT nor the reducing agent $NaEt_3BH$ were deuterated.

The SANS by cobalt nanoparticles is compared with SANS by samples containing only the reducing agent or NaAOT in equivalent concentrations in d_8-toluene as presented in Figure 4.3.20. NaAOT and $Co(AOT)_2$ do not reveal any flat scattering background in the measured Q range, and the NaAOT scattering curve is even lower in

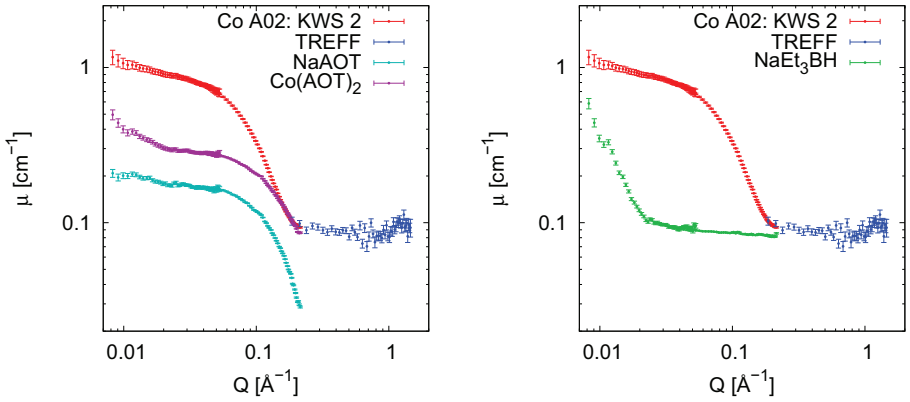

(a) Comparison with SANS by 0.02 M NaAOT (a reaction byproduct) and 0.01 M $Co(AOT)_2$ (the starting material).

(b) Comparison with 0.02 M $NaEt_3BH$ which was used as reducing agent.

Figure 4.3.20.: SANS by cobalt nanoparticles in comparison with possible byproducts.

intensity than the incoherent scattering contribution in the cobalt sample. AOT reverse micelles can thus be excluded as possible source of the high incoherent scattering contribution. In contrast, the SANS by $NaEt_3BH$ reveals an incoherent scattering background with the same absolute intensity as for the nanoparticle sample and is thus considered as origin of the incoherent scattering of the cobalt nanoparticle sample.

In order to remove this incoherent scattering contribution and possibly reveal the first form factor minimum, either the sample has to be extracted before measurement or the different scattering contributions have to be separated by means of scattering techniques. Strategies for extraction of the cobalt nanoparticles from the solution, which contains excess AOT micelles and further byproducts resulting from the reducing agent, have been discussed in section 4.3.1.6. Because an optimum technique has not been found yet, separation of the different scattering contributions was attempted by means of small-angle neutron scattering with polarization analysis.

Polarized small-angle neutron scattering with polarization analysis in a momentum transfer range of $0.1\ \text{Å}^{-1} \leq Q \leq 0.6\ \text{Å}^{-1}$ is not a standard experiment because it hits the gap in between the momentum transfer ranges generally covered by polarized small-angle scattering and diffraction instruments. The entire chapter 6 will be dedicated to this experiment, including discussion of the technical details such as choice of the instrument, correction of possible multiple scattering, and separation of coherent, incoherent, and magnetic scattering contributions (see also section 2.2.4 for the theoretical background). Here, the results of the polarized SANS experiments with polarization

analysis on cobalt nanoparticles performed at J-NSE, JCNS, are discussed. Magnetic scattering contributions were not detected, and oxidation of the nanoparticles can thus not be excluded. For this reason, the results are evaluated for a structural analysis only. In Figure 4.3.21 the separated coherent scattering cross section is presented. Whereas the KWS 2 measurement is normalized to absolute units, the J-NSE data set is scaled to overlap the KWS 2 data after subtraction of an assumed constant incoherent scattering contribution from the KWS 2 data. A slightly different particle size of the samples measured at KWS 2 and J-NSE is indicated by the difference between the two data sets in the momentum transfer range of 0.08 $Å^{-1} \leq Q \leq 0.13$ $Å^{-1}$. This may be due to either a poor reproducibility of the synthesis route or a different degree of oxidation of the samples as discussed in section 4.3.1.4.

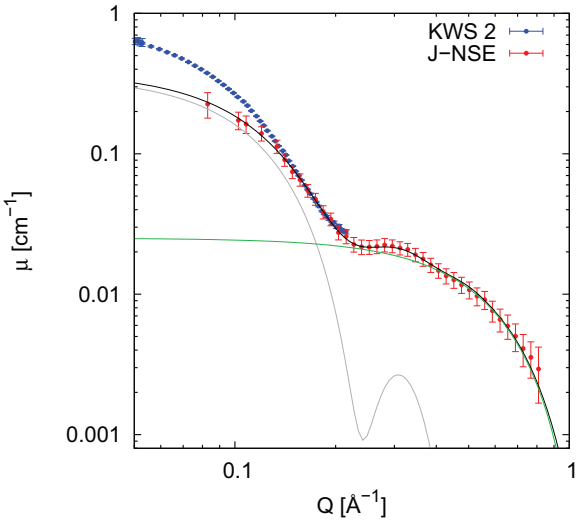

Figure 4.3.21.: Coherent SANS by cobalt nanoparticles measured at J-NSE. The separated coherent scattering contribution has been scaled to overlap with the normalized KWS 2 data. Refinement of a core shell form factor with a core radius of 10 Å and a shell thickness of 7.7 (2) Å is presented as a black line. The pure core shell form factor and the form factor accounting for smaller aggregates are presented as grey and green lines, respectively.

A first form factor minimum is visible in the separated coherent scattering contribution at Q ~ 0.24 $Å^{-1}$, and a second form factor minimum can be estimated as a step at Q ~ 0.4 $Å^{-1}$. The refinement of a core shell form factor is presented as a black line in Figure 4.3.21. Since only the first form factor minimum is significant and the second form factor minimum is rather estimated, it is not possible to refine both the particle

core radius and the shell thickness. Thus, the particle core radius was set to 10 Å, a reasonable value compared to the range of cobalt nanoparticle sizes estimated from SAXS, and a shell thickness of 7.7 (2) Å was refined. This shell thickness is reasonable for the AOT molecule, if a certain degree of interpenetration of toluene into the particle shell is considered. The lognormal particle size distribution was determined as 10 (4) % by calibration of the angular divergence with a reference sample of known size distribution. The large uncertainty of the found value results from the large contribution of smaller excess particles shadowing the cobalt form factor minima.

In order to represent the entire data set, a phenomenological spherical form factor was implemented to account for even smaller aggregates giving rise to the high intensity at $Q \geq 0.4$ Å^{-1}. The radius corresponding to this additional spherical form factor was refined as 3.94 (3) Å. This radius is too small to be related to excess NaAOT micelles, which usually have a radius of ~ 6 Å. The small radius determined here is in the size range of single molecules rather than nanosized particles. Since molecules certainly have a different density distribution than spherical nanoparticles, the form factor of a solid sphere may not be correct. It is here rather considered a phenomenological description of a form factor plateau observed in the higher Q range.

The found total core shell nanoparticle radius is much smaller than 23.9 Å as estimated by Guinier approximation of the KWS 2 SANS measurement, which underlines the limited applicability of the Guinier approximation. Although the samples for the polarized SANS experiments were prepared by the same synthesis route as the one measured at KWS 2, a difference in particle size can not be excluded due to the low reproducibility of the particle size as discussed in section 4.3.1.4.

4.3.1.8. Summary: Results of the primary characterization

A new, entirely water-free synthesis route for cobalt nanoparticles based on the direct reduction of $Co(AOT)_2$ reverse micelles in toluene has been investigated. Superparamagnetic blocking temperatures below 10 K were determined for the prepared samples, indicating that a magnetic cobalt core is present. The particle size determined by SAXS varies for many samples, but an average particle diameter of 3 nm can be deduced. A changing degree of oxidation has been observed, and X-ray absorption spectroscopy revealed the coexistence of a defined amount of cobalt and cobalt oxide within the particles with a gradually changing fraction of cobalt oxide, which has not been reported so far for such small cobalt nanoparticles. By polarized small-angle neutron scattering with subsequent polarization analysis, a first form factor minimum was separated, and a cobalt core radius of 10 Å with an AOT shell thickness of 7.7 (2) Å is obtained. The

lognormal particle size distribution is accessible exclusively by polarization analysis of SANS and was determined as 10 (4) %.

For a more precise particle size determination and synthesis optimization regarding reproducibility and a lower degree of oxidation, the reliability of both magnetization measurements and small-angle scattering was found insufficient in case of such small nanoparticles. Temperature dependent magnetization measurements were not fully reliable because of unstable temperatures in our instrument below 10 K, where the superparamagnetic blocking temperature is expected. A changing residual field during zero field cooling further impedes the relative particle size determination by temperature dependent magnetization. Obstacles in particle size determination by small-angle scattering are the too narrow Q range of the in house SAXS instrument, the superposition of the first form factor minimum by excess surfactant micelles, which could not be separated by neither particle extraction nor ASAXS, and the varying degree of interparticle interactions impeding particle size estimation by Guinier approximation.

For somewhat larger nanoparticles, a larger magnetic moment is expected along with a higher blocking temperature in a more stable temperature range of the instrument, yielding more reliable magnetic measurements and thus facilitating synthesis optimization. In small-angle scattering, a larger particle size will shift the form factor minimum to a lower Q range and increase the intensity of the cobalt nanoparticle form factor. Consequently, the impact of SAXS by excess AOT micelles on the first form factor minimum will be lower, which will again facilitate the particle size determination.

The challenge is to optimize the synthesis route towards a larger particle size and less oxidation despite the poor applicability of the primary characterization methods for the present particle size. For synthesis optimization aiming at a variation of the particle size a relative information may be obtained under certain conditions. If the degree of oxidation is similar for an entire experimental series as observed by field dependent magnetization measurements, a continuous variation of the blocking temperature within the experimental series can be related to a variation in particle volume. SAXS measurements can similarly be evaluated by a comparison of an entire experimental series yielding information on the relative variation of the particle size or a continuous development of a structure factor indicating particle agglomeration.

However, the reliability of the characterization methods is still crucial. The comparison of blocking temperatures requires the detection of a blocking temperature. If this is not the case, whether because of a non zero cooling field, oxidation of the particles or extremely small particles with a blocking temperature below the minimum measurement temperature, a relative information of the particle size variation can not be obtained. Similarly for small-angle scattering, if measurements reveal neither a Guinier plateau

nor a Q^{-4} asymptotic behavior allowing to estimate the Q position of a form factor minimum, even a relative comparison of particle sizes will not be possible.

4.3.2. Possible Routes to Size Variation

As discussed in the previous section, an absolute determination of the cobalt nanoparticle size has not been obtained consistently, due to a combination of low reproducibility of the synthesis route and low reliability of the applied primary characterization methods. Consequently, experiments aiming at optimization of the synthesis route and variation of the produced particle size can only give relative tendencies of the particle size and degree of agglomeration.

Wherever possible, entire experimental series were characterized by means of both small-angle X-ray scattering and magnetization measurement, and the observed continuous tendencies throughout an experimental series are discussed in this section. However, due to the different time scale of SAXS and magnetization measurements, the full characterization is not available for all samples. During one day of SAXS beamtime at a synchrotron X-ray source, 40 - 50 samples can easily be measured. Magnetization measurements on all those samples would require months depending on the availability of the instrument. Thus, in some cases only selected samples were investigated by magnetization measurements. Furthermore, a change of the samples within months after preparation can not be excluded, which limits the amount of samples measured by both SAXS and magnetization measurements.

4.3.2.1. Concentration Variation

Several of the intended approaches to a particle size variation involve variation of the reaction components, which may also lead to different concentrations of $Co(AOT)_2$. In order to rule out concentration effects on a possible size variation, the dependence of the prepared cobalt nanoparticles on the micellar concentration was investigated by synchrotron SAXS at the JUSIFA beamline, HASYLAB.

Figure 4.3.22 presents the SAXS by cobalt nanoparticles in different concentrations. For the samples shown in Figure 4.3.22a, $Co(AOT)_2$ micellar solutions of different concentrations were reduced to form cobalt nanoparticles, whereas Figure 4.3.22b presents for comparison the SAXS by cobalt nanoparticles that were reduced at a concentration of 0.046 M and subsequently diluted. All of the presented SAXS curves exhibit a small structure factor in the lower Q range due to particle agglomeration. For this reason, a determination of the particle size by Guinier approximation is not possible. However,

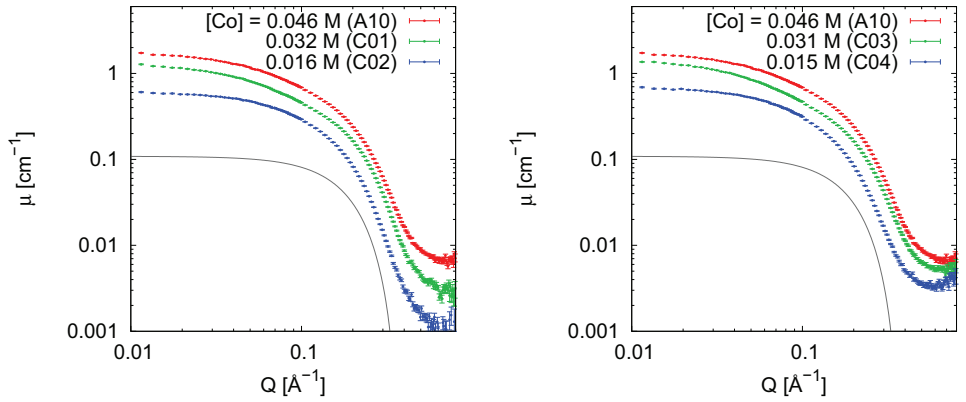

(a) SAXS by cobalt nanoparticles reduced in different concentrations.

(b) SAXS by cobalt nanoparticles diluted after reduction.

Figure 4.3.22.: Synchrotron SAXS by cobalt nanoparticles in different concentrations. A spherical form factor with a radius of 12 Å is indicated as a guide to the eye.

the particle size seems to be independent on the concentration, and matching with a spherical form factor leads to an approximate particle radius of ~ 12 Å.

If the nanoparticles are reduced after dilution, the scattering background at high Q is lower than for the samples diluted after reduction. It may be speculated that for cobalt nanoparticles reduced in lower concentrations the surface coverage with AOT is more dense, leading to a lower concentration of excess AOT micelles and thus a lower scattering background at high Q. In contrast, the degree of agglomeration is not affected by reduction before or after dilution, which does not support the hypothesis of a variation in surface coverage of the particles. However, it was confirmed that the particle size is independent on the concentration, which is important for subsequent synthesis optimization.

4.3.2.2. Temperature Variation

The reaction temperature is expected to influence the synthesis process for several reasons. First, the particle growth is mediated through intermicellar exchange. At elevated temperatures, the mobility of the micelles is faster, leading to a faster intermicellar exchange, which may result in faster nucleation and growth. Secondly, the synthesis procedure involves formation of byproducts such as triethyl borane. While these byproducts are supposed to remain dissolved in the nanoparticle dispersion, elevated temperature treatment may contribute to decomposition and evaporation of the byproducts. Furthermore, a higher temperature might increase the crystallinity of the nanoparticles,

since crystalline cobalt nanoparticles have mostly been obtained at elevated temperatures [65, 66]. So far no diffraction experiments could be performed to determine their internal structure due to the small size of the nanoparticles resulting in a significant reflection broadening. It is nonetheless of special interest to know whether they would be of amorphous or crystalline nature. An increase in crystallinity at constant particle size might be observable in the magnetization measurements.

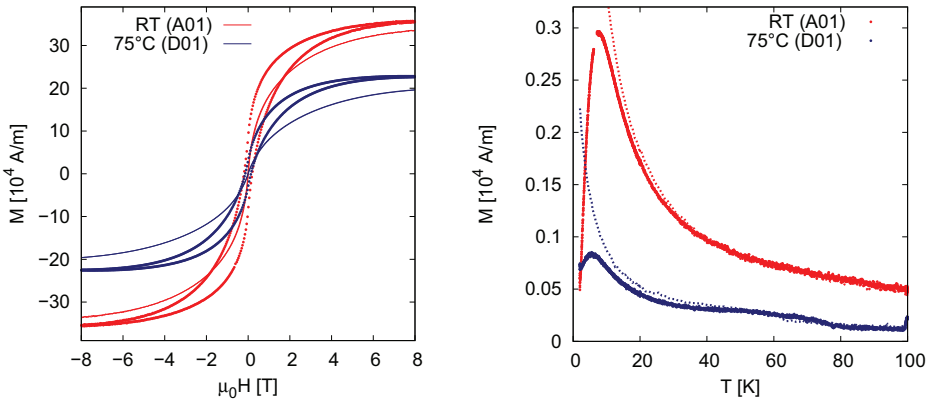

(a) Field dependent magnetization.

(b) Temperature dependent magnetization.

Figure 4.3.23.: Magnetization by nanoparticles prepared at different temperatures. Hystereses were measured at 3 K (points) and 10 K (lines). Temperature dependent magnetization measurements were performed in a magnetic field of 5 mT after zero field cooling (lines) and field cooling (points).

Figure 4.3.23 compares magnetization measurements and SAXS for cobalt nanoparticles prepared at room temperature and 75°C. Both field and temperature dependent magnetization measurements reveal a lower magnetization for the sample prepared at elevated temperature, despite the equal cobalt concentration of both samples. An increase in crystallinity is thus not indicated. The coercive field of the nanoparticles prepared at 75°C and measured at 3 K is slightly smaller than the coercive field of the reference sample (Figure 4.3.23a). This corresponds to the lower blocking temperature of 5.5 K as compared to 7.8 K for the reference sample (Fig 4.3.23b) and leads to the conclusion that the elevated reaction temperature results in smaller nanoparticles. In contrast, the small-angle scattering of the same samples as presented in Figure 4.3.24 suggests a larger particle size for the nanoparticles prepared at higher temperature. Both measurements exhibit a mass fractal behavior with a dimension of 1 in the low Q range, as well as the onset of a form factor intensity decrease around 0.15 $Å^{-1}$, close to the maximum accessible Q range. While the data does not allow for refinement of a form factor or a

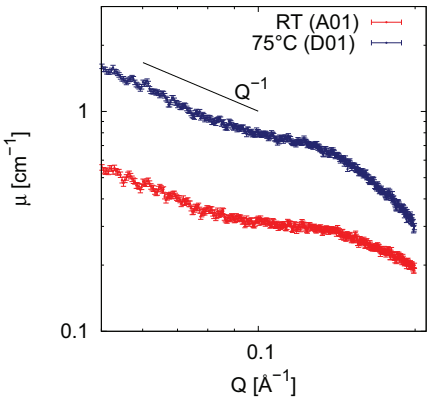

Figure 4.3.24.: SAXS by nanoparticles prepared at different temperatures.

Guinier law, the slope of the sample prepared at higher temperatures is steeper than the reference sample, indicating a form factor minimum in a lower Q range, *e. g.* larger particles. The SAXS results are thus contradicting the observations made by magnetization measurements.

For a more detailed investigation of the effect of temperature variation, cobalt nanoparticles were prepared at three different temperatures and studied using synchrotron SAXS at the JUSIFA beamline, HASYLAB. In order to distinguish between effects due to reduction at elevated temperatures, corresponding to a faster intermicellar exchange, and effects due to heating of the product, such as the removal of byproducts, reference samples were prepared. For each sample reduced at a certain temperature, a reference sample was reduced at room temperature. After reduction all samples were heated to the respective elevated temperature for 1 hour. A comparison of the SAXS results for all samples is given in Figure 4.3.25.

Figure 4.3.25a shows the small angle scattering by cobalt nanoparticles reduced at different reaction temperatures. The sample prepared at room temperature exhibits a curve that can not be described by a Guinier law and might be due to a mixture of particle sizes. In the higher Q range, a large background is observed that may be attributed to excess AOT reverse micelles that remain in the particle dispersion along with side products of the reaction. The cobalt nanoparticles prepared at higher reaction temperatures exhibit a significantly lower background and a slope corresponding to a Q^{-4} power law as expected for hard spheres. The lower background suggests that the organic side products of the cobalt reduction are removed from the dispersion at relatively low temperatures of 40°C. Furthermore, the nanoparticles prepared at 40°C reveal

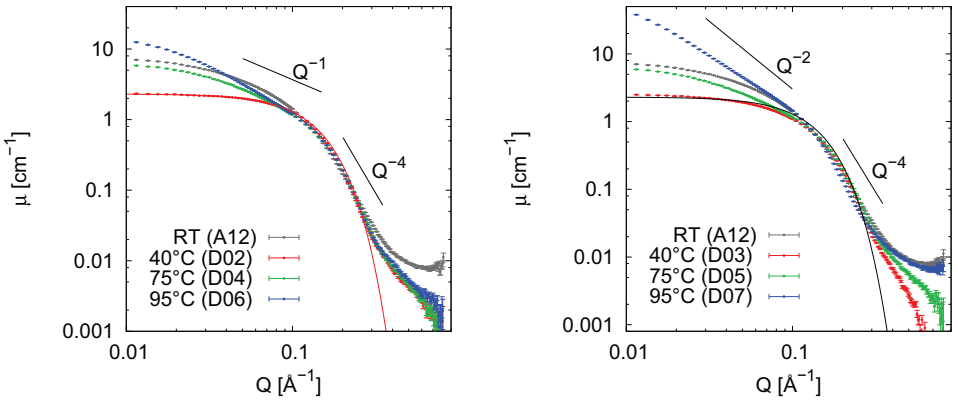

(a) SAXS by cobalt nanoparticles reduced at elevated temperatures.

(b) SAXS by cobalt nanoparticles heated after reduction.

Figure 4.3.25.: Synchrotron SAXS by nanoparticles prepared at different temperatures. Porod laws and Guinier curves are given as a guide to the eye.

a precise Guinier behavior over a wide Q range from 0.008 Å^{-1} up to 0.2 Å^{-1}, indicating a particle diameter of 3.5(1) nm as deduced from the Guinier radius of gyration. The fact that even after removal of the organic side products a well-defined form factor is missing results from the presence of excess AOT reverse micelles that can not be removed from the nanoparticle dispersion easily due to the very small size of the particles. These micelles have a radius of ~0.8 nm and their scattering is superposed to the first form factor minimum, preventing a precise determination of the particle size distribution. With increasing reaction temperature, structure factors appear. Both the samples prepared at 75°C and 95°C exhibit curves with linear regions, suggesting correlated interparticle interactions instead of a larger size distribution. For the sample prepared at 75°C, the presence of linear dimers or trimers is likely, due to the small region exhibiting a Q^{-1} power law. The sample prepared at 95°C exhibits a larger slope in a wider Q range, suggesting longer, slightly more flexible, chains of nanoparticles.

The reference samples that were prepared at room temperature and subsequently heated to the respective temperatures are presented in Figure 4.3.25b. As a guide to the eye, the same Guinier law as given in Figure 4.3.25a is shown. The main differences to the samples reduced at elevated temperatures are observed in the lower background for the sample prepared at 40°C, and the higher dimension of ~ 2 of the mass fractal of the sample prepared at 90°C.

Comparing all measured samples, an increasing structure factor is observed with increasing reaction temperature. This might be explained by a starting decomposition of

the AOT surfactant, resulting in a lower surface coverage of the formed nanoparticles and thus leading to agglomeration. Finally, a dependence of the particle size on the reaction temperature could not be confirmed. However, a preparation temperature of 40°C seems promising for preparation of non-interacting cobalt nanoparticles.

4.3.2.3. Addition of nonionic and anionic surfactants

In order to increase the nanoparticle size, the use of additional nonionic and anionic surfactants was investigated, with the objective to decrease the cobalt content per micelle. For a cobalt content below the critical aggregation number, a smaller amount of cobalt nuclei is expected, which can subsequently grow larger. A similar effect has been observed in the formation of silver nanoparticles [95].

The investigated surfactants include nonionic surfactants such as Igepal CO 520 and $C_{12}E_5$ as well as the anionic surfactant NaAOT. The total surfactant concentration was kept constant, with a variation of the ratio of the mixed surfactants. If mixed micelles of a comparable size are formed, the cobalt concentration per micelle is thus decreased.

4.3.2.3.1. Igepal CO 520 Igepal CO 520 (poly(oxyethylene) nonylphenyl ether) was investigated as a nonionic surfactant and added to the $Co(AOT)_2$ solution before reduction. Because the total surfactant concentration was constant for all samples, the cobalt concentration decreases with increasing amount of Igepal, which is visible in the transparency of the resulting nanoparticle dispersions as presented in Figure 4.3.26. Some of the samples additionally exhibit a different color than the reference sample prepared without Igepal, ranging from an olive green to a light blue for AOT:Igepal surfactant ratios of 1:5 to 1:9.

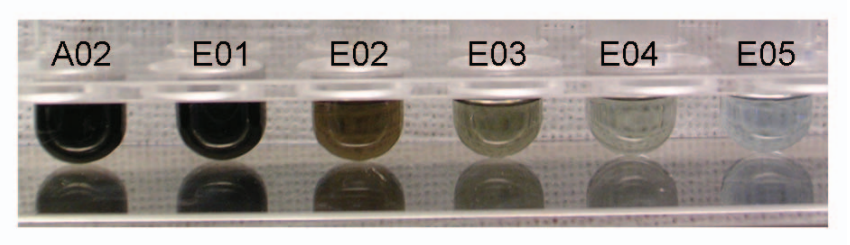

Figure 4.3.26.: Cobalt nanoparticle dispersions prepared with Igepal CO 520. Ratios of AOT:Igepal are 1:0, 1:1, 1:3, 1:5, 1:7, and 1:9 (from left to right).

Magnetization measurements on cobalt nanoparticles prepared from reverse micellar solutions with a varying ratio of AOT:Igepal are presented in Figure 4.3.27. The

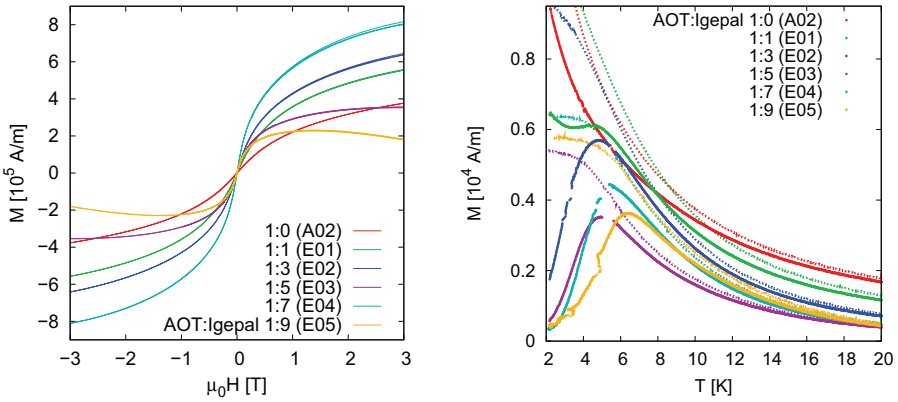

(a) Field dependent magnetization.

(b) Temperature dependent magnetization.

Figure 4.3.27.: Magnetization measurements on cobalt nanoparticles prepared by addition of Igepal CO 520. Hystereses were measured at 10 K. Temperature dependent magnetization measurements were performed in a magnetic field of 10 mT after zero field cooling (lines) and field cooling (points).

measured magnetic moment has been converted to a mass magnetization taking into account the different cobalt concentrations for each sample. The presented magnetization values are thus comparable relative to each other. Field dependent magnetization measurements as presented in Figure 4.3.27a reveal in general an increasing saturation magnetization with increasing Igepal content. The samples prepared with an AOT:Igepal ratio of 1:5 (E03) and 1:9 (E05) exhibit a much smaller saturation magnetization along with a larger diamagnetic contribution (which has not been corrected for any of the measurements in Figure 4.3.27). The temperature dependent magnetization measurements presented in Figure 4.3.27b reveal increasing blocking temperatures for an increasing Igepal content, suggesting an increase in particle size. Again, the magnetization of the samples with an AOT:Igepal ratio of 1:5 and 1:9 is significantly lower than that of the remaining samples. However, because the observed blocking temperatures are continuously increasing with Igepal content for the whole experimental series, the lower magnetization is not related to a higher degree of oxidation. The reference sample prepared without addition of Igepal does not exhibit a blocking temperature. The observation that the field cooled and zero field cooled magnetization curves do no coincide at low temperatures, suggests that the blocking temperature of this sample is below the measured temperature range. The dependence of the measured blocking temperature on the Igepal:AOT ratio is given in Figure 4.3.28. The blocking temperature increases nearly linearly, suggesting even higher blocking temperatures achiev-

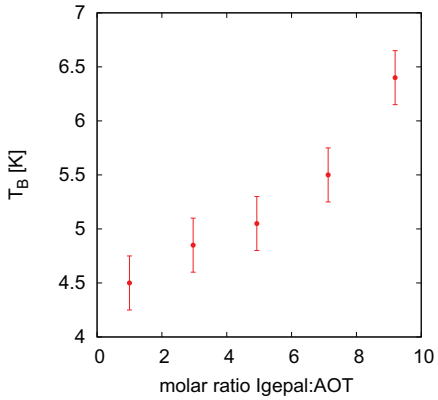

Figure 4.3.28.: Blocking temperatures of cobalt nanoparticles depending on the Igepal content.

able with more Igepal. However, because the total surfactant concentration was kept constant, the cobalt content decreases with increasing Igepal content, and the obtained cobalt nanoparticle dispersions may become too dilute to detect a clear signal in either magnetization measurements or small-angle scattering (note again the transparency of the sample with highest Igepal content in Figure 4.3.26).

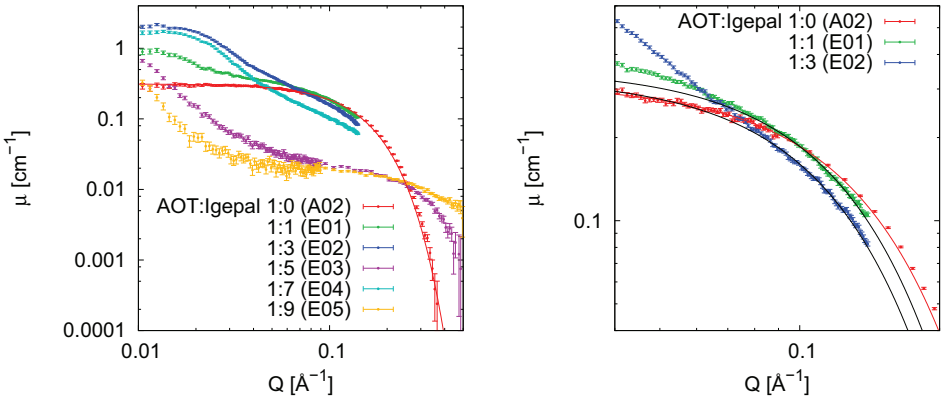

(a) SAXS by cobalt nanoparticles prepared with Igepal. The red Guinier law was fit to the data in the lower Q range (Q < 0.06 Å^{-1}).

(b) Magnification of (a). The black Guinier laws are simulations.

Figure 4.3.29.: Synchrotron SAXS by nanoparticles prepared with Igepal CO 520.

SAXS measurements of the same samples at the JUSIFA beamline at HASYLAB are presented in Figure 4.3.29. Due to limited beamtime not all of the samples were measured in the full achievable Q range. The reference sample prepared without Igepal

exhibits a Guinier behavior over a wide Q range, and a particle radius of 16.0(2) Å has been determined from its radius of gyration obtained by a Guinier fit in the low Q region ($R_G Q < 1$). The form factor of a spherical particle, however, shows a much steeper intensity decrease at high Q and can not be refined to the data because the first form factor minimum is not in the achieved Q range.

The samples with an AOT:Igepal ratio of 1:5 and 1:9 deviate from the observed trends of the other samples as was observed for the saturation magnetization. A particle size may be estimated for AOT:Igepal 1:5 due to the intensity decrease around 0.4 $Å^{-1}$. However, this particle size would be much smaller than that of the other samples, which does not correlate with the blocking temperatures determined in Figure 4.3.27b.

The remaining samples exhibit an increasing structure factor in the low Q range and the onset of an intensity decrease around 0.1 $Å^{-1}$ as magnified in Figure 4.3.29b. Although this decrease is observed in a narrow Q range, particle radii of 18 and 19 Å can be estimated for AOT:Igepal ratios of 1:1 and 1:3, respectively. This observation is in agreement with the trend of increasing particle size with Igepal content, as was observed by the increasing blocking temperatures (see Figure 4.3.28).

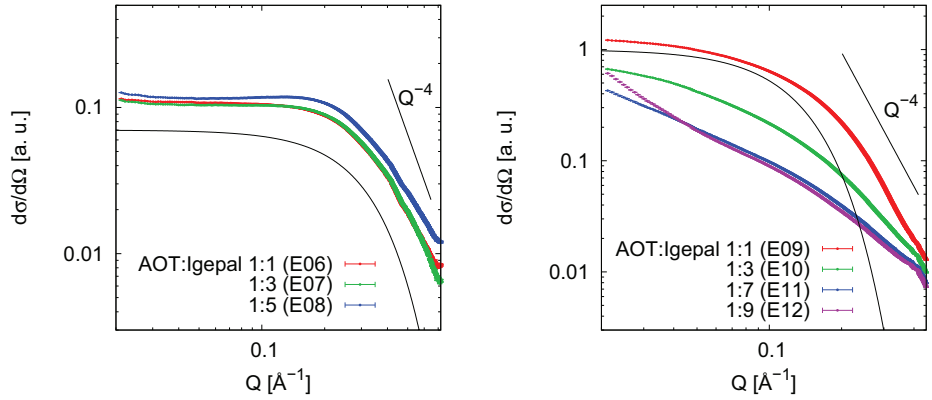

(a) SAXS by mixed micelles of $Co(AOT)_2$ and Igepal. A Guinier law with R = 7 Å is given as a guide to the eye.

(b) SAXS by cobalt nanoparticles prepared with Igepal CO 520. The Guinier law indicates the particle size of the sample with AOT:Igepal 1:1 in Figure 4.3.29b.

Figure 4.3.30.: Synchrotron SAXS by nanoparticles prepared with Igepal CO 520. Porod laws are given as a guide to the eye.

In order to get more precise information on the particle sizes, the samples were reproduced and studied in a wider Q range before and after reduction with SAXS at the SWING beamline at synchrotron SOLEIL. The SAXS by micellar solutions with Igepal presented in Figure 4.3.30a exhibits a small structure factor indicating repulsive inter-

particle interaction and preventing the determination of the micelle size by Guinier approximation. Instead, a Guinier law with R = 7 Å is given as a guide to the eye. The asymptotic behavior at high Q does not follow the Q^{-4} power law expected for spheres. Because it is known that Igepal forms ellipsoidal rather than spherical micelles [69], the studied mixed micelles may have a non-spherical shape resulting in a different asymptotic behavior. However, the investigated micellar solutions are comparable in size regardless the amount of added Igepal and are not agglomerated. The only influence of Igepal on the micellar solutions is a slight repulsive interaction. The SAXS by reduced cobalt nanoparticles is presented in Figure 4.3.30b. The sample with lowest Igepal content follows the Q^{-4} power law expected for spherical particles. However, the particle size seems to be smaller than observed for the same Igepal content in Figure 4.3.29b as given by the Guinier law in Figure 4.3.30b. With increasing Igepal content, an increasing structure factor is observed in the lower Q range, indicating agglomeration of the nanoparticles, which is in agreement with the observation in Figure 4.3.29. Note that in Figure 4.3.30b the scattering intensity is lower for samples with higher Igepal content due to the lower cobalt content, while the samples for SAXS measurements presented in Figure 4.3.29 had been diluted to a comparable cobalt content. The sample with AOT:Igepal 1:9 in Figure 4.3.30b is in agreement with the general trend of the remaining samples, indicating that the deviations in Figure 4.3.29 are not related to Igepal.

Thus, by addition of Igepal CO 520 during preparation of cobalt nanoparticles a larger particle size with increasing Igepal content was achieved as indicated by the superparamagnetic blocking temperature and first SAXS measurements. However, a precise determination of the particle sizes by SAXS was not achieved due to the low reproducibility of the samples. The reproducible property found is an increasing tendency of particle agglomeration with increasing Igepal content.

4.3.2.3.2. $C_{12}E_5$ Pentaethylene glycol monododecyl ether ($C_{12}E_5$) was studied as a further nonionic surfactant added to the $Co(AOT)_2$ solution before reduction. Solutions of mixed reverse micelles of $Co(AOT)_2$ and $C_{12}E_5$ as well as the reduced cobalt nanoparticle dispersions were investigated by SAXS at the SWING beamline at synchrotron Soleil and are presented in Figure 4.3.31.

The mixed reverse micelles are comparable in size regardless the surfactant composition, and the first form factor minimum in Figure 4.3.31a can be expected at ~ 0.8 $Å^{-1}$, corresponding to a particle diameter of ~ 8 Å. A refinement of the particle size within the Guinier approximation is not possible due to a small structure factor observed in the lower Q range. In contrast to the observations for mixed micelles with Igepal, the observed structure factor seems to be lower for a higher $C_{12}E_5$ content.

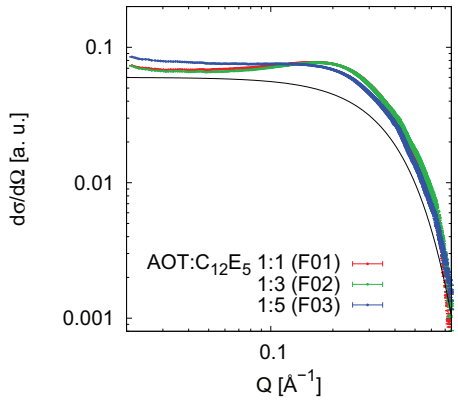

(a) SAXS by mixed micelles of $Co(AOT)_2$ and $C_{12}E_5$. A Guinier law with R = 6 Å is given as a guide to the eye.

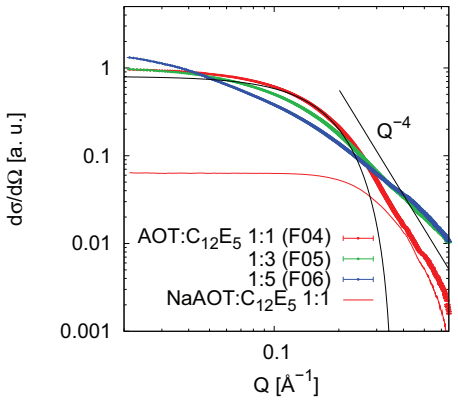

(b) SAXS by cobalt nanoparticles prepared with $C_{12}E_5$. A spherical form factor for a radius of 12.5 Å is indicated (black line). SAXS by a reverse micellar solution of NaAOT and $C_{12}E_5$ illustrates the superposition of the first form factor minimum (red line).

Figure 4.3.31.: Synchrotron SAXS by nanoparticles prepared with $C_{12}E_5$. Porod laws are given as a guide to the eye.

The cobalt nanoparticles prepared from these micellar solutions exhibit in general the same tendencies as observed with Igepal. For a low content of $C_{12}E_5$, a Q^{-4} power law is observed, indicating spherical particles with a smooth surface. The particle size is estimated to ~ 12.5 Å by matching with a spherical form factor in the range of 0.1 - 0.2 $Å^{-1}$. The possible superposition of the first form factor minimum by excess AOT and $C_{12}E_5$ micelles is illustrated by the scattering curve of a NaAOT and $C_{12}E_5$ mixed micellar solution presented as a red line in Figure 4.3.31b. With increasing $C_{12}E_5$ content, an increasing structure factor due to particle agglomeration is found in the lower Q range, along with an increasing background at higher Q, which may be due to even more excess $C_{12}E_5$ micelles. Because both the low Q and the high Q asymptotic behavior are altered by these effects, the particle size can not be determined.

As a general result for the use of nonionic surfactants in cobalt nanoparticle preparation, an increased agglomeration with increased content of nonionic surfactants was found.

4.3.2.3.3. NaAOT In order to decrease the cobalt concentration per micelle while maintaining the same type of surfactant, NaAOT was added to $Co(AOT)_2$ reverse mi-

cellar solutions. Samples were studied with SAXS at the SWING beamline before and after reduction to cobalt nanoparticles (Figure 4.3.32).

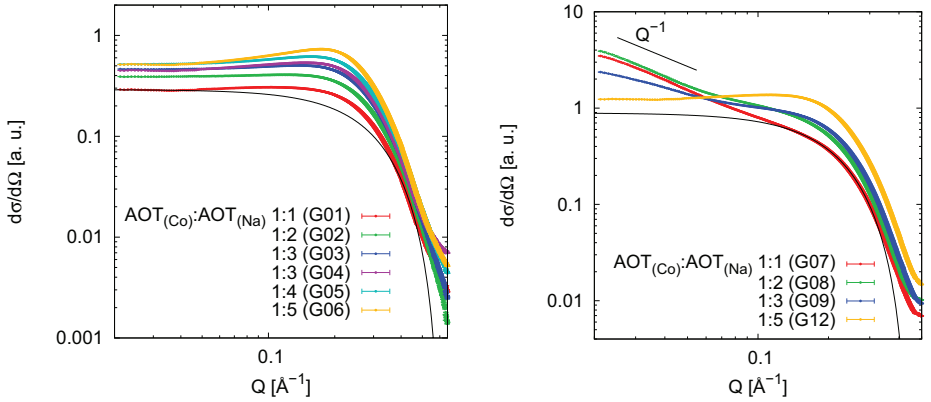

(a) SAXS by mixed micelles of $Co(AOT)_2$ and NaAOT. A spherical form factor with R = 7.4 Å is given as a guide to the eye.

(b) SAXS by cobalt nanoparticles prepared with NaAOT. A spherical form factor for a radius of 10.2 Å is indicated (black line).

Figure 4.3.32.: Synchrotron SAXS by nanoparticles prepared with NaAOT.

SAXS by the micellar solutions as presented in Figure 4.3.32a reveals an almost constant micelle size regardless the NaAOT concentration. The micellar radius is estimated to 7.4 Å by matching with a spherical form factor. For all micellar solutions, a small repulsive structure factor is observed which increases with NaAOT content.

The reduced cobalt nanoparticles form linear chains as revealed by the Q^{-1} power law in the SAXS measurements presented in Figure 4.3.32b. With increasing NaAOT content the mass fractal is reduced, revealing a slight repulsive structure factor for a AOT(Co):AOT(Na) ratio of 1:5. The particle radius can be estimated to 10.2 Å by matching with a spherical form factor and seems to be constant for all measured samples. A precise determination of the particle size is again prevented by the absence of a form factor minimum.

Due to a capillary leakage, two of the samples were dried up during the measurement, and the SAXS represents the agglomerated nanoparticles in Figure 4.3.33. The much higher structure factors exhibit maxima due to a hard sphere potential, and the maxima positions indicated in Figure 4.3.33 correspond to real space distances of 26.3 (3) and 25.6 (5) Å for AOT(Co):AOT(Na) ratio of 1:3 and 1:4, respectively. Assuming a constant AOT ligand shell thickness of 8 Å, the cobalt nanoparticle cores are estimated as small as 10.3 (3) Å and 9.6 (5) Å in diameter, and even taking into account interpenetration of the ligand shells of adjacent nanoparticles, the core diameters are likely smaller than

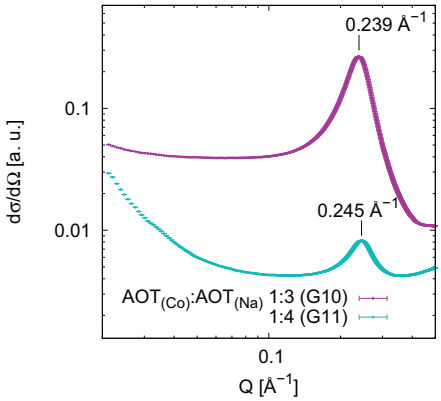

Figure 4.3.33.: SAXS by agglomerated cobalt nanoparticles.

15 Å. However, the relative particle size is observed to be slightly smaller for a larger NaAOT content.

Thus, the addition of the anionic surfactant NaAOT during cobalt nanoparticle synthesis leads to a decrease of the cobalt concentration per micelle, but does not increase the obtained particle size. A small decrease in particle size is rather suggested. However, an increasing amount of AOT surfactant leads to a better surface coverage of the prepared nanoparticles resulting in a lower degree of agglomeration as observed by a lower mass fractal with higher NaAOT content.

4.3.2.3.4. NaAOT and Igepal CO 520 In the previous subsections, the addition of the nonionic surfactant Igepal CO 520 to the initial Co(AOT)$_2$ micellar solution was found to be a promising route for preparation of larger cobalt nanoparticles. However, the achieved particle size could not be determined due to enhanced agglomeration with increasing Igepal content. In contrast, the addition of NaAOT was found to reduce agglomeration of the prepared nanoparticles with a small effect on the particle size. In order to prepare larger particles with less agglomeration, a combination of the Igepal and NaAOT surfactants was thus investigated.

Figure 4.3.34 presents the SAXS by cobalt nanoparticles prepared from reverse micellar solutions with a constant Co(AOT)$_2$:NaAOT ratio of 1:2 and a variation of the AOT:Igepal ratio. Indeed, the degree of agglomeration observed here is lower than for nanoparticles prepared without addition of NaAOT (Figure 4.3.30b). For the two samples with lower Igepal content the particle radius was determined by Guinier refinement within the valid range for Guinier approximation ($QR_g < 1$). For an AOT:Igepal

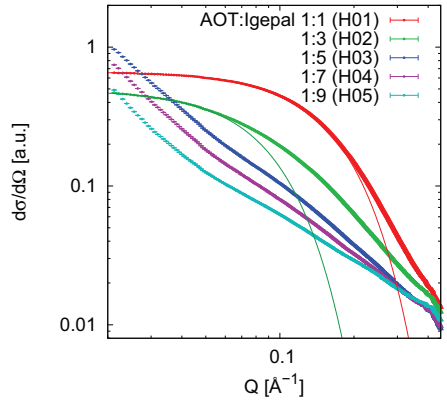

Figure 4.3.34.: SAXS by cobalt nanoparticles prepared with NaAOT and Igepal CO 520. Refined spherical form factors are presented in red and green.

ratio of 1:1 and 1:3 particle radii of 14.1(1) and 25.4(1) Å were determined, respectively. These results deviate from the particle sizes obtained with Igepal without addition of NaAOT. Here, a volume increase of ~580 % is observed. However, while the quantitative results are subject to further reproducibility studies, the general trend of increasing particle size with increasing Igepal content is confirmed.

The larger degree of agglomeration observed for the samples with higher Igepal content in Figure 4.3.34 is obviously not compensated by the added NaAOT. Larger amounts of NaAOT in combination with Igepal may lead to even larger particle sizes. Again, addition of further surfactants involves lower cobalt concentration which marks a limit of particle size increase by this method.

4.3.2.4. Microemulsion

A further possibility for preparation of larger nanoparticles is to increase the micellar size. When water-in-oil microemulsions are used as reaction media, the micellar size is increased by adjustment of the water to surfactant ratio [58].

Due to the high sensitivity of cobalt to oxidation, the standard synthesis procedure was developed using reverse micelles as reaction media, avoiding thus the use of water. In order to increase the micellar size substantially, the synthesis route has been changed back to microemulsions, but with a different polar medium. The polar media studied in this section are formamide, a polar solvent, and ethyl ammonium nitrate, EAN, an ionic liquid.

4.3.2.4.1. Formamide microemulsion Before employing formamide as polar medium in a microemulsion, a phase diagram of the system toluene/$Co(AOT)_2$/formamide was measured in the required temperature range and is presented in Figure 4.3.35. The amount of formamide that can be emulsified by a 0.1 M solution of $Co(AOT)_2$ in toluene of a given concentration increases with temperature. The maximum emulsified amount

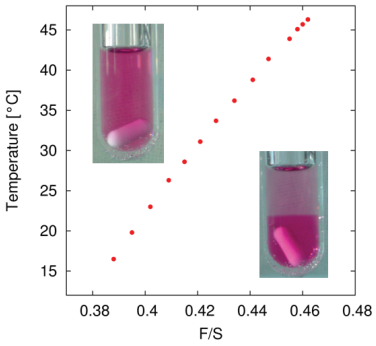

Figure 4.3.35.: Phase diagram of the toluene/$Co(AOT)_2$/formamide system. The transition temperature is given in dependence of the mass ratio of formamide and surfactant F/S. The inset pictures mark the single and double phase regions.

of formamide at room temperature corresponds to a formamide to surfactant mass ratio F/S of 0.4.

Cobalt nanoparticles were prepared in microemulsions with formamide as polar solvent and F/S ratios up to 0.394. Upon reduction of the clear microemulsion, two phases are formed. This is explained by the large amount of the surfactant bound to the particle surface upon formation of the nanoparticles. Consequently, the amount of free surfactant that contributes to the stabilization of formamide in toluene is reduced, and the effective F/S ratio is increased beyond the phase boundary in Figure 4.3.35. The lower phase, which comprises less than 10 % of the total volume, is supposed to contain the formamide due to its larger mass density (ρ_F = 1.13 g/ml) as compared to toluene (ρ_T = 0.871 g/ml). The formamide rich phase contains also an undetermined amount of cobalt nanoparticles, as observed by its dark color. Several weeks after preparation, a larger amount of the nanoparticles had transferred to the lower phase, resulting in a solid precipitate.

The magnetization measurements presented in Figure 4.3.36 were performed on the upper, toluene phase containing cobalt nanoparticles. Field dependent magnetization measurements performed the day after preparation exhibit a small hysteresis at a tem-

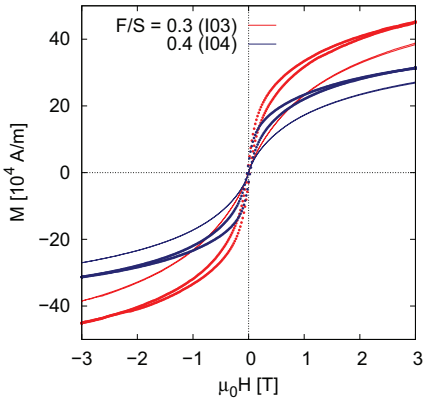

(a) Hystereses measured few days after preparation.

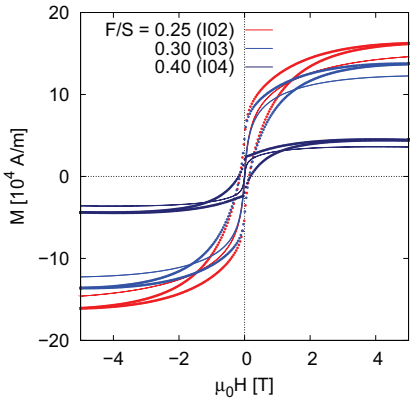

(b) Hystereses measured six weeks after preparation.

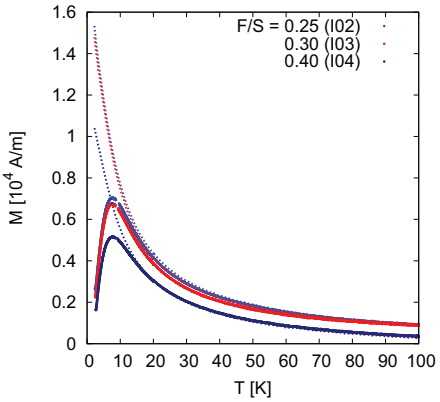

(c) Temperature dependent magnetization measured six weeks after preparation.

Figure 4.3.36.: Magnetization measurements on cobalt nanoparticles prepared in formamide microemulsion. Hystereses were mesured at 3 K (points) and 10 K (lines). Temperature dependent magnetization measurements were performed in a magnetic field of 10 mT after zero field cooling (lines) and field cooling (points).

perature of 3 K (Figure 4.3.36a). Repetition of these measurements six weeks later reveals a much larger coercive field that is independent on the formamide concentration (Figure 4.3.36b). The lower saturation magnetization as compared to the earlier measurements is explained by the transfer of particles to the lower phase, while the measured magnetization was corrected for the average cobalt content in the sample. Partial oxidation of the nanoparticles is suggested by the hysteresis curve with a minimization of the coercive field [84]. The hysteresis curve of the sample prepared with a F/S ratio of 0.4 exhibits a peculiar behavior that was not observed for any other cobalt nanoparticle sample. Temperature dependent magnetization measurements did not reveal any blocking temperature when performed briefly after preparation. However, after six weeks all samples reveal a blocking temperature with constant values of 7.6 K. Along with the slope of the hysteresis curves, the increase of the blocking temperature with time indicates a slow oxidation process which remained partial even after six weeks. This oxidation may originate from some traces of water in the used formamide, although the formamide was purchased and stored under inert atmosphere. SAXS mea-

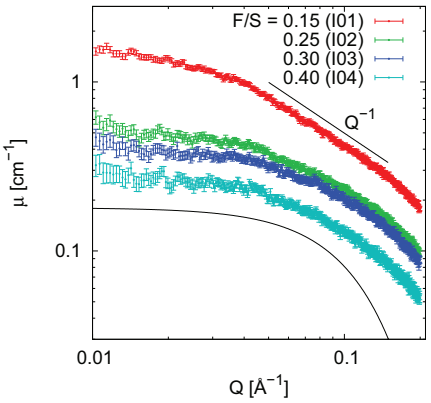

Figure 4.3.37.: In house SAXS by nanoparticles prepared from formamide microemulsion. The Q^{-1} power law and a Guinier curve are given as guides to the eye.

surements on these samples are presented in Figure 4.3.37. All samples, but in particular the sample prepared with a F/S ratio of 0.15, exhibit a Q^{-1} asymptotic behavior in the range of 0.06 to 0.15 Å^{-1} suggesting linear particle aggregates. The lower Q asymptotic behavior may be interpreted by Guinier approximation with a radius of the large aggregates in the range of 30 - 35 Å for all samples. The high Q boundary of the power law is close to the edge of the accessible Q range, and a radius of the particles in the range

of 15 -19 Å may only be speculated. This would correspond to linear aggregates of two particles each.

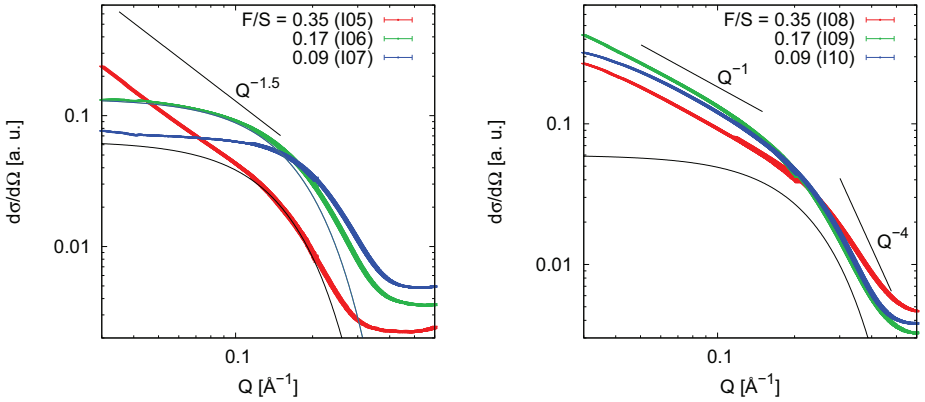

(a) SAXS by the microemulsion before reduction. The blue and green Guinier laws are fits to the data in the lower Q range.

(b) SAXS by reduced cobalt nanoparticles.

Figure 4.3.38.: Synchrotron SAXS by nanoparticles prepared from formamide microemulsion. Porod and Guinier laws are given as a guide to the eye.

In order to determine the particle sizes more precisely, synchrotron SAXS was performed at the ID01 beamline in a wider Q range on freshly prepared samples as well as the microemulsions before reduction. The microemulsions prepared with a F/S ratio of 0.09 and 0.17 exhibit micelle radii of 9.25 (2) and 13.80 (1) Å, respectively, thus confirming the intended increase of micelle size with addition of polar solvent (Figure 4.3.38a). For a F/S ratio much closer to the phase boundary (F/S = 0.35), an even larger micelle size is observed for which a radius of ~16 Å is suggested. This radius can not be determined precisely because of the mass fractal behavior observed in the lower Q range. The fractal dimension of 1.5 indicates agglomeration of the micelles in a linear, but flexible arrangement, in between that of a stiff linear aggregate (dimension = 1) and a coiling aggregate (dimension = 2).

The difference in particle sizes of the reduced cobalt nanoparticles (Figure 4.3.38b) is not as pronounced as the difference in micelle sizes. For the lower F/S ratios of 0.09 and 0.17 particle sizes of ~10 and ~11 Å are estimated, respectively, by comparison with Guinier laws. The mass fractal in the lower Q range with a fractal dimension of 1 is in agreement with the in house SAXS measurements (Figure 4.3.37), as is the change of the slope around 0.05 $Å^{-1}$ for the F/S = 0.09 sample, indicating aggregation of few particles. While the Q^{-4} power law supports the existence of spherical nanoparticles

with a smooth surface for these samples, the sample prepared with higher amount of formamide (F/S = 0.35) exhibits a scattering behavior with a smaller power law exponent, pointing to a rougher surface. Along with the mass fractal in the lower Q range, a reliable determination of the particle size is not possible. The different particle structure of this sample may be a result of the different structure of the microemulsion for this high F/S ratio, which may result in a less defined particle shape or size.

Thus, while adding formamide significantly increases the micelle size in a certain concentration range, the particle size achieved after reduction is almost constant. This is in agreement with the magnetization measurements exhibiting the same blocking temperature for all samples as shown in Figure 4.3.36c. Due to the change of the magnetic properties with time, the blocking temperature determined after six weeks may not correspond to the particle size of ~11 Å, which was determined on rather freshly prepared samples. It is speculated that the determined blocking temperature corresponds to the larger aggregates of 2-3 particles, which may turn into hard aggregates with time.

4.3.2.4.2. EAN microemulsion As a further polar medium, the ionic liquid ethyl ammonium nitrate (EAN) was investigated. Microemulsions with EAN as polar component in EAN to surfactant ratios of E/S = 0.06 and 0.24 were prepared and investigated using synchrotron SAXS at the ID01 beamline. The scattering data presented in Figure 4.3.39a suggests a larger micelle size for E/S = 0.24. Due to a slightly lower intensity in the lower Q range, the Guinier approximation is not applicable. In order to estimate the micelle sizes, spherical form factor curves have been matched to the SAXS curve at 0.2 - 0.3 $Å^{-1}$. The form factors presented in Figure 4.3.39a correspond to a micelle radius of ~7.2 and ~8 Å for a EAN to surfactant ratio of E/S = 0.06 and 0.24, respectively.

Figure 4.3.39b compares the small-angle scattering by cobalt nanoparticles prepared from the discussed microemulsions and cobalt nanoparticles prepared without addition of EAN. The addition of a low amount of EAN (E/S = 0.06) does not have a significant effect on the particle size as compared to the nanoparticles prepared without EAN. Matching of a spherical form factor in the range of 0.15 - 0.3 $Å^{-1}$ reveals a particle radius of ~10 Å. The sample prepared with E/S = 0.24 has a significantly larger particle size with a radius of ~14 Å. All nanoparticle samples exhibit a mass fractal behavior in the lower Q range, which is divided into two regimes for a low EAN to surfactant ratio of a linear subunits that are coiled to larger aggregates. For a high E/S ratio, an average fractal dimension of 1.5 is deduced.

Thus, addition of the ionic liquid as a polar solvent results in a significant increase of the obtained particle size, although the increase of micellar size is rather small. In contrast, application of formamide as polar solvent resulted in a more pronounced increase

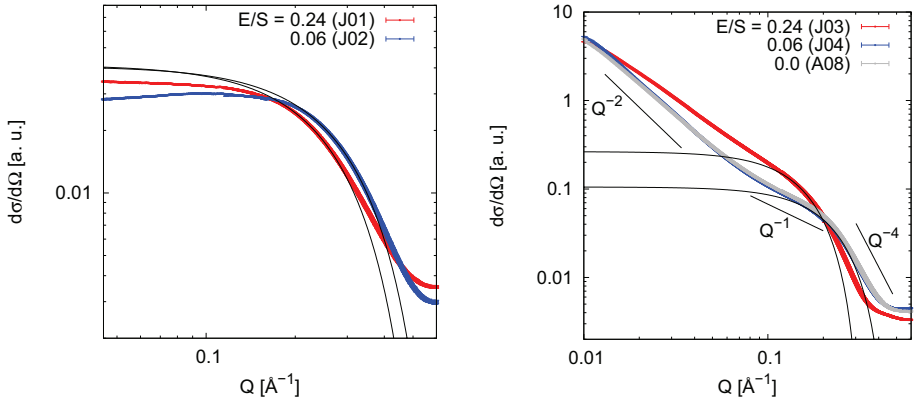

(a) SAXS by the microemulsion before reduction.

(b) SAXS by reduced cobalt nanoparticles.

Figure 4.3.39.: Synchrotron SAXS by nanoparticles prepared from EAN microemulsion. Porod laws and Guinier laws are given as a guide to the eye.

of the micelle size than the particle size. An increase in nanoparticle size of 40 % has been achieved with a large amount of EAN close to the maximum emulsified amount. In order to further increase the particle size, a precise determination of the phase diagram would be required. If the maximum emulsified amount of EAN is known, addition of an even larger amount of EAN at slightly elevated reaction temperatures is expected to further increase the particle size.

4.3.2.5. Variation of the reducing agent

As nanoparticle nucleation and growth in micellar systems depend on the interplay of the critical aggregation number of the reduced cobalt atoms and the intermicellar exchange, the velocity of the reduction process certainly has an influence on the achieved particle size. For a fast reduction process, many nanoparticle seeds are produced at the same time. If the reduction occurs more slowly, comparable to the intermicellar exchange rate, a lower amount of cobalt seeds is initially produced which can grow larger while reduction continues.

4.3.2.5.1. Hydrazine In order to investigate the influence of the reduction rate on the particle size, hydrazine (N_2H_4), which reduces Co^{2+} more slowly [58], was studied and compared to $NaEt_3BH$. Mixtures of a varying equivalent ratio of $NaEt_3BH$ and N_2H_4 were used for reduction of $Co(AOT)_2$ reverse micelles in toluene. While for a large amount of $NaEt_3BH$ the reduced cobalt nanoparticle dispersion is black or dark

brown, a higher amount of N_2H_4 leads to lighter dispersions in a pale pink color as presented in Figure 4.3.40. For a composition of 0.5 equivalent of $NaEt_3BH$ and N_2H_4 each, a brown color is observed initially, which turns into a bright green over night. The bright dispersion color is attributed to surface plasmon resonance, which is particle size dependent. A variation of particle sizes may thus be speculated from the different dispersion colors.

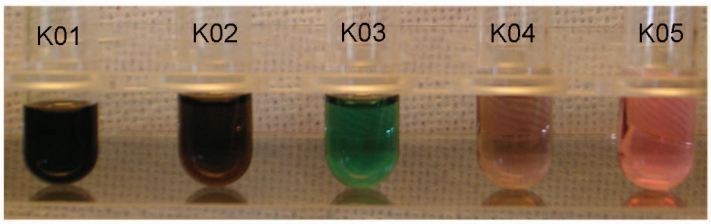

Figure 4.3.40.: Cobalt nanoparticle dispersions as reduced by a variation of reducing agents. Equivalent ratios of $NaEt_3BH$:N_2H_4 are 1.0:0, 0.75:0.25, 0.5:0.5, 0.25:0.75, and 0:1.0 (from left to right).

Magnetization measurements on the obtained nanoparticle dispersions are presented in Figure 4.3.41. The field dependent magnetization measurements presented in Figure 4.3.41a reveal a variation in saturation magnetization values that seems not to be directly related to the composition of reducing agents. The saturating field appears to be lower for a higher amount of N_2H_4, which may indicate a larger integral particle moment according to the Langevin approximation.

The temperature dependent magnetization measurements in Figure 4.3.41b are scaled and offset in magnetization for display and comparison of the observed blocking temperatures. For the sample reduced with $NaEt_3BH$ no blocking temperature is observed. Due to the difference in magnetization of the field cooled and zero field cooled measurements at low temperatures, however, it can be assumed that the particles are blocked at a temperature slightly lower than the measured temperature range. With increasing amount of N_2H_4, a blocking temperature is observed that increases from 3.0 K for an equivalent ratio of $NaEt_3BH$:N_2H_4 of 0.75:0.25 to 3.9 K for 0.5:0.5. Thus, a larger particle size is suggested for an increased amount of N_2H_4.

In order to account for the variation in dispersion color, UV-VIS spectra measured for the same samples are presented in Figure 4.3.42. There are basically two broad absorption bands observed around 450 - 550 nm and 600 - 650 nm. Both exhibit a small fine structure modulation. Surface plasmon resonance (SPR) is observed for metal nanopar-

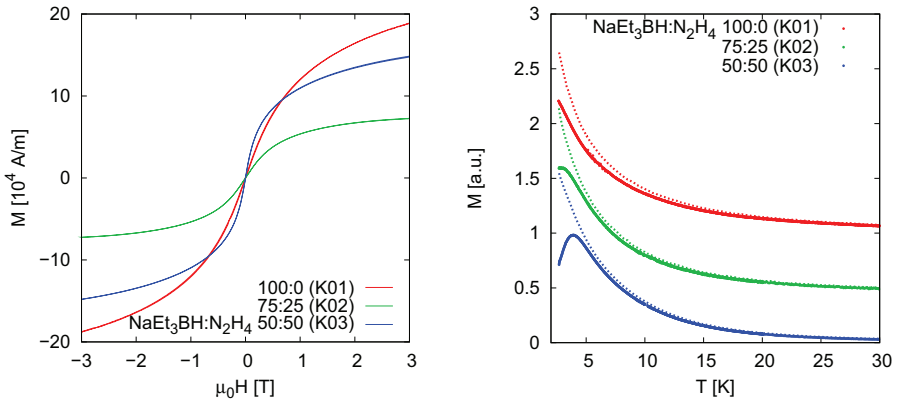

(a) Field dependent magnetization measured at 10 K.

(b) Temperature dependent magnetization. Data have been scaled and offset for display.

Figure 4.3.41.: Magnetization measurements on cobalt nanoparticles prepared by a variation of the reducing agent. Temperature dependent magnetization measurements were performed in a magnetic field of 10 mT after zero field cooling (lines) and field cooling (points).

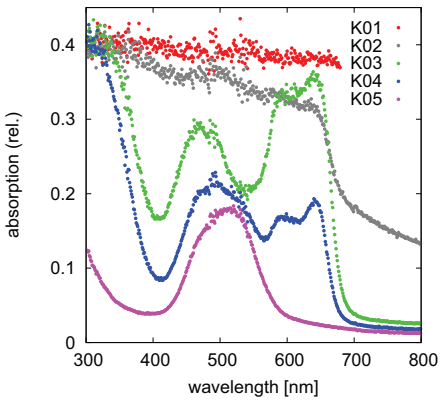

Figure 4.3.42.: UV-VIS spectra of cobalt nanoparticle dispersions as reduced by a variation of the ratio of reducing agents $NaEt_3BH$ and N_2H_4 ranging from $NaEt_3BH$:N_2H_4 100:0 (K01) via 50:50 (K03) to 0:100 (K05).

ticles, with resonance wavelengths in the visible range depending on the particle size, shape, and chemical environment. An increasing particle size has been observed to lead to a red shift of the SPR band [96–98]. The red shift of the absorption band around 450 - 550 nm with increasing amount of N_2H_4 may thus be explained by a shifted SPR band due to an increased particle size, because the chemical environment and supposedly also the particle shape is the same for all samples. An increasing particle size with amount of N_2H_4 is in agreement with the magnetization results. The absorption band around 600 - 650 nm does not shift in energy, but increases in absorbance with increasing amount of $NaEt_3BH$ from nearly zero up to saturation for a reducing agent ratio of 0.75:0.25. Due to the very light pink color of the sample reduced with pure N_2H_4, similar to the $Co(AOT)_2$ reverse micellar solution, it may be speculated whether N_2H_4 reduces $Co(AOT)_2$ at all or possibly only in a small fraction. In that case, the absorption band around 600 - 650 nm may be understood as related to the oxidation state of cobalt and resulting in the dark brown or black color of a concentrated cobalt nanoparticle dispersion. The question whether N_2H_4 has an influence on cobalt reduction will be discussed in the following subsection.

Small-angle X-ray scattering was performed at the JUSIFA beamline, HASYLAB. The sample prepared with an equivalent ratio of the reducing agents of 0.5:0.5 is compared to a sample reduced with $NaEt_3BH$ in Figure 4.3.43a. Because this sample was measured

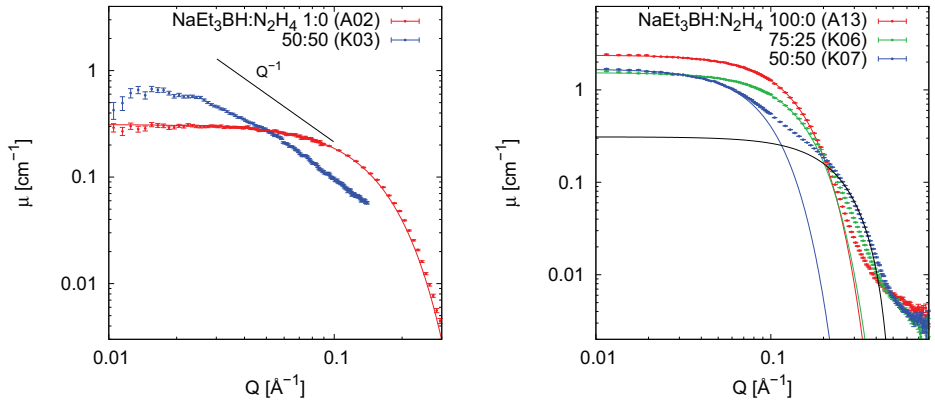

(a) Cobalt nanoparticles as presented in Figure 4.3.40.

(b) Reproduction of the discussed cobalt nanoparticles.

Figure 4.3.43.: Synchrotron SAXS by nanoparticles prepared by variation of the reducing agent. Colored Guinier curves are fits in the Guinier regime, the black line indicates a spherical form factor.

in a smaller Q range, the position of a form factor minimum can not be determined.

The Q^{-1} power law prevents particle size determination by Guinier approximation and indicates a linear nanoparticle arrangement. Reproduced samples were measured in a wider Q range and are presented in Figure 4.3.43b. For these samples, the scattering intensities at low Q allow for a particle size determination by Guinier approximation. Spherical particle radii of 17.9(1) and 16.7(1) Å are determined for the samples prepared with $NaEt_3BH$:N_2H_4 equivalent ratios of 1.0:0 and 0.75:0.27, respectively, indicating a decrease of particle size with increasing amount of N_2H_4. An equivalent ratio of 0.5:0.5 leads to a more complex scattering curve. Matching with a spherical form factor in the higher Q range leads to a particle radius of ~ 9.7 Å, while the lower Q range of the scattering curve can be refined by a Guinier law, yielding a radius of gyration of 20.8(1) Å. The $Q^{-1.5}$ power law observed between the Guinier and form factor regimes indicates a linear arrangement of nanoparticles. Despite the flexible conformation of the entire aggregate, an elliptic cylinder is assumed as an approximation of the shape of the whole aggregate. With a radius of its cross section of 9.7 Å, the length of the aggregate is estimated from the radius of gyration as 63.7(5) Å (equation in Table 2.2.2). Thus, an average chain length of 3 particles is estimated.

The tendency of a decreasing particle size with increasing amount of N_2H_4 as observed by SAXS in not in agreement with the increasing blocking temperatures as observed by magnetization measurements. Furthermore, the bright green color of the sample prepared with an equivalent ratio of the reducing agents of 0.5:0.5 is not exhibited by the respective sample investigated by SAXS in Figure 4.3.43b. Thus, reproducibility of the observed size variation is questionable.

4.3.2.5.2. Reduction agent deficiency In order to investigate the influence of N_2H_4 on the reduction of $Co(AOT)_2$ and the color of the prepared cobalt nanoparticle dispersions, the experiments of the previous section were repeated without addition of N_2H_4.

Samples prepared with deficient amounts of $NaEt_3BH$ are presented in Figure 4.3.44, and for 0.5 equivalents of reducing agent, a green color similar to that produced with a mixture of reducing agents is found. Magnetization measurements on the colored samples are presented in Figure 4.3.45. Both field dependent magnetization curves exhibit a linear increase at high magnetic field. The curve of the sample prepared with less reducing agent reaches the linear field dependence in a magnetic field below 1 T, corresponding to a larger magnetic particle moment as compared to the sample prepared with 0.5 eq $NaEt_3BH$ (~ 1.5 T). Temperature dependent magnetization measurements presented in Figure 4.3.45b reveal blocking temperatures of 3.7 and 4.0 K for reducing agent equivalents of 0.5 and 0.4, respectively. These values confirm the larger particle

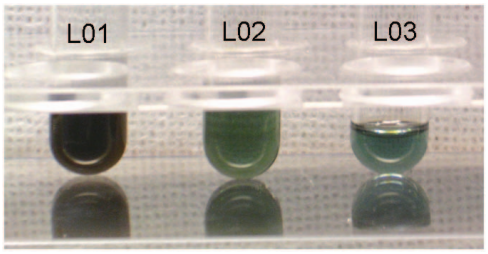

Figure 4.3.44.: Cobalt nanoparticle dispersions as reduced with a deficient amount of reducing agent. Equivalent ratios of $NaEt_3BH$ are 0.687, 0.491, and 0.381 (from left to right).

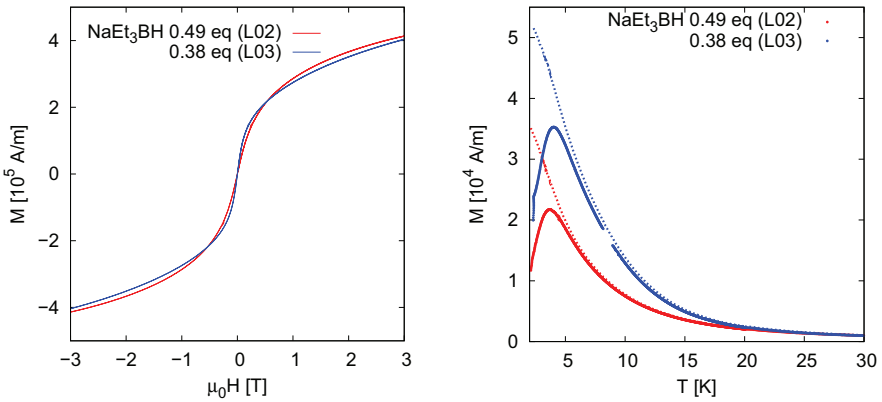

(a) Field dependent magnetization measured at 10 K.

(b) Temperature dependent magnetization.

Figure 4.3.45.: Magnetization measurements on cobalt nanoparticles prepared by reducing agent deficiency. Temperature dependent magnetization measurements were performed in a magnetic field of 10 mT after zero field cooling (lines) and field cooling (points).

size for a reduced amount of reducing agent, and the observed blocking temperatures are in the same temperature range as observed with N_2H_4. Thus, taking into account the dispersion colors and the results from magnetization measurements, it is suggested that the variation in particle size observed here and in the previous subsection is entirely due to the deficiency of $NaEt_3BH$ reducing agent, while N_2H_4 has only a minor influence on the reduction process.

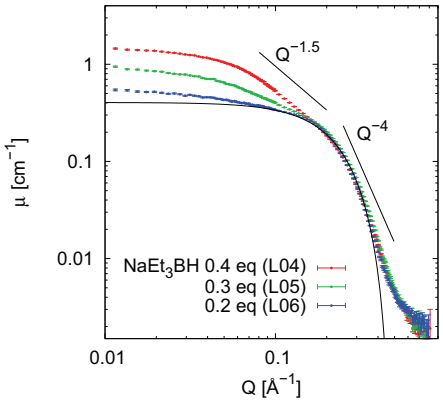

Figure 4.3.46.: SAXS by cobalt nanoparticles prepared with reducing agent deficiency. A spherical form factor is shown (black line). Power laws are given as a guide to the eye.

Synchrotron SAXS measurements were carried out on reproduced samples at the JUSIFA beamline, HASYLAB, for particle size determination and are presented in Figure 4.3.46. The particle size estimated by matching the data with a spherical form factor is constant for all investigated samples, and the estimated particle radius is ~ 9.5 Å. The different degree of reduction in these samples has a direct influence on the particle agglomeration leading to a fractal dimension of 1.5 for 0.5 equivalents of reducing agent. However, the samples investigated by SAXS did not reveal the same colors as observed for the samples investigated by magnetic measurements. For this reason, reproducibility is again not confirmed.

Thus, the nanoparticle dispersion color is strongly correlated to the particle size, and an increase of particle size has been achieved by deficient reduction of the $Co(AOT)_2$ reverse micellar solution. The precise particle size determination by SAXS is still missing due to low reproducibility of the samples.

4.3.2.5.3. Stepwise nanoparticle reduction After a deficient amount of reducing agent was found to result in larger cobalt nanoparticles, the effect of a stepwise reduction

was investigated. A partially reduced nanoparticle dispersion still contains $Co(AOT)_2$ which can be reduced in a further injection of the reducing agent. If this second reduction step can be directed to nanoparticle growth instead of nucleation, a further increase of nanoparticle size is expected.

Cobalt nanoparticle dispersions that were initially reduced partially and subsequently reduced stepwise with a constant reduction rate of 0.2 equivalents per day are presented in Figure 4.3.47. All the presented samples have received the total amount of

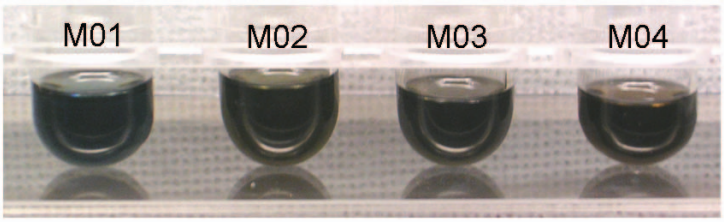

Figure 4.3.47.: Cobalt nanoparticle dispersions as reduced stepwise with a constant reduction rate of 0.2 eq/day. Starting equivalent ratios of $NaEt_3BH$ are 0.1, 0.2, 0.4, and 0.6 (from left to right).

1 eq $NaEt_3BH$. The very dark color results from the high cobalt concentration of 0.03M, which is entirely reduced to Co(0). Nonetheless, the dispersion prepared with the lowest initial reducing agent amount of 0.1 eq exhibits a blue color, whereas a dark green color is observed for the dispersion prepared with an initial amount of reducing agent of 0.2 eq.

Magnetization measurements of these samples are compared in Figure 4.3.48. The field dependent magnetization exhibits a lower saturation field for the sample reduced with an initial amount of reducing agent of 0.1 eq, indicating a higher particle moment and thus a larger particle size. Temperature dependent magnetization measurements on this sample (presented in Figure 4.3.48b) reveal a blocking temperature of 5.7(1) K. Due to an instrumental failure, the zero field cooled temperature dependent magnetization of the sample prepared with a higher initial amount of reducing agent of 0.2 eq was not measured, and the blocking temperature can not be determined. However, according to dispersion color and field dependent magnetization this sample is supposed to consist of smaller particles.

For comparison, a further set of nanoparticle dispersions was prepared with varying initial amounts of reducing agent and subsequent reduction within an equal period. All the samples received the full equivalent of reducing agent within 5 days. The resulting nanoparticle dispersions are presented in Figure 4.3.49. The evolution of colors follows

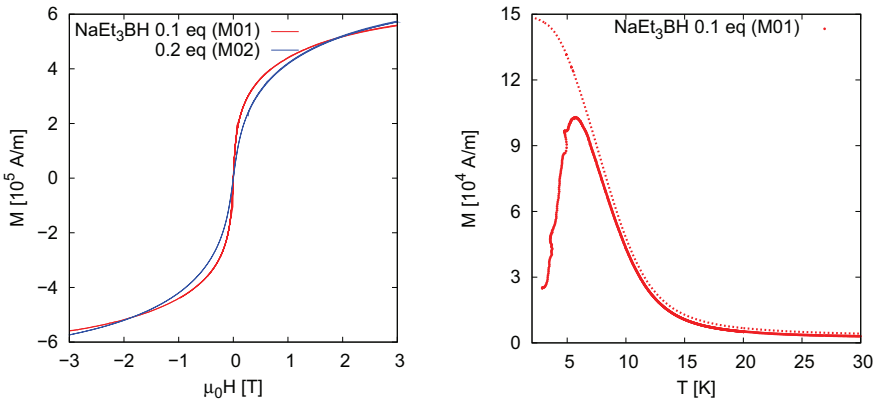

(a) Field dependent magnetization measured at 10 K.

(b) Temperature dependent magnetization. The discontinuous slope of the zero field cooled magnetization is due to instabilities in the PPMS temperature regulation.

Figure 4.3.48.: Magnetization measurements on cobalt nanoparticles prepared by a stepwise reduction. Temperature dependent magnetization measurements were performed in a magnetic field of 10 mT after zero field cooling (line) and field cooling (points).

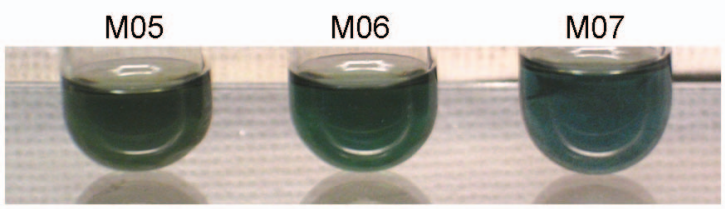

Figure 4.3.49.: Cobalt nanoparticle dispersions as reduced stepwise within a total reduction time of 5 days. Starting equivalent ratios of $NaEt_3BH$ are 0.1, 0.2, and 0.4 (from left to right).

the same trend for all samples. After the first day, the dispersions prepared with initial amount of reducing agent of 0.1, 0.2, and 0.4 eq were pink, purple, and green, respectively. With further reduction, the colors changed to an olive green, a bright green, and blue. The picture in Figure 4.3.49 was taken at the third day of reduction. The final dispersion colors are bright green, blue, and blue (from left to right).

Combining the particle sizes determined for cobalt nanoparticle dispersions with variation of the amount of reducing agent and the observed dispersion colors, it is concluded that a larger particle size is achieved by initial reduction with a lower amount of reducing agent. The dispersion colors are indicative of the relative particle size and vary from brown to olive green to bright green and blue with increasing particle size. The blue nanoparticle dispersions mark the largest particle sizes observed in the respective sample series, with blocking temperatures up to 6 K (see Figures 4.3.27b, 4.3.45b, and 4.3.48b). Finally, further growth of cobalt seed dispersions by a stepwise reduction has been performed successfully according to the observed dispersion colors.

4.3.2.6. Nanoparticle growth by decomposition of dicobalt octacarbonyl

The cobalt nanoparticles prepared by the micellar methods presented in the above subsections represent a variation of the particle size in a small range with particle diameters of few nanometers. For most of the investigated approaches a higher increase in particle size was not achievable, *e. g.* by addition of further surfactants, which is limited by a minimum concentration of cobalt required to perform a precise structural analysis.

Thermal decomposition techniques were shown to be powerful in order to access larger nanoparticles, *i. e.* particles with diameters above 10 nm [65, 66, 85]. The preparation strategy for large nanoparticles involves the separation of nucleation and particle growth, *e. g.* by a precursor that exhibits temperature dependent decomposition rates [99]. These can be used to initiate nucleation at a certain temperature with fast decomposition and mediate particle growth at a different temperature with slower decomposition rate.

In order to achieve a significantly larger size of the cobalt particles prepared so far, particle growth experiments were performed on as prepared cobalt nanoparticles with dicobalt octacarbonyl ($Co_2(CO)_8$) as decomposition precursor. If the thermal decomposition of $Co_2(CO)_8$ can be tuned to result in particle growth without nucleation of new nanoparticles, the narrow size distribution of the very small starting nanoparticles will be maintained and the increase in particle size should be directly controllable by addition of $Co_2(CO)_8$.

For preliminary experiments presented in this subsection, different amounts of solid $Co_2(CO)_8$ were added to dilute cobalt nanoparticle dispersions in toluene. The dispersions were heated to 100°C in ~ 30 K/h, maintained at 100°C for 1 hour, and slowly cooled to room temperature. The decomposition was performed in the inert atmosphere of a Schlenk line in order to prevent oxidation of the nanoparticles.

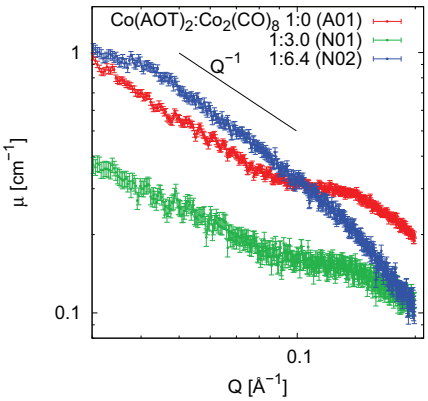

Figure 4.3.50.: SAXS by cobalt nanoparticles prepared with $Co_2(CO)_8$.

SAXS by the obtained nanoparticle dispersions as well as the seed solution is presented in Figure 4.3.50. The sample prepared with a $Co(AOT)_2$:$Co_2(CO)_8$ ratio of 1:3 exhibits a particle size comparable to that of the sample prepared without $Co_2(CO)_8$ as indicated by the SAXS intensity decrease at high Q. The sample prepared with a higher amount of $Co_2(CO)_8$ exhibits a much steeper slope indicating a form factor minimum in a lower Q range corresponding to a larger particle size. However, all samples exhibit a Q^{-1} power law in the lower Q range which indicates a linear agglomeration of the particles and impedes the particle size determination by Guinier approximation. Because the Q^{-4} asymptotic behavior expected at high Q is not reached within the available momentum transfer range, particle size determination by matching with a spherical form factor is not possible either.

Thus, the presented experiments suggest the tendency of a larger particle size achieved by nanoparticle growth by decomposition of $Co_2(CO)_8$ although a precise particle size can not be given. In order to investigate decomposition-mediated particle growth more precisely, a detailed study of the decomposition behavior of $Co_2(CO)_8$ is required. A lower heating rate seems advisable in order to achieve a slow decomposition and thus rule out nucleation. With increasing particle size, a larger particle surface has to be covered by AOT ligand in order to prevent agglomeration. Thus, the addition of NaAOT

with $Co_2(CO)_8$ is suggested. Furthermore, synchrotron SAXS is required to determine the particle size in a wider Q range, and magnetization measurements should be performed to confirm the presence of magnetic, non-oxidized cobalt nanoparticles.

4.4. Summary

Within this study, the synthesis of cobalt nanoparticles by a water-free micellar synthesis technique has been explored. Reduction of a $Co(AOT)_2$ reverse micellar solution in toluene yields nanoparticle dispersions that are stable against precipitation for months. Magnetization measurements reveal superparamagnetic blocking temperatures below 10 K and saturation fields of several T indicating a large magnetic anisotropy. A blocking temperature of 10 K corresponds to a barrier energy of $KV = 3.45 \cdot 10^{-21}$ J and (including the magnetic anisotropy of the bulk material) a magnetic particle diameter of 2.5 nm. The particle size was investigated by small-angle scattering techniques, and an average particle diameter of 3 nm was found.

Both particle size and blocking temperature are affected by a varying degree of oxidation which could not be eliminated entirely. X-ray absorption spectroscopies revealed the coexistence of cobalt and cobalt oxide in the nanoparticles. Magnetization measurements exhibiting exchange bias suggest a core shell particle structure of a cobalt core with a cobalt oxide shell. Such a stable core shell structure with different shell thicknesses has not been observed before for small nanoparticles with ~ 3 nm diameter.

A precise determination of the particle size and size distribution by small-angle scattering techniques is challenging because the first form factor minimum is superposed by excess surfactant micelles. Extraction of a pure cobalt nanoparticle dispersion by ligand exchange resulted in strong aggregation along with a broadening of the size distribution as suggested by temperature dependent magnetization measurements. Separation of the pure cobalt scattering contribution by ASAXS failed for technical reasons. The applicability of the available primary characterization methods to such small nanoparticles was found further limited by both reproducibility as well as oxidation of the prepared nanoparticles and reliability of the used instruments in the required measurement range. A rough determination of the particle size distribution was achieved by polarized SANS with polarization analysis. A lognormal particle size distribution of 10 (4) % was found. However, this technique is too complex and time-consuming to serve as a primary characterization method.

Despite these obstacles, relative tendencies for preparation of larger nanoparticles were derived by synthesis optimization experiments. An increase of nanoparticle size

was achieved by addition of the nonionic surfactant Igepal CO 520, whereas simultaneously occurring agglomeration was suppressed by addition of the anionic surfactant NaAOT. A further approach for size variation is the implementation of a polar solvent and reduction of $Co(AOT)_2$ inside the formed microemulsion. The application of the ionic liquid EAN as polar phase was found promising for preparation of larger cobalt nanoparticles. Finally, an incomplete reduction of the $Co(AOT)_2$ micellar solution leads to less nanoparticle seeds which can grow to larger particles. A stepwise reduction was shown to gradually increase the cobalt nanoparticles, and the development of different dispersion colors was related to the different particle sizes.

The most promising route for particle size variation in sufficient nanoparticle concentrations is the stepwise reduction. Further development of this technique may involve a more gradual reduction in order to entirely separate the nucleation and growth processes. As long as the reduction remains incomplete, addition of more $Co(AOT)_2$ starting material is possible without new nucleation and promises opportunities for preparation of much larger nanoparticles. However, for a successful further development, improvement of both the inert synthesis conditions and the available primary characterization methods are crucial. In order to entirely exclude oxidation of the samples, an improved atmosphere inside the glove box, *e. g.* by additional predrying of the used N_2 or Ar, may be required. For the transport to the instruments for primary characterization, freezing of the samples below the solvent melting point and transport at low temperatures is also advisable [100]. The most important characterization technique is the measurement of field and temperature dependent magnetization. In particular, a reliable performance of zero-field cooled magnetization measurements in a temperature range below 10 K is required.

5. Iron Oxide Nanoparticles

5.1. Morphological and Magnetic Characterization

5.1.1. Introduction of the samples

The focus of this study concerns investigation of the spin structure and dynamics of individual magnetic nanoparticles by determination of the magnetization distribution or spin wave modes within the particles, respectively, as well as the investigation of interparticle interactions in nanoparticle superlattices. Because each of these phenomena is strongly correlated to finite size effects and in order to allow for application of scattering methods, high monodispersity is an important requirement to be fulfilled by the chosen model system. Thus, the particles have to be synthesized using a robust synthesis procedure, delivering a reliable and reproducible particle size with extremely narrow size distribution and with sufficient batch masses for neutron scattering experiments. Concerning the particle size, a compromise must be established between the necessities of single domain and preferably small particles exhibiting more pronounced finite size effects on the one hand, and of particles large enough to show a considerable magnetic moment and with scattering in a momentum range covered by most small-angle instruments on the other hand. Variation in particle size and/or shape is further desirable to determine the size/shape dependency of the investigated effects. The requirements of a high reproducibility of particle size and size distribution but also a controlled size variation are essentially contradicting and thus remain hard to achieve. For investigation of individual particle properties, good colloidal stability of the particles is furthermore essential in order to minimize interparticle interactions but at the same time to probe large sample volumes for good statistics. For the investigation of properties depending on the local order, such as magnetic properties and spin wave modes, the nanoparticles must be reproducible even in the atomic size range. Thus, good crystallinity of the nanoparticles is an additional requirement.

Iron oxide nanoparticles were chosen as material for the study in this chapter. Iron oxides have interesting magnetic properties, and reproducible synthesis methods have been developed to yield large amounts of iron oxide nanoparticles with a narrow size distribution [99,101]. Iron has a lower incoherent scattering cross section than *e.g.* cobalt or nickel, along with a coherent cross section large enough to provide a sufficient contrast to most (especially non-deuterated) organic side materials, which considerably enhances the signal to noise ratio for neutron scattering experiments. The use of an oxide material is also advantageous for sample handling, as it is sensitive to neither oxygen nor air moisture.

This section will provide an introductive description of several iron oxide nanoparticle systems and focus on their magnetic and morphological precharacterization leading to the decision on the adequate samples for the intended study. Special emphasis will be laid on the morphological characterization including particle size and size distribution.

Hyeon group particles - variation in particle size An excellent control of nanoparticle size and size distribution through a large scale synthesis route based on thermolysis of metal oleate complexes was reported by Park *et al.* [99]. Extremely narrow size distributions below 5% can be achieved by a complete separation of nucleation and growth of the particles, which occur at different temperatures. As nucleation precursor, iron oleate is used for the preparation of iron oxide nanoparticles, which is less expensive and nontoxic as compared to the previously more commonly used decomposition of iron pentacarbonyl [102]. The first decomposition step of iron oleate in high-boiling solvents at 200 – 240 °C marks the nucleation temperature. In order to synthesize monodisperse nanoparticles, a precursor solution is heated up slowly through this temperature range to even higher temperatures required for ageing of the seeds. Nanoparticle growth is initiated by the oleate's entire dissociation above 300 °C. Because the growth process is time and temperature dependent, the particle size is controlled mainly by choice of the ageing time and the type of solvent, where higher boiling solvents and longer ageing at the boiling point lead to larger particles. Additional fine-tuning of the particle size is achieved by an increased amount of excess oleic acid during synthesis. The excellent monodispersity of nanoparticles prepared by this approach was confirmed by TEM [99] and muon spin relaxation [103].

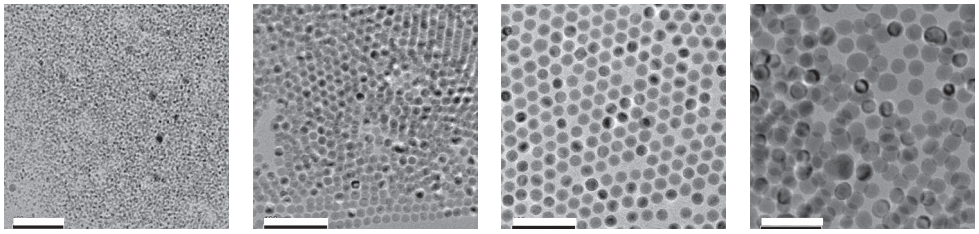

(a) Hs 4 (b) Hs 12 (c) Hs 20 (d) Hs 25

Figure 5.1.1.: Hyeon group nanoparticles. Scale bars represent 100 nm [104].

Four samples with different particle sizes were obtained through collaboration with Prof. T. Hyeon, University of Seoul, South Korea, and were investigated in this project. TEM pictures of the samples [104] are presented in Figure 5.1.1. As all these samples are comprised of spherical particles, they will be referred to in the following by 'Hs' and the approximate particle diameter in nm as determined from TEM.

Bergström group particles - variation in particle shape Iron oxide nanoparticle samples obtained through collaboration with Prof. L. Bergström, Stockholm University, Sweden, were prepared using a similar method [101]. Here, shape and size of the nanoparticles were controlled by the amount of additional oleic acid and the heating rate. It was found that the small reduction in heating rate from 3 K/s to < 2.6 K/s along with a lower amount of additional oleic acid promotes the formation of nanocrystals with a nonspherical, faceted shape [105]. Iron oxide nanocubes prepared by this approach are observed to show a varying degree of truncation at the corners. Nonetheless, these nanocubes can be arranged on TEM grids into 2 dimensional structures that form either glass-like, disordered arrays or, if subjected to a magnetic field during deposition, form highly ordered superlattices [105]. Routes to a deposition of these particles onto flat substrates instead of TEM grids and structural characterization of the obtained nanostructures will be discussed in section 5.4.

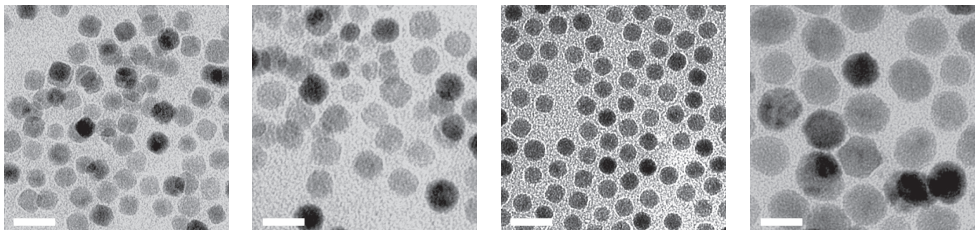

(a) Bc 9 (b) Bc 14 (c) Bs 10 (d) Bo 22

Figure 5.1.2.: Bergström group nanoparticles. Scale bars represent 20 nm [106].

The samples studied in this project include two samples of nanocubes and one sample each of nanospheres and nanooctahedra as presented in Figure 5.1.2. Accordingly, they will be referred to as 'Bc', 'Bs', and 'Bo' samples with their approximate particle diameter in nm.

Magnetization measurements revealed a superparamagnetic behavior at ambient temperatures for all samples with blocking temperatures increasing with particle size. As the increase was observed to be nonlinear with particle volume, the magnetic anisotropy constant was deduced to increase with decreasing particle size [99]. This is typical for nanoparticles and has been attributed to the enhanced influence of surface anisotropy in smaller particles [107]. Mössbauer spectroscopy and muon spin relaxation indicate a linear particle size dependency of the magnetic anisotropy [103].

X-ray diffraction confirmed the crystallinity of the particles and reveals the inverse spinel structure, which is characteristic for both magnetite (Fe_3O_4) and maghemite ($\gamma - Fe_2O_3$). The structural difference between magnetite and maghemite is the occupancy of the iron sites, where maghemite shows vacancies that can be either ordered or statistically distributed [108]. Several more probes have been applied to determine the atomic structure of these nanoparticles, including X-ray absorption [99, 109] and Mössbauer spectroscopies [101, 103]. A more detailed discussion of the local order will be given in section 5.2.

5.1.2. Methods

5.1.2.1. Sample preparation and data treatment

SAXS For SAXS measurements, 2.4 mg of Hs 4, 2.6 mg of Hs 12, 1.9 mg of Hs 20, 2.8 mg of Hs 25, 1.0 mg of Bc 9b, 2.7 mg of Bc 14, and 2.5 mg of Bo 22 were dispersed in 1 ml of toluene each. Readily dispersed Bs 10 and Bc 9a samples were obtained from our collaborators in concentrations of 4 x 10^{15} particles/ml. The nanoparticle dispersions were filled into Hilgenberg quartz capillaries with an inner diameter of 1.5 mm and a wall thickness of 0.01 mm, and sealed by PMMA stoppers using Loctite 408 glue. SAXS measurements at the JUSIFA beamline were performed with an incident energy of 12.02 keV and two different detector distances. The beam size was set to 0.8 x 0.8 mm for the 935 mm detector distance, and 0.8 x 0.5 mm for the 3635 mm detector distance. The data of the H samples was recorded on a multiwire proportional chamber gas detector (Gabriel detector) with 256 x 256 pixels of 0.8 mm pixel size. For measurement of the B samples during a different beamtime a PILATUS 300k detector with 487 x 619 pixels of 0.172 mm pixel size was used. The data were radially averaged and normalized to absolute units by use of glassy carbon with a thickness of 1 mm as a reference material. To take into account the Q resolution in SAXS refinement, a wavelength spread of $\Delta\lambda/\lambda = 5 \cdot 10^{-5}$ and an angular resolution parameter of $d\theta = 0.3$ mrad was implemented [48].

SANS For SANS measurements, 6.9 mg of Hs 4, 7.0 mg of Hs 12, 6.7 mg of Hs 20, and 6.8 mg of Hs 25 were dispersed in 2 ml of 99.6 atom% d_8-toluene each. The Bs 10 and Bc 9 samples were obtained from our collaborators readily dispersed in concentrations of 4 x 10 ^{15} particles/ml in d_8-toluene. Measurements at KWS 2 were performed using Hellma quartz cuvettes with a sample thickness of 1 mm as sample holders. A wavelength of 5 Å was chosen, and SANS was measured at 2 m and 8 m detector distances with a sample aperture of 9 x 9 mm. Collimation distance and aperture at KWS 2 are at the moment fixed to 8 m and 30 x 30 mm, respectively, regardless the detector distance. Along with the detector pixel size of 5.25 mm, these configurations lead to angular resolution values of $d\theta_{2m} = 0.00335$ and $d\theta_{8m} = 0.003545$ as calculated using equation (2.2.35). The measured data was circularly averaged and normalized to absolute units.

Details of sample preparation and data treatment for the SANS measurements performed at D 22 are given in section 5.3.2.1.

Magnetization measurements The temperature dependent magnetization measurements were performed using a Quantum Design MPMS XL SQUID. For measurements of liquid nanoparticle dispersions, performed in an evacuated sample chamber, an air-tight sample holder was developed. The characteristics of the sample holder are similar to the sample holder developed for VSM measurements (see section 4.2.2.1), and Vespel® polyimide was again chosen as the sample holder material. The sample is held in a cylindric cavity of 3.5 mm in diameter and 4 mm in height (see Figure 5.1.3). For air-tight sealing of the sample holder a thread length of 7 mm is required, which is

Figure 5.1.3.: Sample holder designed for measurements of liquid samples using the MPMS. The drawing on the left represents a cut through the sample holder. A technical drawing including all measures can be found in the Appendix C.2.

longer than the sample cavity. An asymmetric sample holder results in a slightly shifted sample position as compared with the center of the sample holder, leading to an asymmetric primary signal in case of a low sample moment in the range of the sample holder moment (as is the case for superparamagnetic nanoparticles). In order to facilitate the

correction of the sample holder moment, the sample holder was thus designed symmetrically, with the center of the sample in the center of the sample holder. In order to tighten the sample holder, a teflon ring is inserted and the threads are greased with vacuum grease before closing the sample cavity. Such a sample holder filled with toluene lost less than 1% of the toluene when heated to 50°C for several hours under the low pressure of a vacuum oven.

3.0 mg of Hs 4, 4.1 mg of Hs 12, and 4.2 mg of Hs 20 were wrapped in cotton and held by a the developed Vespel® polyimide sample holder. For measurement of the Bs 10 and Bc 9 samples, the sample volume of these holders of 0.0385 ml was filled entirely with nanoparticle dispersions in concentrations of 8.4 x 10 ^{14} particles/ml in toluene. For zero field cooled measurements, the ultra low field option of the MPMS was applied, and the sample was cooled to a base temperature of 2 K before application of a magnetic field of 5 mT. The temperature dependent magnetization was measured with a heating rate of 1 K/min up to 300 K. For field cooled magnetization measurements, the same conditions were applied except for a 5 mT magnetic field that was applied to the sample during cooling prior to the measurement. The blocking temperatures for each ZFC measurement have been determined by fitting a Lorentzian with a linear background to the data.

Magnetic field dependent magnetization measurements were performed on a Quantum Design PPMS using the VSM option. The volumes of 20 μl of liquid nanoparticle dispersions were filled in a specifically designed Vespel® polyimide sample holder (see section 4.2.2.1), and magnetization curves were measured with a magnetic field sweep rate of 20 mT/s up to 8.5 T at 300 K. The measured magnetic moment $M[emu]$ was converted into magnetization $M[A/m]$ by normalization with the sample volume according to

$$M[A/m] = \frac{M[AM^2]}{V[m^3]} = \frac{M[emu] \cdot 10^{-3}}{V[m^3]} \tag{5.1.1}$$

The inorganic mass concentrations of the measured samples were 7.2 mg/ml for Bs 10 and 1.5 mg/ml for Bc 9. For compensation of any diamagnetic contribution, *e.g.* due to the toluene matrix, a linear susceptibility term was added to the Langevin function during refinement.

5.1.2.2. Oleic acid

Molecular dimensions The oleic acid molecule ($C_{18}H_{34}O_2$, cis-9-Octadecenoic acid) is an amphiphile consisting of a hydrophilic head group (-COOH) and a hydrophobic

unbranched hydrocarbon tail (-$C_{17}H_{33}$) with one double bond.

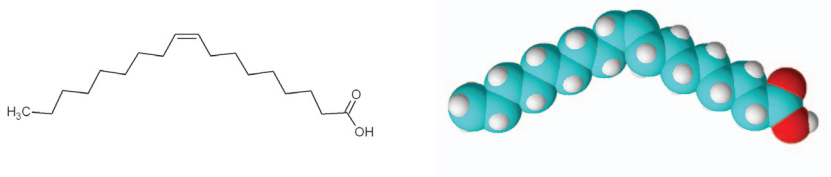

(a) Molecular formula of oleic acid.

(b) Geometric representation of the oleic acid molecule. Carbon, hydrogen, and oxygen atoms are represented as balls in cyan, white, and red, respectively.

Figure 5.1.4.: Oleic acid.

In Figure 5.1.4, the oleic acid molecule is represented in the conformation of maximal elongation. In order to estimate the maximal thickness of an oleic acid shell around nanoparticles, the distance between the carboxylic group and the final methyl group is determined. The length of an unbranched, linear hydrocarbon with n_c carbon atoms is given by [110]

$$l(n_c) = 0.15 + 0.127 \cdot n_c \quad \text{nm} \tag{5.1.2}$$

where 0.15 nm are calculated for each terminal methyl group. For the two linear parts of the oleic acid molecule the chain lengths of l_1 = 1.293 nm and l_2 = 1.016 nm are derived. With the included angle of 130.5°, a maximal head to tail distance of 2.1 nm is calculated.

Determination of excess oleic acid The excess amounts of oleic acid in the Hyeon group nanoparticle samples were determined by elementary analysis of the iron content in the samples and calculation of the amount of oleic acid in the particle shell. For an iron oxide sample of an assumed composition of Fe_2O_3 with a given mass percentage of iron m(Fe), the mass percentage of oxygen m(O) is calculated by

$$m(\mathrm{O}) = \frac{3 \cdot M(\mathrm{O})}{2 \cdot M(\mathrm{Fe})} \cdot m(\mathrm{Fe}) \tag{5.1.3}$$

with M(O) and M(Fe) being the molar mass of oxygen and iron, respectively. For the remaining part of the sample, which is the mass percentage of oleic acid, the oleic acid bound in the particle shell and the free excess oleic acid must be distinguished. The

amount of oleic acid in the particle shell is determined via the particle volumes. The mass ratio of the particle shell with thickness dR_{shell} and core R_{core} is given by

$$\frac{m_{shell}}{m_{core}} = \frac{V_{shell} \cdot \rho_{shell}}{V_{core} \cdot \rho_{core}} = \left[\left(1 + \frac{dR_{shell}}{R_{core}} \right)^3 - 1 \right] \cdot \frac{\rho_{shell}}{\rho_{core}} \tag{5.1.4}$$

Table 5.1.1 gives the mass percentage of iron as obtained by elementary analysis and the mass percentages of oxygen and bound and excess oleic acid for the respective samples as calculated by the above equations. The mass densities of the iron oxide particle core $\rho_{Fe_2O_3}$=5.19 g/cm^3 and the oleic acid shell ρ_{OA}=0.895 g/cm^3 were used along with the respective core radius as determined by SAXS and an average shell thickness of 16.5 Å.

Table 5.1.1.: Composition of the iron oxide nanoparticle samples.

sample	Fe [%]	O [%]	OA [%]	OA_{shell} [%]	OA_{excess} [%]
Hs 4	35.5	15.3	49.2	31.3	17.9
Hs 12	57.4	24.7	17.9	12.4	5.6
Hs 20	30.1	12.9	57.0	4.4	52.5
Hs 25	55.8	24.0	20.2	5.5	14.7

Oleic acid particle number density The number density of oleic acid micelles observed by SANS can be related to the refined scale factor I_0:

$$\frac{d\sigma(Q)}{d\Omega} = I_0 \cdot P(Q) \tag{5.1.5}$$

where *P(Q)* is the form factor of a sphere (see equation (2.2.23)). Comparison with equation (2.2.20) leads to

$$n_{OA} = \frac{I_0}{\Delta\varphi^2 V^2} = I_0 \cdot 9.27 \cdot 10^{17} \text{cm}^{-3} \tag{5.1.6}$$

with $\Delta\varphi = 5.141 \cdot 10^{10}$ cm^{-2} the scattering contrast for oleic acid in d_8-toluene and V = 2.02 $\cdot 10^{-20}$ cm^3 the micelle volume.

5.1.2.3. Development of the cubic form factors

Cubic form factor The definition of the form factor of a rectangular parallelepipedon is given by Pedersen [18][1]. The scattering amplitude for a given scattering vector $\vec{Q}$ of an oriented perfect cube of edge length a is given by

$$F_c(Q_x, Q_y, Q_z) = \frac{8}{a^3 Q_x Q_y Q_z} \cdot \sin\frac{a}{2}Q_x \sin\frac{a}{2}Q_y \sin\frac{a}{2}Q_z \tag{5.1.7}$$

The correct form factor of a perfect nanocube is thus given by conversion to polar coordinates and rotational averaging of the squared scattering amplitude

$$FF_c(Q) = \int_0^{\pi/2}\int_0^{\pi/2}\left[\frac{\sin(\frac{a}{2}Q\sin\theta\sin\phi)}{\frac{a}{2}Q\sin\theta\sin\phi}\frac{\sin(\frac{a}{2}Q\sin\theta\cos\phi)}{\frac{a}{2}Q\sin\theta\cos\phi}\frac{\sin(\frac{a}{2}Q\cos\theta)}{\frac{a}{2}Q\cos\theta}\right]^2 \sin(\theta)\mathrm{d}\theta\mathrm{d}\phi \tag{5.1.8}$$

Due to the cubic symmetry, it is sufficient to integrate over one octant of the cube instead of the full range. For this reason the integrals in equation (5.1.8) range from 0 to $\pi/2$ for both θ and ϕ.

Truncated cubic form factor The form factor of a truncated nanocube can be derived in an approach similar to the one used by Hendricks, Schelten, and Schmatz for the description of truncated octahedra [112]. In a geometric representation (Figure 5.1.5a), the truncated octahedron is separated into 8 octants of a perfect octahedron showing truncation at three tips. For calculation of the scattering amplitude, the scattering amplitude for the first octant of an untruncated octahedron is used with subtraction of the contribution of the truncated parts. The truncated parts are geometrically similar to the complete octant and have the same orientation, but are homothetically reduced and shifted by a given vector. For the complete truncated octahedron, the amplitudes are summed for all octants and the orientational average is performed on the scattering intensity.

The geometrical representation of a truncated nanocube is depicted in Figure 5.1.5b. The truncated corners of the cube with edge length a can be described by the octants of

[1] It has to be mentioned that the orientational average has to be applied to the intensity of the scattering function instead of the amplitude of the form factor, in contrast to what is reported by Pedersen [18], as can be found in the original publication on the form factors of parallelepipedons by Mittelbach and Porod [111].

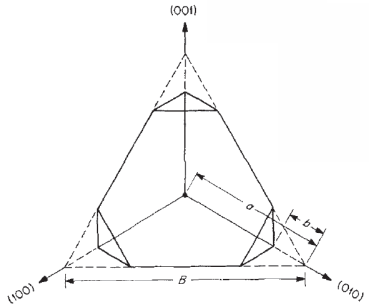

(a) Geometric representation of a truncated octahedron. Figure from [112]

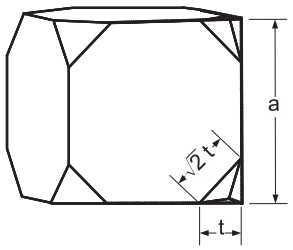

(b) Geometric representation of a truncated cube.

Figure 5.1.5.: Geometric representations of truncated polyhedra.

an octahedron with edge length $\sqrt{2} \cdot t$ that are inverted and shifted by $\sqrt{3} \cdot 1/2a$ in the (111) directions.

The scattering amplitude for the first octant of an untruncated octahedron with edge length $\sqrt{2} \cdot t$ is given by [112]

$$F_o^1(Q_x, Q_y, Q_z) = i[\frac{\exp(itQ_x)}{Q_x(Q_x - Q_y)(Q_x - Q_z)} + \frac{\exp(itQ_y)}{Q_y(Q_y - Q_x)(Q_y - Q_z)} + \frac{\exp(itQ_z)}{Q_z(Q_z - Q_x)(Q_z - Q_y)} - \frac{1}{Q_x Q_y Q_z}] \tag{5.1.9}$$

The scattering amplitude of the truncated nanocube can then be derived by taking into account all the eight translated truncated corners with the appropriate symmetry operations resulting in

$$
\begin{aligned}
F_{tc}(Q_x, Q_y, Q_z) = F_c(Q_x, Q_y, Q_z) - [&F_o(-Q_x, -Q_y, -Q_z) \cdot \exp(i\frac{a}{2}(Q_x + Q_y + Q_z)) \\
&+ F_o(-Q_x, Q_y, -Q_z) \cdot \exp(i\frac{a}{2}(Q_x - Q_y + Q_z)) \\
&+ F_o(-Q_x, -Q_y, Q_z) \cdot \exp(i\frac{a}{2}(Q_x + Q_y - Q_z)) \\
&+ F_o(Q_x, -Q_y, -Q_z) \cdot \exp(i\frac{a}{2}(-Q_x + Q_y + Q_z)) \\
&+ F_o(-Q_x, Q_y, Q_z) \cdot \exp(i\frac{a}{2}(Q_x - Q_y - Q_z)) \\
&+ F_o(Q_x, Q_y, -Q_z) \cdot \exp(i\frac{a}{2}(-Q_x - Q_y + Q_z)) \\
&+ F_o(Q_x, -Q_y, Q_z) \cdot \exp(i\frac{a}{2}(-Q_x + Q_y - Q_z)) \\
&+ F_o(Q_x, Q_y, Q_z) \cdot \exp(i\frac{a}{2}(-Q_x - Q_y - Q_z))]
\end{aligned}
\tag{5.1.10}
$$

where the exponential terms account for the linear shift of the inverted octahedral octants and the scattering amplitude of the perfect cube is given in eq. 5.1.7. As a last step, the orientational average is performed on the intensity of the truncated nanocube in the same way as for the perfect nanocube (eq. 5.1.8). For refinement of the collected small-angle scattering data, the derived form factor was furthermore convoluted with a lognormal distribution of the edge length a (see section 2.2.2 for implementation of the size distribution). The code of the resulting form factor is given in Appendix D.1[2].

Figure 5.1.6 presents simulated small-angle scattering curves for truncated nanocubes with a varying degree of truncation

$$\tau = t \cdot a \tag{5.1.11}$$

The cubic edge length is $a = 9$ nm for $\tau = 0$. With increasing τ the edge length is adjusted in order to maintain a constant particle volume. The distance between the form factor minima of the truncated cubic form factors decreases with increasing degree of truncation. For the maximal possible degree of truncation of $\tau = 0.5$ the distance between the minima is comparable to the spherical form factor. Considering the position of the first form factor minimum, a spherical form factor of a somewhat larger particle volume will be hard to distinguish from the heavily truncated cubic form factor. The refinement of a truncated cubic form factor is thus feasible for the lower degrees of truncation up to $\tau = 0.3$.

[2]The codes for the truncated cubic form factors were written by Denis Korolkov, JCNS, Garching, Germany.

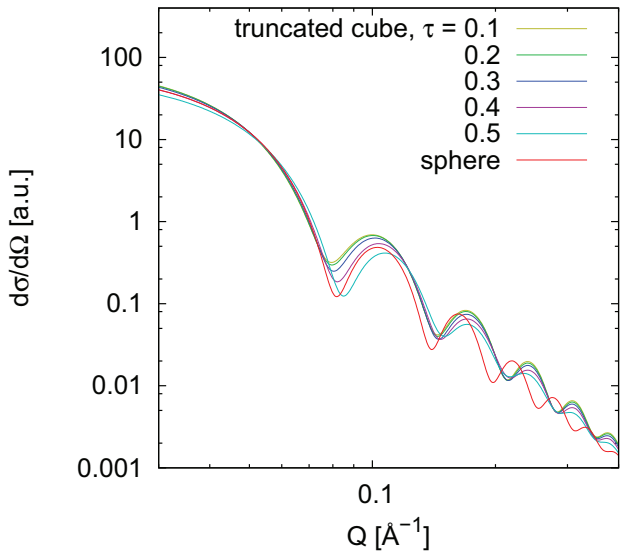

Figure 5.1.6.: Comparison of truncated cubic form factors. Form factors for an increasing degree of truncation are presented along with a spherical form factor. Cubic edge length and spherical radius are chosen to maintain a constant particle volume of 729 nm^3 for all shown form factors.

Truncated cubic core shell form factors For SANS data analysis, core shell form factors of the truncated nanocube taking into account the organic ligand shell were developed. The organic ligand shell can be assumed to result in an either truncated cubic or spherical outer shape of the particle as depicted in Figure 5.1.7.

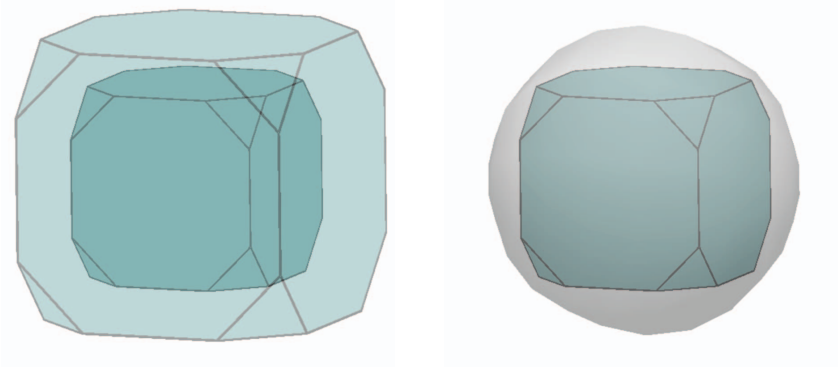

(a) Geometric representation of a truncated cubic core shell particle.

(b) Geometric representation of a truncated cube with a spherical shell.

Figure 5.1.7.: Geometric representations of truncated nanocube core shell particles.

Both core shell form factors were modelled by linear combination of the truncated cubic scattering amplitude with the respective shell amplitudes weighted by their contrasts and volumes as discussed in section 2.2.2. Rotational averaging of the scattering intensity was performed as described for the cubic form factor, and size distribution was implemented for the cubic edge length. Instrumental resolution was implemented as discussed in section 2.2.2. The codes for both form factors are given in Appendices D.2 and D.3.

5.1.3. Results and Discussion

5.1.3.1. SAXS: size and size distribution

For a precise determination of the size and size distribution of the inorganic nanoparticle core, the Small-Angle X-ray Scattering by dilute nanoparticle dispersions in toluene was investigated at the JUSIFA beamline at HASYLAB, DESY (3.1.1). For the Bc 9 batch, two different samples were investigated by SAXS: Bc 9a, which had been stored in dispersion, and Bc 9b, which had been received in powder form and was dispersed in

toluene for the measurement. The data was reduced and normalized to absolute values and is presented in Figure 5.1.8.

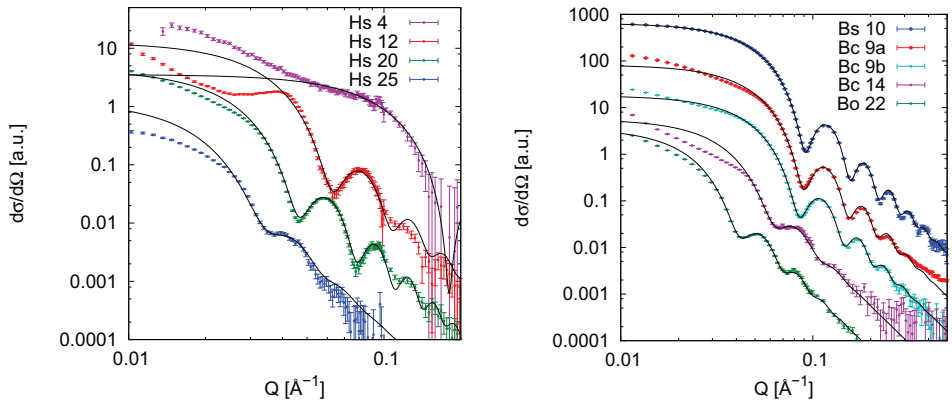

(a) SAXS by nanoparticles of different sizes

(b) SAXS by nanoparticles of different shapes

Figure 5.1.8.: Small-Angle X-ray Scattering by iron oxide nanoparticles. The two measurements of Bc 9 samples denote a) a sample received and stored in dispersion and b) a sample stored in powder form, dispersed in toluene for the SAXS measurement. Intensities have been scaled for display. Refinements of spherical form factors are presented by solid lines.

Most of the scattering curves exhibit several (up to six) form factor oscillations, which is indicative of a reasonably narrow size distribution. Indeed, the refined particle size distributions for most of the samples are close to 6 %, which is in agreement with earlier reports based on electron microscopy techniques [99]. Note that the extremely narrow size distribution of some samples requires the instrumental resolution to be taken into account for a proper refinement, although this is usually negligible for synchrotron experiments. Because the Q resolution is correlated with the particle size distribution, it had to be determined *a priori* from the instrumental set up and to be fixed during refinement.

The desired information on size and size distribution is expressed by the position and smearing-out of the form factor minima. Since these are generally not affected by any structure factors, structure factors appearing in the lower Q range have been neglected in a first approximation. This approach is particularly illustrated by the Hs 12 sample (Figure 5.1.8a). Due to a capillary leakage, the nanoparticle dispersion had dried during

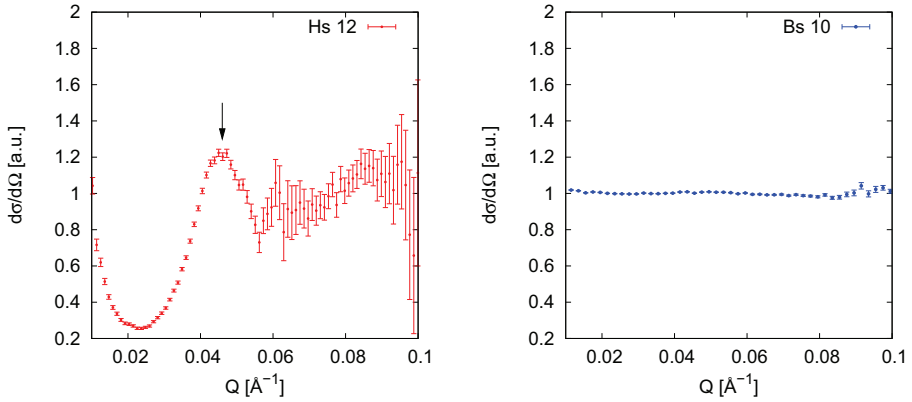

(a) structure factor of an agglomerated nanoparticle sample

(b) structure factor of a well dispersed nanoparticle sample

Figure 5.1.9.: Structure factors for Hs12 and Bs10 as derived by division of the measured data by the refined form factors.

the measurement, leaving a solid sample of aggregated nanoparticles. This soft agglomeration leads to a large structure factor in the lower Q range (Figure 5.1.9a). Nonetheless, several minima of the form factor are still visible in the higher Q range, allowing for a refinement of the particle size and size distribution. The separated structure factor presented in Figure 5.1.9a resembles that of a hard spheres potential between the particles. Its maximum at Q = 0.045 (1) Å^{-1} corresponds to a real space distance of 140 (2) Å between the particle centers, which indeed indicates strong agglomeration if compared to the determined particle radius. The Bs 10 sample, on the other hand, exhibits a perfect form factor behavior, showing no structure factor at all (Figure 5.1.9b), which illustrates the quality of this nanoparticle dispersion. Results of the form factor refinements for all measured samples are listed in Table 5.1.2 on page 159. The respective particle sizes have been determined with good accuracy even for those samples with wider size dispersion as expressed by the narrow error bars.

The non-spherical nanoparticles were first refined using a spherical form factor, which is a common approximation of an orientationally averaged cube or octahedron. Depending on the size distribution, the different form factors may not be distinguished at all. For the very monodisperse sample Bc 9 however, exhibiting as much as four oscillations, the form factor of a truncated nanocube was modelled in order to possibly determine the exact edge length along with the truncation of the cube's corners as ob-

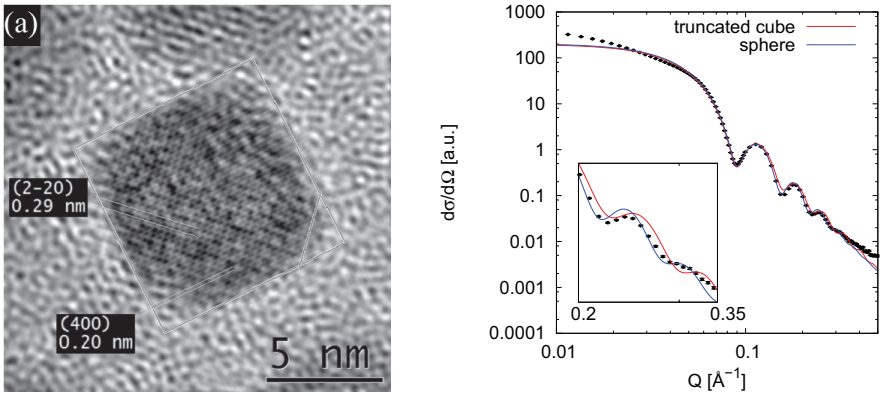

(a) HRTEM of a single iron oxide nanocube. Truncation of the corners is shown [106].

(b) SAXS by iron oxide nanocubes Bc 9 refined with truncated cubic and spherical form factors. Refinement with the truncated cubic form factor lead to a_0 = 84.9 (2) Å with b = 0.5·a_0 = 42.45 Å. The inset covers a range of 0.2 Å^{-1} ≤ q ≤ 0.35 Å^{-1}.

Figure 5.1.10.: SAXS by iron oxide nanocubes.

served by HRTEM [106] (Figure 5.1.10a; see section 5.1.2.3 for the development of the truncated cubic form factor). Figure 5.1.10b compares the spherical and the truncated cubic form factor as refined to the nanocubes sample Bc 9. The truncated cubic form factor could only be refined with the degree of truncation b of the nanocubes set to the maximal possible truncation of $0.5 \cdot a_0$ (a_0 = edge length), representing a cuboctahedron rather than a cube. While both the spherical and the cubic form factors represent a large part of the data, neither of them seems to fit entirely, particularly to the smaller oscillations in the wider Q range (as shown in the inset of Figure 5.1.10b). Here, both form factors mismatch in different directions, suggesting an average of them to match the data better. It has to be noted that the quality of the refinements is far from a good fit for both form factors, as expressed by the reduced χ^2. The large χ^2 values may be partially due to the deviation between fit and data in the low Q range, where the onset of a structure factor is visible. The quality of the spherical form factor refinement is considered better with a reduced χ^2 of 164 as compared to 617 for the truncated nanocube. Since with SAXS an ensemble average of the form factor is measured, it is thus suggested that the degree of truncation might be different for different particles and even at different cube edges of the same particle, giving rise to an effective form factor between that of a cuboctahedron and a sphere. The HRTEM image in Figure 5.1.10a suggests also a rounded truncation instead of flat crystal facets.

Nonetheless, the cubic shape of the Bc 9 sample leads to a significantly different behavior as compared to the nanospheres (Bs 10) when arranged in a higher dimensional superlattice, owing to its cubic symmetry (as will be discussed in section 5.4.3).

5.1.3.2. SANS: core shell structure

Small-Angle Neutron Scattering was performed at the KWS 2 (JCNS) (3.1.4) and D 22 (ILL) (3.1.5) instruments in order to determine the thickness of the oleic acid ligand layer around the core particle. This is possible due to the probe dependent scattering contrast variation. Because the electron density difference between the organic ligand shell and the toluene matrix is low, X-rays mainly probe the large contrast between the inorganic nanoparticle core and the organic surroundings. For neutrons, the contrast between the non-deuterated oleic acid and the deuterated toluene is much higher and allows for determination of the entire core shell morphology, in particular if the core size is previously determined by X-ray scattering. Refinement of the normalized and radially averaged SANS data was thus performed with a core shell form factor. The inner core radius and its size dispersion are confined to the respective sample and independent on the probe, so that the parameters derived from SAXS can be applied as starting values or even fixed for the SANS refinement. Since neutron scattering length densities are tabulated [12], the fit parameters were in this case the shell thickness and the Q resolution parameters, whereas the latter are in principle technically fixed and well-known for each instrumental configuration.

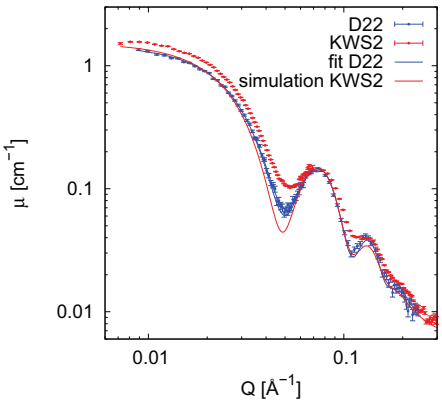

Figure 5.1.11.: Small-Angle Neutron Scattering by Bs 10 at KWS 2 and D 22.

Figure 5.1.11 shows the Small-Angle Neutron Scattering by Bs 10 as measured at D 22 and KWS 2. The larger smearing of the experimental KWS 2 data is intuitively understood with respect to the larger wavelength spread (20 % for KWS 2 and 10 % for D 22). For the refinement of the D 22 data (shown in blue), the Q resolution as obtained by equation (2.2.35) was implemented, and the particle size distribution was used as obtained from SAXS. Note that the smearing of the form factor minima is described very well by the instrumental resolution in combination with the known particle size distribution, thus proving their correct determination. The shown refinement results in a core radius of 48.5(1) Å, which is in agreement to the value obtained by SAXS, and a shell thickness of 16.2(1) Å.

The simulation of the KWS 2 data with all the parameters as refined with the D 22 data, but with implementation of the instrumental resolution of KWS 2 as calculated by use of equation (2.2.35), is shown as red line in Figure 5.1.11. As the smearing of this theoretical scattering curve is deviating strongly from the experimental data, either the Q resolution or the size distribution have to be corrected to represent the data. Because the latter was determined with good accuracy by SAXS and is proven by the D 22 measurement, the Q resolution is the parameter to be adjusted. This is also suggested by the sharper simulated KWS 2 scattering curve as compared to the experimental D 22 data despite the larger wavelength spread at KWS 2. For this reason the Q resolution of KWS 2 was refined for all data sets, while the size distributions were fixed to the values obtained from SAXS. With the wavelength spread of KWS 2 of ~ 20%, the angular divergence contribution to the Q resolution was refined individually for both measured detector distances.

The SANS data sets presented in Figure 5.1.12a have been refined to the core shell model via R_{core}, R_{shell}, and the angular resolution parameter $d\theta$. The deviation between the observed and calculated scattering curves at higher Q particularly for Hs 20 suggests the presence of excess oleic acid forming small reverse micelles in toluene. Analysis of the difference curve of the Hs 20 refinement (Figure 5.1.13) by refinement of a spherical form factor leads to a micellar radius of 16.9 (7) Å. This micelle size is in rough agreement with the shell thickness determined by refinement of the core shell form factor. The maximal length of an elongated oleic acid molecule can be estimated to 21 Å (see section 5.1.2.2). The much smaller values for micelle size and shell thickness determined here can be explained in two ways. First, the oleic acid does not necessarily have to be elongated, and some degree of coiling can be expected for this long chained hydrocarbon, leading to a smaller nanoparticle shell thickness. Secondly, and more likely in case

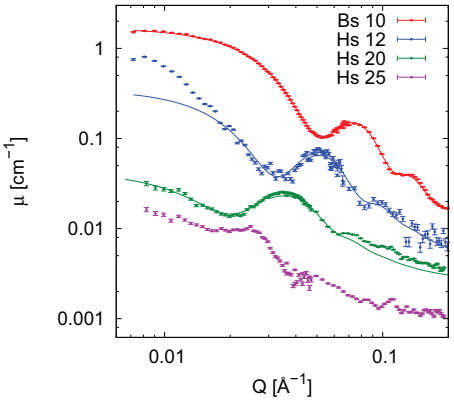

(a) Refinement of a core shell model.

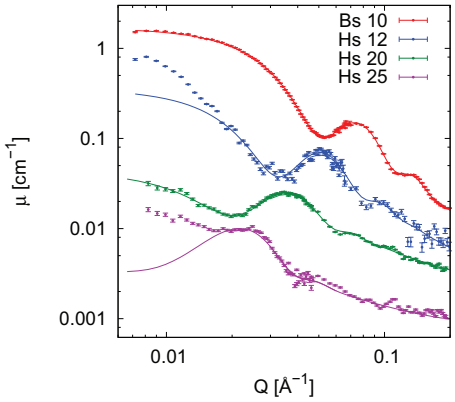

(b) Refinement of a core shell model including excess oleic acid micelles. For Hs 25 a simulation is shown.

Figure 5.1.12.: Small-Angle Neutron Scattering by iron oxide nanoparticles. Intensities have been scaled for display.

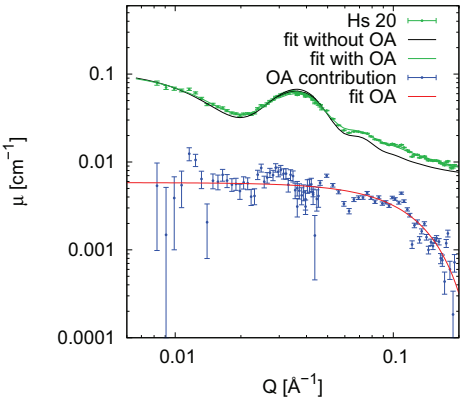

Figure 5.1.13.: Determination of the oleic acid contribution.

of dispersed particles such as discussed here, some of the solvent may penetrate into the ligand layer, leading to a decrease in shell contrast depending on the distance from the particle core. Refinement of a straight core shell model thus underestimates the real shell thickness.

Table 5.1.2.: Morphological characterization of iron oxide nanoparticles. Small-angle scattering results are given for the particle core radius R_{core}, the particle size distribution σ, the ligand shell thickness R_{shell}, the angular resolution parameters $d\theta$, and the particle number density of excess oleic acid micelles n_{OA}.

	SAXS		SANS				
sample	R_{core} [Å]	σ [%]	R_{core} [Å]	R_{shell} [Å]	$d\theta_{2m}$	$d\theta_{8m}$	n_{OA} [10^{15} cm^{-3}]
Hs 4	25.0 (4)	-[a]					
Hs 12	72.6 (2)	6.8 (4)	71.0 (7)	15.1 (6)	0.007 (1)	0.0053 (4)	0.6 (5)
Hs 20	99.7 (3)	4.7 (4)	98.3 (5)	15.3 (2)	0.0057 (3)	0.0050 (2)	5.4 (5)
Hs 25[b]	138.0 (1)	12.1 (6)	141	17	0.0027	0.0025	1.75
Bs 10	49.56 (2)	5.54 (7)	48.9 (1)	16.0 (3)	0.0079 (4)	0.0074 (1)	53 (2)
Bc 9a[c]	50.60 (6)	6.6 (1)	49.3 (1)	15.1 (1)	0.0058 (1)	0.0063 (1)	0
Bc 9b[d]	53.25 (7)	7.2 (2)					
Bc 14	72.4 (3)	12.2 (4)					
Bo 22	112.4 (2)	8.8 (2)					

[a] size distribution could not be determined due to the lack of a form factor minimum in the measured momentum range
[b] SANS parameters for this sample were derived by simulation
[c] sample had been stored in dispersion
[d] sample had been stored in powder form

Introduction of a variable amount of oleic acid micelles into the core shell model refinements leads to the results presented in Figure 5.1.12b and the refined parameters shown in Table 5.1.2. Note that the refined R_{core} values are close to the values obtained from SAXS, which proves the consistency of the refinements. The Hs 25 data set did not allow for a successful refinement due to the poor data quality and large size distribution. Therefore, Figure 5.1.12b presents only a simulation for this sample. The number densities of oleic acid micelles given in Table 5.1.2 were calculated using equation (5.1.6). After normalization to the sample masses used for these measurements, the micelle number densities of oleic acid in the samples Hs 12, Hs 20, and Hs 25 follow the ratio 1:9.4:3.0. Even though the error on this ratio is quite large, it is in good agreement with the 1:9.4:2.6 ratio of excess oleic acid in the respective samples as determined

by elementary analysis (see 5.1.2.2 for the determination of excess oleic acid) and thus justifies the implementation of this additional phase during refinement.

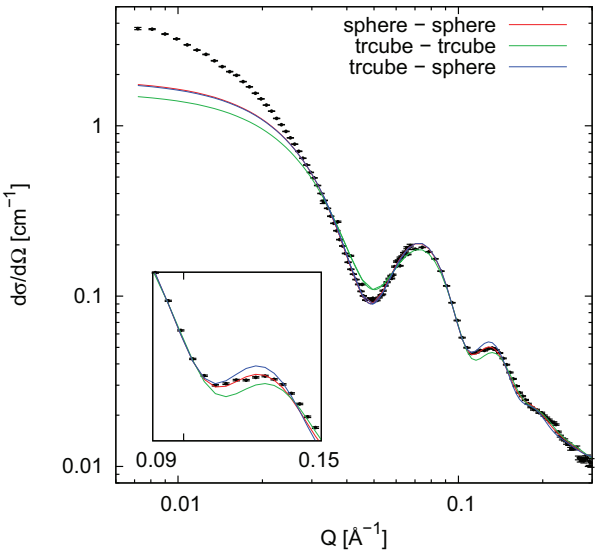

Figure 5.1.14.: SANS by truncated nanocubes. Refinements with a sphere core shell (red line), a truncated cubic core shell (green line), and a truncated cubic core - spherical shell (blue) form factor are shown.The inset covers a range of 0.09 Å^{-1} ≤ Q ≤ 0.15 Å^{-1}.

The different storage of the two Bc 9 samples may have had an influence on the particle size and/or shape as expressed by the different SAXS results. The larger size (refined by a spherical form factor) and wider size distribution can be speculated to result from a lower degree of truncation of the nanocubes stored in powder form (Bc 9b). As the Bc 9 sample for SANS was prepared freshly for the experiment and not stored for long, its structural parameters may be expected to be close to those of Bc 9b. However, the particle core radius determined by SANS is closer to that of Bc 9a. A more precise determination of the purely nuclear SANS of this sample will be given in section 5.3. The SANS data for the truncated cubic nanoparticles Bc 9 was refined by both spherical and cubic form factors as presented in Figure 5.1.14. Two different shell geometries for the truncated nanocubes were considered, namely either a truncated cubic shell or a spherical shell around the otherwise truncated cubic core (see section 5.1.2.3 for the development of the applied core shell form factors). The most precise description of a truncated cube with an organic shell of uniform thickness requires a truncated cubic shell. Refinement of the data with this core shell form factor however leads to a poor reduced χ^2 of 439. Refined parameters for this model include the cubic edge length of

a_0 = 85(2) Å, the size distribution of the edge length σ = 0.003(2), and the uniform shell thickness da_0 = 11.8(4) Å, whereas the degree of truncation $\tau = t/a_0$ was fixed to its maximal possible value of 0.5. The fact that size distribution as well as shell thickness as refined here are exceptionally low as compared to SAXS and SANS results of this and the remaining samples along with the large reduced χ^2 leads to the conclusion that the model of a truncated cube with a truncated cubic shell does not represent the sample sufficiently.

The model with a spherical organic ligand shell around the truncated nanocubes appears more realistic for the present case of iron oxide nanocubes dispersed in a solvent. The shell thickness at the truncated (111) facets of the nanocubes can be considered thinner than at its (100) facets due to the lower surface coverage of oleic acid on these surfaces. This can be explained by the atomic structure of the spinel facets. While the (100) facets of the spinel structure consist of mixed iron and oxygen layers, where oleic acid can bind, the (111) facets are terminated by either iron-only or oxygen-only layers, where coordination of oleic acid is suppressed. In addition, the oleic acid molecules connected to the iron oxide core are not rigid, but somewhat flexible. Especially in solution, they will smear out the truncated cubic shape of the core to a more spherical one at the shell surface. Refined parameters in this model include the edge length a_0 = 87.0(3) Å, the size distribution of the edge length σ = 0.053(4), and the radius of the surrounding spherical shell R = 65.2(2) Å. The degree of truncation was again fixed to τ = 0.5. The size of the surrounding shell leads to maximal shell thicknesses of 15 Å at the (111) facets and 21 Å at the (100) facets which is in agreement with shell thicknesses determined for spherical particles. However, if compared by their reduced χ^2 values, the refinement by the spherical core shell model (χ^2_{red} = 90) still represents the data better than the truncated nanocube with a spherical shell (χ^2_{red} = 119). This is in agreement with the SAXS results for this sample, and the parameters obtained with the spherical model are given in Table 5.1.2. However, because the parameters obtained for both models (*e.g.* the outer shell radius) are in good agreement, the cubic edge length determined here can be considered realistic.

Finally, the obtained angular resolution values (Table 5.1.2) are in the range of 5 to 8 mrad and thus larger than those calculated from the instrument geometry using equation (2.2.35). This may originate in instrumental difficulties that could in principle have led to a larger entrance aperture which was not recorded in any logfile. The origin of the variation of the angular resolution values for the different measurements is unclear, and a variation in entrance apertures due to electronic noise may only be speculated. However, because neither Q resolution nor size distribution are correlated to the shell thickness and the size distribution is accessible by SAXS in high precision, the core shell

structure has been determined by a combination of SAXS and SANS in good accuracy.

5.1.3.3. Magnetization measurements

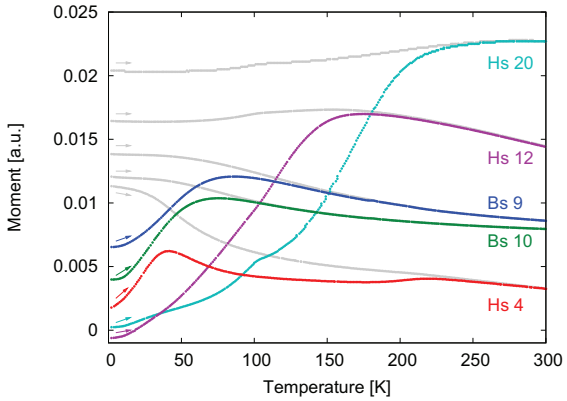

Figure 5.1.15.: Magnetization measurements of iron oxide nanoparticles in a field of 5 mT. ZFC measurements are displayed for Hs 4, Bs 10, Bc 9, Hs 12, and Hs 20. The respective FC measurements are shown as grey lines. The data sets for the different samples have been scaled and offset for display.

Figure 5.1.15 shows the temperature dependent magnetization of iron oxide nanoparticles as measured after cooling in either an applied field of 5 mT or in zero field. The blocking temperatures, obtained from the maxima in the zero field cooled curves, increase with increasing particle size as expected. For an experimental measuring time in the range of few seconds, an approximative relation between particle volume V and blocking temperature T_B is derived from equation (2.1.6)

$$KV \approx 25 \cdot k_B T_B \tag{5.1.12}$$

where k_B denotes the Boltzmann constant and K the magnetic anisotropy constant. As shown in Figure 5.1.16a, the relation between the particle volume and blocking temperature is not linear which indicates a particle size dependence of the magnetic anisotropy as presented in Figure 5.1.16b. The found values for the magnetic anisotropy are in agreement with earlier reports on the same samples [99], and the linear dependence on the particle size for particle diameters larger than 5 nm has also been reported [103]. The extraordinarily high value for the Hs 4 sample of $20 \cdot 10^4$ J/m^3 does not fit into the linear size dependence, but is in agreement with earlier reports [99] and results from

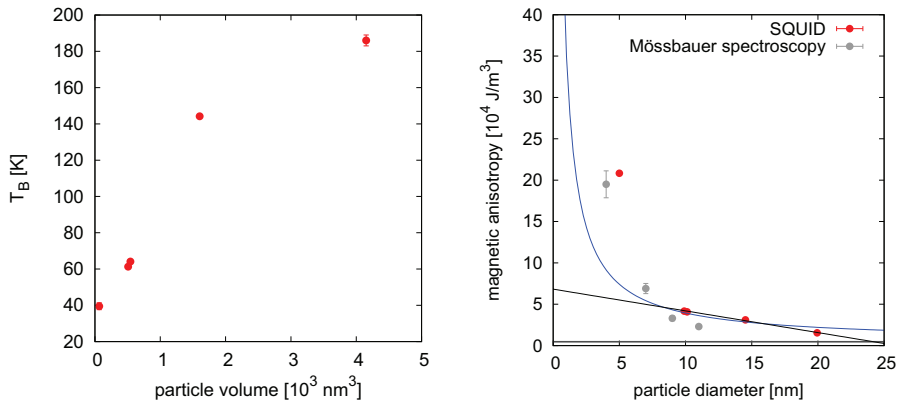

(a) Particle volume as a function of the blocking temperature.

(b) Magnetic anisotropy as a function of the particle diameter. The magnetocrystalline anisotropy of bulk maghemite is shown as horizontal line. A linear size dependence (black line) as well as a dependence on the surface to volume ratio (blue line) of the magnetic anisotropy are presented. Mössbauer data are taken from [103].

Figure 5.1.16.: Blocking temperatures and magnetic anisotropy of iron oxide nanoparticles as determined by SQUID measurements. Particle volumes and diameters were determined from SAXS.

Mössbauer spectroscopy [103]. The magnetic anisotropy can be separated into volume and surface dependent terms according to

$$K = K_v + K_s \cdot \frac{6}{D} \tag{5.1.13}$$

where D denotes the particle diameter and K_v and K_s are the volume and surface anisotropies, respectively. With a bulk maghemite volume anisotropy of $0.47 \cdot 10^4$ J/m^3 [103], a surface anisotropy of 5.8 (4) $\cdot 10^{-5}$ J/m^2 is obtained from the fit presented in Figure 5.1.16b (blue line). This value is in agreement with the range of surface anisotropies of $2 \cdot 10^{-5} \leq K_s \leq 6 \cdot 10^{-5}$ J/m^2 reported previously [113, 114]. However, the magnetic anisotropies of nanoparticles smaller than 6 nm in diameter are still not well represented by the fit. As the magnetic anisotropy is very sensitive to the particle size in this particle size range, the discrepancy may result from a significant magnetic dead layer at the particle surface. The number of collected data points is, however, not sufficient for a more precise determination of the particle size dependence of the magnetic anisotropy in the lower size range.

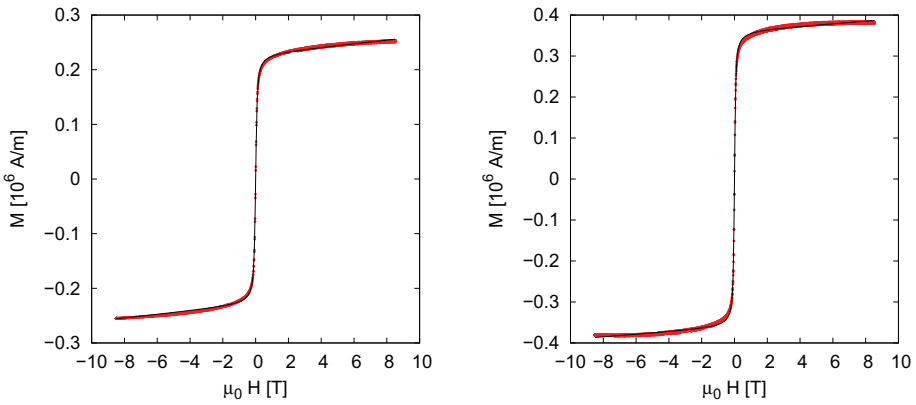

(a) Hysteresis of Bs 10.

(b) Hysteresis of Bc 9.

Figure 5.1.17.: Field dependent magnetization measurements.

Figure 5.1.17 shows field dependent magnetic measurements of the spherical Bs 10 and the cubic Bc 9 nanoparticles. The data were fitted with the Langevin equation

$$M = M_S[coth(\mu\mu_0 H/k_B T) - (k_B T/\mu\mu_0 H)] + \chi\mu_0 H \tag{5.1.14}$$

where M_S denotes the saturation magnetization, μ the integral particle moment, k_B the Boltzmann constant, T the temperature, and μ_0H the applied magnetic field. Because no diamagnetic correction was performed on these measurements, the phenomenological term $\chi\mu_0$H was included to account for the observed excess constant susceptibility χ at high magnetic fields. The magnetic volume of the particles was determined according to

$$\mu = M_S V_{mag} \tag{5.1.15}$$

For the spherical nanoparticles Bs 10, a magnetic volume of 479 (4) nm^3 was obtained, which is equivalent to a particle radius of 4.85 nm and in good agreement with results from SANS. If compared to the particle radius determined by SAXS of 4.95 nm, the observed difference might be attributed to a magnetically dead layer at the particle surface of ~ 0.1 nm thickness. The magnetic volume of the nanocubes Bc 9 was determined to be 380 nm^3, which would correspond to an edge length of 7.24 nm for a perfect cube or an edge length of 7.7 nm for a cube with maximal truncation (of $0.5 \cdot a_0$).

The difference to the edge length determined by SAXS of 8.5 nm might be attributed to a magnetically dead layer at the particle surface of ~ 0.4 nm thickness. Because this

would be an extraordinarily thick dead layer as compared to the nanospheres, it is rather assumed that the difference arises from uncertainties in sample preparation.

The constant increase of magnetic moment at high applied fields has not been corrected for diamagnetic contributions of substrate and sample holder and can thus only be discussed qualitatively. It is assumed to result from a gradual alignment of the surface spins in the particle. While the bulk spins of a ferromagnetic or ferrimagnetic material are aligned parallel or antiparallel with a net magnetic moment, respectively, for a ferro- or ferrimagnetic nanoparticle the spins of the surface atoms can be expected to be canted. Field dependent magnetization measurements on ferrofluids not only result in alignment of the ferromagnetic domains (the particles), but also, in much higher applied fields, in a gradual alignment of these surface spins. The complete saturation of all spins including a "decanting" of the surface spins requires an extremely high applied magnetic field that was not reached during the experiment.

5.1.4. Summary

The scope of this chapter was the introduction and morphological as well as magnetic characterization of iron oxide nanoparticles of different sizes and shapes. Particle sizes and size distributions have been determined in good accuracy by application of small-angle scattering, and results are displayed in Table 5.1.2. The obtained values for the oleic acid shell thickness are in good agreement for several samples and as compared to the oleic acid chain length. Magnetization measurements clearly show the particle size dependence of the blocking temperature, exhibiting a size dependent magnetic anisotropy.

The samples with the most narrow size distributions, and therefore most appropriate for further investigation of finite size effects, are Hs 12, Hs 20, Bs 10, and Bc 9. Particularly Bs 10 is remarkably well dispersed in toluene and thus qualifies as a suitable model system for investigations on the magnetization distribution within single particles using polarized small-angle neutron scattering (see section 5.3).

It is emphasized that the truncated nanocube morphology was not confirmed by SAXS nor SANS. Nonetheless, the cubic shape of the Bc 9 nanoparticles is clearly visible in TEM images and also expressed by the higher dimensional packing types of the nanocubes (see section 5.4.3). Thus, it may be concluded that either the resolution of the SAS experiments was not sufficient to resolve the correct form factor behavior, or the non-perfect truncation of the nanocubes resulted in SAS curves of a more spherical form factor.

5.2. Local Structure

5.2.1. Introduction

After the morphology, including nanoparticle size and size distribution, has been determined in the previous section, this section will focus on the atomic structure of the nanoparticles under study. A detailed investigation of the average and local atomic order is important for further investigations on the spin structure. First, the exact composition and oxidation state of the investigated nanoparticles is required. As mentioned in section 5.1.1, the iron oxide nanoparticles have the inverse spinel structure, which is observed for both magnetite (Fe_3O_4) and maghemite (γ-Fe_2O_3). The main structural difference between these compounds is the occupancy of the iron sites and the resulting different oxidation state, leading to a different saturation magnetization. Secondly, the nanometer size range may affect the nanoparticle structure, leading to deviations from the bulk crystal structure. Commonly observed is a decrease of the lattice constant, which has been related to surface stress [115]. A relaxation of bond lengths of surface atoms has been observed to induce internal strain by correlated atomic displacements [116, 117]. The influence of the nanoparticle surface on structural distortions is important as even surface chemical interactions were found to affect the interior disorder of ZnS nanoparticles, with a more crystalline nanoparticle structure for a more covalent surface termination [118]. These and further structural surface effects such as a reduced coordination number of the surface atoms [119] or vacancy order-disorder transitions [120] are expected to affect the magnetic properties. For these reasons, an analysis of the atomic structure is required before further investigations on the magnetic structure.

The most widely applied methods for investigation of atomic nanoparticle structures include analysis of the atomic Pair Distribution Function (PDF) and X-ray Absorption Spectroscopy (XAS) techniques. PDF analysis combines both Bragg and diffuse scattering and give thus information on both long range and local structural correlations. Information on the atomic structure of the nanoparticles including the degree of crystallinity, local bonding and the degree of internal disorder are thus achieved [116, 117]. Investigation of $LiFe_5O_8$ nanoparticles, which are isotypic to maghemite, revealed an order-disorder structural transition at elevated temperatures and a disordered shell region [121].

XAS techniques give element-specific information of local correlations, by identifying the electronic configuration of the probed atom and the geometry of its first coordination

spheres. By this technique more complex disorder phenomena such as surface texturing and bond relaxation are accessible [115]. More specifically, the compositions of iron - iron oxide core shell nanoparticles were investigated, revealing a maghemite surface layer with a magnetite layer underneath depending on the particle size [122].

Previous investigations of the atomic structure of the nanoparticle samples under study include XAS and Mössbauer spectroscopy. For the Hs nanoparticle samples, both XAS and XMCD experiments indicated a transition of a pure maghemite to magnetite with increasing nanoparticle size [99, 109]. Due to the higher oxidation state of maghemite, a core shell structure consisting of a magnetite core with a maghemite shell is likely. In contrast, Mössbauer spectroscopy measurements revealed that the nanoparticles predominantly consist of maghemite [101], and magnetite contributions were found not to exceed 5-10 % even for the largest nanoparticles [103].

The subject of this chapter will be a detailed structural analysis of the nanoparticles at the atomic scale with the aims of determining their structure type and composition as well as revealing possible local structural deviations due to surface stress. X-ray diffraction will be analyzed in both reciprocal and real space. The average long range crystal structure will be determined in reciprocal space, by Rietveld analysis of the Bragg intensities. By analysis of the PDF in real space, local structural details deviating from the long range structure will become accessible. For more detailed investigation on the Fe oxidation state and the geometry of the first coordination shells, XANES and EXAFS will be applied.

5.2.2. Methods

5.2.2.1. Wide Angle Scattering

For high-energy X-ray scattering experiments, only dried iron oxide nanoparticle samples were investigated. Nanoparticle powders of the Hs sample series and the Bc 9, Bc 14, and Bo 22 samples introduced in chapter 5.1 were filled into flat plate powder sample holders of 1 mm sample thickness and fixed with kapton tape windows.

Diffraction experiments were carried out at the MuCAT beamline 6-ID-D (3.3.1) at APS, Argonne. Data were collected at room temperature using a high incident energy of 99.88 keV, corresponding to an X-ray wavelength of 0.124269 Å. In order to achieve a good angular resolution for investigation of the powder diffraction as well as a wide Q range as required for PDF analysis, two different sample detector distances of 1601.14 and 245.7 mm were utilized for the two different evaluation techniques. An image plate

camera (Mar345) was used as detector, and its precise orientation and distance to the sample were determined using a silicon standard sample. For the short sample detector distance, an additional nickel reference was measured in order to determine the instrumental resolution. Measured data were integrated radially and converted to 2θ space (with 2θ the scattering angle) using the program Fit2D [123].

5.2.2.1.1. Diffraction The data collected at large sample detector distance and exhibiting a better angular resolution were refined using the GSAS program package [14]. For all refinements, a modified [124] pseudo-Voigt profile function according to Thompson, Cox, and Hastings was applied [125].

The magnetite reference sample was refined according to the Rietveld method [126]. For a constrained size-dependent determination of the lattice constants and profile parameters of the Bc 9, Bc 14, and Bo 22 samples, these data sets were refined simultaneously with the reference sample by profile extraction according to the Le Bail approach [127]. Two different sets of reflections were refined for each data set. In particular, the (400) and (440) reflections were refined with a set of profile parameters, and the (220) and (511) reflections were refined simultaneously with a constrained lattice parameter, but were allowed to take different particle size dependent profile parameters in order to account for different observed profile functions. The instrumental Gaussian reflection broadening parameters were constrained for all samples, and the Lorentzian strain broadening parameter as well as a Gaussian size broadening parameter were refined for each sample. The instrumental Gaussian broadening was thus directed by the magnetite reference sample, for which the particle size broadening parameter was set to zero.

The particle diameter was estimated from the refined Gaussian broadening parameter GP according to the phenomenological Debye-Scherrer equation

$$P = \frac{18000K\lambda}{\pi\sqrt{(8\ln 2)\mathrm{GP}}} \tag{5.2.1}$$

with GP the gaussian particle size broadening in $0.01^\circ 2\theta$, λ the used wavelength, and K the Scherrer constant which was set to 1 in this case. The Lorentzian contribution to the reflection profile can result from either particle size broadening or strain broadening, which exhibit a different scattering angular dependence. Due to the narrow refined angular range, a clear assignment of the two Lorentzian contributions cannot be made. However, the obtained Lorentzian contribution does not increase with decreasing particle size and was thus assumed to result from strain broadening rather than particle

size broadening. For this reason, the Lorentzian particle size broadening parameter was neglected. The lattice strain was thus determined according to

$$S = \frac{\pi}{18000}(LY - LY_i)100\% \tag{5.2.2}$$

with LY and LY_i the Lorentzian strain broadening parameter in $0.01°2\theta$ determined from the sample and the bulk reference, respectively.

The zero shift parameter was found to have a strong influence on the lattice parameter obtained for the nanoparticle samples. For this reason, the constrained Le Bail fits were carried out without a zero shift. For the magnetite reference sample, the lattice constants with and without refinement of the zero shift parameter differ by ~ 0.01%.

5.2.2.1.2. Pair Distribution Function The data collected at a short sample detector distance was normalized to the average monitor counts. Further corrections and normalization were carried out using the program PDFgetX2 [128], that yields the total scattering function S(Q) and the PDF G(r). For the Fourier transform of S(Q) to G(r), a maximum momentum transfer of Q_{max} = 22 Å^{-1} was used. Refinements of the obtained PDF were performed using the program PDFgui [129], which applies a full-profile real-space local-structure refinement method [130] analogous to Rietveld refinement [126].

Structural parameters refined during a global refinement in the range of 0.5 - 50 Å include the lattice constant, atomic displacement parameters, and the occupancy of the octahedrally coordinated Fe sites. The particle size was refined after determination of the instrumental damping using the nickel reference sample. Further refined parameters include a low-r correlated motion peak sharpening factor [131] and the scale factor. For R dependent refinements of the lattice constant or the Fe occupancy, narrow R ranges of R ± 2 Å were refined with only the scale factor and the desired parameter. All remaining parameters were fixed at the values determined during global refinement.

5.2.2.2. XAS

For XAS measurements at the Fe K edge, pellets of the Hs nanoparticle powders as well as magnetite and hematite (α-Fe_2O_3) reference materials were produced with an average sample content of 5 mg in 60 mg cellulose. The Bs 10 and Bc 9 nanoparticle samples were measured in toluene dispersions in concentrations of 4 x 10^{15} particles/ml as received from our collaborators. The dispersions were sealed in quartz capillaries with the same technique applied for SAXS measurements (see section 5.1.2.1).

The experiments were performed at the SAMBA beamline (3.4.1) at the Synchrotron Soleil. All the samples were measured at room temperature. XAS data were obtained by

detecting the iron fluorescence using a Rontec detector. Simultaneously, three ionization chambers were used in order to detect the incident flux (I_0), the transmission of the sample (I_1/I_0), and the transmission of a standard Fe foil (I_2/I_1).

Data analysis was performed using the Athena and Artemis programs [81,132]. Data correction was performed by a polynomial fit of the pre-edge range and a spline fit of the normalization range. The radial distribution function in real space was obtained by Fourier transformation of the processed EXAFS in a k range of 3.2 - 10 $Å^{-1}$ weighted by a k^3 factor. Refinements of the EXAFS were performed in real space in a fitting range of 1 - 3.7 Å.

5.2.2.3. The magnetite/maghemite structure

The unit cell content of magnetite in the inverse spinel structure can be described as $(Fe^{III})^{t}_{8}[Fe^{III}_{\frac{1}{2}}Fe^{II}_{\frac{1}{2}}]^{o}_{16}O_{32}$, where t denotes the tetrahedrally coordinated 8a site and o denotes the octahedrally coordinated 16d site of the cubic $Fd\bar{3}m$ space group. From this structure type, the maghemite structure is derived by introducing $\frac{8}{3}$ vacancies (□) at the octahedral site, leading to $(Fe^{III})^{t}_{8}[Fe^{III}_{\frac{5}{6}}\square_{\frac{1}{6}}]^{o}_{16}O_{32}$. Maghemite can exhibit different degrees of vacancy order, whereas the vacancies are always found at the octahedral sites. The most disordered maghemite structure is represented by a random distribution over all octahedral positions, corresponding to the magnetite space group $Fd\bar{3}m$. A partial degree of vacancy order observed by maghemite is related to the $LiFe_5O_8$ structure with unit cell content $(Fe^{III})^{t}_{8}[Fe^{III}_{\frac{3}{4}}Li^{I}_{\frac{1}{4}}]^{o}_{16}O_{32}$. In the corresponding $P4_332$ space group, the octahedral Wyckhoff 4b and 12d sites are occupied by Fe and Li, respectively, whereas for maghemite the vacancies are constrained to the $\frac{8}{3}$ of the 4b sites [133]. A completely ordered maghemite structure was found to be a tetragonal superstructure of the latter with $\frac{c}{a} = 3$ [134,135]. For this structure the space group $P4_12_12$ is reported with lattice constants of a = 8.347 Å and c = 25.042 Å [108].

Refinements of the nanoparticle structure are performed using the most disordered maghemite structure type in a first approximation, because the first aim is the determination of the integral occupancy of the octahedral Fe sites before a determination of a possible vacancy order.

In order to get insight into the first nearest neighbor correlations of the magnetite/maghemite structure type, a simulated PDF is compared to selected partial contributions in Figure 5.2.1. Although not all possible contributions are presented, it is clearly visible that the first nearest neighbor correlation peak consists of two separate correlations, namely the Fe_t-O and Fe_o-O correlations, with slightly different real space distances. Since the Fe_o-O correlation is larger in intensity (due to the larger site multiplicity), this

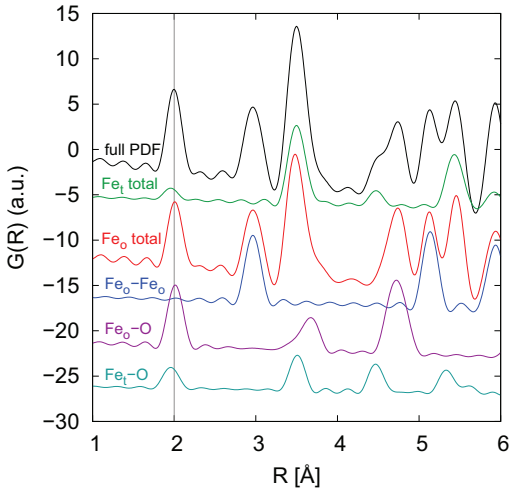

Figure 5.2.1.: Simulated PDF of magnetite. A simulation of the full PDF is presented (black) and compared with selected partial contributions. The first nearest neighbor correlation peak in the full PDF is marked by a grey line as a guide to the eye.

correlation peak will be largely affected by a reduced Fe_o occupancy due to vacancies. The second nearest neighbor correlation is almost pure Fe_o-Fe_o, with only a small O-O correlation (not shown), and will also indicate vacancies on this site.

5.2.3. Results and Discussion

5.2.3.1. Selection of samples for evaluation

In order to exclude samples affected by impurities prior to a more detailed analysis, qualitative phase analysis is carried out on the diffraction data measured at 6-ID-D, APS. In Figure 5.2.2 the diffraction intensities of all measured samples are compared with the diffraction by a bulk magnetite reference sample. For all samples, a considerable reflection broadening as compared to the bulk magnetite reference is observed, which indicates the nano size range of structural correlations in the samples.

The H nanoparticle series presented in Figure 5.2.2a exhibits many impurity phase reflections which are much sharper than the magnetite reflections and cannot be assigned to any further known iron oxide phase. The observed reflections were found independently with several instruments and configurations including an in house diffractometer operated with Mo Kα radiation, the neutron powder diffractometer NPDF at LANSCE, Los Alamos, and both detector distances at 6-ID-D. These measurements are

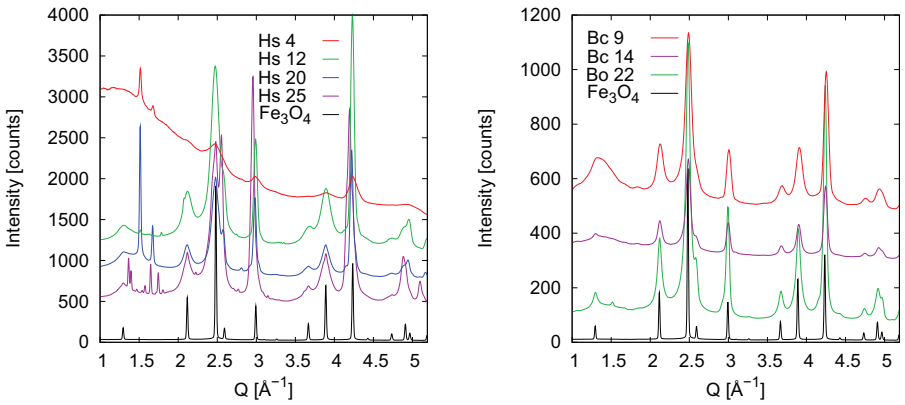

(a) Synchrotron powder diffraction by iron oxide nanoparticles of different sizes. Intensities have been scaled for display.

(b) Synchrotron powder diffraction by iron oxide nanoparticles of different shapes and sizes.

Figure 5.2.2.: Synchrotron powder diffraction by iron oxide nanoparticles. The studied samples are compared with a bulk magnetite reference sample.

exemplarily presented for the Hs 20 sample in Figure 5.2.3. As visible in the Figure,

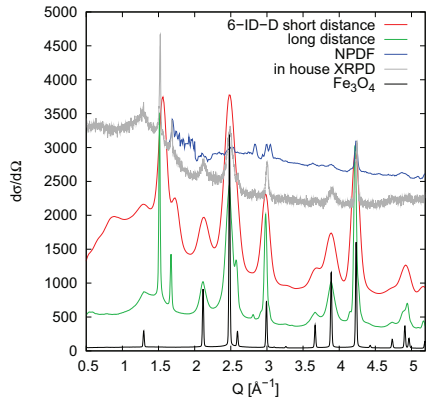

Figure 5.2.3.: Phase analysis of the Hs20 nanoparticles. Data have been scaled for display.

the impurity phase reflections are observed reproducibly and independent on the instrument. The impurity reflection at Q = 1.5 Å^{-1} is the strongest reflection observed in this pattern. Its peak width is extremely narrow and comparable to the bulk magnetite reference rather than the nanoparticle magnetite reflections. For these reasons the phase impurity is considered a major phase of the sample, which will affect the reliable evaluation of the data in reciprocal (Rietveld) as well as real space (PDF analysis). Con-

sequently, the H nanoparticle sample series will not be evaluated by wide angle scattering methods. Since the phase impurities were not identified as iron oxides, they can be assumed to be iron-free byproducts of the synthesis, such as a large excess of organic compounds in crystalline form. For this reason, the H nanoparticle samples can still be considered for evaluation of X-ray absorption spectroscopy, which is element-specific and was measured at the Fe K edge.

The B nanoparticle series presented in Figure 5.2.2b exhibit all reflections observed for the bulk magnetite reference, and there is no evidence for phase impurities. For this reason, the investigation of the local structure by using powder diffraction and PDF analysis will focus on the B nanoparticle series.

5.2.3.1.1. Diffraction analysis Diffraction data were analyzed in reciprocal space in order to get information on the average crystal structure of the nanoparticles. Intermediate compositions between magnetite and maghemite are characterized by a variation of both the lattice constant and the occupation of the iron sites. Furthermore, reflection broadening gives information on the average structural correlation length in the nanoparticles, which is expected to be close to the nanoparticle size as determined by SAXS in section 5.1.3.1.

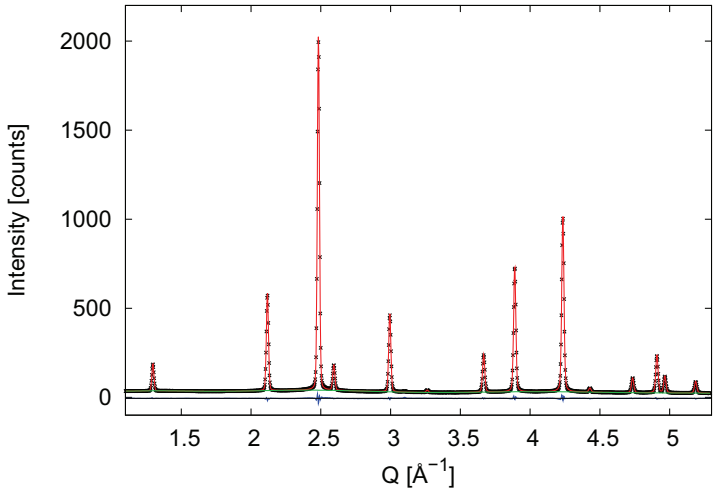

Figure 5.2.4.: Rietveld refinement of bulk magnetite. The observed, calculated, and difference diffraction pattern are presented in black, red, and blue, respectively. The background is presented by a green line. Refined parameters are listed in Table E.1.1.

A Rietveld refinement of the bulk magnetite reference sample is presented in Figure 5.2.4. The reflection profiles were best matched using a modified pseudo-Voigt profile function with both Gaussian and Lorentzian contributions. A list of all refined parameters is given in Table E.1.1 in the Appendix E.

For refinement of the diffraction by nanoparticle samples, the reflection intensities may be affected by a variation of the Fe occupancies. In order to obtain reasonable values for the lattice constant and a good description of the reflection profiles, the unit cell content was neglected, and refinement of the lattice parameters was performed in a first step by profile matching according to the Le Bail approach [127]. In Figure 5.2.5,

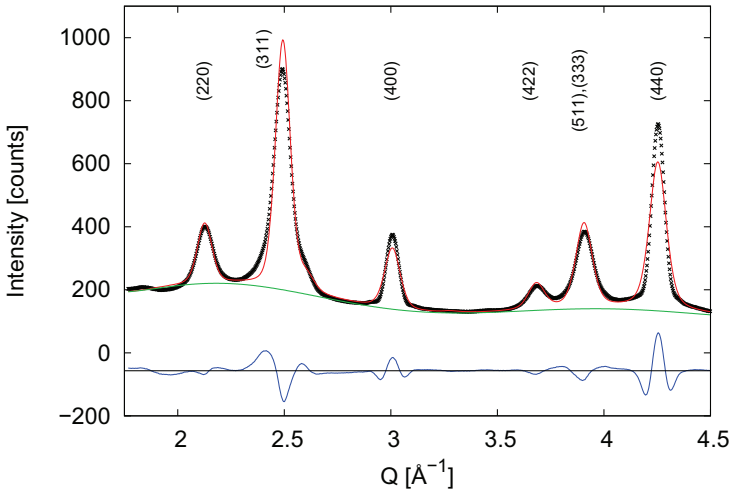

Figure 5.2.5.: Le Bail intensity extraction of the Bc 9 nanoparticles. The observed, calculated, and difference diffraction pattern are presented in black, red, and blue, respectively.

the result of a Le Bail fit of the entire diffraction pattern of the Bc 9 nanoparticle sample is presented. The poor fit of the data results from the different reflection profiles. The behavior of the difference curve in Figure 5.2.5 indicates that the (220), (311), (422), and (511) reflection profiles may be matched better with a larger Gaussian contribution, while the (400) and (440) reflections require a larger Lorentzian contribution. Since this variation in profile is not directly correlated to the scattering angle, an isotropic reflection profile function is not sufficient for description of the entire diffraction pattern.

Anisotropic particle size broadening, anisotropic strain broadening, or preferred orientation may be considered to cause such reflection profiles. However, the reflection profiles of the (220) and (440) reflections in Figure 5.2.5 deviate in opposite directions

from the average profile, whereas anisotropic lattice distortions are expected to be equal for reflections belonging to the same crystallographic direction, such as (220) and (440).

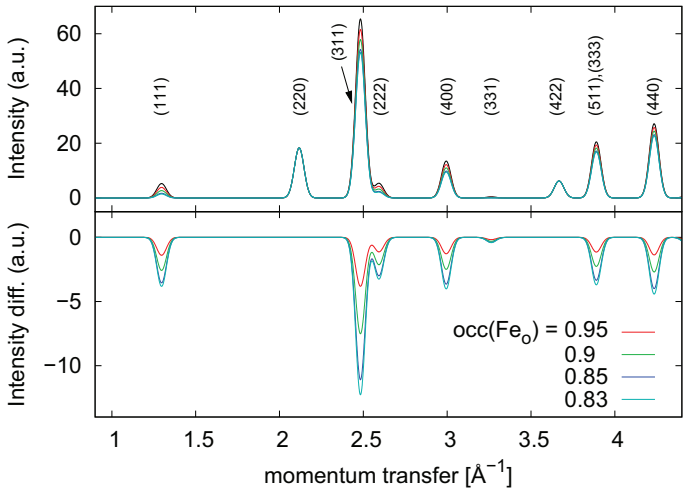

Figure 5.2.6.: Simulations of powder diffraction data for magnetite and variation of the Fe occupancy. Diffraction profiles are presented at the top for full occupancy of all Fe sites (black) and lower occupancies of the octahedrally coordinated Fe site down to the nominal composition of maghemite (cyan). In the bottom graph difference curves of the respective intensity profiles with the profile for full occupancy are given in order to identify the reflections affected from a variation of Fe occupancy.

A further possible origin of the observed variation in reflection profiles is the expected variation in Fe occupancies. Figure 5.2.6 presents theoretical diffraction patterns calculated for different occupancies of the octahedrally coordinated Fe site. It is clear from the difference curves at the bottom of Figure 5.2.6 that many of reflections are affected by a reduced Fe occupancy. Only the (220) and (422) reflections exhibit a constant intensity regardless the Fe occupancy. The set of reflections affected by a variation of Fe occupancy shows different deviations from the average profile function in Figure 5.2.5. The Fe occupancy is thus not directly related to the observed different profile functions.

In order to account for the observed variation in reflection broadening, selected reflection sets were refined by intensity extraction according to the Le Bail approach. The profile and lattice parameters were constrained as given in section 5.2.2.1. The refinement results, which will be discussed later, are presented in Figure 5.2.7, and the obtained parameters are listed in Table E.1.2 in the Appendix E.

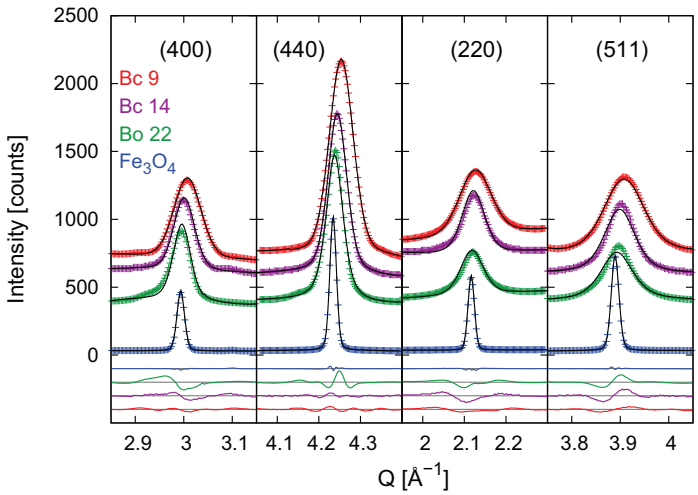

Figure 5.2.7.: Le Bail fits of the diffraction data. Diffraction profiles of bulk Fe_3O_4 (blue), Bo 22 (green), Bc 14 (purple), and Bc 9 (red) are presented along with the respective fits (black lines). The difference curves are displayed in the respective colors at the bottom. Data have been scaled and offset for display.

Whereas the reflections of the magnetite bulk reference and the Bc 9 nanocubes seem reasonably well fitted, some differences are observed for the Bc 14 and Bo 22 samples. In particular the reflection position seems to shift in different direction with respect to the fit (note the difference curves of the (400) and (511) reflections). The origin of this behavior is not clear. Lattice strain may contribute to this effect but would be expected to result in anisotropic broadening rather than a shift of selected reflections. A reflection shift (or rather reflection splitting) may indicate a decrease in symmetry, *e. g.* from cubic to tetragonal symmetry as known for maghemite. However, the deviation is expected to be the same for reflections belonging to the same crystallographic direction, such as (220) and (440), which is not observed here.

5.2.3.1.2. PDF analysis The obtained PDF data of the selected samples is presented in Figure 5.2.8. Refinements of the entire data range match the data reasonably well, and the refined parameters are listed in Table E.2.1 in Appendix E and discussed in the following sections. Due to the instrumental resolution, the PDF data of the bulk Fe_3O_4 reference is heavily damped in the higher R range (up to 50 Å). However, a stronger damping of the nanoparticle PDF data due to the finite particle size is visible and allows for refinement of the nanoparticle diameter. The remarkably large residual intensity observed in the low R range will be discussed in detail in section 5.2.3.5.

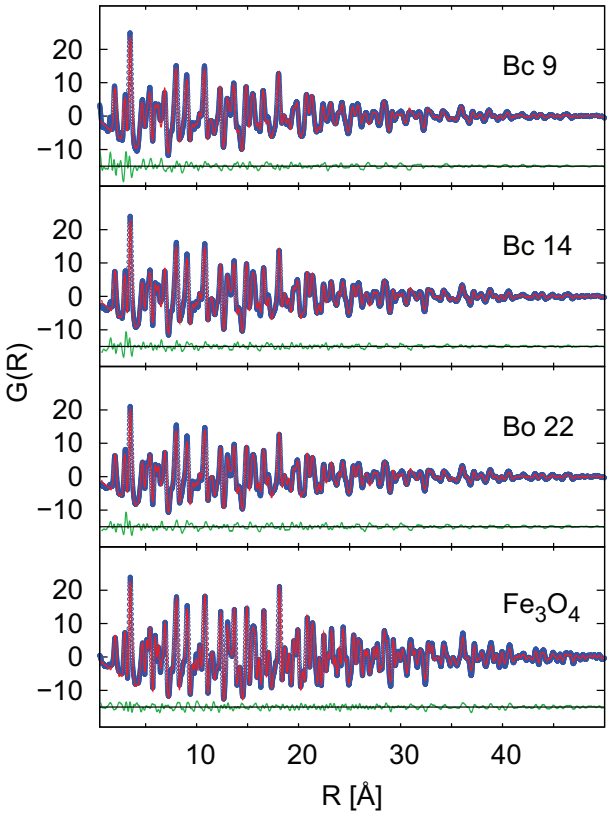

Figure 5.2.8.: Refinements of the studied PDF data. Observed, calculated, and difference intensities are presented in blue, red, and green, respectively. Refined parameters are listed in Table E.2.1.

5.2.3.2. Particle size

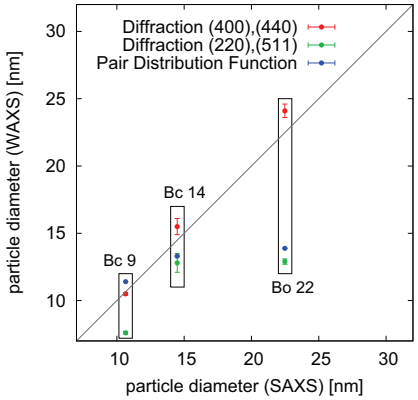

Figure 5.2.9.: Particle size as determined by Scherrer broadening and PDF analysis as compared to SAXS. Equal particle sizes for SAXS and XRD/PDF are marked by the line.

The particle size can be determined from diffraction data by either analysis of the Scherrer reflection broadening or refinement of a particle size envelope function of the PDF. Nanoparticle diameters obtained by both approaches are presented in Figure 5.2.9 corresponding to the particle sizes determined by SAXS in section 5.1. The particle sizes obtained by the (400) and (440) reflection broadening are in agreement with the SAXS results. In contrast, the particle sizes determined by the (220) and (511) reflection broadening and PDF are significantly smaller, but consistent to each other (except for Bc 9). A smaller particle size as determined by diffraction methods relates to a range of structural coherence smaller than the entire nanoparticle and may thus indicate either a loss of crystallinity or lattice strain close to the nanoparticle surface. However, the parameters discussed in what follows will be compared to the SAXS particle sizes.

5.2.3.3. Lattice constant

The variation of the average cubic lattice parameter with nanoparticle size was studied by both diffraction and PDF analysis. As presented in Figure 5.2.10, the lattice parameter reveals the same particle size dependence for both methods. The lattice constants determined from diffraction data vary systematically for the different sample detector distances, with the smaller lattice constants determined at a larger distance. However, the lattice constants determined by PDF analysis are intermediate of the diffraction results. as all data sets exhibit the same particle size dependent behavior, proper determi-

nation of the lattice constants from the respective data sets is justified. In what follows, parameters presented in dependence of the lattice constant will be related to those lattice constants determined by the same method.

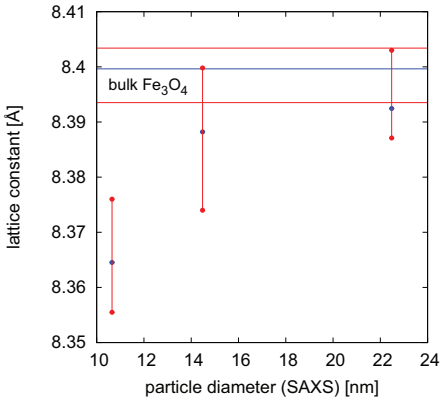

Figure 5.2.10.: Lattice constants as determined by diffraction (red) and PDF analysis (blue) in dependence of the nanoparticles size. The lattice constants obtained from bulk magnetite are indicated as red and blue lines. Two different values were obtained systematically from diffraction data, where the larger values for each sample correspond to the shorter sample detector distance.

The lattice constant is close to the bulk magnetite lattice constant for the largest Bo 22 nanoparticles and decreases with decreasing nanoparticle size to ~ 8.36 Å for the smallest studied nanoparticles (Bc 9). The maghemite lattice constant is published as 8.348 Å [135], which is still smaller than the lattice constants determined for the Bc 9 nanoparticles. As all determined nanoparticle lattice constants are in between those of bulk references, a gradual transition from maghemite to magnetite with increasing particle size is likely.

While the lattice constants determined above are average values related to the entire nanoparticle, the local lattice constant can either be equal to the average value throughout the nanoparticle or deviating from the center to the surface of the nanoparticles. Considering both the higher oxidation state and the smaller lattice constant of maghemite as compared to magnetite, a magnetite core with larger lattice constant surrounded by a maghemite shell with a smaller lattice constant at the surface is likely.

The only parameter accessible by analysis of the diffraction data in reciprocal space that may indicate such an intra-particle lattice constant variation is the strain reflection broadening.

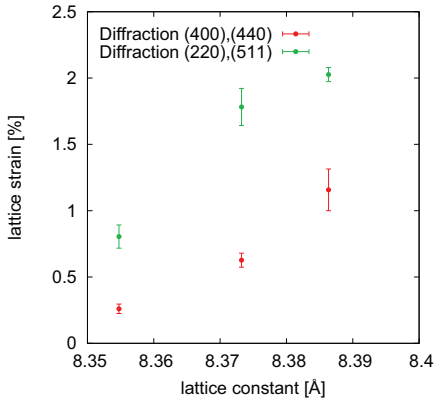

Figure 5.2.11.: Lattice strain as determined by diffraction in dependence of the nanoparticle lattice constant.

The lattice strain deduced from the Lorentzian strain broadening coefficient determined from the Le Bail fits in Figure 5.2.7 is presented in Figure 5.2.11. For both reflection sets, an increasing lattice strain with lattice constant is deduced.

The maximal difference in lattice constants for magnetite (a = 8.39 Å) and magnetite (a = 8.348 Å) is in the range of 0.04 Å, which corresponds to a maximal expected lattice strain of ~ 0.5 %. The significantly higher lattice strain values presented in Figure 5.2.11 indicate that the Lorentzian broadening does possibly not entirely result from strain broadening. However, the larger strain observed for the larger nanoparticles (with a larger lattice constant) may indicate a possibly more pronounced core shell arrangement of magnetite and maghemite in the larger particles with a more pronounced relaxation of the lattice constants. At the same time, the smaller nanoparticles appear to be rather homogeneous in lattice constant, suggesting an almost entire oxidation to maghemite.

More local information on the intra-particle lattice constant variation can be obtained by PDF analysis in dependence of the atomic pair distance R. Figure 5.2.12a presents the variation of the lattice constant with the observed pair distances relative to the average lattice constant determined over the entire pair distance range. The relative variation of the lattice constant is less than 0.1 % for all nanoparticle samples, and comparable to the variation observed for the bulk magnetite sample, which should not exhibit any variation in lattice constant. However, a clear, systematic difference between the lattice constant variation of the nanoparticle samples and the bulk magnetite reference is observed. The variation of the lattice constant normalized with the bulk lattice variation is thus presented in Figure 5.2.12b and will be discussed briefly.

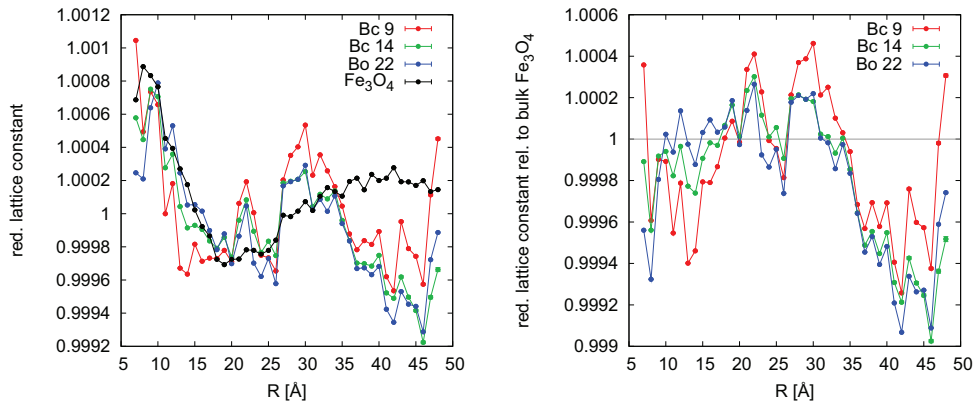

(a) Lattice constants in dependence of the atomic pair distance R, relative to the average lattice constant.

(b) Relative lattice constants, normalized to the relative lattice constants of the bulk Fe_3O_4 reference.

Figure 5.2.12.: Variation of the lattice constants in dependence of the atomic pair distance R.

The lattice constants obtained for specific atomic pair distances R and displayed in Figure 5.2.12 correspond to the average lattice constants derived for the respective R distances around all atoms within the nanoparticle. The difference of obtained lattice constants for small and large R is illustrated for a two dimensional case in Figure 5.2.13. For an atom at a particular distance from the surface s, atomic pair distances with $R \leq s$ are possible in all directions around the starting atom, while for $R > s$ only the fraction of atomic pair distances in direction to the particle core is possible. Thus, for a larger R a lower number of interatomic distances contributes to the average lattice constant determined for the specific R distance, while interatomic distances close to the particle surface are systematically underrepresented. For a homogeneous lattice constant within the nanoparticle, the lower amount of considered distances for large R does not affect the average lattice constant for this particular R (Figure 5.2.13a). In contrast, if the lattice constant deviates close to the particle surface (Figure 5.2.13b), the large R distances will reveal a lattice constant closer to that in the particle core, because the lattice constant contributions near the surface are underestimated. With decreasing R, the obtained lattice constant consequently approaches the average lattice constant determined by diffraction or long range PDF refinement.

The normalized R dependent lattice constants presented in Figure 5.2.12b are close to the average value for small R as expected. For $R \geq 35$ Å, the lattice constants are smaller than the average, indicating a transition from a smaller lattice constant in the nanoparticle core to a larger lattice constant at the surface. This does not support the

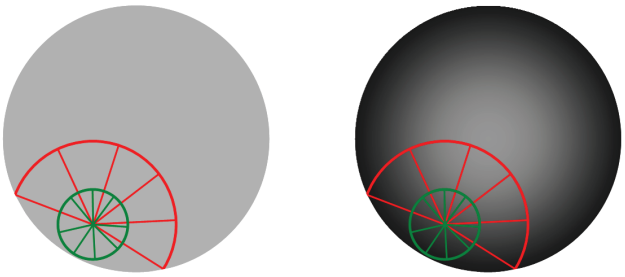

(a) homogeneous distribution of the lattice constant.

(b) Variation of the lattice constant from the particle core to the surface.

Figure 5.2.13.: Schematic of the dependence of the determined lattice constant on the atomic pair distance R. Possible atomic pair distances R larger and shorter than the distance between the starting atom and the particle surface are presented in red and green, respectively. A variation of the lattice constant is indicated as a variation of the particle color.

assumption of a magnetite core (with a larger lattice constant) and a higher oxidized maghemite shell (with a smaller lattice constant). However, for R $\geq$ 45 Å, the lattice constants increase up to the average value, and it is unclear whether this trend continues at higher R. As can be estimated from Figure 5.2.13b, the effect of an intra-particle lattice constant variation is better observable with larger probed R and with larger gradient of the lattice constant towards the particle surface. Due to the instrumental decrease of the PDF signal, atomic pair distances above R = 50 Å can not be refined reliably. This corresponds to only 50 % of the smallest nanoparticle diameter and even less of the larger nanoparticle diameters.

Due to the variation of the average lattice constant and the lattice strain with nanoparticle size, the intra-particle lattice constant variation is furthermore expected to depend on the nanoparticle size as well. Instead, the observed effect in Figure 5.2.12b is similar for all investigated nanoparticle samples. Considering furthermore the very small relative lattice constant variation (in the same order of magnitude as the bulk reference), the significance of the observed effect is questionable.

Summarizing, a variation of the average lattice constant with nanoparticle size was found by both diffraction and PDF analysis, suggesting a larger contribution of magnetite in the larger particles and a larger contribution of maghemite in the smaller nanoparticles. Increasing lattice strain with particle size suggests a variation of the lattice constant within the larger nanoparticles. A small intraparticle variation of the lattice

constant was observed by R dependent PDF analysis. However, this effect is small, constant with particle size, and favors a larger lattice constant in the particle shell than in the core, which is not in agreement with the earlier conclusions. In order to confirm the significance of the R dependent lattice constant variation, a more detailed theoretical model and PDF data in a wider R range may be required.

5.2.3.4. Oxidation state

X-ray Absorption Near Edge Structure (XANES) investigations were carried out in order to estimate the average oxidation state of Fe in the iron oxide nanoparticles. Normalized X-ray absorption spectra of the investigated samples and Fe_3O_4 and α-Fe_2O_3 reference materials are presented in Figure 5.2.14. A shift of the white line to lower energies with increasing particle size is observed. As the energy of the main absorption edge is directly related to the Fe oxidation state, a shift towards a higher oxidation state with decreasing particle size is indicated by direct comparison with the reference materials.

Since maghemite is not available free of impurities in bulk, its polymorph hematite (α-Fe_2O_3), which has a comparable bond-valence sum, was used as Fe(III) reference material. The average Fe oxidation states of magnetite and hematite are +2.66 and +3, respectively, and the corresponding absorption edges are observed in Figure 5.2.14 at energies of 7120.9 and 7123.2 eV, respectively. Assuming *a priori* a linear relation between average oxidation state and absorption energy, the oxidation state of the investigated nanoparticle samples is determined as presented in Figure 5.2.15a. As introduced in section 5.2.2.3, iron vacancies in maghemite are preferentially located on the octahedrally coordinated iron sites. This preference is confirmed by refinement of the iron sites occupancy in the nanoparticle PDF data sets. With the average Fe oxidation state obtained from XANES, the number of iron atoms per unit cell and subsequently the occupancy of the octahedral Fe site is derived. The atomic ratio of Fe:O atoms as determined by XANES is presented in Figure 5.2.15b and compared with Fe:O ratios obtained by PDF analysis. The general trend of an increasing Fe:O atomic ratio with increasing particle size is observed by both X-ray absorption and PDF analysis, which is in agreement with the expected larger contribution of magnetite and the proposed magnetite core of the larger nanoparticles. The Fe:O atomic ratio of the smallest nanoparticle sample investigated with PDF (*i. e.* Bc 9) is even lower than the minimal atomic ratio expected for pure maghemite, which diminishes the significance of this value.

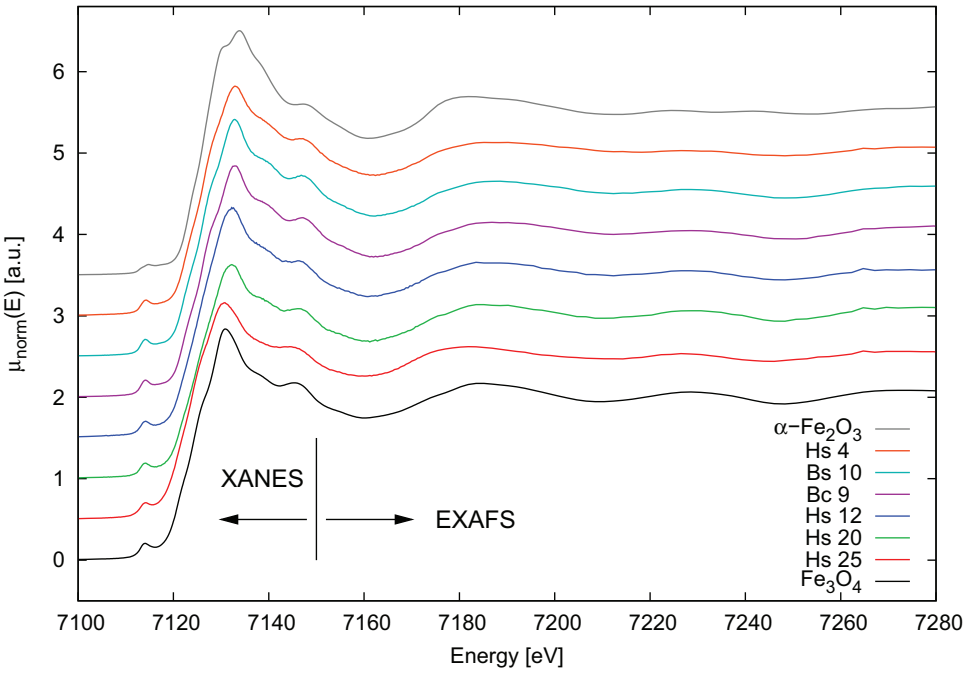

Figure 5.2.14.: XAS by iron oxide nanoparticles. XANES and EXAFS regions of the spectra are indicated and reference measurements of magnetite and hematite (α-Fe_2O_3) are shown.

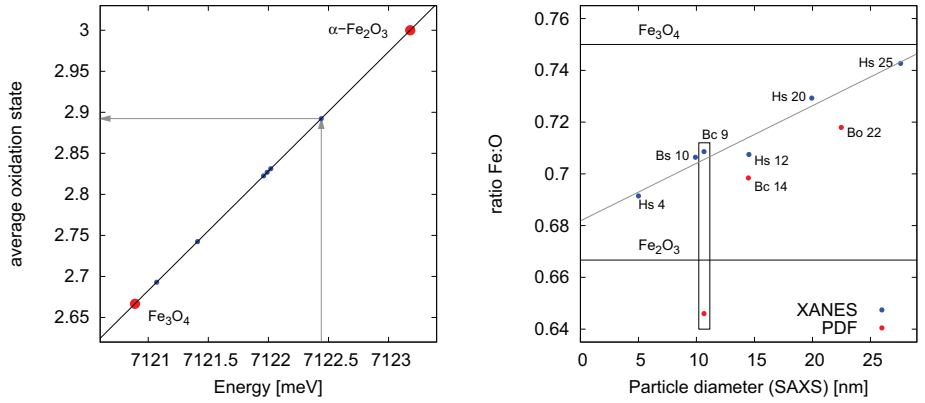

(a) Oxidation state of iron oxide nanoparticles as determined from the Fe absorption energy.

(b) Fe:O atomic ratio as determined by absorption spectroscopy and PDF analysis. A linear trend of the XAS data is given as grey line.

Figure 5.2.15.: Fe oxidation state and atomic ratio in iron oxide nanoparticles.

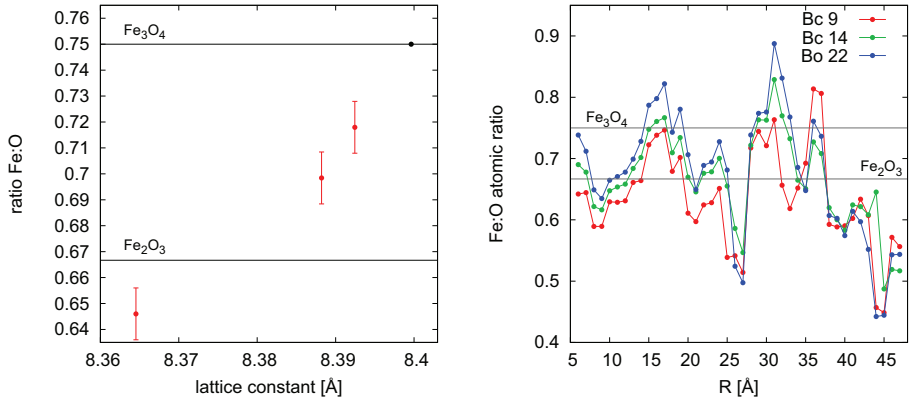

(a) Fe:O atomic ratio as determined by PDF analysis corresponding to the lattice constant.

(b) R dependent Fe:O atomic ratio.

Figure 5.2.16.: Fe:O atomic ratio as determined by PDF analysis.

As presented in Figure 5.2.16a, the found particle size dependence of the average Fe oxidation state is correlated with the respective lattice constants, which is expected due to the smaller lattice constant of the higher oxidized maghemite as compared to magnetite. Considering the variation of the Fe:O atomic ratios in between 3:4 and 2:3, the Bc 9 sample with a lattice constant of 8.364 Å can be assumed to be fully oxidized to γ-Fe_2O_3, whereas the determined Fe:O ratio for this sample is unphysically low.

Analogous to the intraparticle variation of the lattice constants, R dependent refinements of the occupancy at the octahedrally coordinated Fe site were carried out in order to detect a possible vacancy order close to the particle surface. The obtained Fe:O atomic ratios are presented in Figure 5.2.16b. The general trend of the atomic ratios with pair distance appears systematic for all nanoparticle samples, and the absolute Fe:O ratio is largest for the largest nanoparticles as shown for the integral particles in Figure 5.2.16a. However, the atomic ratios deviate strongly with the atomic pair distance R and exceed the limits of the pure magnetite and maghemite compositions significantly. For this reason, the obtained R dependent variation of the atomic ratios is considered artificial, and a reliable statement on a possible distribution of Fe vacancies within the nanoparticle cannot be given.

5.2.3.5. Local structural distortions

As mentioned in section 5.2.3.1, the difference curves of the nanoparticle PDF refinements exhibit an increased mismatch of the structural model and data in the low R

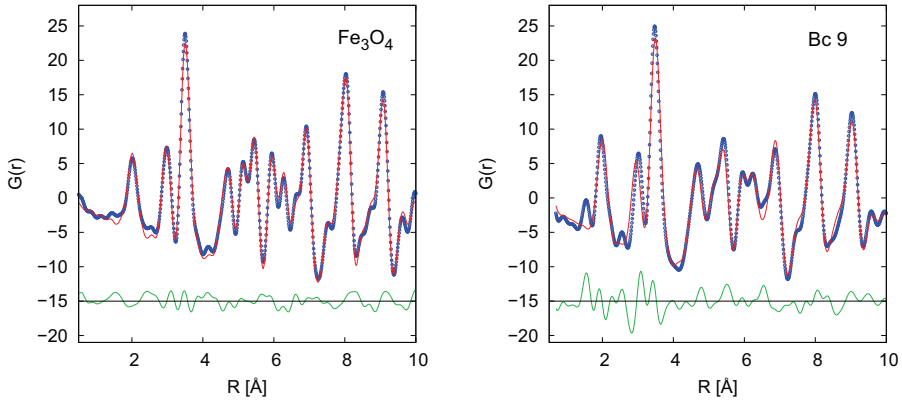

(a) PDF of the bulk magnetite reference.

(b) PDF of the Bc 9 nanoparticles.

Figure 5.2.17.: PDF refinements of the bulk reference and the smallest investigated nanoparticles. Observed, calculated, and difference curves are presented in blue, red, and green, respectively.

range. For a better visualization, an intermediate R range of the smallest nanoparticles and the magnetite reference are presented in Figure 5.2.17. The two data sets exhibit slight differences in peak positions and intensities, which are well described by a variation of the lattice constant and the Fe occupancy of the refined structural model. However, discrepancies of the first nearest neighbor correlation peaks, with R ≤ 4 Å, are not well represented. Figure 5.2.18a compares the variation of the first nearest neighbor correlations for the different nanoparticle sizes. A small shift of the atomic pair distances to lower R with decreasing particle size is correlated with the variation of the lattice constant discussed in section 5.2.3.3. Intensity variations observed for the pair correlations at R ≥ 4 Å are in agreement with a variation of the Fe occupancy as discussed in section 5.2.3.4. The relative increase of the intensity ratio of the first two nearest neighbor correlations can also be described by a decreasing occupancy of the octahedrally coordinated Fe site.

An additional correlation peak is observed at R = 1.540 (2) Å, which increases in intensity with decreasing particle size. This atomic pair distance corresponds to the C-C bond length and is thus attributed to the increasing relative amount of oleic acid in the sample with decreasing particle size.

Furthermore, the first nearest neighbor correlation distance at ~ 2 Å decreases at a significantly larger rate than found for the larger atomic distances, whereas the second nearest neighbor correlation distance at ~ 3 Å is almost constant. The distance variation normalized by the distances obtained for the Bo 22 sample is presented in Figure

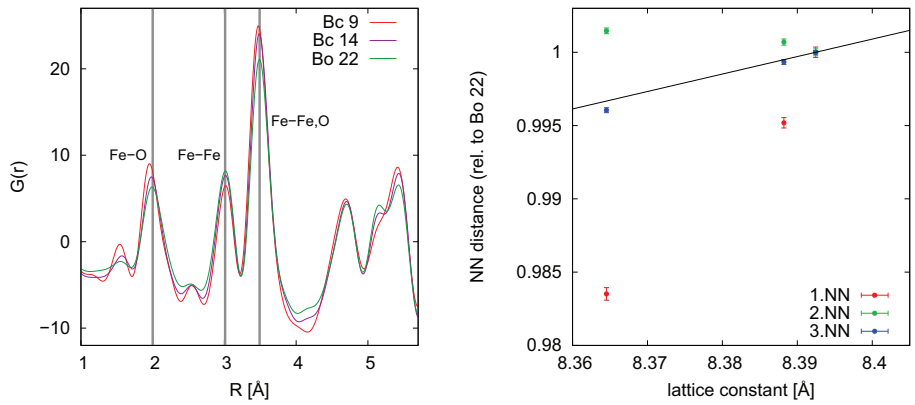

(a) Local PDF of the nanoparticle samples. The nearest neighbor distances containing Fe contributions are marked by grey lines.

(b) Relative shift of the nearest neighbor distances marked in (a). The grey line indicates a proportional shift of the nearest neighbor distances as expected for a lattice constant variation without local dislocations.

Figure 5.2.18.: Nearest neighbor distances as obtained from PDF analysis.

5.2.18b. Assuming a variation of the lattice constant without dislocations of the unit cell content, all nearest neighbor distances are expected to be directly proportional to the lattice constant as indicated by the grey line in Figure 5.2.18b. The variation of the third nearest neighbor distance (at R ~ 3.5 Å in Figure 5.2.18a) reflects this expected behavior, as do the larger nearest neighbor distances (not shown). The first nearest neighbor distance decreases significantly faster than expected, whereas the second nearest neighbor distance remains almost constant. Since these observations are not in agreement with the long range structural model, structural distortions are indicated, which are likely related to the nanoparticle surface.

EXAFS EXAFS data of the magnetite reference and the Bc 9 nanoparticle sample were analyzed in order to confirm the variation of the nearest neighbor distances as observed by PDF analysis. Refinements of the first three coordination shells of the Fourier transformed EXAFS data are presented in Figure 5.2.19. The obtained parameters are listed in Table E.3.1 in the Appendix E. The appropriateness of the applied structural model is confirmed by the good agreement of data and fit in the k^3 weighted EXAFS presented in Figure 5.2.20. The first coordination shell contains the two Fe-O first nearest neighbor paths of the octahedrally and tetrahedrally coordinated Fe sites merging into the first nearest neighbor peak observed at R ~ 2 Å in the PDF. The second coordination shell observed at R ~ 3 Å in the PDF is a pure Fe-Fe correlation of the octahedrally coordinated

Fe site. In the real space EXAFS data, this contribution merges with the third coordination shell, which is comprised of both Fe-O and Fe-Fe correlations and observed at R ~ 3.5 Å in the PDF. Only the dominant contributions, the Fe-Fe correlation paths, are considered for refinement of this third coordination shell in the EXAFS. Note that the observed peak position by EXAFS usually underestimates the real atomic pair distance. This is taken into account by refinement of the EXAFS, and the resulting atomic pair distances listed in Table 5.2.1 are directly comparable to the PDF results.

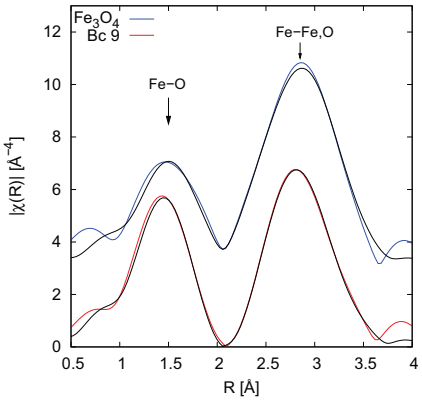

Figure 5.2.19.: Fourier transform of the EXAFS by magnetite and Bc 9. Fits of the real space magnitude performed in the R range of 1.0-3.7 Å are presented as black lines. The corresponding EXAFS are given in Figure 5.2.20.

Table 5.2.1.: Distances and amplitudes in iron oxide nanoparticles.

shell	method	Fe_3O_4 [Å]	Bc 9 [Å]	path	rel. dist. ($\frac{Bc9}{Fe_3O_4}$)
	PDF	2.0116 (3)	1.9629 (7)		0.9758 (4)
1. NN	EXAFS	1.87 (5)	1.932 (7)[a]	Fe_t-O	1.03 (3)
		2.02 (1)	1.932 (7)[a]	Fe_o-O	0.957 (6)
2. NN	PDF	2.9784 (6)	3.0132 (3)		1.0117 (2)
	EXAFS	2.97 (1)	2.98 (1)	Fe_o-Fe_o	1.003 (6)
	PDF	3.5005 (3)	3.4776 (5)		0.9935 (2)
3. NN	EXAFS	3.47 (1)	3.43 (1)	Fe_t-Fe_o	0.988 (4)[b]
		3.63 (1)	3.59 (1)	Fe_t-Fe_t	0.988 (4)[b]

[a] Refinement of the first nearest neighbor peak of the Bc 9 sample was only possible with a single Fe-O distance.
[b] the relative variation of the 3.NN path distances was constrained for the Bc 9 sample.

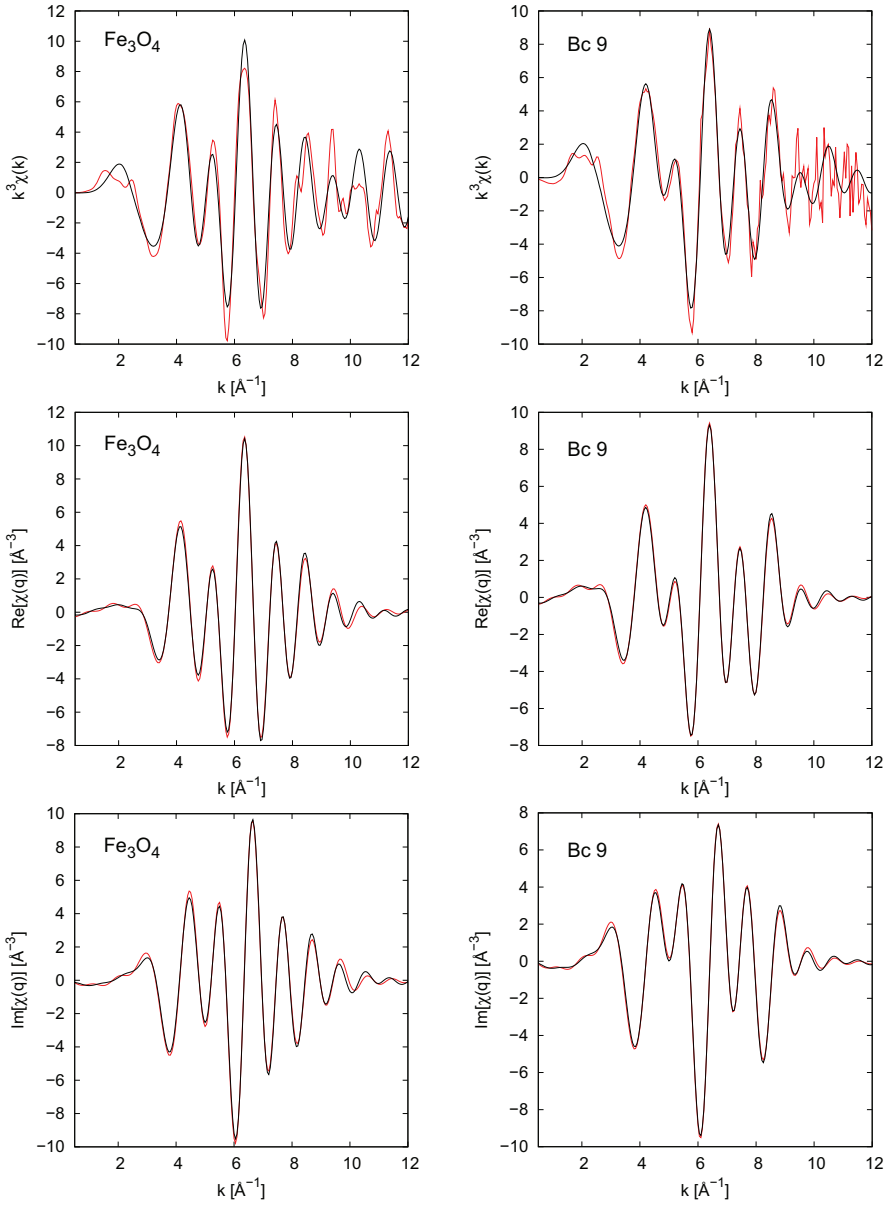

Figure 5.2.20.: The k^3 weighted EXFAS (top row) as well as the real (center row) and imaginary parts (bottom row) of the backtransformed EXAFS of bulk magnetite (left column) and Bc 9 iron oxide nanocubes (right column). Fits corresponding to the magnitude fit shown in Figure 5.2.19 are shown as black lines.

The distances obtained from EXAFS agree roughly with the nearest neighbor correlations, and the observed trend of smaller distances in the nanoparticles (with the exception of the Fe_o-Fe_o distance) is confirmed. The refinement of separate paths reveals a different variation of the atomic pair distances depending on the Fe sites involved. The relative variation of paths contributing to the third nearest neighbor coordination shell corresponds to the decrease of the lattice constant and is in agreement with the PDF results. The observation of a constant pure Fe_o-Fe_o distance despite the lattice variation is confirmed by EXAFS. For the first nearest neighbor coordination shell, EXAFS provides more detailed information than PDF. For the bulk magnetite sample, two separate Fe_t-O and Fe_o-O distances have to be considered for a reliable fit. In the Bc 9 nanoparticle sample, these distances converge, allowing only a single distance parameter for refinement. In comparison with the bulk magnetite distances, the Fe_t-O path distance appears to be constant, which may partially result from the imprecise distance determination of this path in the bulk sample. In contrast, the Fe_o-O path reveals a significantly stronger distance decrease than expected for a pure lattice contraction. According to these results, the variation of the local structure is related to the Fe_o paths, indicating selective distortions of the Fe_o site, while the Fe_t and O sites remain constant. Since this effect becomes more important with decreasing particle size, it is assumed that to be related to the nanoparticle surface.

Summarizing and interpreting the investigation of the first coordination shells in iron oxide nanoparticles, a deviation of the local structure from the average magnetite/maghemite structure was found. Particle size dependent variations of the first and second nearest neighbor distances as observed by PDF analysis are not in agreement with the average structure model which was used to refine the larger size range.

EXAFS reveals these variations to be selectively related to the Fe_o atoms, exhibiting shorter Fe_o-O and longer Fe_o-Fe_o distances than in the average model. The shortened Fe_o-O distance along with a reduced Fe_o occupancy leads to a higher contribution of the even shorter Fe_t-O distance to the first nearest neighbor correlation observed in the PDF and may thus explain its shorter distance and slight asymmetry as observed in Figure 5.2.17b. Additionally, the decrease of the lattice constant with decreasing particle size observed by XRD and PDF is confirmed by EXAFS.

The constant Fe_o-Fe_o distance despite the variation in lattice constant suggests an incremental displacement of the Fe_o positions within the unit cell in a way that the Fe_o sublattice has a larger lattice constant than the unit cell. This would involve further disorder of the first nearest neighbor correlations and a lower occupancy of the Fe_o site, which was both observed as related to the average lattice parameter. Such a dis-

placement may require a reduction in symmetry on the local scale, while the long range order is well described with the cubic magnetite structure. A similar variation of the first and second nearest neighbor peaks in the PDF has been reported for nanoparticles, which are isotypic with maghemite [121]. While disorder of the O site was suggested in $LiFe_5O_8$, the combination of EXAFS and PDF analysis indicates the Fe_o site to induce disorder in this case.

Furthermore, a concentration of the structural disorder at the nanoparticle surface is suggested by the particle size dependence of the observed nearest neighbor shifts. Appearing C-C correlation peaks in the PDF illustrate the more important contribution of the surface and ligand shell for the smaller nanoparticles. For the Bc 9 nanoparticles with a radius of 5 nm, ~ 17 % of the particle volume belongs to a surface region of 3 Å thickness, which is within the second nearest neighbor correlation distance. For this reason, surface effects such as coordination by the oleic acid ligands may have to be taken into account for an exhaustive description of the local structure.

5.2.4. Summary

Within this chapter, a detailed structural characterization of iron oxide nanoparticles has been given. A decreasing lattice constant with decreasing nanoparticle size has been found by both XRD and PDF analysis, which is correlated to an increasing oxidation state found by XANES and an increased amount of vacancies found by PDF analysis. These observations indicate a larger maghemite contribution in the smaller particles with a larger magnetite contribution in the larger particles, suggesting a magnetite/maghemite core shell structure with nearly constant shell thickness. However, such a core shell structure is not supported by R dependent PDF refinements, because the observed lattice variation is insignificantly small in the evaluated R range. For a more precise investigation of the intraparticle lattice and vacancy variation, PDF data with better instrumental resolution, resulting in a lower damping at large R, is required. A lower damping of the PDF may be achieved by neutron PDF. However, for neutron scattering the amount of oleic acid at the nanoparticle surface has to be reduced significantly (see Appendix F for a comparison of synchrotron and neutron PDF).

Combining the PDF and EXAFS analysis, local structural distortions were identified. These structural distortions are found to be selectively related to the octahedrally coordinated Fe sites and increase with decreasing particle size. This leads to the conclusion of correlated displacements of the Fe_o atoms, which originate at the nanoparticle surface.

Thus, the studied iron oxide nanoparticles are affected by the particle size reduction in two ways. First, the composition and oxidation state is varied on a long range scale, exhibiting a higher degree of oxidation for the smaller nanoparticles. Secondly, surface strain has been found to affect the local structure significantly. Although these local displacements appear to have only a short structural coherence, they may affect the internal nanoparticle structure by introduction of strain. This kind of surface disorder as well as the varied oxidation state certainly need to be considered during investigation of the magnetic nanoparticle structure.

5.3. Magnetic Structure

5.3.1. Introduction

The different magnetic properties exhibited by nanomaterials in contrast to the bulk materials are dominated by finite size effects which become increasingly important with decreasing particle size. For example, as the surface to volume ratio increases with decreasing particle size, surface effects have an increasing contribution to the magnetic properties of nanoparticles. Structural surface effects include changes in the average coordination number resulting in different magnetic environments for surface atoms [119], and for vacancy structures such as γ-Fe_2O_3, vacancy order-disorder transitions have been reported to reduce the saturation magnetization [136].

Surface spin disorder may be understood as a consequence of structural disorder, because magnetic superexchange is sensitive to bond angles and lengths which can change dramatically at the surface [119]. An amorphous surface layer can thus be related to a magnetically dead layer [137]. Even organic ligand molecules have been observed to influence the magnetic properties due to different coordination geometries at the particle surface [138].

Most investigations on surface spin disorder and nanoparticle magnetization density are performed by macroscopic probes such as SQUID magnetometry [139, 140], where the presence of a magnetically disordered layer is concluded from reduced magnetization densities [119, 136, 141] and unsaturated magnetization at high fields [119, 142]. Theoretical models complement results from magnetization measurements [119, 141] and allow to predict the spin structure taking into account interatomic superexchange interaction as well as surface and magnetocrystalline anisotropies [143, 144].

The subject of this section will be the microscopic investigation of the spatial magnetization distribution within magnetic particles, a study which has not been carried out before in such detail. The microscopic magnetization density distribution is correlated to the magnetic particle form factor by a Fourier transform. Thus, polarized small-angle scattering will be applied as the method of choice for magnetic scattering by nanoparticles. The cross sections for a dilute system of non-interacting particles as derived by Wiedenmann *et al.* [46,145] allow for refinement of the magnetic form factor by the magnetic contrast variation induced by the polarized neutron beam. A simple description of a magnetic composite has already been given for investigation of cobalt ferrofluids as well as weak magnetic interfaces in soft magnetic metallic glasses [46], consisting of a core shell model with a magnetic core and a nonmagnetic shell. However, no discrim-

ination has been made between the nonmagnetic organic ligand shell and a possible magnetic dead layer at the surface of the (core) particle.

As a second subject of this section, the field-induced ordering of concentrated nanoparticle dispersions will be investigated in dependence of the particle shape. For cobalt ferrofluids, a pseudocrystalline ordering has been reported resulting in a hexagonal superstructure [146].

5.3.2. Methods

5.3.2.1. Sample preparation and data treatment

Sample concentrations The spherical and cubic nanoparticles dispersed in d_8-toluene as received from our collaborators in different particle concentrations were suitable for investigation of pure form factor behavior and interparticle interactions. The exact concentrations of the samples are listed in Table 5.3.1. Because several concentrations of each particle batch were investigated, the samples Bs 10 and Bc 9 introduced in section 5.1 were renamed for this study to s and c, respectively, followed by the mass concentration. The individual sample labels are given in Table 5.3.1.

Table 5.3.1.: Nanoparticle dispersions used for SANSPOL.

	Bs 10 (spheres)			Bc 9 (cubes)			
label	s7	s50	smax	c7	c50	tc50[a]	cmax
$c_{Fe_2O_3}$ [mg/ml]	7	50	261	7	50	50	271
vol %[b]	0.142	1.03	5.29	0.142	1.03	1.03	5.49

[a] 'tc' denotes a sample with larger degree of truncation as determined from TEM [106].
[b] the sample volume was determined using a mass density of 4.937 g/ml as derived from the nuclear scattering length density determined in section 5.3.3.1

SANSPOL Polarized small-angle neutron scattering measurements were performed at the D22 instrument at ILL (3.1.5). The nanoparticle dispersions were filled into Hellma quartz cuvettes with a sample thickness of 1 mm. A variable magnetic field up to 1.5 T was applied at the sample position in a horizontal direction perpendicular to the incoming beam. The incoming wavelength was set to 6 Å, and the small angle scattering was detected in dependence of the polarization state of the incoming neutrons. The collimation was set to 8 m, and two detector distances of 2 and 8 m were combined in

order to achieve a wide momentum transfer range. With a collimation aperture of 55 mm, a sample aperture of 7 mm, and a detector pixel size of 8 mm, the angular divergence of 7.36 mrad and 6.84 mrad for detector distances of 2 m and 8 m, respectively, was obtained using equation (2.2.37).

Measurements were performed at 21 different applied magnetic fields in the range of 0.005 T up to 1.54 T for the samples with lowest and highest concentration, whereas the s50, c50, and tc50 samples were studied at 0.005 T and 1.54 T. For each magnetic field, the small angle scattering was recorded for the polarization of the incoming neutron spins parallel (+) and antiparallel (-) to the applied magnetic field. The polarization at the chosen wavelength was 0.89, and the flipper efficiency was 0.99.

Data correction to the scattering background of pure d_8-toluene and cadmium, normalization to absolute intensities, and sector integrations were performed using the program grasp [147]. Cuts of the SANS intensity parallel or perpendicular to the applied magnetic field were performed by radial integration of sectors with a width of 10° in the respective azimuthal angle. Because the magnetic scattering depending on the azimuthal angle follows a $\sin^2(\alpha)$ slope, the error induced in the magnetic scattering contribution by this approach is as low as 0.26 %. As this error is lower than the statistical error bars of the data, no further correction was performed to account for the averaging effect of the radial integration.

5.3.2.2. Development of the magnetic form factor model

In order to refine the magnetic small angle scattering, a geometric model has to be developed for the magnetic form factor. This model should allow for a successive implementation of more parameters to describe the magnetization density close to the particle surface. The magnetic form factor was modelled according to a core shell model of a spherical core with constant scattering length density (SLD) and a linear decreasing shell. The scattering length density profile of the chosen magnetization density model is presented in Figure 5.3.1a. It can be separated into four simple partial contributions as presented in Figure 5.3.1b in order to obtain an analytical derivation of the scattering. Similar to the core shell form factor of a sphere with a constant shell thickness derived in section 2.2.2, the scattering amplitude is derived by linear combination of the amplitudes of these partial scattering length density profiles weighted by the respective scattering contrasts [19]. The resulting expression for the magnetic form factor is

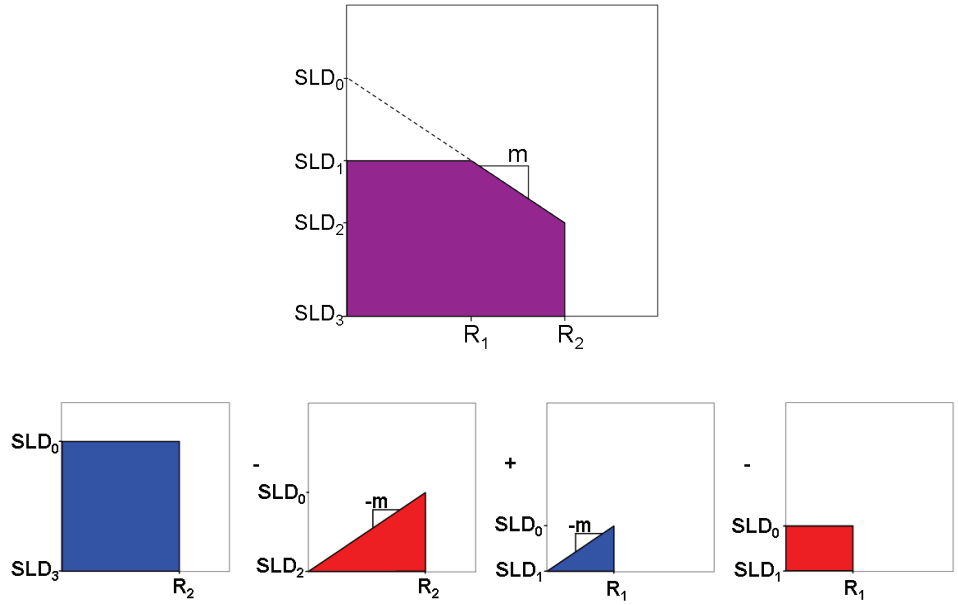

Figure 5.3.1.: SLD profile of the magnetization density model (top) and its separation into four partial contributions (bottom), where m is the slope of the linear density variation towards the surface (here: $m < 0$).

$$\begin{aligned} F_M(Q) = (SLD_0 - SLD_3) \cdot F_{sph}(Q, R_2) \\ - F_{lin}(Q, R_2, -m) \\ + F_{lin}(Q, R_1, -m) \\ - (SLD_0 - SLD_1) \cdot F_{sph}(Q, R_1) \end{aligned} \tag{5.3.1}$$

as presented in Figure 5.3.1b with the amplitudes of a sphere with constant SLD $F_{sph}(Q, R)$ and a sphere with linearly deviating SLD $F_{lin}(Q, R, m)$ as introduced in equations (2.2.23) and (2.2.24), respectively, as well as the slope m and the scattering length density SLD_0

$$m = \frac{SLD_1 - SLD_2}{R_1 - R_2} \tag{5.3.2}$$

$$SLD_0 = SLD_1 - \frac{(SLD_1 - SLD_2) \cdot R_1}{R_1 - R_2} \tag{5.3.3}$$

In case of $R_1 = R_2$, equation (5.3.1) is reduced to

$$F_M(Q) = (SLD_1 - SLD_3) \cdot F_{sph}(Q, R) \tag{5.3.4}$$

Because the scattering length density of the matrix is nonmagnetic ($SLD_3 = 0$), the magnetic form factor amplitude $F_M(Q)$ depends on four independent parameters: R_1, R_2, SLD_1, and SLD_2. In order to derive the four different form factor models discussed in section 5.1.3.3, some parameters were constrained as given in Table 5.3.2.

Table 5.3.2.: Magnetic amplitude constraints. R_m, R_n, and SLD_m denote the magnetic and nuclear particle radius as well as the magnetic scattering length density.

model	R_1	R_2	SLD_1	SLD_2
1	$R_m \equiv R_n$	$R_1 + 0.01$	SLD_m*	0
2	R_m*	$R_1 + 0.01$	SLD_m*	0
3	R_m*	R_n	SLD_m*	0
4	R_m*	R_n	SLD_m*	$SLD_{m,shell}$*

*Fit parameter. All remaining parameters were either fixed or constrained during refinement.

As nuclear form factor amplitude F_N, the core shell amplitude of a sphere with a uniform shell thickness as derived in section 2.2.2 with a core radius R_n was implemented. The codes for calculation of the scattering cross sections for magnetic contrast varia-

tion and the magnetic-nuclear cross term according to equations (5.3.11) and (5.3.12), respectively, are given in Appendices D.4 and D.5.

5.3.2.3. Determination of the magnetization density

There are two independent routes to calculate the atomic and volume magnetization densities of the investigated nanoparticles by the results of the Langevin fits in section 5.3.3.1. First, the obtained saturation magnetic SLD can be converted into magnetization densities directly via equation (2.2.57)

$$M_v^{\perp} = \frac{\Sigma M_j^{\perp}}{V_m} = \frac{SLD_m^{sat}}{0.27 \cdot 10^{-12} cm} \tag{5.3.5}$$

with V_m the molecular volume of the formula unit Fe_2O_3, M_v the volume magnetization, and $M_j^{\perp}$ the atomic magnetization of the atom j perpendicular to the scattering vector Q. The molecular volume can be derived from the determined nuclear scattering length density and the tabulated scattering lengths for iron and oxygen

$$V_m = \frac{\Sigma b_j}{SLD_n} \tag{5.3.6}$$

With the scattering length densities determined by purely nuclear SANS in section 5.3.3.1, volumes of the formula unit Fe_2O_3 of 5.37 (4) $\cdot 10^{-2}$ nm^3 and 5.51 (4) $\cdot 10^{-2}$ nm^3 are calculated for the nanospheres s7 and the nanocubes c7, respectively. These are in good agreement with the volume of the formula unit V_m = 5.45 $\cdot 10^{-2}$ nm^3 derived from the bulk lattice constant of maghemite (a = 8.348 Å).

The second approach to calculate the magnetization density originates in the integral particle moment M(R) determined by the argument of the Langevin function (see equation (5.3.18)). For a particle of uniform magnetization density, the volume magnetization density is obtained by

$$M(R) = M_v \cdot V(R) \tag{5.3.7}$$

For the magnetic form factor model with a linear magnetic shell, an effective magnetic particle volume has to be derived that fulfills

$$M(R_m, R_n) = M_v^c \cdot V_{eff}(R_m, R_n) \tag{5.3.8}$$

with M_v^c the magnetization density in the magnetic particle core. The effective magnetic particle volume is derived by integration of the magnetic scattering length density profile:

$$M(R_m, R_n) = M_v^c \cdot V(R_m) + \int_{R_m}^{R_n} M_v^c \cdot \frac{R - R_m}{R_n - R_m} \cdot 4\pi R^2 dR \tag{5.3.9}$$

resulting in

$$M(R_m, R_n) = M_v^c \cdot V_{eff}(R_m, R_n) = M_v^c \cdot \frac{4}{3}\pi \left[R_n^3 + \frac{R_m(R_n^3 - R_m^3) - \frac{3}{4}(R_n^4 - R_m^4)}{(R_n - R_m)} \right] \tag{5.3.10}$$

An estimated value for the bulk magnetization density, neglecting any temperature effects that would decrease the average magnetization density, can be determined form the bulk crystal structure. Magnetite, Fe_3O_4, has an inverse spinel structure consisting of 8 tetrahedral positions, occupied by Fe^{3+} ions, and 16 octahedral sites, occupied by 8 Fe^{3+} and 8 Fe^{2+} ions. The spins at the tetrahedral and octahedral sites are aligned antiparallel, leading to a ferrimagnetic arrangement. With S = $5/2$ for Fe^{3+} and S = 2 for Fe^{2+}, an average magnetic moment of $4/3\ \mu_B$ per Fe atom is calculated.

Maghemite, γ-Fe_2O_3, crystallizes in the same inverse spinel structure with vacancies at the octahedral sites $[Fe^{3+}]_t[Fe^{3+}_{5/3}[]_{1/3}]_oO_4^{2-}$. For this crystal structure, an average magnetic moment of 1.25 μ_B per Fe atom is calculated.

5.3.3. Results and Discussion

For investigation of the magnetization density in individual nanoparticles and possible magnetic interparticle interactions, a SANSPOL study on the magnetic form factor was performed on the Bs 10 nanospheres and the Bc 9 nanocubes samples that were precharacterized in section 5.1. Dispersions in d_8-toluene were used in three different concentrations as denoted in Table 5.3.1. Concerning the nanocubes, two different sample batches were investigated. While the sample labelled 'tc50' consists of slightly truncated nanocubes of the same batch as those characterized before, the samples labelled 'c7' and 'c50', and 'cmax' had been observed by TEM to be less truncated [106] and were thus expected to show a stronger shape dependent behavior. Different concentrations were investigated ranging from 0.14 vol-% for the investigation of the magnetic form factor and the magnetization density of single particles up to 5 vol-% for the study of magnetic and nuclear interparticle correlations as expressed by structure factors.

5.3.3.1. Approaching the magnetic form factor

For very dilute and thus non-interacting nanoparticle dispersions, interparticle interaction contributions to the small-angle scattering can be neglected and the structure factor

is set to S(Q)= 1. If a complete alignment of the magnetic moments in a saturating external field is assumed, equations (2.2.64) and (2.2.68) are simplified to

$$\begin{aligned} I^{+}(Q,\alpha) &= F_N^2(Q) + [F_M^2(Q) - 2PF_N(Q)F_M(Q)]sin^2\alpha \\ I^{-}(Q,\alpha) &= F_N^2(Q) + [F_M^2(Q) + 2P\varepsilon F_N(Q)F_M(Q)]sin^2\alpha \end{aligned} \tag{5.3.11}$$

$$I^{+}(Q,\alpha) - I^{-}(Q,\alpha) = -2P(1+\varepsilon)F_N(Q)F_M(Q)sin^2\alpha \tag{5.3.12}$$

$$I^{+}(Q,\alpha) + I^{-}(Q,\alpha) = 2F_N^2(Q) + 2F_M^2(Q)sin^2\alpha \tag{5.3.13}$$

with α the azimuthal angle between Q and the magnetic field direction, P the degree of polarization of the incoming neutron beam, and ε the flipper efficiency. In equation (5.3.13), the flipper efficiency is neglected.

Exemplarily for the dilute samples used for determination of the magnetic form factor, detector images of the s50 sample, measured with a detector distance of 8 m, are presented in Figure 5.3.2. The visible difference between Figures 5.3.2a and 5.3.2b indicates the presence of magnetic scattering contributions. In the horizontal direction parallel to the magnetic field (α = 0) pure nuclear scattering is observed, and I(+) and I(-) are equal in intensity, leading to zero intensity in the difference as visible in Figure 5.3.2c.

As visible in equation (5.3.13), conventional non-polarized SANS without application of a magnetic field as performed in section 5.1.3.2 always contains magnetic scattering contributions. The primary purpose of the conventional SANS experiments described in section 5.1.3.2 was the determination of the oleic acid ligand shell thickness. As the magnetic scattering is small compared to the nuclear scattering, the determination of the ligand shell is in a first approximation not affected by disregard of the magnetic scattering contribution. For the precise determination of the magnetic form factor, however, it is important to determine the purely nuclear form factor with good precision. Knowing the nuclear form factor parameters will allow for refining solely the magnetic scattering contribution in the polarized SANS via both the magnetic contrast variation and the magnetic-nuclear cross term.

The purely nuclear form factor Magnetic scattering - both with and without use of polarized neutrons - is proportional to the projection of the magnetic moment onto a plane perpendicular to the scattering vector Q. This is expressed by the $\sin^2(\alpha)$ terms in equations (5.3.11) - (5.3.13). Consequently, the pure nuclear scattering can be separated by a SANS measurement with Q ∥ H (*i.e.* α= 0) in a saturating magnetic field, where all

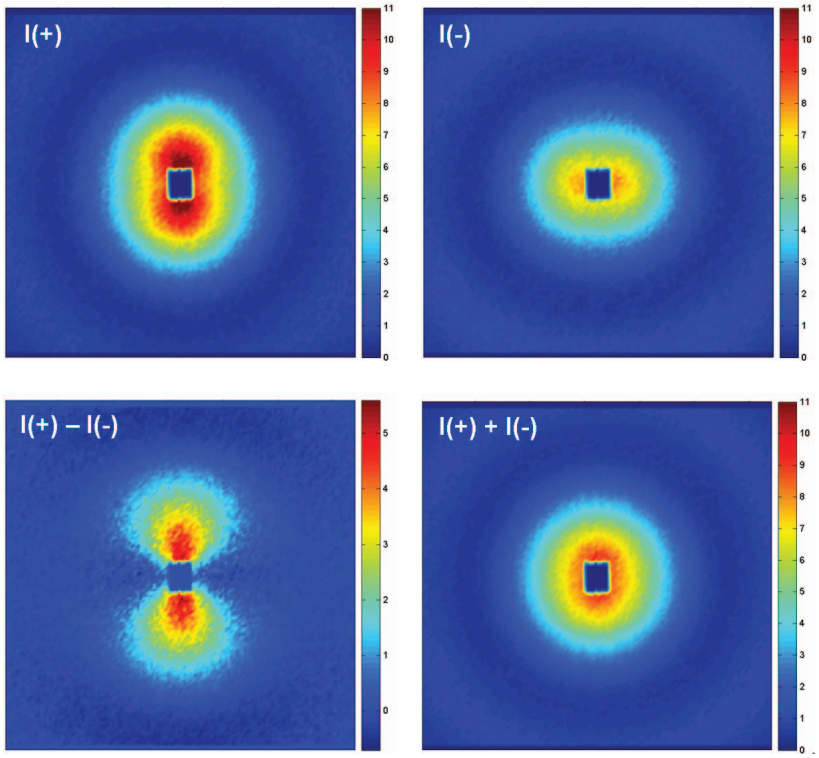

Figure 5.3.2.: 2D SANSPOL data by s50. a) and b) show the measured and normalized data for the two polarization states at 8 m detector distance. A magnetic field was applied horizontally. c) and d) show combinations thereof according to equations (5.3.12) and (5.3.13), respectively. The unit of the color bar is cm^{-1}.

particle spins are aligned. For better statistics, a 10° sector was integrated around α= 0 in the nonpolarized (I(+) + I(-)) SANS detector images measured in high magnetic field. The resulting scattering curves for the nanospheres samples s7 and s50 are presented in Figure 5.3.3b.

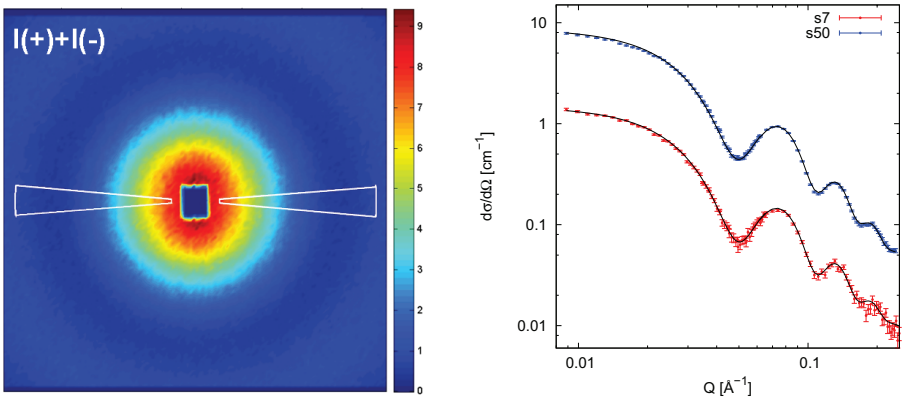

(a) Sector integration of the pure nuclear scattering by s50 with 8 m detector distance.

(b) Purely nuclear SANS by s7 and s50.

Figure 5.3.3.: Purely nuclear SANS.

The scattering length density (SLD) of the core material is not known with high precision because it depends on the mass density of the nanoparticles that can slightly change with particle size. A determination of the mass density and thus the SLD by diffraction methods and refinement of the nuclear SANS led to inconsistent results for parameters such as the core radius and the shell thickness, which should be independent on the particle concentration. For this reason a different approach for determination of the core SLD was applied.

The particle number density, which is equal to the absolute intensity of normalized small-angle scattering, depends on the mass of the inorganic fraction of the sample, the particle core radius, and the mass density. The mass concentration of the samples is known in high precision (see Table 5.3.1). Thus, the particle number density was constrained to the core radius and the SLD, which were both fit parameters in the nuclear form factor refinement. As explained in section 5.1.3.2, scattering contributions of a constant incoherent background and free oleic acid micelles were included to the fit. The resultant parameters for s7 and s50 are presented in Table 5.3.3. The good agreement of the obtained values for SLD, core radius, and shell thickness for the two differently concentrated dispersions justifies the approach of a constrained refinement of the SLD. The determined SLD is in between those of magnetite (6.96 $\cdot 10^{10}$ cm^{-2}) and maghemite

($6.68 \cdot 10^{10}$ cm^{-2}) as calculated using bulk mass densities. The obtained core radius is furthermore in good agreement with the results obtained by SAXS in section 5.1.3.1.

Table 5.3.3.: Purely nuclear nanospheres form factor. The particle number density N was constrained with SLD_{core}, R_{core}, and the mass concentration of the samples. N_{OA} denotes the number density of excess oleic acid micelles.

		s7	s50
N	[10^{16} ml^{-1}]	0.284	1.943
SLD_{core}	[10^{10} cm^{-2}]	6.76 (5)	6.78 (1)
R_{core}[a]	[Å]	49.7 (2)	49.89 (9)
dR_{shell}	[Å]	14.8 (1)	14.18 (6)
background	[cm^{-1}]	0.0072 (4)	0.0318 (8)
N_{OA}	[10^{16} ml^{-1}]	0.987 (2)	10.4 (5)
χ^2_{red}		1.19	2.49

[a]The core radius is thus close to that determined to 49.56 (2) Å by SAXS in section 5.1.3.1

The amount of excess oleic acid micelles as compared to the particle number density may seem high. However, such amounts of oleic acid are required for well dispersed nanoparticle systems exhibiting a pure form factor behavior [106]. The iron oxide nanoparticles exhibit a high coherent scattering cross section, larger contrasts, and a larger particle size as compared to the oleic acid micelles. Thus, the iron oxide form factor minima are not superposed significantly by the oleic acid scattering contribution (while for the same reasons excess ligand micelles do constitute a problem for small angle scattering by cobalt nanoparticles). However, because the purely nuclear scattering contributions will not be refined simultaneously with the magnetic form factor, it is sufficient to model the nuclear scattering as precisely as possible and keep these parameters fixed afterwards. The magnetic scattering does not contain any scattering contributions by excess oleic acid micelles. In contrast, interparticle interactions might contribute to the magnetic scattering and thus complicate the determination of the magnetic form factor. This justifies a posteriori the tolerance of a high amount of excess oleic acid.

The results of SAXS and unpolarized SANS in section 5.1.3 show that the shape difference between nanocubes and nanospheres can not be resolved by small angle scattering for the studied orientationally averaged nanocubes. For this reason, the small angle scattering by iron oxide nanocubes discussed in this section will be refined with spherical form factors. Refinement of the purely nuclear form factor was initially performed by the same approach as explained for the nanospheres. Due to remaining inconsisten-

cies for the three samples c7, c50, and tc50 during initial refinements, the purely nuclear scattering was finally refined simultaneously with the data obtained by magnetic contrast variation with polarized neutrons. For this purpose, sectors of 10° were integrated around Q ⊥ H in the polarized SANS detector images measured in a saturating magnetic field (I(+) and I(-)). These curves were refined by equation (5.3.11) with a simple spherical magnetic form factor of the same radius as the nuclear form factor[5]. Thus, the nuclear contrast was constrained to be in between the varied contrasts by the two polarization states I(+) and I(-). The results of the form factor refinement of the nanocubes are shown in Figure 5.3.4. While the dilute sample c7 can be refined with a pure form factor behavior, the more concentrated sample c50 exhibits a small structure factor preventing the form factor refinement at smaller Q. The sample with the same particle concentration but higher truncation, tc50, can still be refined with a pure form factor behavior, and the resulting parameters for c7 and tc50 are compared in Table 5.3.4.

Table 5.3.4.: Purely nuclear nanocubes form factor. The particle number density N was constrained with SLD_{core}, R_{core}, and the mass concentration of the samples. N_{OA} denotes the number density of excess oleic acid micelles.

		c7	tc50
N	[10^{16} ml^{-1}]	0.221	1.529
SLD_{core}	[10^{10} cm^{-2}]	6.60 (5)	6.83 (1)
R_{core}[a]	[Å]	54.4 (3)	53.9 (1)
dR_{shell}	[Å]	14.3 (1)	13.1 (1)
background	[cm^{-1}]	0.0074 (4)	0.0674 (8)
N_{OA}	[10^{16} ml^{-1}]	2.1 (2)	21.1 (5)
χ^2_{red}		2.09	5.04

[a]The core radius was determined to 53.25 (7) Å by SAXS in section 5.1.3.1

Due to their slightly different particle shape and the error introduced by refinement with a spherical form factor, the parameters for the c7 and tc50 samples are not as comparable as those of the nanospheres. The density of an orientationally averaged cube is underestimated if described by the density profile of a sphere, as observed by the lower SLD of c7. The tc50 sample, which is supposed to have a larger degree of truncation,

[5]This corresponds to the first model for the magnetic form factor which will be introduced later in this section.

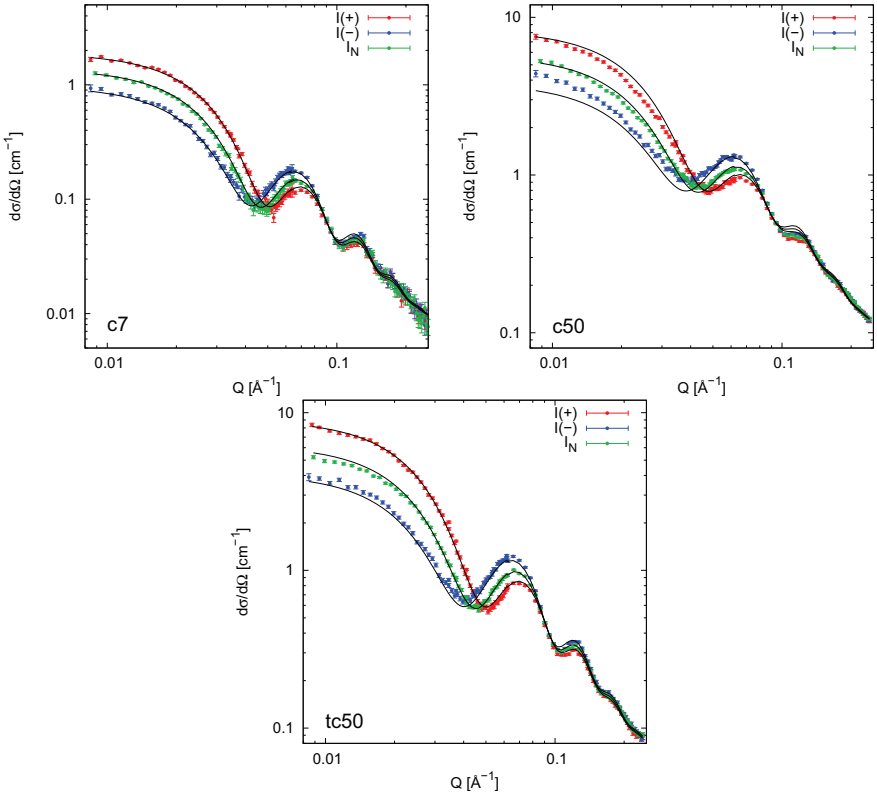

Figure 5.3.4.: Purely nuclear SANS by c7, c50, and tc50.

has a shape somewhat closer to that of a sphere, and thus the determined SLD is also closer to that of the nanospheres.

The obtained particle sizes for the two nanocubes samples are in rough agreement and are closer to the particle size of the Bc 9b sample as determined by SAXS (see section 5.1.3.1). This is in agreement with the fact that the samples were dispersed rather freshly for the SANSPOL measurements, as was the Bc 9b sample. The slightly smaller particle size of tc50, in combination with the smaller particle size of Bc 9a as compared to Bc 9b, suggests an increase of the degree of truncation if the nanocubes are stored in toluene dispersion. This observation will also be discussed regarding the nanoparticle assembly into higher dimensional nanostructures in section 5.4.3.4.

For the determination of the magnetic form factor, a pure form factor behavior of the samples is crucial. This criterion is not fulfilled by the c50 sample, exhibiting a small structure factor in the lower Q range. For this reason, this samples is excluded for the refinement of the magnetic form factor.

Magnetic form factor models In order to refine the magnetic form factor, four different models with increasing complexity and number of parameters were investigated. The contrast profiles for the applied models are presented in Figure 5.3.5. As the most simple model (Figure 5.3.5a), the magnetic form factor was assumed to be a sphere of the same size as in the nuclear form factor. The only fit parameter for this model is the magnetic scattering length density (SLD_m). In the second model (Figure 5.3.5b), the radius of the magnetic core was refined as a further parameter independent of the nuclear particle radius. A smaller magnetic radius accounts for a possible magnetic dead layer at the surface of the nanoparticle. Because the decrease of magnetization is not likely to occur in a sharp step at the edge of the magnetic core, a linear decrease of SLD_m was introduced in the third model (Figure 5.3.5c). Here, the SLD_m at the surface of the particle is constrained to 0, with the result of SLD_m and the magnetic core radius as the only fit parameters, same as in model 2. A fourth model was introduced to account for a residual magnetic moment at the particle surface (Figure 5.3.5d). The magnetic scattering length density at the particle surface was added as additional fit parameter that can be either higher or lower than the magnetic scattering length density of the magnetic core. In order to enhance the computational comparability of the four models, one global model was applied with different constraints leading to the discussed magnetic form factor models. For the development of the global model see section 5.3.2.2.

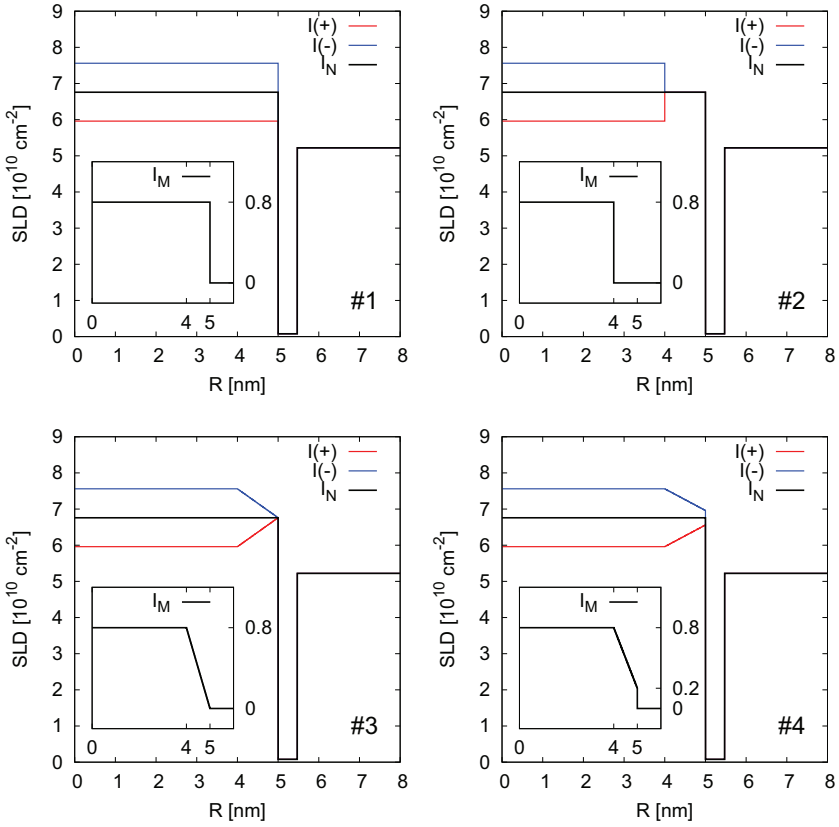

Figure 5.3.5.: Four contrast profile models for the magnetic form factor. The magnetic contrast variation for polarized neutrons is simulated according to equation (5.3.11). The contrast profiles for the purely magnetic form factors are presented in the insets.

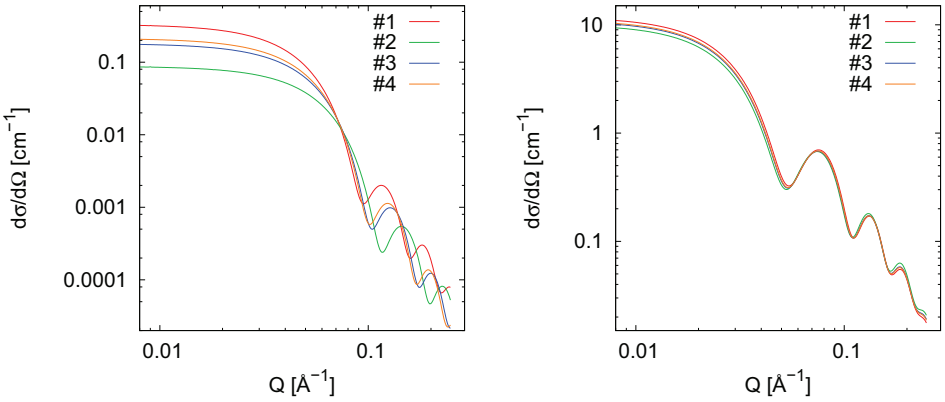

(a) Simulation of the magnetic form factor.

(b) Simulation of the polarized small angle scattering I(+) = $(F_N - F_M)^2$. The nuclear parameters were applied as determined for the s50 nanospheres.

Figure 5.3.6.: Simulated magnetic SANS according to the four contrast profile models given in Figure 5.3.5. Parameters applied for the magnetic form factor are R_m = 4 nm, R_n = 5 nm, SLD_m = 0.8 ·10^{10} cm^{-2}, and $SLD_{m,shell}$ = 0.2 ·10^{10} cm^{-2}. A lognormal size distribution of the magnetic form factor of 5.5 % and the Q resolution of the D22 instrument were implemented .

In Figure 5.3.6, simulated scattering curves for the four different models with parameters as given in Figure 5.3.5 are compared. Comparison of the pure magnetic form factor in Figure 5.3.6a reveals a significant difference between the first two models due to the relatively large difference of the magnetic radius R_m. The third and fourth model magnetic form factors are intermediate between the extreme values of the first two models as are the scattering length density profiles. Note that the magnetic form factors with model 3 and 4 are very similar in a wide range of the observed momentum transfer range.

Figure 5.3.6b compares polarized neutron scattering curves I(+) simulated for the four different models by taking into account the nuclear form factor. These are scattering curves experimentally accessible by polarized neutron scattering. Due to its large core shell contrast the nuclear form factor is two orders of magnitude higher in intensity than the magnetic form factor. As a result, the relative influence of the magnetic contrast profile is low, and the difference between the simulated scattering curves for the four models is small. Note that the difference of the magnetic and nuclear radius of 1 nm was chosen relatively large for display. In reality, the radii difference is expected significantly smaller. This further illustrates the importance of a precise determination

of the structural parameters before refinement of the magnetic scattering contribution.

The similarity of the scattering curves simulated for the third and fourth models indicates the limit of this method and justifies the simple linear decay of the magnetic scattering length density towards the particle surface. A more complicated model of a smoother magnetic contrast profile is more realistic than a linear decay, but the resulting scattering curve is probably not specifiable against the linear models.

Refinement of the magnetic form factor There are two possible strategies for determination of the magnetic form factor by SANSPOL experiments. First, the magnetic contrast variation by the polarization state of the incoming neutrons allows for a simultaneous refinement of the magnetic scattering contribution in I(+) and I(-) according to equation (5.3.11). Alternatively, the magnetic-nuclear cross term, which is derived by the difference I(+) - I(-), is linear in both the magnetic and the nuclear form factor amplitudes and can be refined by equation (5.3.12). If the nuclear form factor is well known and $|F_M| \ll |F_N|$, the two approaches are equivalent.

The magnetic form factor was refined by both approaches for two different nanoparticle concentrations each for the nanospheres and nanocubes. The magnetic contrast variation and magnetic-nuclear cross term intensities of the s7 and s50 samples are presented in Figure 5.3.7, along with fits according to the third model of the magnetic form factor (Figure 5.3.5c). Resultant parameters of the fits of the four different models to the four data sets are given in Table 5.3.5. The parameters determined for each form factor model are consistent for both sample concentrations and the two different refinement approaches. Generally, a significant decrease in χ^2_{red} is observed between the first and second models, which justifies the implementation of the magnetic core radius as a fit parameter. Along with a decrease of the magnetic core radius, the magnetic scattering length density increases, because each refinement will approximately result in the correct integral magnetization density of the whole particle. If the volume of the magnetic particle is constrained to the nuclear particle volume, the refined SLD_m is consequently lower than for the smaller, true magnetic particle volume. The χ^2_{red} values for the third model are comparable to the second model, but slightly lower in case of the s50 sample. The trend of rising SLD_m with decreasing magnetic core radius is still observed, although to a lower extent as for the first and second models. For the fourth model, the SLD_m is unchanged compared to the third model, while the magnetic core radius decreases with an increased magnetic scattering length density at the nuclear particle surface ($SLD_{m,shell}$), which was constrained to 0 for the third model. However, the χ^2_{red}

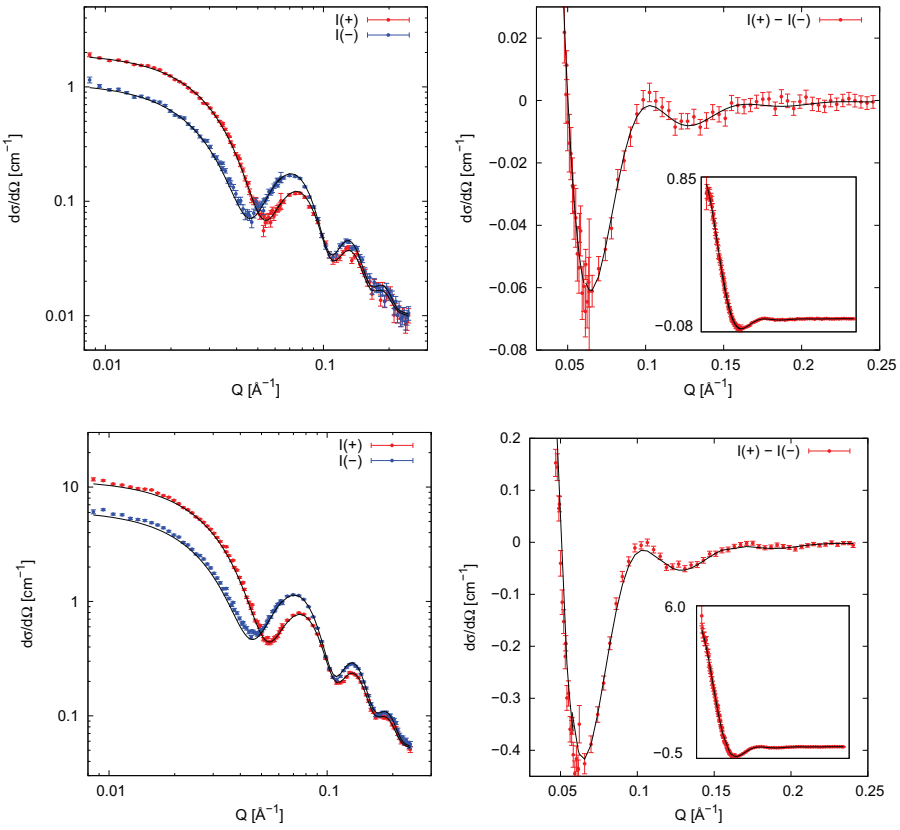

Figure 5.3.7.: Refinement of the nanospheres magnetic form factor. Refinements according to the third model (Figure 5.3.5c) of the magnetic form factor via the magnetic contrast variation (left column) and the magnetic-nuclear cross term (right column) are presented for both the s7 (top row) and s50 (bottom row) samples. The full intensity range of the cross term is given in the inset.

is not reduced, but rather slightly increased for the fourth model, despite the additional fit parameter. For this reason, the second and third models appear to be the best description of the true magnetic form factor as far as obtainable from the present data sets. While the fits to the second and third models are hard to distinguish, the third model itself seems more realistic because of the gradual decrease of the magnetization towards the particle surface instead of a sharp step. For this reason, the third model of a magnetic core with constant magnetization and a linear decrease towards the particle surface is preferred. The determined magnetic particle core has a size of 4.7 (1) nm in radius, which is 0.3 nm smaller than the nuclear particle radius. These 0.3 nm may be result from a magnetic dead layer at the particle surface, originating from either spin canting or vanishing magnetic moments towards the surface.

Table 5.3.5.: Magnetic form factor determined for nanospheres.

			s7		s50	
model	parameter		contrast	cross term	contrast	cross term
#1	SLD_m	[10^{10} cm^{-2}]	0.77 (1)	0.764 (4)	0.75 (1)	0.747 (6)
	χ^2_{red}		2.27	0.63	7.77	3.28
#2	SLD_m	[10^{10} cm^{-2}]	0.81 (1)	0.824 (8)	0.81 (1)	0.83 (1)
	R_m*	[nm]	4.76 (5)	4.74 (5)	4.60 (5)	4.81 (5)
	χ^2_{red}		2.20	0.52	6.61	1.35
#3	SLD_m	[10^{10} cm^{-2}]	0.83 (1)	0.807 (8)	0.86 (2)	0.83 (1)
	R_m*	[nm]	4.70 (9)	4.74 (5)	4.40 (9)	4.51 (4)
	χ^2_{red}		2.20	0.50	6.40	1.34
#4	SLD_m	[10^{10} cm^{-2}]	0.82 (1)	0.81 (1)	0.86 (2)	0.83 (1)
	R_m*	[nm]	4.7 (2)	4.6 (2)	4.3 (2)	4.2 (2)
	$SLD_{m,shell}$	[10^{10} cm^{-2}]	0.2 (1)	0.3 (1)	0.1 (1)	0.3 (1)
	χ^2_{red}		2.21	0.52	6.44	1.33

* R_n was determined as 4.97(2) nm

As for the nanospheres, both the magnetic contrast variation and the magnetic-nuclear cross term intensities of the nanocubes samples c7 and tc50 were refined by the four models of the magnetic form factor. Plots of the data as refined according to the third model (Figure 5.3.5c) are presented in Figure 5.3.8. The resulting parameters are given in Table 5.3.6. In general the same tendencies are observed as for the nanospheres, with a magnetic core radius smaller than the particle radius and a core magnetic scattering

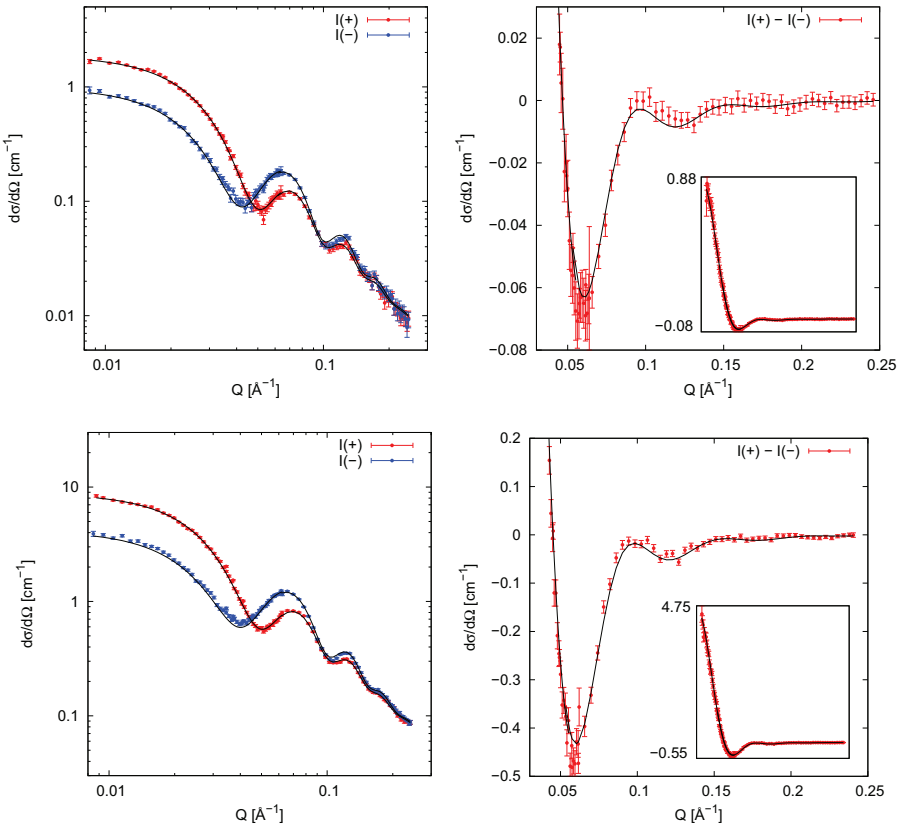

Figure 5.3.8.: Refinement of the nanocubes magnetic form factor. Refinements according to the third model (Figure 5.3.5c) of the magnetic form factor via the magnetic contrast variation (left column) and the magnetic-nuclear cross term (right column) are presented for both the c7 (top row) and tc50 (bottom row) samples. The full intensity range of the cross term is given in the inset.

length density of comparable magnitude for both particle shapes. According to the obtained χ^2_{red} values, the third model is again considered the best fit, which is furthermore supported by the better consistency of the parameters obtained by the different approaches and particle concentrations for this model.

The observation of $\chi^2_{red} < 1$ for the cross term refinements of the c7 and s7 samples indicates that either the noise of the data has been fit by the model or the data uncertainties have been overestimated. Considering the large data uncertainties and the good agreement of the fit results with the parameters obtained from magnetic contrast variation, overestimation of the data uncertainties seems likely. This is supported by the much better quality of the cross term refinements for the s50 and tc50 samples nonetheless yielding results comparable to the s7 and c7 samples.

Table 5.3.6.: Magnetic form factor determined for nanocubes.

			c7		tc50	
model	parameter		contrast	cross term	contrast	cross term
#1	SLD_m	[10^{10} cm^{-2}]	0.708 (5)	0.70 (1)	0.720 (6)	0.719 (7)
	χ^2_{red}		2.01	1.34	5.49	4.23
#2	SLD_m	[10^{10} cm^{-2}]	0.82 (1)	0.84 (1)	0.84 (1)	0.817 (8)
	R_m*	[nm]	5.28 (8)	5.10 (8)	4.62 (9)	4.72 (6)
	χ^2_{red}		1.62	0.54	3.80	1.65
#3	SLD_m	[10^{10} cm^{-2}]	0.82 (2)	0.79 (2)	0.84 (1)	0.82 (1)
	R_m*	[nm]	4.82 (9)	4.88 (9)	4.63 (9)	4.71 (9)
	χ^2_{red}		1.63	0.49	3.78	1.65
#4	SLD_m	[10^{10} cm^{-2}]	0.83 (2)	0.80 (2)	0.86 (2)	0.84 (1)
	R_m*	[nm]	4.3 (2)	4.7 (2)	4.2 (2)	4.0 (2)
	$SLD_{m,shell}$	[10^{10} cm^{-2}]	0.3 (1)	0.1 (1)	0.2 (1)	0.4 (1)
	χ^2_{red}		1.63	0.47	3.83	1.65

* R_n was determined as 5.44(3) nm

The determined magnetic core of the cubic nanoparticles has a radius of 4.8 (1) nm, equivalent to a surface layer with a lower magnetic moment of 0.6 nm thickness, which is twice as thick as observed for the nanospheres. In order to rule out the systematic error arising from refinement with spherical form factors instead of a cubic form factor, the volumes and edge lengths of the nuclear and magnetic form factors can be determined. The nuclear particle radius of 5.4 nm corresponds to a nuclear volume of 660 nm^3, which in turn corresponds to edge lengths of 8.7 nm and 9.25 nm for a perfect and

a maximal truncated cube (with $t = \frac{1}{2}a$), respectively. Similarly, the magnetic core radius of 4.8 nm corresponds to a magnetic volume of 463 nm^3 and edge lengths of 7.7 nm and 8.2 nm for the perfect and truncated magnetic cubes, respectively. Thus, even considering the cubic shape the surface layer of lower magnetic moment has a thickness of ~ 0.5 nm regardless the degree of truncation.

Consistently for both particle shapes, a magnetically dead surface layer with a thickness in the range of 0.3 - 0.5 nm is thus found. The decreasing magnetization density in this region may be due to either vanishing moments towards the particle surface or spin canting due to the surface anisotropy. The larger thickness of this surface layer found for the nanocubes indicates a higher spin canting at the cube corners and may thus be a direct consequence of the shape anisotropy. In order to determine the origin of the magnetic dead layer, SANS experiments with polarized neutrons and polarization analysis are required. By measurement of the spin flip and non spin flip intensities for up to three different magnetic field directions the magnetic scattering by those moments that are not aligned in the external magnetic field can be separated.

Field dependent magnetization density The determination of the magnetic form factor by refinement of the magnetic contrast variation and the magnetic-nuclear cross term, was performed by measurements in a high magnetic field H > 1.2 T, which was assumed to saturate the sample according to the magnetization measurements discussed in section 5.1.3.3. In what follows, the field dependence of the magnetic form factor will be investigated.

The magnetic scattering length density, which depends on the projection of the magnetic moment onto a plane perpendicular to Q, can be treated as a measure of the orientation of the particles in the applied magnetic field. The magnetic form factor amplitude in equations (5.3.11)-(5.3.13) is thus scaled by a Langevin function

$$L(x) = coth(x) - \frac{1}{x} \tag{5.3.14}$$

with

$$x = \frac{M(R)H_{eff}}{k_B T} \tag{5.3.15}$$

where M(R) is the nanoparticle moment, H_{eff} the effective magnetic field, k_B the Boltzmann constant, and T the temperature. After the magnetic form factor has been determined in high magnetic fields, a determination of the field dependence and the

Langevin behavior will give quantitative information on the magnetization density extrapolated to saturation.

For the most dilute samples, s7 and c7, both magnetic contrast variation and magnetic-nuclear cross term were refined in dependence of the applied magnetic field using the third model of the magnetic form factor with the parameters as determined in high magnetic field. The magnetic scattering length density as a measure of the orientation of the particles in the applied magnetic field was refined as the only fit parameter. The resulting variation of the magnetic scattering length density in dependence of the applied magnetic field is presented in Figure 5.3.9.

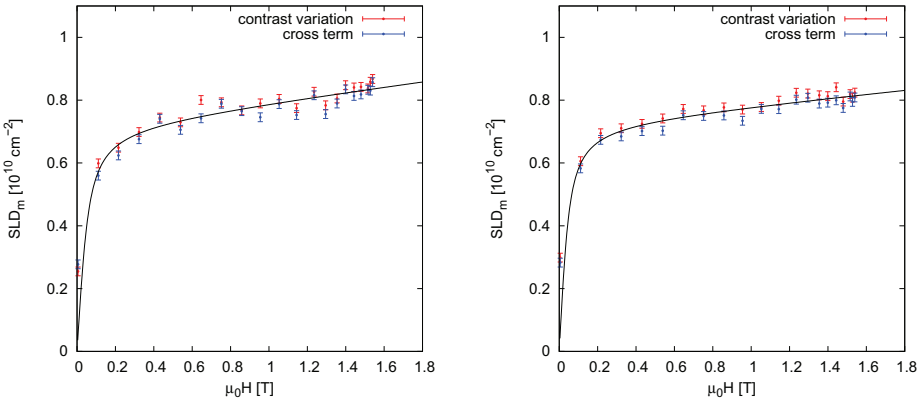

(a) Langevin behavior of the nanospheres s7.

(b) Langevin behavior of the nanocubes c7.

Figure 5.3.9.: Field dependent magnetic scattering length density.

When refining the magnetic contrast variation (by a simultaneous refinement of $I(+)$ and $I(-)$), the nonperfect alignment of the particle moments in low magnetic fields has to be taken into account. According to equation (2.2.64), the magnetic contrast variation of non-interacting nanoparticles (S(Q) = 1) and Q $\perp$ H (sinα = 1) is given by

$$I(\mp) = F_N^2 \pm 2F_N F_M L(x) + F_M^2 \left(1 - \frac{L(x)}{x}\right) \tag{5.3.16}$$

as opposed to

$$I(\mp) = F_N^2 \pm 2F_N F_M L(x) + F_M^2 L^2(x) \tag{5.3.17}$$

which was assumed for the refinements leading to Figure 5.3.9. From equations (5.3.16) and (5.3.17) it follows that the correction of nonperfect particle moment alignment does not influence the magnetic-nuclear cross term. Because the magnetic form factor is con-

siderably smaller in intensity than the nuclear form factor, the F_M^2 term in equation (5.3.16) has a much lower weight than the $F_N F_M$ term, and the contribution of nonperfect alignment is thus close to negligible. This is justified by the good agreement of the field dependent SLD_m as determined by either magnetic contrast variation or the magnetic-nuclear cross term using equation (5.3.17) and presented in Figure 5.3.9.

The field dependent magnetic scattering length density exhibits a Langevin behavior that can be fit with an additional linear contribution at high fields according to

$$SLD_m = SLD_m^{sat} \cdot L(M(R)\mu_0 H/k_B T) + \chi\mu_0 H \tag{5.3.18}$$

with fit results given in Table 5.3.7.

Table 5.3.7.: Field dependent magnetic scattering length density.

		s7	c7
SLD_m^{sat}	[10^{10} cm^{-2}]	0.72 (2)	0.73 (1)
M(R)	[$10^4 \mu_B$]	1.8 (3)	2.1 (3)
χ	[10^{10} cm^{-2} T^{-1}]	0.08 (1)	0.061 (9)

With both the saturation magnetic scattering length density SLD_m^{sat} and the integral magnetic particle moment M(R) as independent parameters of the Langevin fit, two independent routes are given for calculation of the atomic magnetic moments and volume magnetization densities of the investigated nanoparticles. A detailed description of the calculation of magnetization densities is given in section 5.3.2.3. First, the obtained saturation magnetic SLD can be converted into magnetization densities directly via equation (5.3.5). As a second approach, the magnetization density in the particle core is determined from the integral particle moment M(R) via equation (5.3.10). For this purpose, effective magnetic particle volumes of 474(15) nm^3 and 564(17) nm^3 are derived for the nanospheres and the nanocubes, respectively, using the nuclear and magnetic particle radii R_n and R_m refined in section 5.3.3.1. The determined effective volume of the nanospheres is in good agreement with the magnetic particle volume determined from magnetization measurements in section 5.1.3.3. The deviation in magnetic particle volumes determined for the nanocubes is supposedly due to uncertainties in sample preparation as discussed in section 5.1.3.3. The larger effective magnetic volume determined here is more reasonable considering the larger nuclear volume as compared to the nanospheres.

Table 5.3.8.: Magnetization densities and atomic magnetic moments determined by SANSPOL and SQUID measurements. The values determined from SANSPOL denote the core magnetization density, whereas the values determined by SQUID measurements relate to the average magnetization density in the entire nanoparticle.

			M_v [μ_B nm^{-3}]	M_{Fe} [μ_B]
s7	SLD_m^{sat}		26.7 (7)	0.72 (2)
	$M(R_m, R_n)$	SANSPOL	38 (6)	1.0 (2)
		SQUID	22.9 (2)	0.61 (1)
c7	SLD_m^{sat}		27.0 (4)	0.75 (2)
	$M(R_m, R_n)$	SANSPOL	37 (5)	1.0 (1)
		SQUID	20.2 (2)	0.56 (1)

The finally obtained values for the volume and atomic magnetization densities of the studied nanoparticles are presented in Table 5.3.8. Comparative average macroscopic values can be deduced from the SQUID measurements presented in section 5.1.3.3. Instead of calculating the magnetic particle volume as performed in section 5.1.3.3, the saturation magnetization, which strongly depends on the sample amount used for the measurement, is neglected here. Only the information on the integral magnetic particle moment $M(R_m, R_n)$ is converted with the nuclear particle volume determined by SANS to obtain the average atomic magnetic moments and volume magnetization densities.

The determined magnetization densities of the nanospheres and the nanocubes are consistent, but change in dependence of the applied methods. Concerning the values obtained from SANSPOL measurements, those determined by the saturation magnetization are considered better not only due to the smaller error bars. The value for the integral particle moment determined by the Langevin approach is very sensitive to the slope of the magnetization in small applied magnetic fields. As in this region only few data points are available by the performed SANSPOL measurements, the error bar on this value may still be underestimated.

The average atomic magnetic moments determined by macroscopic magnetization measurements are in good agreement with further published results [148] and are significantly lower than the bulk magnetite moment of 1.1 μ_B [149]. This is furthermore in agreement with earlier studies of the particle size dependent magnetization [149] as well as Monte Carlo simulations of the magnetic structure of maghemite and magnetite nanoparticles based on a three-dimensional classical Heisenberg-Hamiltonian [143,144]. The magnetic moment of 0.72 - 0.75 μ_B per Fe atom as determined by SANSPOL is larger

than the macroscopic results, which results from the lower magnetization density found at the particle surface. However, the core magnetic moment is still significantly lower than the bulk value. This may indicate a certain degree of magnetic disorder even in the nanoparticle core, as may result from lattice strain as discussed in section 5.2. In order to detect such a magnetic disorder in the nanoparticle core, SANS measurements with polarized neutrons and polarization analysis are again required. By evaluation of the spin-flip and non-spin-flip intensities the magnetization component perpendicular to the applied magnetic field can be separated. For magnetic disorder even inside the magnetic nanoparticle core, a non-zero magnetization component is expected.

5.3.3.2. Magnetic interparticle correlations

For investigation of interparticle correlations between magnetic nanoparticles in dependence of the particle shape, highly concentrated dispersions of ~ 5 vol% nanocubes (cmax) and nanospheres (smax) were studied by SANSPOL. In this high concentration the dispersions exhibited ferrofluid behavior, *i.e.* the dispersion is heavily attracted by a magnet. The detector images of both samples measured in dependence of the neutron polarization (I(+), I(-)) and the applied magnetic field (0 T, 1.5 T) are presented in Figure 5.3.10. The common feature for both samples is a correlation ring visible in the non-polarized detector images (I(+)+I(-)) and the magnetic scattering contributions in the polarized detector images (I(+), I(-)). The different position in Q of this correlation ring reflects the smaller particle size of the nanospheres as compared to the nanocubes. The main difference between the two samples is a feature at low Q, *i.e.* in the center of the detector images. If the respective I(-) images are compared, the dumbbell-shaped high intensity region in the center is rotated by 90° for the nanocubes. For the nanospheres, this feature exhibits the same directional symmetry as observed in the pure form factor measurements in Figure 5.3.2. The nonpolarized measurements reveal some degree of magnetic field dependence of this feature, which may point to either magnetic or magnetically induced structural correlations.

In general, a correlation peak, observed as a ring in the 2D detector images, points to a defined distance between the particles, resulting from an equilibrium of attractive and repulsive interaction forces. The higher intensity in the lower Q range may be due to agglomeration on these higher length scales, according to a mass fractal with the fractal dimension giving information on the dimensionality of the agglomeration.

In Figure 5.3.11, the nonpolarized scattering is compared for high and low applied magnetic fields. For the nanospheres, a small deviation with magnetic field and azimuthal angle is observed in the lower Q range. The extracted structure factor has a

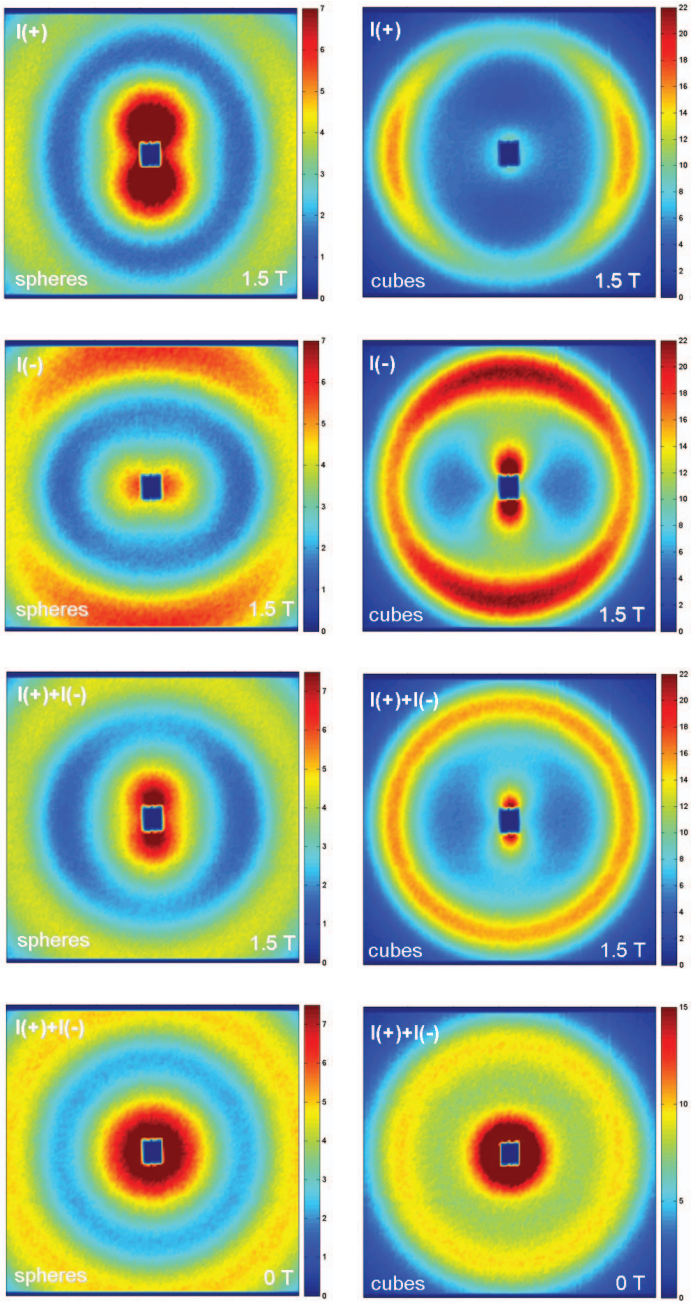

Figure 5.3.10.: 2D SANSPOL data by concentrated nanoparticle dispersions (> 5 vol%). A magnetic field was applied horizontally. The maximum Q in horizontal and vertical directions is 0.063 $Å^{-1}$. The unit of the color bar is cm^{-1}.

shape that results from a common hard spheres interaction, and the correlation peak is unchanged by the applied magnetic field. The peak maximum at 0.0560(5) $Å^{-1}$ corresponds to a particle distance of 112(1) Å, which is in agreement with the particle diameter of 99 Å and an interpenetrating ligand shell. In contrast, the nanocubes exhibit a strong dependence on the applied magnetic field concerning both the correlation peak and the scattering contribution in the low Q range. The correlation peak gains intensity and possibly also sharpens in higher magnetic fields, indicating a larger affected volume with a larger correlation length. The separated structure factor is much larger in intensity than for the nanospheres and even exhibits higher order correlations. The correlation distance, determined by the peak positions at 0.0481(5) $Å^{-1}$ and 0.0503(5) $Å^{-1}$, varies from 131(1) Å in zero field to 125(1) Å in high applied field. The observed mass fractal has a fractal dimension of ~ 1.2 in zero magnetic field, which is characteristic for linear aggregates that are somewhat flexible in between stiff columns and highly flexible polymer coils. With application of the magnetic field the fractal dimension reduces drastically for $Q \parallel H$ and significantly less to a fractal dimension of ~ 1 for $Q \perp H$. These observations suggest a stiffening of the nanoparticle chains into rigid linear aggregates (as expressed by the more pronounced correlation peak and the fractal dimension) that orient themselves into the direction of the magnetic field (as expressed by the angular dependence of the mass fractal).

Although both samples reveal an interaction potential that is qualitatively similar to a hard spheres potential, refinements to either a hard spheres or a sticky hard spheres structure factor were not successful. Instead of developing a more adequate structure factor by numerical methods, a phenomenological description of the observed features will be given in this section. As the separation of possible magnetic and nuclear structure factor contributions is furthermore complex, the following evaluation will focus on the nonpolarized data.

In order to extract the most precise information on the interparticle correlations, it is required to separate magnetic (anisotropic), nuclear isotropic, and structural anisotropic scattering contributions and to determine whether the magnetic scattering originates in the magnetic form factor or in magnetic interparticle correlations. Therefore, the two observed features are studied in dependence of both the applied magnetic field and the azimuthal angle.

In order to study the dependence of the correlation peak on the direction and magnitude of the applied magnetic field, the dependence of the respective peak maximum

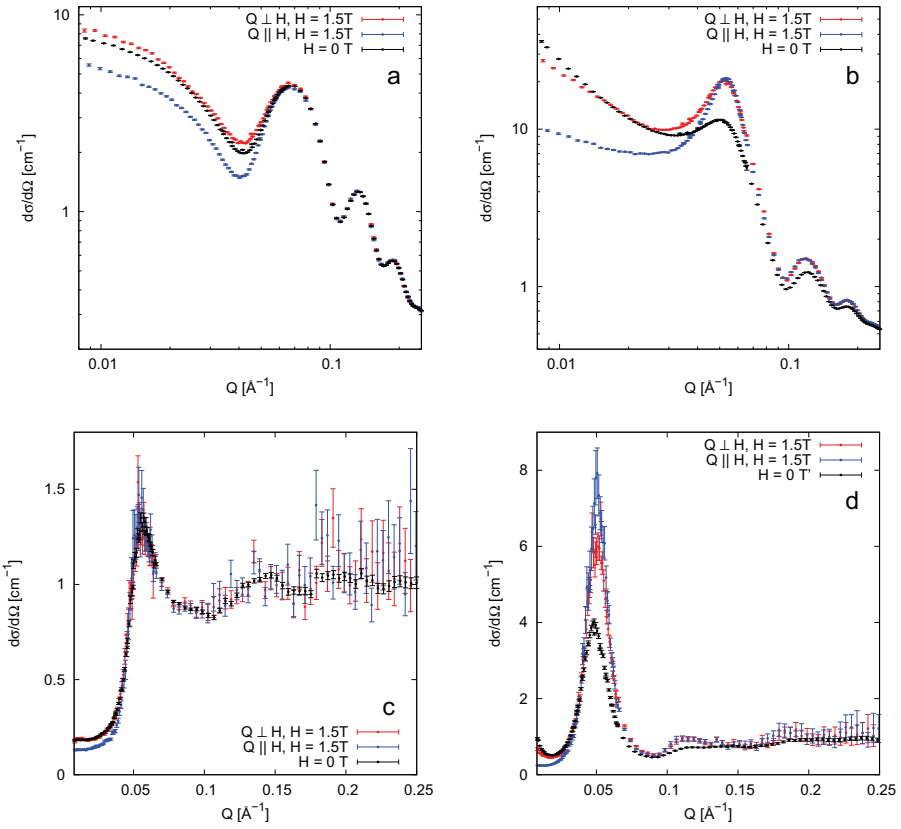

Figure 5.3.11.: Nonpolarized SANS by concentrated nanoparticle dispersions of nanospheres (left) and nanocubes (right). (c) and (d) show the corresponding structure factors as extracted by division by the respective scaled form factor measurement.

intensity on both the azimuthal angle and the applied magnetic field is presented in Figure 5.3.12. For the nanospheres, an angular dependence close to a $\sin^2(\alpha)$ behavior is found which seems to be field independent. Note the small range in intensity and the large degree of noise illustrating the small amplitude of the angular dependence. This points to a rather small magnetic contribution to the interparticle correlation, which supposedly results from the contribution of the magnetic form factor instead of being an excess magnetic structure factor. It can thus be concluded that the interparticle correlation of the nanospheres is a disordered arrangement of particles that is not changed by application of a magnetic field up to 1.5 T.

The nanocubes correlation peak exhibits a significant change in intensity in dependence of the applied magnetic field as suggested by Figure 5.3.11b and 5.3.11d. A more complex field dependence as well as an angular dependence different from $\sin^2(\alpha)$ is revealed in Figure 5.3.12b in a much larger intensity range than observed for the nanospheres.

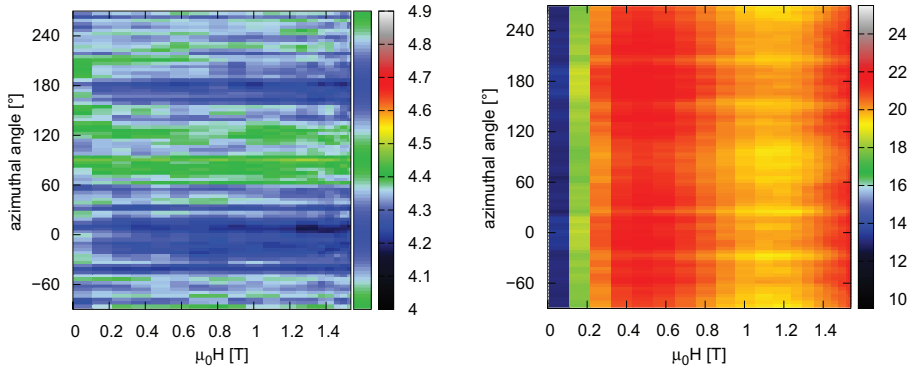

(a) Interparticle correlation peak intensity of the nanospheres at Q = 0.068 Å^{-1}. A $\sin^2(\alpha)$ behavior is shown to the right as a guide to the eye.

(b) Interparticle correlation peak intensity of the nanocubes at Q = 0.053 Å^{-1}

Figure 5.3.12.: Field dependence of the interparticle correlation peak for the nanospheres and nanocubes.

The slope of the field dependence of the nanocubes interparticle correlation is independent on the azimuthal angle, but is scaled by a field independent angular dependence of the intensity. Cuts of the field dependence and the angular dependence are presented in Figure 5.3.13.

The magnetic field dependence may be explained by either a Langevin behavior with linear increase at high fields and an additional peak at ~ 0.4 T or a Langevin behavior

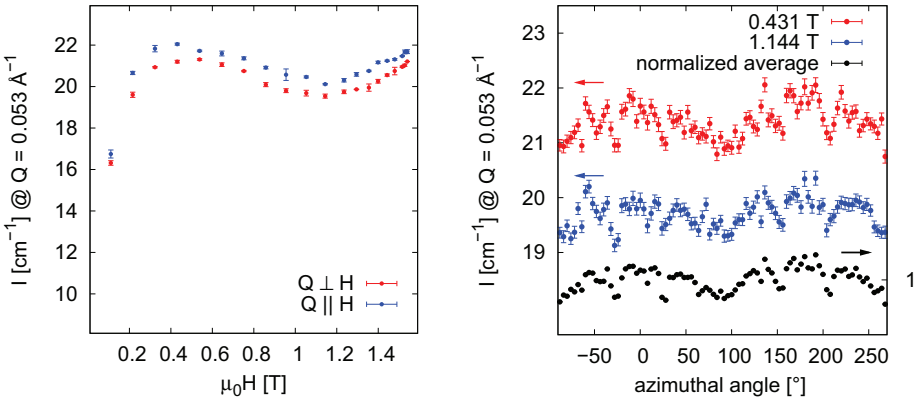

Figure 5.3.13.: Intensity of the nanocube interparticle correlation peak in dependence of the applied magnetic field (left) and the azimuthal angle (right). For the average angle dependent intensity, scans at different applied magnetic fields were first normalized by the average field dependence and then averaged for better statistics.

with a destructive peak around 1.1 T. As the slope is independent on the azimuthal angle between Q and the applied field, the field-dependent contribution can hardly be of magnetic origin. It is rather supposed to be due to structural order induced by a magnetic field of ~ 1.1 T.

A description of the angular dependence of the scattering intensity is more complicated. On the first view, a very noisy $\sin^2(\alpha)$ behavior with a small amplitude is observed. However, because the noise is reproducible for different applied magnetic fields, it may have to be treated as individual correlation peaks or be related to systematic errors. The angular dependence of the scattering intensity can be described by either a set of positive correlation peaks at azimuthal angles of 0, 50, 130, 180, 230, and 310°, or a set of negative correlation peaks at angles of 25, 90, 155, 205, 270, and 335°. However, this strong angular dependence indicates a complex preferred spatial orientation of the interparticle correlations.

In order to study the dependence of the scattering intensity in the lower Q range, which was observed to be different for nanospheres and nanocubes in Figure 5.3.10, on the direction and magnitude of the applied magnetic field, the azimuthal angular dependence of the intensity at Q = 0.0105 Å^{-1} has been correlated to the applied magnetic field in Figure 5.3.14. For the nanospheres, an angular dependence close to a $\sin^2(\alpha)$ behavior expected for anisotropic magnetic scattering is observed again. The small amplitude suggests the magnetic scattering contribution to originate in the magnetic form factor. For the nanocubes, the slope and width of the maxima around azimuthal an-

gles of 90° and 270° appear different from the $\sin^2(\alpha)$ behavior, exhibiting more narrow maxima than minima.

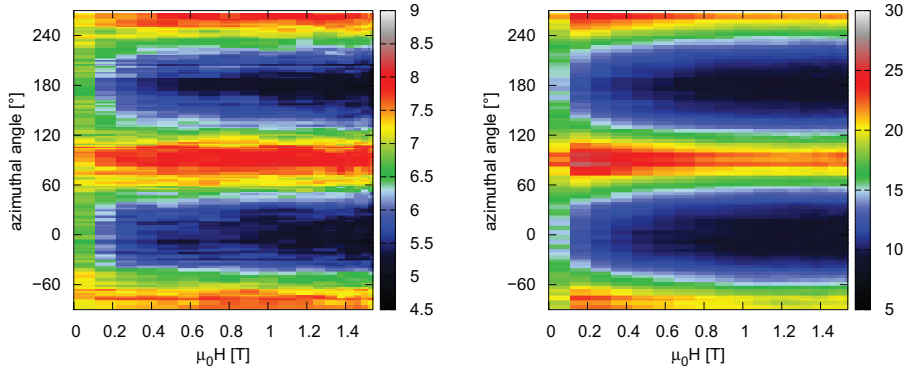

Figure 5.3.14.: Field dependence of the scattering intensity at Q = 0.0105 $Å^{-1}$ by nanospheres (left) and nanocubes (right).

A closer investigation of the azimuthal angular scattering intensity in high fields as presented in Figure 5.3.15 reveals indeed additional anisotropic scattering contributions at these angles for both samples, which is more pronounced in case of the nanocubes. The magnetic and isotropic nuclear scattering contributions were fit with a $\sin^2(\alpha)$ function in the minima between -40° and 40°, and the remaining excess scattering contribution, which can be attributed to anisotropic structural scattering, was fit with a Gaussian function.

The magnetic field dependence of the magnetic, isotropic nuclear, and anisotropic structural scattering contributions is presented in Figure 5.3.16. The decrease of the isotropic scattering contribution follows a negative Langevin slope and can be explained by the simultaneous increase of magnetic and structural anisotropic scattering contributions. In low magnetic fields, the isotropic scattering still contains magnetic scattering contributions from those moments not aligned with the field as well as the structural contributions by not yet oriented features. The isotropic scattering contribution separated in a high magnetic field can be regarded as the pure nuclear isotropic scattering. The main difference between both samples is the fraction of magnetic and anisotropic scattering, which is much larger for the nanocubes than for the nanospheres. The nanocubes exhibit an intensity maximum around 0.2 T which can be attributed to the fast increase of magnetic and structural anisotropic scattering that is not compensated by the decrease of the isotropic scattering. This leads to the conclusion that application of the magnetic field not only orients the existing structures, but also induces additional structural and magnetic correlations. This behavior is also reflected by the magnetic

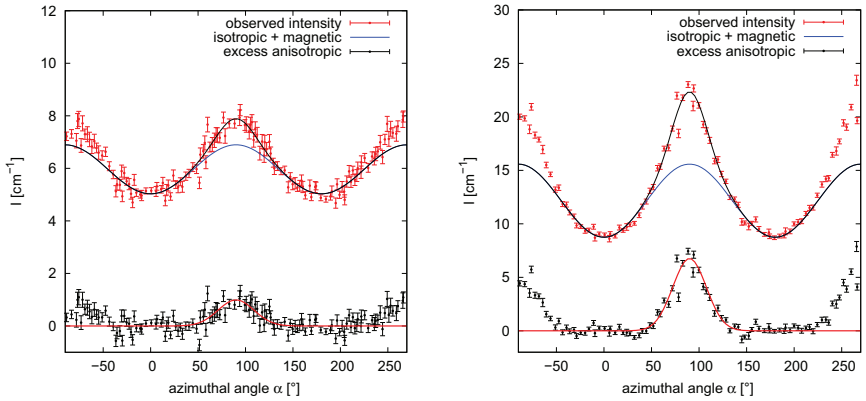

Figure 5.3.15.: Angular dependence of the scattering intensity at Q = 0.0105 Å^{-1} by nanospheres (left) and nanocubes (right) in an applied magnetic field of 1.5 T. The observed scattering contributions (red points) can be separated into isotropic and magnetic scattering (blue line) and excess anisotropic scattering (black points). The excess anisotropic scattering contribution is modelled with a Gaussian (red line, shown in the range of $20° < \alpha < 160°$). The total scattering intensity is simulated as a black line.

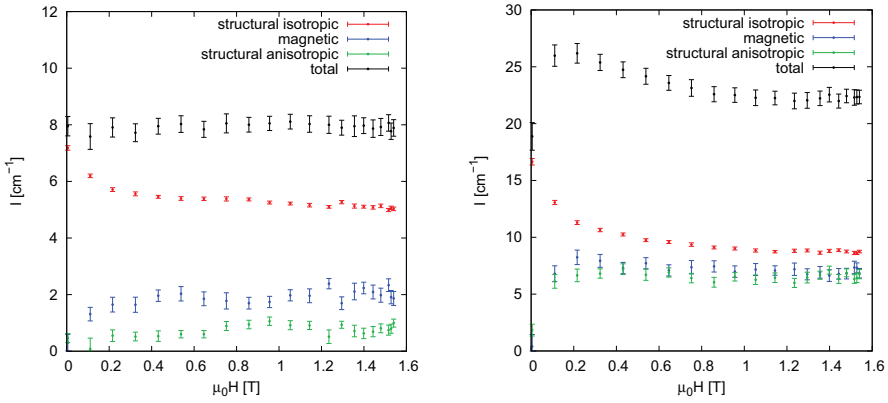

Figure 5.3.16.: Field dependence of the separated scattering contributions at Q = 0.0105 Å^{-1} by nanospheres (left) and nanocubes (right).

field dependence of the fractal dimension perpendicular to the magnetic field as presented in Figure 5.3.17. Thus, the structure factor of the nanocubes contains a magnetic contribution, which is reasonable because magnetic nanoparticles have been observed to form chains with orientation of the particle moments parallel to the chain [89–91]. The structural anisotropic scattering contribution can be attributed to the orientation of the linear nanoparticle aggregates into the magnetic field direction.

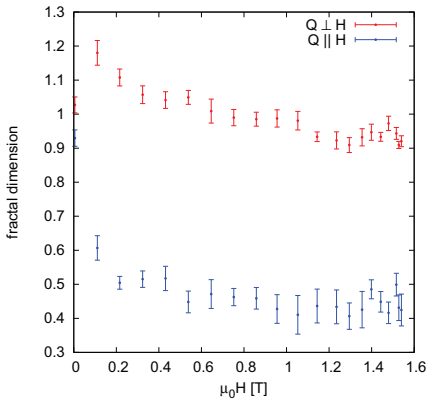

Figure 5.3.17.: Field dependence of the nanocubes fractal dimension.

Concluding the investigations on interparticle interactions in highly concentrated nanospheres and nanocubes dispersions, interaction potentials similar to a hard spheres potential are found for both samples, but with a different extent and quality. The nanospheres exhibit a rather weak and spatially disordered interaction potential, similar to the short range order of a liquid with a nearest neighbor distance of 11.2 nm. A very small structural anisotropic scattering contribution has been found in the low Q range.

The nanocubes exhibit a strong interparticle interaction potential leading to a particle arrangement into flexible chains, which is well in agreement with Monte Carlo simulations [92] and theoretical investigations of pair interactions in colloidal ferrofluids, resulting in a preferential parallel nose-to-tail arrangement into rings and chains of nanoparticles [150]. Upon application of a magnetic field, the chains are observed to stiffen into linear particle aggregates that orient themselves parallel to the magnetic field direction. A similar field dependence has been reported for spherical iron oxide nanoparticles with a diameter of 20 nm [151]. Additionally in the present case, the interparticle distance shortens upon application of the magnetic field from 130.9 Å to 125.6 Å. The shortening of the interparticle distance may be understood as a rearrangement of the nanocubes into a face to face oriented attachment. Such an oriented assembly en-

hances the van der Waals attraction between faceted particles as compared to spherical particles [152]. The preference for oriented attachment may also explain the observation of a small structure factor in the lower concentrated and presumably non-interacting samples discussed in section 5.3.3.1. While the less truncated nanocubes sample (c50) exhibited a small structure factor that prevented determination of the pure nuclear form factor, the sample of the same concentration but larger truncation of the nanocube corners did not reveal a structure factor. This illustrates the shape dependence of the interparticle interactions even in lower particle concentrations.

The magnetic contribution of the structure factor in the lower Q range points to a linear (ferromagnetic) arrangement of the nanoparticle moments along the chain direction parallel to the magnetic field. While origin and composition of the mass fractal appearing in the lower Q range are explained in detail, the spatial orientation and field dependence of the hard spheres correlation peak are not yet fully understood. The field dependence exhibits either an intensity maximum around 0.4 T or an intensity minimum around 1.1 T which is magnetically induced, but of structural origin, because it appears regardless of the azimuthal angle. The angular dependence of the correlation peak can be described by 6 individual maxima that are distributed in rather complex symmetry.

5.3.4. Summary

Within this study, the spatial distribution of the magnetization density in individual magnetic nanoparticles was determined. Consistently for all samples and refinement approaches, the radius of the magnetization density distribution is smaller than the nanoparticle radius by ~ 3 - 5 Å. Within the magnetic particle core, a magnetization density of 0.75 μ_B was found, which decreases towards the particle surface. Thus, microscopic evidence has been given for the existence of a lower magnetized layer at the nanoparticle surface, as suggested by macroscopic methods. This surface layer may originate in either vanishing magnetic moments towards the particle surface or spin canting of the surface spins due to magnetic surface anisotropy. In order to determine the origin of the magnetic dead layer and possibly to monitor the surface spin canting, SANS experiments with polarized neutrons and polarization analysis are required.

Such a key experiment has been reported very recently on mesoscopically arranged iron oxide nanoparticles [153]. By evaluation of the spin-flip and non-spin-flip intensities in a saturating magnetic field, the magnetization density perpendicular to the applied magnetic field was extracted. A magnetization contribution perpendicular to the core magnetization was found in the surface-near region of the nanoparticles. Note that

this approach is sensitive exclusively to the projection of the magnetization perpendicular to the applied magnetic field and perpendicular to Q and does thus not allow for the discrimination of ordered spin structures from disordered spin canting at the particle surface. In order to determine the magnetization density contributions in all directions, measurements with polarization analysis in a saturating magnetic field perpendicular as well as parallel to the incoming neutron beam are required. Moreover, a quantitative determination of the spatial magnetization distribution perpendicular to the core magnetization is desired. Here, a possible magnetization contribution in the nanoparticle core might indicate magnetic disorder and explain the low magnetization density parallel to the applied magnetic field found in this study. Approaching the nanoparticle surface, a possible increasing magnetization density perpendicular to the applied magnetic field would complement the linear decrease of the magnetization density parallel to the applied field and indicate an increasing spin canting close to the particle surface.

Polarized SANS measurements on highly concentrated nanoparticle dispersions revealed a changing degree of interparticle order for different nanoparticle shapes. While the nanospheres exhibit a spatially disordered, short range ordered hard spheres interaction potential, the nanocubes reveal a more pronounced interparticle interaction and the formation of linear aggregates. These linear aggregates are observed to stiffen and orient themselves into the direction of an applied magnetic field and can be understood as oriented face to face attachment of the nanocubes. The nanoparticle moments are expected to orient in a ferromagnetic chain parallel to the applied magnetic field.

Ordered interparticle aggregation strongly depends on the interplay of hard core repulsion forces and attractive interparticle forces such as dipole-dipole interaction and van der Waals attraction. While the hard spheres interaction potential and the dipolar interaction are apparently of comparable magnitude for the investigated systems, only the increase in van der Waals attraction induced by the faceted shape of the nanocubes results in a defined degree of order, which is not observed for the nanospheres.

5.4. Superlattices

5.4.1. Introduction

Self assembly is generally understood as of matter ordering into higher structures without human intervention [154]. One of the most complex examples for self organized systems is certainly the living cell, which includes not only the formation of lipid bilayer cell surface membranes but also the incorporation of highly functionalized organelles with hierarchical order down to the scale of the DNA. Self assembly of particles is known from several natural systems as well, *e.g.* the iridescent appearance of natural opal results from Bragg scattering on an ordered arrangement of silica particles. Self assembly is thus a widely observed phenomenon, and its understanding promises insight into understanding of life on the one side, and the formation of large scale ordered structures for nanotechnology on the other side [139, 154–156].

For artificial formation of nanostructures, however, the defect-free long range order exhibited by natural superlattices has not been achieved yet. First investigations of particle self-assembly were based on micrometer sized colloids. An early description of artificially prepared 2D colloid arrays was given by Perrin [157]. Denkov *et al.* revealed the self assembly of colloids in a thin film of colloidal dispersion to be a two stage process of nucleation and superlattice growth due to a convective flow [158].

While the self assembly of atoms into crystalline compounds and the interparticle forces governing self assembly of larger colloids are well explored, the transfer to the intermediate scale of particles in the nanometer range is not straight forward. Bentzon *et al.* reported early investigations on 3D nanoparticle superlattices obtained by deposition of a nanoparticle dispersion onto a substrate [159]. Important parameters for the achievement of long range order in nanoparticle assemblies are the availability of nanoparticles, which are uniform in particle size, shape, and chemical composition and stable in dispersion, as well as a gradual destabilization of the nanoparticle dispersion and the interplay of attractive and repulsive interparticle interactions [155]. Owing to the strong development in the field of nanoparticle synthesis techniques, the preparation of nanoparticle dispersions with extremely narrow size distribution in the range of few % is feasible even in large scales [99]. For arrangements of particles as small as a few nm, the convection-driven self assembly route for assembly of larger colloids [158] does not hold anymore. For this reason, an even more gradual destabilization of the dispersion is required for preparation of long range ordered superlattices from nanocrystal dispersions [159, 160], in order to provide sufficient time for the nanoparticles to organize in a stable supercrystal structure. The influence of a controlled evaporation rate

of the solvent has been found to be crucial for formation of large and virtually defect-free supercrystals of both colloids and nanocrystals [158, 161, 162]. Further approaches to gradually destabilize the nanoparticle dispersion include established two-solvent re-crystallization methods based on addition of a second solvent to the dispersion that acts as a non-solvent and has a lower vapor pressure [160]. As the solvent evaporates faster, the concentration of the non-solvent in the dispersion is increased slowly, resulting in a gradual destabilization of the nanocrystal suspension. Superlattices of long range order in two and three dimensions were also prepared by diffusion of a non-solvent through a buffer layer into the nanoparticle dispersion [163].

The degree of order obtained in superlattices furthermore depends on the interplay of a variety of attractive and repulsive interparticle forces as well as interactions between the particles and the substrate-liquid or liquid-gas interfaces. Formation of 2D lattices of Au nanoparticles has been observed to occur at the liquid air interface [164]. With a lower evaporation rate, however, the nanocrystals were observed to diffuse away from the interface and form 3D superlattices in the bulk of the dispersion droplet [162].

Interparticle forces such as van der Waals, electrostatic, and magnetic interactions are investigated widely and represent a variety of parameters to tune nanoparticle self assembly [165]. Attractive van der Waals forces are known to induce self-assembly while repulsive forces such as steric interactions provide the balancing force to create stable, ordered structures [166, 167]. Electrostatic interactions were successfully employed for self assembly of binary nanoparticle superlattices [168]. Weak dipolar attractions can be induced by application of a weak magnetic field during self-assembly. By this approach long range ordered nanoparticle arrays of superparamagnetic nanocubes were prepared [105].

Different close packed structure types have been reported for self assembled 3D superlattices. Whetten *et al.* relate the observed superstructure type to the ratio of particle size and ligand shell thickness [169]. With increasing relative shell thickness, transitions from *hcp* to *fcc*, *bcc*, and *bct* structure types are reported for spherical nanoparticles regardless of the material. Further variation of the observed structure types has been observed in two different directions of superlattice preparation, namely binary nanocrystal superlattices as well as superlattices of anisotropic nanocrystals.

Binary superlattices have been prepared by mixtures of nanocrystals with different particle sizes and chemical compositions. Additional variation of the electrostatic interactions lead to a variety of formed structure types [168, 170]. Binary superlattices thus represent a versatile route to metamaterials.

Concerning anisotropic nanocrystals, structural preferences are altered as compared to spherical particles because the interparticle van der Waals forces are influenced by

the nanocrystal shape and orientation. A surface-to-surface arrangement of anisotropic nanocrystals maximizes van der Waals attraction between facets of neighboring nanocrystals, leading to oriented supercrystals [160, 166, 171]. The strong preference of parallel alignment of anisotropic nanocrystals has even been observed to lead to a shape-selective self-segregation of nanocrystal dispersions containing different particle shapes [152]. This preference is (next to a higher magnetic anisotropy) one of the reasons for the use of anisotropic nanocrystals, because such a self orientation of nanocrystals is critical to many applications of magnetic nanoparticles *e.g.* information storage [139].

In order to understand the attractive and repulsive interactions leading to nanoparticle superstructures, a precise determination of their full 3D structure is required. Electron microscopy techniques are commonly used for structural characterization of nanoparticle superlattices, and for many examples three dimensional structures were determined qualitatively by HRTEM and HRSEM [139, 152, 160, 167, 168, 170, 171].

However, electron microscopy imaging techniques provide in general a local top view of the structure [172] which complicates a determination of the structure out of plane. Scattering methods such as grazing incidence small angle X-ray scattering (GISAXS) and reflectometry provide information on the surface as well as the inner morphology of structures deposited on a substrate. GISAXS has previously been applied to nanostructured block-copolymers [173–175]. Nanoparticle superlattices were investigated by GISAXS in either lateral or specular directions [176, 177], giving information on the supercrystal structure. Recently, also the first full 3 dimensional structure determination of binary superlattices was reported [178]. Due to the large footprint of the X-ray beam onto the sample, GISAXS provides averaged information over a large sample volume.

This section will focus on the preparation of highly ordered superlattices of iron oxide nanocubes and nanospheres by a drying-mediated self-assembly process. Full 3 dimensional structural characterization of the obtained nanostructures is performed by a combination of GISAXS, reflectivity, and SEM. Special emphasis will be laid on the shape dependence of the super crystal formation.

5.4.2. Methods

5.4.2.1. Deposition Techniques

For all deposition techniques, dispersions of iron oxide nanocubes Bc 9 and nanospheres Bc 10 were used as received from our collaborators (see section 5.1). Three different par-

ticle concentrations were available for each particle shape: approximately $1.0 \cdot 10^{14}$ particles/ml, $4.6 \cdot 10^{14}$ particles/ml, and $8.4 \cdot 10^{14}$ particles/ml. It is emphasized that those nominal particle concentrations (nom. conc.) had been calculated under the assumption of a cubic edge length of 9 nm and a spherical radius of 4 nm as obtained from TEM. For calculation of the used molarities and particle concentrations, the assumption of Fe_2O_3 as the only inorganic phase with a mass density of 5.49 g/ml was made. Molarities (c_{Fe}) were calculated using the molar mass of Fe_2O_3 of 159.6 g/mol, and for the precise particle concentrations, the particle volume was calculated using the particle sizes as determined in section 5.1.3.1(r = 4.956 nm for the nanospheres and a = 8.4 nm for the nanocubes). The exact molarities of the used dispersions are listed in Table 5.4.1.

Table 5.4.1.: Nanoparticle dispersions used for self-assembly.

shape	nom. conc. $[10^{14}ml^{-1}]$	m(paste) [mg]	c_{paste} [wt%]	$V_{toluene}$ [ml]	c_{Fe} [M]	particle conc. $[10^{14}ml^{-1}]$
spheres	1.0	6.0	60	20	0.0023	0.64
spheres	4.7	13.8	60	10	0.0104	2.96
spheres	8.4	24.7	60	10	0.0185	5.29
cubes	1.0	10.0	40	10	0.0050	1.23
cubes	4.7	47.0	40	10	0.0235	5.78
cubes	8.4	84.0	40	10	0.0421	10.3

As substrates, single crystalline germanium (111) wafers (Crystec GmbH) of 450 μm thickness were used. The wafers of 2 inch diameter were cut into 9 pieces of approximately 1.6 cm edge length and cleaned by sonicating for 20 min each in toluene first, followed by ethyl acetate and ethanol. Precleaned substrates were stored in ethanol for no more than a few days and dried in nitrogen flow prior to particle deposition. For reflectivity samples, silicon wafers of 1 mm thickness were cleaned by the same approach.

The choice of substrate material was motivated by the different scattering contrasts between iron oxide and the substrates depending on the probe. For X-rays, the contrast between iron oxide and germanium is larger, while for neutrons, the contrast between iron oxide and silicon is larger. The contrast between sample and substrate is more important for reflectivity measurements, especially if a monolayer is probed. For GISAXS measurements on mesocrystals or reflectivity measurements on multilayers of nanoparticles, the contrast between the particles and the oleic acid ligand shell is more important.

Spin Coating A disordered but homogeneous layer of nanocubes was prepared by spin coating an excess amount of nanocube dispersion in toluene with a concentration of approximately 8.4 $\cdot 10^{14}$ particles/ml for 20 s with 1000 rpm at maximal ramping speed onto a germanium substrate. The produced thin layer of nanoparticle dispersion dried within seconds.

Drop Casting Enhanced short range order of the deposited nanoparticles was achieved by the drop casting approach. The substrates were covered with nanoparticle dispersions in toluene with concentrations of approximately 4.7 $\cdot 10^{14}$ (nanocubes) and 8.4 $\cdot 10^{14}$ (nanospheres) particles/ml, and the dispersion was evaporated (within 2 hours) in a solvent concentrated atmosphere inside closed petri dishes. Evaporation without this controlled atmosphere failed to generate ordered nanoparticle layers. Further extension of the evaporation process by placing a small reservoir of toluene inside the petri dishes did not exhibit a significant influence on the long range order.

Drop Casting in Magnetic Field Self assembly of the nanocrystals was performed by an evaporation induced process with application of a magnetic field [105]. The substrates were covered with nanoparticle dispersions and kept in closed petri dishes same as for the drop casting method. During evaporation of the solvent a static magnetic field of 30 mT was applied perpendicular to the substrate (as shown schematically in Figure 5.4.1a and b) yielding highly ordered superlattices. In contrast to the approach in [105], here the applied magnetic field was static and applied throughout the entire drying process. A possible gradient of the applied magnetic field was not determined.

For preparation of the samples discussed in section 5.4.3.4, several variations of the evaporation setup were investigated. For evaporation of the nanoparticle dispersion in a stray field, the substrate was placed inside closed petri dishes directly on the top edge of a round magnet (Figure 5.4.1d and e). In order to investigate a variation of the field strength, samples were placed in the homogeneous region of a U-shaped magnet, but laterally displaced (Figure 5.4.1a and c). The sample discussed in section 5.4.3.5 was prepared by tilting the substrate for about 10° out of the horizontal position inside vertical magnetic field.

5.4.2.2. Data treatment

Imaging techniques Scanning electron microscopy (SEM) images were obtained using a LEO 1550 SEM operated at 20 keV. Atomic force microscopy measurements were carried out at ambient temperatures with an Agilent 5400 AFM. The instrument was

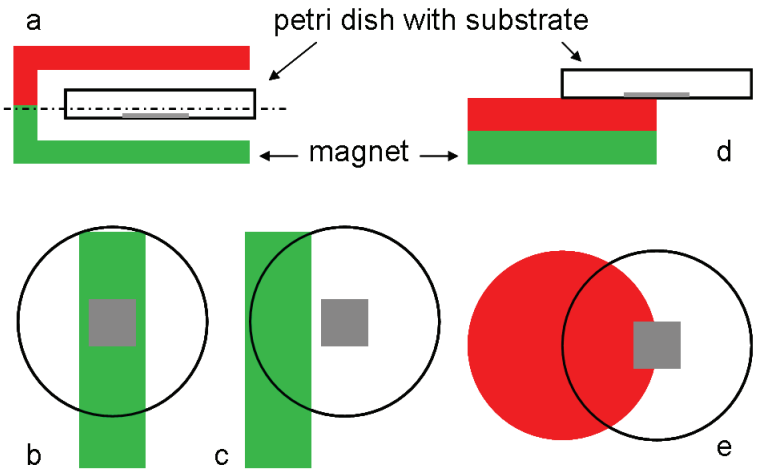

Figure 5.4.1.: Schematic of the applied deposition technique. a) side view of a substrate positioned inside closed petri dishes in a U-shaped magnet. Cut views along the dashed line are presented for b) a sample in the homogeneous region and c) a laterally displaced sample. d) side view and e) top view of a substrate placed on the top edge of a round magnet.

operated in non-contact (AC) mode using a cantilever with a nominal spring constant of 40 Nm^{-1}.

GISAXS Grazing incidence small-angle scattering (GISAXS) measurements on the deposited superlattices were performed at the ID01 beamline at ESRF (3.1.3) and the SWING beamline at Soleil (3.1.2). At ID01, a CCD detector with 1242 x 1151 pixels and a pixel size of 110 μm was set at a distance of 0.519 m from the sample. The incident energy was set to 7.105 keV, just below the Fe K edge at 7.112 keV, and the incident angle of the primary beam was varied between 0.30 and 0.60°. At SWING, a sample detector distance of 1.600 m and an incident energy of 7.000 keV were chosen. The incident angle of the primary beam was varied between 0.10° and 0.80°. The scattering was recorded on an Aviex CCD detector of 4096 x 4096 pixels with a software binning to 1024 x 1024 pixels with a pixel size of 164 μm.

The critical angle of total reflection of the samples at the chosen conditions is 0.125°. A description of the mesocrystal structure determination procedure is given in section 5.4.2.3.

Reflectivity X-ray reflectivity measurements were performed in house using a Bruker D8 Advance reflectometer equipped with a Cu Kα X-ray tube. Specular reflectivity scans were measured up to $2\theta = 8°$. Off-specular reflectivity scans were measured with a fixed incident angle of 0.30° up to $2\theta = 4°$. Neutron reflectivity measurements were performed at the TREFF instrument at JCNS (3.2.1). An incident wavelength of 4.73 Å was chosen, and the specular neutron reflectivity was measured up to $2\theta = 6°$.

All reflectivity data sets were converted from the scattering angle 2θ [°] to the wave vector Q [$Å^{-1}$]. Specular reflectivity data was also corrected for the shadowing effect of the sample at low angles by $\sin(\theta)$, and the scattering intensity was scaled to 1 at the critical angle of total reflection.

Magnetization measurements Field dependent magnetization measurements of nanoparticle superlattices on a substrate were performed on a PPMS using the VSM option. The samples were cut into pieces of approximately 3 x 4 mm^2, wrapped with Teflon tape, and glued into a copper sample holder using Loctite 408 glue. Magnetization curves were measured at 10 and 300 K with a magnetic field sweep rate of 20 mT/s up to 8.5 T. The diamagnetic magnetization contribution was determined at high fields at 300 K and subtracted in the 10 K measurements. In order to guarantee comparability, each in plane and out of plane magnetization measurement was always performed on the same sample.

5.4.2.3. GISAXS evaluation

As a first step in evaluation of GISAXS measurements, the exclusively lateral scattering information exhibited in the Yoneda line was analyzed. Reflections observed in the Yoneda line appeared either as broad features suggesting a glass-like short range correlation or as sharp Bragg reflections suggesting a crystalline order in plane. In all cases, the correlation length was determined for the first nearest neighbor correlation peak around 0.5 nm^{-1}. Lorentzian fits give the full width at half maximum of the reflection, and conversion into real space with implementation of the instrumental resolution was performed using

$$\xi_{corr} = \frac{1}{\sqrt{\left(\frac{FWHM_{reflection}}{2}\right)^2 + \left(\frac{FWHM_{primarybeam}}{2}\right)^2}} \tag{5.4.1}$$

The implemented instrumental resolution values were $FWHM_{ID01}$ = 0.0031 Å^{-1} and $FWHM_{SWING}$ = 0.00122 Å^{-1}. A list of the determined FWHM and the correlations lengths ξ_{corr} calculated by equation (5.4.1) is given in Table 5.4.2.

Table 5.4.2.: Correlation lengths in iron oxide superlattices.

	spin coated cubes	drop casted cubes	*bct* cubes	R$\bar{3}$m spheres	R$\bar{3}$ cubes	thin layer cubes
section	5.4.3.1	5.4.3.1	5.4.3.2	5.4.3.3	5.4.3.4	5.4.3.5
instrument	ID01	ID01	ID01	ID01	SWING	SWING
FWHM [Å^{-1}]	0.0128(2)	0.01174(6)	0.0045(1)	0.00301(1)	0.00164(4)	0.0038(1)
ξ [Å]	156(2)	170.4(9)	444(10)	647(4)	1220(30)	526(14)
ξ_{corr} [Å]	161(3)	176(2)	604(69)	-[a]	1825(106)	555(16)

[a] exceeding the resolution limit

The large error bars in the correlation lengths of the mesocrystalline samples indicate that those correlation lengths are close to or even exceeding the instrumental resolution limit. In case of sharp reflections suggesting crystalline lateral order, the reflection positions were analyzed according to the Bragg equation, yielding lattice constants for either square or hexagonal lateral order for the investigated samples. The analysis of the crystal symmetry was simplified by the observation that all reflections appear in a single GISAXS pattern without any rotation of the sample. This suggests a lateral disorder of the internally structural coherent domains. Along with the fact that the Ewald sphere is relatively flat in the studied small angle range, the 2 D powder results in the appearance of all hkl reflections in one single GISAXS pattern (without rotation of the sample as would be required for full 3D single crystals).

A crystalline order of the mesocrystals perpendicular to the substrate is expressed by sharp reflections above the Yoneda line, corresponding to scattering from lattice planes with $l \neq 0$. Those reflections contain a z component of the scattering vector Q and undergo refraction when the beam enters and leaves the particle film. Furthermore, as the incoming or outgoing beam may or may not be reflected at the substrate, the resulting scattering is a set of two signals emanating from each single lattice plane. The square symmetry observed in plane can be the projection of either a cubic or a tetragonal lattice, and for determination of the c lattice constant, a tetragonal lattice has to be assumed for generality. The combination of Snell's and Bragg's laws in Ref. [36] was applied to either tetragonal or hexagonal symmetry resulting in:

$$Q_{z,tet} = k_{i,z} + \sqrt{k_{c,z}^2 + \left[\sqrt{4\pi^2 \cdot \left(\frac{h^2+k^2}{a^2} + \frac{l^2}{c^2}\right) - Q_y^2} \pm \sqrt{k_{i,z}^2 - k_{c,z}^2}\right]^2} \tag{5.4.2}$$

$$Q_{z,hex} = k_{i,z} + \sqrt{k_{c,z}^2 + \left[\sqrt{4\pi^2 \cdot \left(\frac{4}{3} \cdot \frac{h^2+h\cdot k+k^2}{a^2} + \frac{l^2}{c^2}\right) - Q_y^2} \pm \sqrt{k_{i,z}^2 - k_{c,z}^2}\right]^2} \tag{5.4.3}$$

where $k_{i,z}$ is the z component of the wave vector of the incoming beam in vacuum, $k_{c,z}$ is the z projection of the wave vector at the critical angle of total reflection, and h, k, and l are the Miller indices in a tetragonal or hexagonal lattice with the lattice constants a and c. Thus, the Q_z position of the reflections is strongly dependent on the incident angle, and each reflection series can be indexed by refinement of the Q_z position in dependence of the incident angle. Figure 5.4.2 shows projections of the scattering intensity in the (11l) reflection series of the nanospheres mesocrystals discussed in section 5.4.3.3. The position of those reflections in Figure 5.4.2 that were not reflected at the substrate

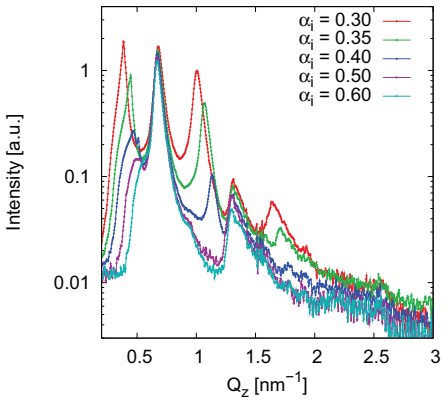

Figure 5.4.2.: (11l) reflection series in GISAXS of iron oxide nanospheres mesocrystals in dependence of the incidence angle. Projections of the GISAXS intensities at Q_y = 0.102 Å^{-1} are shown.

is almost independent on the angle of incidence, whereas reflections that involve a reflection of the incoming or outgoing beam at the substrate exhibit a strong dependence on the angle of incidence. The latter reflections are usually lower in intensity and also broadened as compared to the former. This is due to several contributions such as surface roughness, the reflection coefficient < 1, and attenuation of the beam inside the

material, and as a result, even the absence of reflections that should have been reflected at the substrate is not uncommon. For this reason, the Q_z position of reflections not reflected at the substrate is treated as the more accurate in case of doubt. For indexing the entire reflection series according to equation (5.4.3), the Q_z positions of all reflections were determined by Lorentzian fits. In order to recognize possible extinctions, several reflection series have to be indexed. Figure 5.4.3 shows the hexagonal indexing of the nanospheres superstructure discussed in section 5.4.3.3.

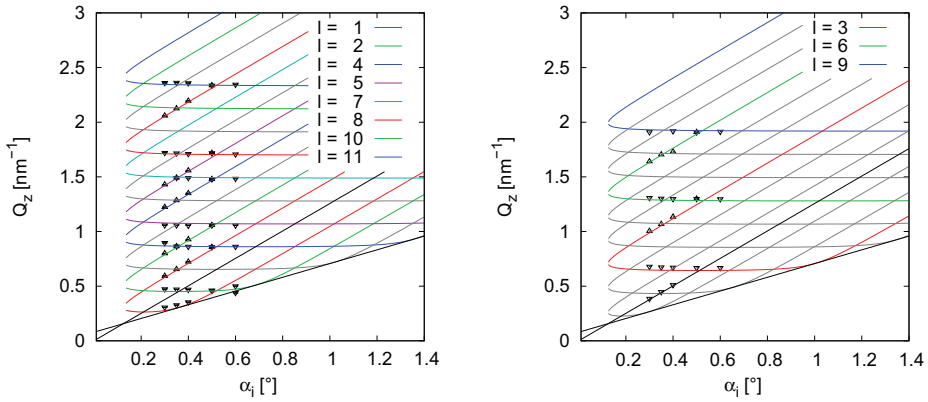

(a) Hexagonal indexing of the (10l) reflection series.

(b) Hexagonal indexing of the (11l) reflection series.

Figure 5.4.3.: Hexagonal indexing of iron oxide nanosphere mesocrystals. Measured reflections both with (△) and without (▽) total reflection of the scattered beam are shown. Theoretical positions of Yoneda line and specular reflections are presented as black lines, and theoretical positions of the extinct reflections are presented as grey lines, i.e. l=3,6,9 for the (10l) series and l=1,2,4,5,7,8 for the (11l) series.

In agreement with all remaining reflection series, a lattice constant perpendicular to the substrate of c = 29.7(1) nm and the critical angle of total reflection of α = 0.125° were determined. The observed extinctions follow the extinction rule $-h+k+l = 3$ n in agreement with the (20l) and (21l) reflection series, suggesting a rhombohedral Bravais lattice.

5.4.2.4. Reflectivity evaluation

Calculation of the scattering length density profiles The scattering length density profiles presented in Figures 5.4.11a and 5.4.16a were calculated according to the crystal structures determined by GISAXS:

$$SLD(d) = fr_{Fe_2O_3}(d) \cdot SLD_{Fe_2O_3} + (1 - fr_{Fe_2O_3}(d)) \cdot SLD_{OA} \tag{5.4.4}$$

where $fr_{Fe_2O_3}(d)$ is the fraction of the unit cell occupied by the iron oxide particle at a distance d to the substrate, and $SLD_{Fe_2O_3}$ and SLD_{OA} are the scattering length densities of iron oxide and oleic acid, respectively. Thus, the space in the unit cell not occupied by iron oxide was assumed to be filled with oleic acid. The fraction of iron oxide can be determined analytically for highly symmetric polyhedra such as a truncated cube and a sphere. For the arrangement of the nanospheres, with lattice constant perpendicular to the substrate exactly three times as large as the nanoparticle diameter, the fraction is calculated as the ratio of particle and unit cell cross sections

$$fr_{Fe_2O_3}(d) = \begin{cases} \frac{\pi d(2R-d)}{a^2 \cos(30°)}, & \text{for } d \leq 2R \\ fr_{Fe_2O_3}(d-2R), & \text{for } d > 2R \end{cases} \tag{5.4.5}$$

where R is the particle radius and a the hexagonal lattice constant parallel to the substrate. For the truncated cubic nanoparticles, three different regions are distinguished. In between the nanocubes there is a small gap, where the iron oxide fraction is zero, the untruncated part of the nanocubes is independent on the distance to the substrate, and the truncated parts of the nanocubes have to be taken into account in dependence of the distance to half the height of the nanocube

$$fr_{Fe_2O_3}(d) = \begin{cases} \frac{l_{cube}^2}{a^2}, & \text{for} \quad |d - \frac{1}{2}l_{cube}| \leq \frac{1}{2}l_{cube} - t \\ \frac{l_{cube}^2 - 2[\frac{1}{2}l_{cube} - |d - \frac{1}{2}l_{cube}|]^2}{a^2}, & \text{for} \quad \frac{1}{2}l_{cube} - t \leq |d - \frac{1}{2}l_{cube}| \leq \frac{1}{2}l_{cube} \\ 0, & \text{for} \quad \frac{1}{2}l_{cube} \leq |d - \frac{1}{2}l_{cube}| \leq \frac{1}{2}(c - l_{cube}) \\ fr_{Fe_2O_3}(d - \frac{c}{2}), & \text{for} \quad \frac{1}{2}(c - l_{cube}) \leq |d - \frac{1}{2}l_{cube}| \end{cases} \tag{5.4.6}$$

with the cubic edge length l_{cube}, the truncation length t, and the tetragonal lattice constants a and c.

5.4.3. Results and Discussion

5.4.3.1. lateral order in magnetic nanoparticle assemblies

Two dimensional assemblies of nanoparticles with varying degree of order were prepared by deposition of iron oxide nanocubes onto germanium substrates. Characterization of the obtained nanoparticle arrays was performed locally by scanning electron microscopy (SEM) and globally by grazing incidence small angle scattering (GISAXS)

measured at ID 01, ESRF (3.1.3). Results for three different self assembly techniques applied to the iron oxide nanocubes Bc 9 are presented in Figure 5.4.4.

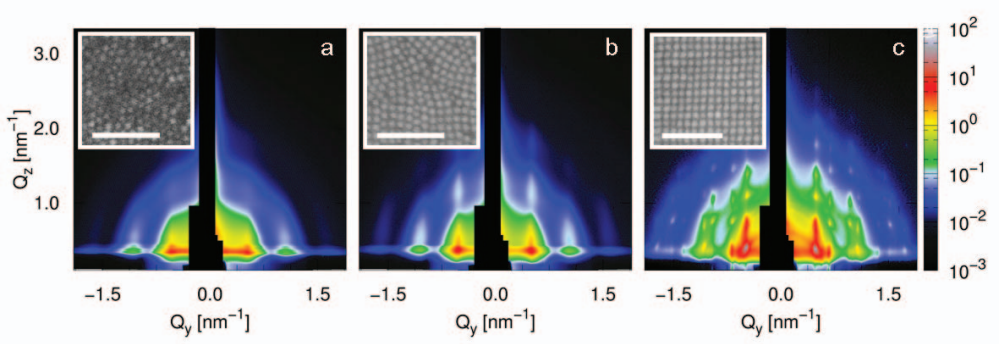

Figure 5.4.4.: GISAXS patterns of iron oxide nanocubes self organized by a) spin coating, b) drop casting, and c) drop casting in an applied magnetic field (α_i = 0.30°). Insets show SEM images of the respective samples. Scale bars represent 100 nm.

Spin coating of nanoparticle dispersion on the substrate yields a thin liquid nanoparticle layer which dries within less than a minute and generates the particle film illustrated by the SEM image in Figure 5.4.4a. The lack of long range order of the spin coated nanocrystal film suggests that the time-frame before the liquid has sufficiently evaporated and arrests further mobility of the nanocubes, is too short to allow for ordering of the particles.

A higher degree of order was obtained by drop casting. The entire substrate was covered with the nanoparticle dispersion generating a thicker film which dried more slowly. In order to further extend the evaporation time, the evaporation process was performed in a closed compartment providing a solvent-saturated atmosphere and evaporation times in the range of hours. The obtained arrays show domains with a square packing symmetry as visible in the inset of Figure 5.4.4b. These domains are relatively small with a lateral size ranging over few particle periods.

Highly ordered superlattices with a lateral dimension of several micrometers were produced by self assembly by inducing dipolar attraction between the superparamagnetic nanocubes [105]. Application of a weak magnetic field perpendicular to the substrate during evaporation of the nanoparticle dispersion yields assemblies of nanocubes highly ordered not only in plane as shown in the inset of Figure 5.4.4c but also perpendicular to the substrate. It has to be emphasized that such a long range order was only achieved by use of the closed compartment during evaporation. A small reservoir of sol-

vent within the compartment however, meant to further extend the evaporation time, did not enhance the long range order.

GISAXS patterns of the mentioned samples, presented in Figure 5.4.4, confirm the observations made on the local scale by SEM also for the statistical average of a large part of the sample. Any correlation between nanoparticles on a substrate is expressed by the structure factor revealed by GISAXS measurements. A detailed description of the GISAXS setup and scattering theory is given in sections 2.2.3.3 and 5.4.2.3. Lateral correlations of the nanoparticle arrays are expressed by scattering in the Yoneda line, which is the sample horizon at $\alpha_f = \alpha_c$, appearing at $Q_z = 0.34$ nm^{-1} in the GISAXS patterns shown in Figure 5.4.4. Figure 5.4.5 compares the scattering intensities in the Yoneda lines for the studied samples. While the spin coated and drop casted samples

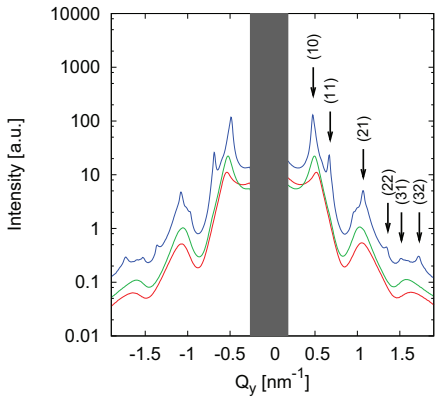

Figure 5.4.5.: In plane scattering of iron oxide nanocube assemblies. Projections of GISAXS intensities in the Yoneda line are shown on a logarithmic scale for the spin coated (red), drop casted (green), and magnetically ordered (blue) sample. Reflections of the latter are indexed according to the *p4mm* plane group.

show broad features of liquid like nearest neighbor correlations, additional sharp reflections are observed for the magnetically ordered sample. Correlation lengths were determined for the first order reflections of the lateral scattering contributions at $Q_y \sim 0.5$ nm^{-1} taking into account a finite resolution of the ID01 instrument of 0.031 nm^{-1} (see section 5.4.2.3 for a detailed description of the evaluation of lateral correlation lengths). For the spin coated and drop casted samples, lateral correlation lengths of 16.1 (3) and 17.6 (2) nm were derived. This illustrates, consistently to the SEM results, the somewhat higher correlation achieved by drop casting, although the overall order remains glass-like. The correlation length of the magnetically ordered sample, determined to 60 (7) nm, is at the instrumental resolution limit of ~ 64 nm. These very well resolved lateral

correlation peaks indicate a crystalline order instead of a glass-like correlation. They were indexed according to the square plane group *p4mm* with a lattice constant of 13.1 (1) nm, which is in good agreement with the observations made by SEM. Due to the observation of broad peaks below the sharp reflections, smaller regions of liquid-like disorder can be expected as well.

The Q_z direction of the GISAXS patterns accounts for scattering contributions perpendicular to the substrate. For the spin coated and drop casted samples, so called Bragg rods are observed to evolve from the nearest neighbor correlation peaks. These are due to smearing of the in plane correlation peaks in Q_z direction, originating from a short correlation length perpendicular to the substrate, which is a strong indication for thin films of a mono- or bilayer of nanoparticles. Thus, these nanoparticle layers are laterally disordered, albeit with a homogeneous thickness. The magnetically ordered sample shows distinct reflections in the Q_z direction, indicating high correlation out of plane and thus suggesting three dimensional mesocrystals. A detailed description of the mesocrystal structure will be given in section 5.4.3.2.

Different degrees of order in the assembled nanoparticle arrangements have been achieved by variation of several parameters: the thickness of the deposited nanoparticle dispersion film, the evaporation rate, and the variation of dipolar attraction between the particles.

The first two parameters are related to the time given to the nanocrystals to arrange in either dispersion or at the interface between dispersion and air, before being arrested when the solvent is evaporated entirely. The very thin film prepared by spin coating dries extremely fast and arrests the nanocrystals immediately. Nonetheless, a good homogeneity of the layer has been achieved, which is the general purpose of the application of spin coating techniques. The use of a controlled atmosphere for extension of the evaporation rate was not reported for superlattice formation on TEM grids [105]. During transfer of the method to solid, flat substrates, however, it has been found to be crucial for long range ordered assembly. It may be speculated that due to the pores of TEM grids, some of the solvent resists evaporation inside the pores, leaving a smaller solvent air interface and thus extending the evaporation time.

Dipolar interaction between the nanocrystals was induced by application of the magnetic field. In contrast to the other parameters extending the evaporation time, the effect of dipolar attraction results in a faster arrangement of the nanocrystals. Thus, highly ordered superstructures can form in a shorter time scale, before the dispersion is entirely evaporated.

Consequently, the highest degree of long range order was achieved here by combining the larger time frame with the induction of dipolar attraction. The assembly of nanocubes has a single crystalline nature and is observed not only in plane, but also perpendicular to the substrate. Determination of the three dimensional structure of the observed nanoparticle mesocrystals is the objective of section 5.4.3.2.

5.4.3.2. Into the third dimension: determination of the nanocubes superstructure

The nanoparticle assemblies prepared by spin coating and drop casting presented in the previous section are arranged in two dimensions parallel to the substrate. It has already been suggested that the magnetically ordered arrangement extends into all three dimensions. These nanoparticle mesocrystals were investigated by several methods in order to unravel the three dimensional supercrystal structure.

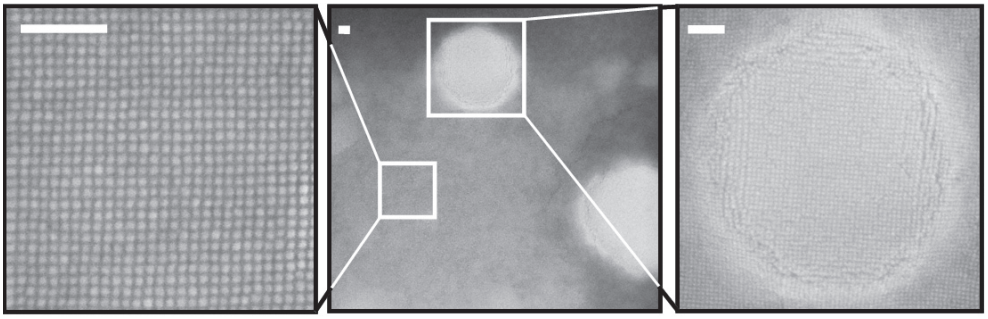

Figure 5.4.6.: Scanning Electron Microscopy images of self assembled iron oxide nanocubes. Scale bars represent 100 nm.

SEM and AFM images, illustrating the mesocrystals on the local scale, are presented in Figures 5.4.6 and 5.4.7, respectively. Whereas SEM provides a better lateral resolution, AFM gives additional information on the height of the observed features. Many islands of nanoparticles are observed on top of a thinner layer of ordered nanocubes. X-ray reflectivity measurements discussed later on will show that this is a defined monolayer of ordered nanocubes (see Figure 5.4.11b on page 250). The islands extend laterally in a micrometer size range and up to 300 nm in height. The top of the islands is remarkably flat, as illustrated by the constant amplitude in Figure 5.4.7b. In this top layer nanocubes are arranged in the same square lattice as in the first monolayer, indicating an ordered stacking of a defined number of monolayers. This observation suggests a single crystalline arrangement of ordered iron oxide nanocubes in three dimensions. In order to verify a crystalline arrangement of the nanocubes, the bulk of the mesocrystal

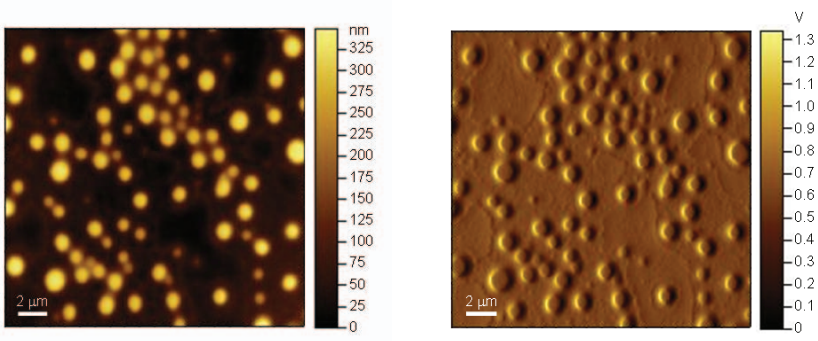

(a) Topography. (b) Amplitude.

Figure 5.4.7.: Atomic Force Microscopy images of self assembled iron oxide nanocubes.

has to be investigated. While SEM and AFM provide a local top view of the sample, GISAXS gives the opportunity of a nondestructive penetrating probe and thus allows for determination of the internal mesocrystal structure.

The in plane symmetry was determined by indexing the reflections in the Yoneda line according to the plane group *p4mm* with a lattice constant of a = 13.10 (5) nm (section 5.4.3.1). Even though locally the order of the nanocube superlattices is high, on the dimension of the sample, of several cm^2, the particles are arranged in domains with each mesocrystal representing one domain. These domains are oriented randomly in plane, but are internally structurally coherent, thus appearing as a 2 D powder. Their existence is reflected by the simultaneous observation of all reflections of the *p4mm* plane group in the Yoneda line without any rotation of the sample during the measurement. The nanocube layers are stacked in a crystalline order along the film normal z, as can be seen from the sharp reflections above the Yoneda line in Figure 5.4.4c, corresponding to scattering from lattice planes with $l \neq 0$. The dimension of the c lattice constant was determined by analyzing the Q_z positions of the GISAXS reflections at different incident angles. Refraction of the beam at the sample - air interface was taken into account by a combination of Bragg's and Snell's Laws as described in section 5.4.2.3. The exact Q_z positions of the GISAXS reflections at different incident angles were determined by Lorentzian fits, and the c lattice constant as well as the critical angle of the sample were fit to the data using relation 5.4.2. Indexing of the (10l) and (11l) reflection series with this relation is presented exemplarily in Figure 5.4.8.

In agreement with all remaining reflection series, a lattice constant perpendicular to the substrate of c = 17.80(5) nm and the critical angle of total reflection of α = 0.125°

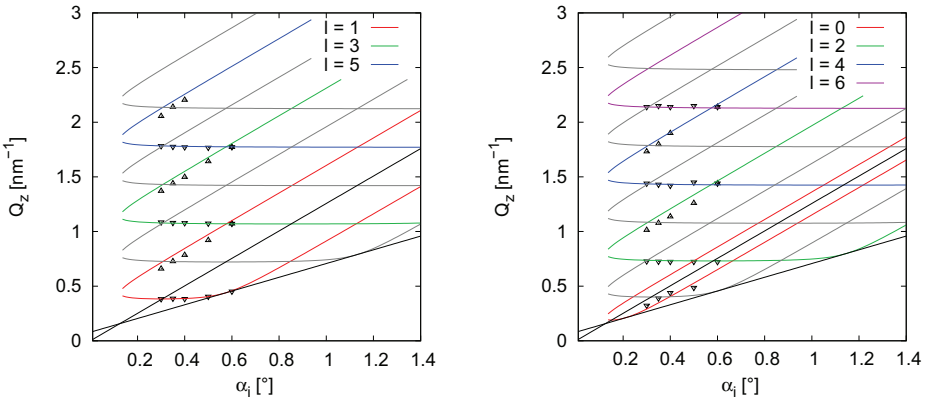

(a) Tetragonal indexing of the (10l) reflection series.

(b) Tetragonal indexing of the (11l) reflection series.

Figure 5.4.8.: Tetragonal indexing of iron oxide nanocube mesocrystals. Measured reflections both with (△) and without (▽) total reflection of the scattered beam are shown. Theoretical positions of Yoneda line and specular reflections are presented as black lines, and theoretical positions of the extinct reflections are presented as grey lines, i.e. l=2,4,6 for the (10l) series and l=1,3,5,7 for the (11l) series.

were determined. Considering the lateral lattice constant a = 13.10(5) nm, the observed structure is indeed tetragonal and thus different from the simple cubic symmetry that could be expected from the SEM images. The observed extinction rule h + k + l = 2 n (Fig. 5.4.8) and steric hindrance lead to the space group *I4/mmm* (No. 139) corresponding to a body centered tetragonal (*bct*) packing with the highest possible symmetry for stacking nanocubes. A fully indexed GISAXS pattern of this mesocrystal structure is presented in Figure 5.4.9, and a schematic representation of the determined structure type is given in Figure 5.4.10. In this crystal structure, the individual nanocubes assemble in an oriented arrangement with their (100) facets facing each other. The preference of this stacking type can be qualitatively understood if the space required by the oleic acid ligand layer is considered. This ligand shell acts as spacer inside the monolayers and favors a square packing of the nanocubes. As the oleic acid coordinates easily on (100) facets of the iron oxide nanocrystals, but not as well on the (111) facets of the truncations [106], each square layer of nanocubes provides gaps in between the nanocubes, upon which the iron oxide cubes of the next layer are preferably located. Thus, the next layer is shifted by (½ ½ ½) (Figure 5.4.10), favoring a body-centered over a primitive packing.

A quantitative justification of the *bct* structure type as compared to a simple cubic (SC) packing of the nanocubes has been given by calculations of the interaction energy as performed by Bergström *et al.* [106]. The model is based on calculation of the van

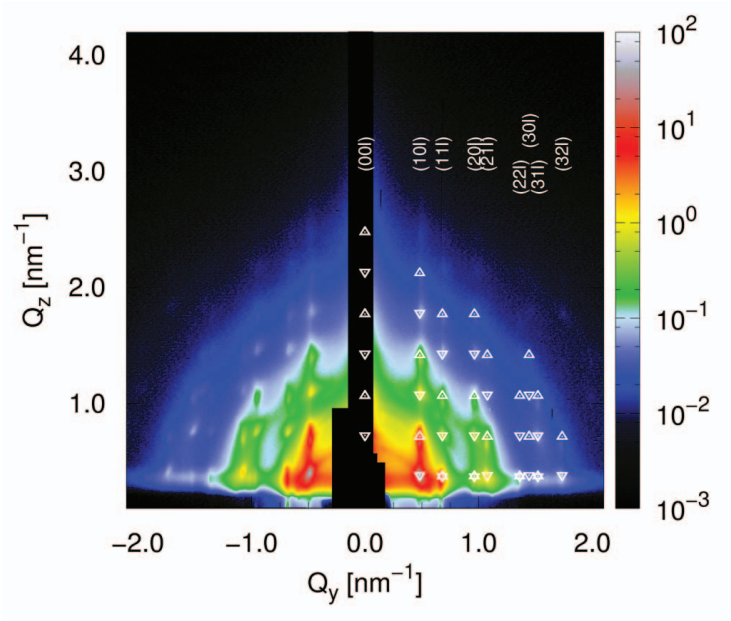

Figure 5.4.9.: GISAXS pattern of iron oxide nanocube mesocrystals (α_i = 0.30°). Reflections are indexed according to the discussed *bct* structure. For each lattice plane both reflections with (△) and without (▽) total reflection of the scattered beam are shown.

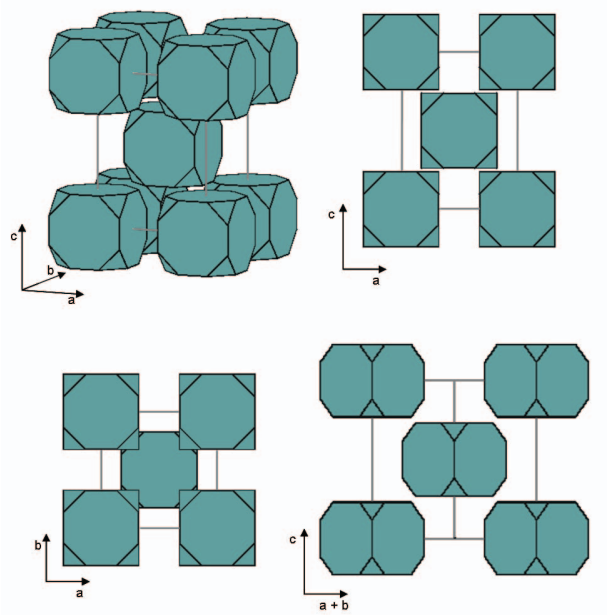

Figure 5.4.10.: Schematic of the body centered tetragonal structure type. A stereographic view is presented along with projections in the [100] (top right), [001] (bottom left), and [110] (bottom right) directions.

der Waals attraction between the nanocubes in the different nearest neighbor directions, taking into account the interparticle distances as determined by GISAXS. The interaction energy was calculated in dependence of the degree of truncation for the *bct* as well as a *sc* arrangement. For a degree of truncation larger than $\tau = 0.35$, the *bct* arrangement was found to be preferred against the *sc* structure.

As a result of the body centering, the distance between the individual nanocubes in c direction is extremely small close to the nanocube corners, as can be seen in the projections in Figure 5.4.10. Only due to the truncation of the corners the distance between the facets of the nanocubes is large enough for a thin organic ligand shell as visible in the [100] and [110] projections in Figure 5.4.10. The interparticle distances perpendicular to the substrate were additionally investigated by X-ray and neutron reflectivity measured in house and at the TREFF instrument at FRM II (3.2.1), respectively. In Figure 5.4.11a the calculated scattering length density profiles of the determined *bct* structure are presented under the assumption of a 1 nm ligand shell between the substrate and the first

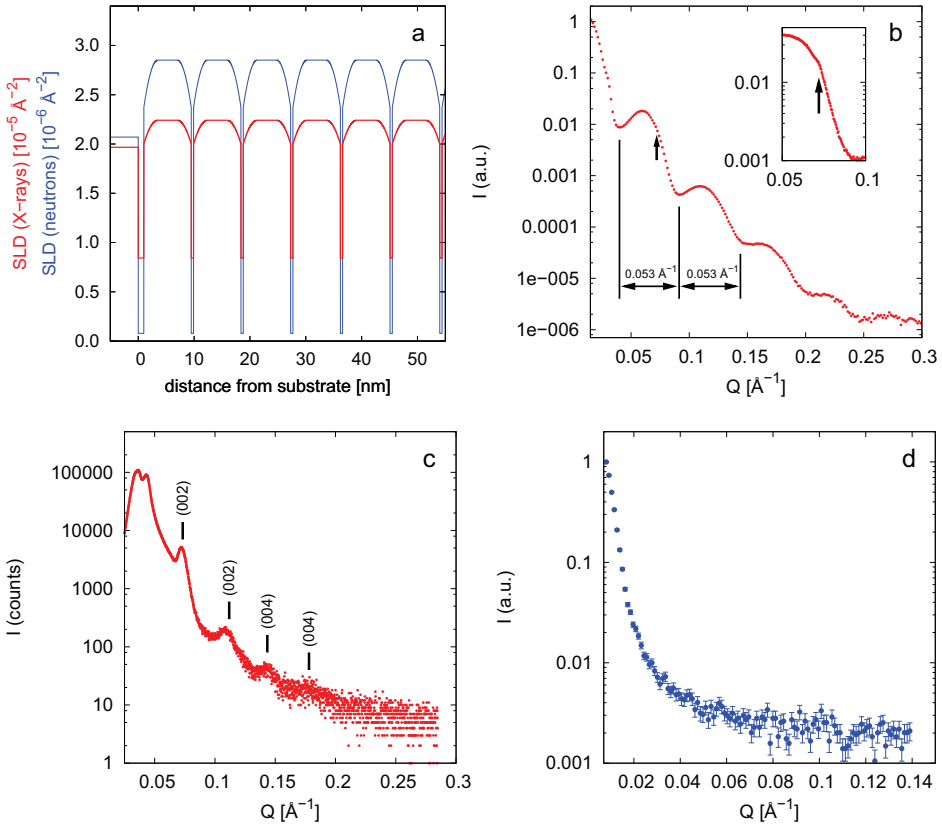

Figure 5.4.11.: Reflectivities of *bct* arranged iron oxide nanocubes. a) Comparison of the scattering length density profiles for X-rays and neutrons. Between the substrate and the first layer of nanocubes, a 1 nm layer of oleic acid is inserted. b) specular X-ray reflectivity. A weak multilayer peak is marked by the arrow. c) off-specular X-ray reflectivity measured at an incident angle of α_i = 0.3°. d) specular neutron reflectivity.

nanoparticle layer. In the X-ray reflectivity measurement, Kiessig fringes are observed which can be attributed to the nanocube monolayer in between the mesocrystals and constituting the first layer of the mesocrystals. This is supported by the distance of the fringes of 0.06 $Å^{-1}$, corresponding to a monolayer thickness of 10.5 nm in real space which is in good agreement with the thickness of a nanocube of ~ 8.5 nm edge length and 1 nm shell thickness.

In another measurement of the same sample with a smaller step size, a weak Bragg reflection is also observed at Q = 0.072 $Å^{-1}$, a reflection that can be attributed to the multilayer structure of the *bct* mesocrystals with a period of ~ 87 Å. This multilayer reflection is extremely weak as compared to the Kiessig fringes due to the poor contrast between iron oxide rich and oleic acid rich layers in the structure. As visible in the projections in Figure 5.4.10 and in the calculated SLD profile, there exist small gaps between the nanocubes in the structure that might lead to a considerable contrast between the nanocube layers and result in strong multilayer reflectivity peaks. However, these gaps are so narrow that even a low degree of roughness of the layers - possibly induced by a variation of the degree of truncation - is sufficient to prevent their detection by reflectivity measurements. Instead, the very small remaining contrast of about $2.5 \cdot 10^{-6} Å^{-2}$ leads to the weak observed Bragg reflections. In order to detect even these weak Bragg reflections the off specular reflectivity was investigated. Here, Kiessig fringes are suppressed, because they require $\alpha_i = \alpha_f$ and thus only appear in specular reflectivity measurements. The off specular scan presented in Figure 5.4.11c shows essentially the scattering along $Q_y = 0$ in the GISAXS pattern in Figure 5.4.9, which is shadowed behind the beam stop for most GISAXS experiments. In this scan, as in all GISAXS patterns, the Bragg reflections for the multilayer structure are clearly observed and can be indexed according to the *bct* structure. For neutron scattering, the multilayer contrast of $\sim 4 \cdot 10^{-7} Å^{-2}$ is even lower than for X-rays (note the factor of 10 in Figure 5.4.11a). Accordingly, no multilayer peaks were observed by neutron reflectivity, as visible in Figure 5.4.11d. The fact that neutron reflectivity does not either reveal any Kiessig fringes is due to the low flux at the TREFF instrument combined with a higher background than in the X-ray reflectivity measurement. Additionally, the monolayer of nanocubes in between the mesocrystals covers only a small part of the total sample area, which is dominated by a huge roughness (with up to 300 nm high mesocrystals). Finally, the presented reflectivity measurements support the extremely dense stacking of truncated nanocubes in c direction of the *bct* mesocrystal structure determined by GISAXS.

5.4.3.3. Supercrystals of nanospheres

In order to determine the influence of the particle shape on degree and type of order, superlattices of the Bs 10 nanospheres were prepared by the same magnetically induced self assembly method. Investigation of the local order by SEM and AFM imaging techniques (Figures 5.4.12 and 5.4.13) reveals a high density of mesocrystals on a layer of nanospheres. The mesocrystals observed here are ordered laterally in a micrometer size range and extend up to 400 nm in height. The hexagonal lateral symmetry expected for closed packed spheres is also inherited by many nanospheres mesocrystals with their hexagonal habit as shown in Figures 5.4.12 and 5.4.13.

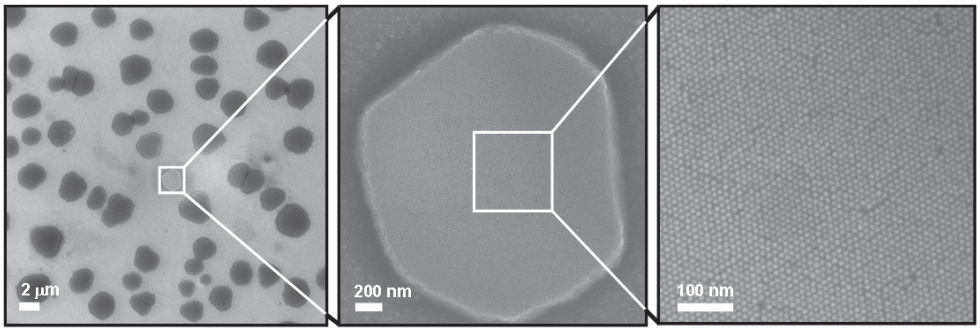

Figure 5.4.12.: SEM images of self assembled Bs 10 iron oxide nanospheres.

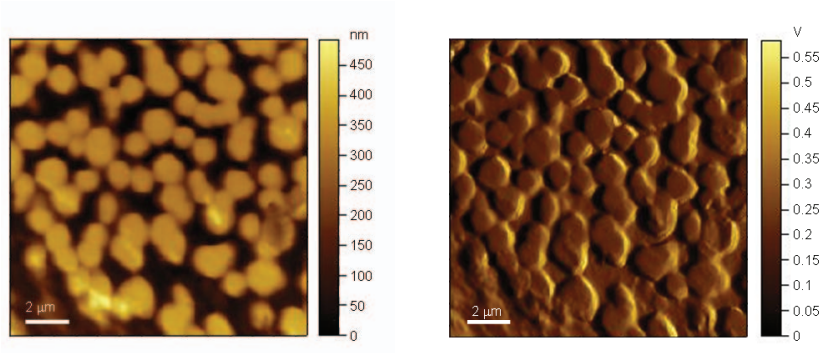

(a) Topography. (b) Amplitude.

Figure 5.4.13.: Atomic Force Microscopy images of self assembled Bs 10 iron oxide nanospheres.

The GISAXS pattern of this sample presented in Figure 5.4.14 shows a large amount of extremely sharp reflections. In the same approach as applied to the nanocubes mesocrys-

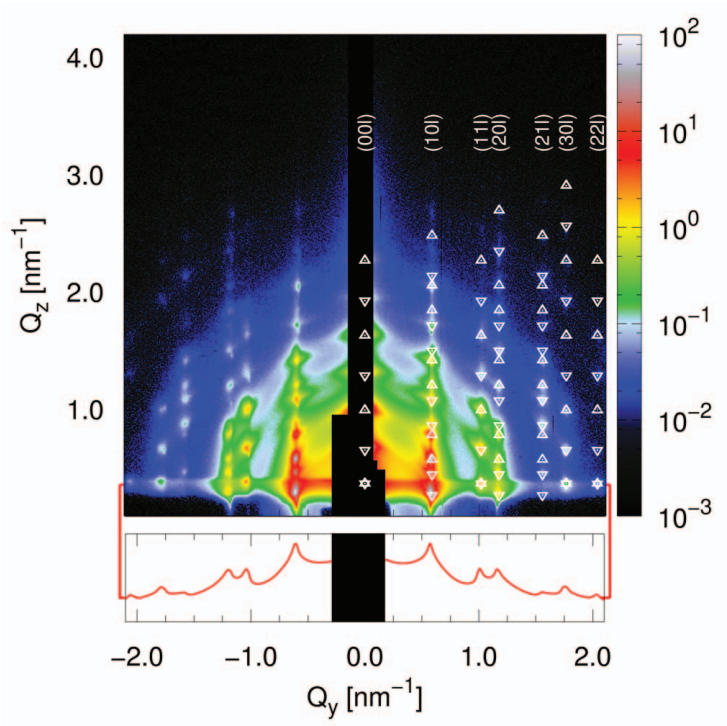

Figure 5.4.14.: GISAXS pattern of Bs 10 iron oxide nanospheres mesocrystals (α_i = 0.30°). Reflections are indexed according to the discussed distorted rhombohedral structure. For each lattice plane both reflections with (△) and without (▽) total reflection of the scattered beam are shown. The intensities observed in the Yoneda line at Q_z = 0.34 nm^{-1} are shown in a logarithmic scale as red line in the bottom.

tals, the lateral correlation peaks appearing in the Yoneda line were indexed. The determined hexagonal plane group *p6mm* is in agreement with the symmetry observed by SEM, and the lattice constant of a = 12.3(1) nm corresponds to a closed packed array of nanospheres of 10 nm diameter and 1.1 nm shell thickness. Correlation lengths determined from the lateral scattering reflections are beyond the resolution limit of 65 nm, which illustrates the high quality of the obtained superlattices.

For the three dimensional structure type, either *hcp* (ABAB), or *fcc* (ABCABC) type stacking or variants with stacking faults of the hexagonal monolayers is expected. Indexing of the GISAXS reflections via their Q_z position in dependence of the incident angle was performed according to equation (5.4.3) and is presented in Figure 5.4.3 (section 5.4.2.3). A lattice constant perpendicular to the substrate of c = 29.7(1) nm is determined

along with the critical angle of total reflection of 0.125° which is equal to that of the nanocubes. The observed extinction rule -h + k + l = 3 n is consistent with the rhombohedral space group $R\bar{3}m$ (No. 166), corresponding to the *fcc* stacking type. A schematic representation of the determined mesocrystal structure is given in Figure 5.4.15.

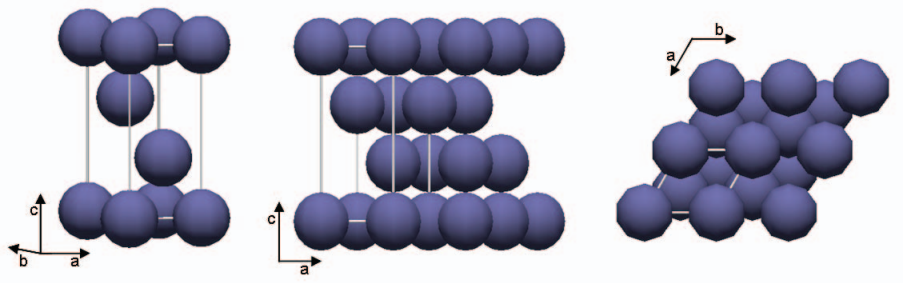

Figure 5.4.15.: Schematic of the rhombohedrally packed nanospheres structure type. A stereographic view is presented along with projections in the [120] (middle) and [001] (right) directions.

Note that the h and k indices of the observed reflections can not be distinguished for a 2 D powder as observed here. The alternative of a *hcp* stacking type, however, corresponds to the space group P 6_3/m m c (No. 194) with a different extinction rule of l = 2, which is unambiguously not observed in this case. For the rhombohedral setting of the *fcc* structure type, a c lattice constant of 30.1 nm is expected for the $R\bar{3}m$ space group. Thus, we observe here a 1.2 % shrinkage of the *fcc* stacking type along its $(111)_{fcc}$ direction (which is perpendicular to the substrate and thus equal to the $(001)_{rhomb}$ direction of the rhombohedral setting). This shrinkage can be understood as an effect of final drying of the nanoparticles after deposition, as the as-deposited mesocrystals might still contain some trace amounts of solvent. The evaporation of the entire solvent will result in a uniaxial shrinkage of the mesocrystals perpendicular to the substrate, because the particles are laterally fixed by adhesion to the substrate. This effect has been observed for many deposited systems including block-copolymers [179] and nanoparticle superlattices [178, 180] with considerably higher degrees of contraction around 10%.

The thickness of the individual nanoparticle layers was additionally investigated by reflectivity measurements. As visible in the [100] projection in Figure 5.4.15, the gaps between the nanoparticle layers are small same as observed for the *bct* arranged nanocubes. Due to the different particle shape, however, the SLD profiles of the nanospheres mesocrystals, shown in Figure 5.4.16a, exhibit much larger contrasts between the layers

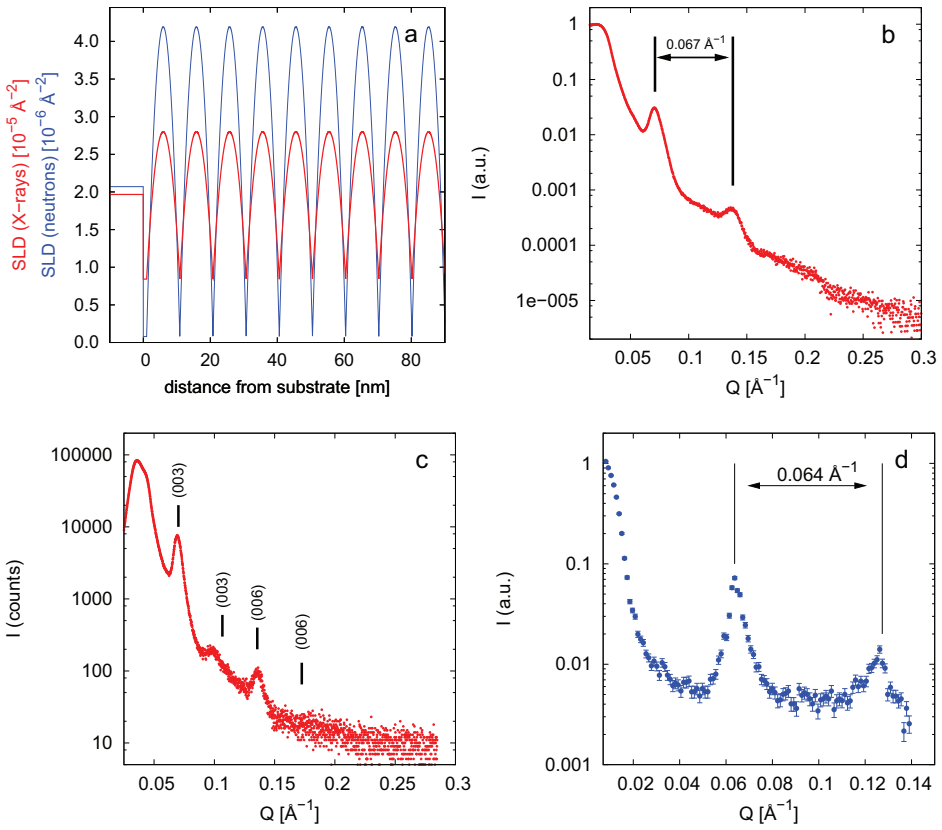

Figure 5.4.16.: Reflectivities of rhombohedrally packed Bs 10 iron oxide nanospheres. a) Comparison of the scattering length density profiles for X-rays and neutrons. Between the substrate and the first layer of nanospheres, a 1 nm layer of oleic acid is inserted. b) specular X-ray reflectivity. c) off-specular X-ray reflectivity measured at an incident angle of $\alpha_i = 0.3°$. d) specular neutron reflectivity.

of iron oxide nanospheres and the oleic acid enriched regions in between them. As expected, multilayer peaks are observed in both X-ray (Fig 5.4.16b) and neutron (Fig 5.4.16d) specular reflectivity measurements corresponding to a layer thickness of ~ 10 nm which is in agreement with the nanoparticle size. Again, off-specular reflectivity (Figure 5.4.16c) confirms the (00l) reflection positions that are shadowed by the beam stop in the GISAXS pattern in Figure 5.4.14.

It is emphasized that both specular and off specular reflectivity measurements provide information on the layer thickness, but the stacking symmetry of these layers can only be clarified by GISAXS, *i.e.* if reflection series at $Q_y \neq 0$ can be indexed. For indexing of the (00l) reflections in Figure 5.4.16c either the extinction rules or the c lattice constant have to be known since the (00l) reflection positions of a structure with l = 3n and c' = 3c generally coincide with those of a primitive structure with a lattice constant c.

In the present case, a distorted *fcc* stacking of the closed packed nanospheres layers was found by GISAXS. According to Whetten *et al.* [169], the ratio of ligand shell thickness and core radius $\chi = l/R$ can for spherical particles and regardless the material be related to the observed packing symmetry. The nanospheres studied here with $\chi = 0.34$ and an inorganic volume fraction in the assembled mesocystals of 39% fit clearly in the region of *fcc* stacking. The transition to the *bcc/bct* region has been given at higher χ ($\chi > 0.4$), and the *fcc-hcp* structural transition has been suggested in the region of higher volume fractions (lower χ) around 50% [169]. The *bct* structure found for the nanocube mesocrystals despite a χ ratio similar to that of the nanospheres illustrates the shape dependence of nanoparticle self assembly. The cubic shape of the nanoparticles allows for a maximization of the van der Waals energy by a surface-to-surface arrangement, resulting in oriented mesocrystals [152]. In case of perfect nanospheres, the crystal facets become infinitely small, and the crystalline arrangement is expected to originate from steric considerations only, leading to either *hcp* or *fcc* stacking. It has to be mentioned that spherical nanocrystals, especially if they are small, will be faceted nanoparticles rather than perfect spheres. However, the size of these facets will be much smaller than for the nanocubes and is sufficiently small not to be detected by any of the characterization techniques employed in this study. Thus, there is no evidence for oriented arrangement in the nanospheres mesocrystals, although the observed preference of *fcc* against *hcp* stacking is in agreement with the atomic symmetry of the iron oxide nanospheres. An even more subtle example for the shape dependence of the mesocrystal structure will be discussed in the following section.

5.4.3.4. Nanocubes revisited

Further investigations were performed on deposition of the truncated nanocubes Bc 9 with the objective to

- enhance the long range order of the obtained mesocrystals,
- obtain larger domains up to a single crystal of nanoparticles, and
- prepare a single, long range ordered monolayer.

Investigated variations of the deposition technique include the application of magnetic stray fields and the variation of magnetic field strength or direction. For most of the investigated samples, two structures different from those discussed before were observed. While all investigated samples were prepared by evaporation of the nanoparticle dispersion inside a closed compartment as discussed before, a systematic dependency of the observed structure on the applied magnetic field strength or direction was not found. However, even reproduction of the *bct* arranged nanocube mesocrystals led to a mixture of those two new structures, while one of those exhibits a highly interesting long-range order.

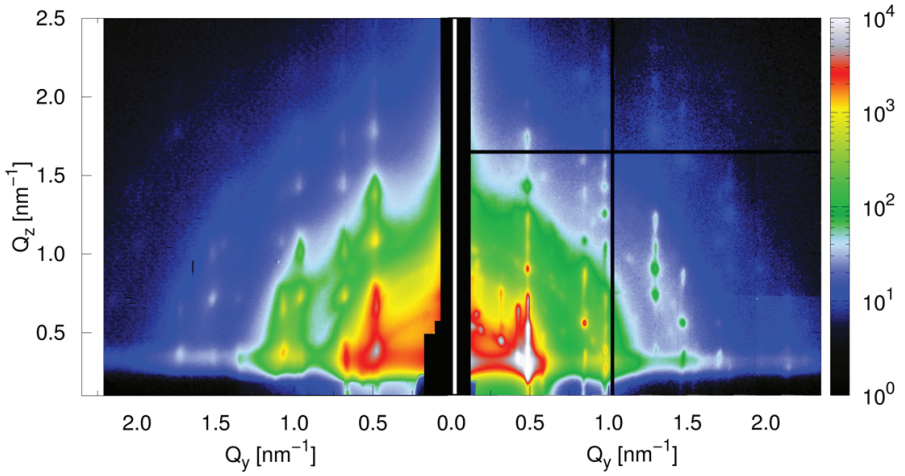

Figure 5.4.17.: Reproduction of the *bct* arranged mesocrystals (α_i = 0.30°). The GISAXS pattern of the *bct* arranged nanocubes (left, for a colorbar see Figure 5.4.9) is compared to the GISAXS pattern of a sample prepared by the same method one year later (right). The overlap regions of different detector elements are masked by black lines.

In Figure 5.4.17, the GISAXS patterns of the reproduction of the *bct* nanocube structure type and the initial mesocrystal sample discussed in section 5.4.3.2 are compared. Although the samples were prepared by the exact same method and from the same dispersion of nanocubes, the two GISAXS patterns show entirely different structural reflections. The only difference in preparation is the date of deposition which was about one year later for the reproduced sample. Indexing of the Yoneda line resulted in two different plane groups for the reproduced sample, namely *p4mm* and *p6mm* with lattice constants different from those observed before for the mesocrystals of iron oxide nanocubes and nanospheres. Figure 5.4.18 shows a comparison of the Yoneda lines of this mixed sample and two samples that exhibit a preference of the respective structure types. For these almost phase pure samples the structures were determined and will be discussed more detailed.

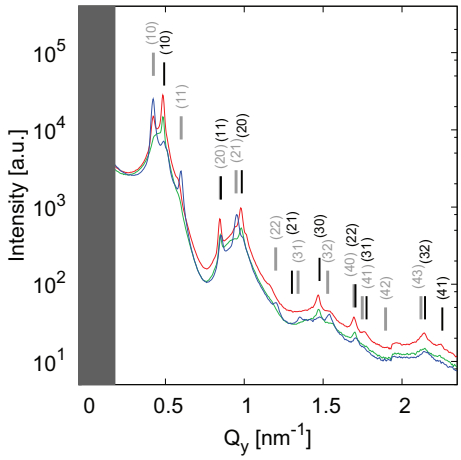

Figure 5.4.18.: Yoneda lines measured with α_i = 0.30° for three samples of nanocube superlattices: the sample presented in Figure 5.4.17b (red), a sample with preferential hexagonal lateral order (green), and a sample with preferential square lateral order (blue). Indexing according to square and hexagonal plane groups is shown in grey and black, respectively.

Rhombohedral stacking of iron oxide nanocubes A sample with hexagonal lateral symmetry as single phase was prepared by evaporation of the nanoparticle dispersion in a divergent magnetic field at the edge of the magnet. Indexing of the Yoneda line in Figure 5.4.18 (green) revealed a lattice constant of a = 14.7(1) nm for the hexagonal plane group *p6mm*. The GISAXS pattern of this sample with indexed reflections is presented in Figure 5.4.19.

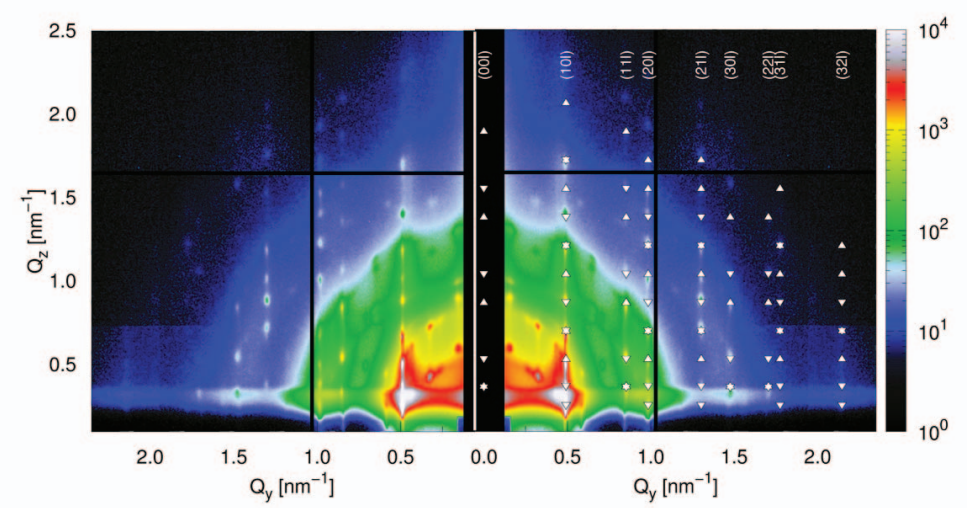

Figure 5.4.19.: GISAXS pattern of rhombohedrally packed iron oxide nanocubes (α_i = 0.30°). Reflections are indexed according to the discussed rhombohedral structure. For each lattice plane both reflections with (△) and without (▽) total reflection of the scattered beam are shown. Unindexed reflections at low Q indicate formation of a superstructure that will be discussed later on. The intensities observed in the Yoneda line at Q_z = 0.34 nm^{-1} are shown as green line in Figure 5.4.18. The overlap regions of different detector elements are masked by black lines and the left hemisphere was produced by mirroring of the right hemisphere without indexing.

The lattice constant perpendicular to the substrate was determined to c = 36.8(1) nm, and the observed extinction rule - h + k + l = 3 n suggests a rhombohedral centering of the unit cell same as observed for the nanospheres mesocrystals. Considering the determined Bravais lattice, steric hindrance, and also the symmetry of the nanoparticles, the same ABCABC stacking type as for the nanospheres is deduced. A schematic of the suggested structure type is presented in Figure 5.4.20.

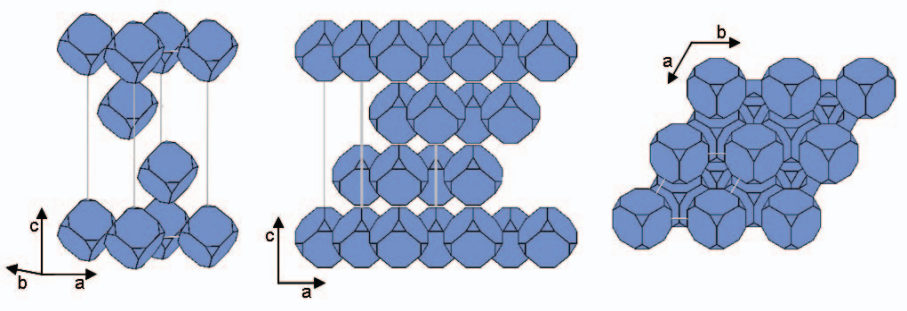

Figure 5.4.20.: Schematic of the rhombohedrally packed nanocubes structure type. A stereographic view is presented along with projections in the [120] (middle) and [001] (right) directions.

The nanocubes must be oriented with their space diagonal parallel to the c lattice constant (perpendicular to the substrate), corresponding to the threefold rotational symmetry in c direction of the unit cell. Because the $\bar{3}$ symmetry of the truncated nanocubes in this direction does not allow a mirror plane, the correct space group of these mesocrystals is R $\bar{3}$ rather than R $\bar{3}$ m as found for the nanospheres. This structure type corresponds to the rhombohedral setting of *fcc* packed nanocubes. The larger unit cell as compared to the nanospheres mesocrystal structure is in agreement with the larger size of the faceted particles as determined in section 5.1.3.1. The packing density of the two rhombohedral structures is comparable as can be seen in the respective [120] projections (Figures 5.4.15 and 5.4.20).

The rhombohedral structure type was observed for almost all nanocubes mesocrystals prepared about one year after determination of the *bct* packing type. The preference of this structure type - even despite the exact same preparation technique - suggests a change of the nanoparticle dispersions with time. The main difference between the structures is the nanocube orientation which changed from lying on its (100) cube facet to standing on its (111) truncation facet on the substrate. A different orientation of the first nanocube layer might arise from different substrate-particle interactions. However, all substrates used for this study have been treated by the same cleaning procedure

described in section 5.4.2.1. For this reason it is rather speculated that ageing of the nanoparticles leads to a larger degree of truncation resulting in larger (111) facets. This is possible because the (111) facets are terminated by either only iron or only oxygen atoms, resulting in a lower surface coverage of oleic acid than the (100) facets. If ageing involves the dissolution of a certain portion of the material, it will thus preferentially occur at the (111) facets, with the effect of increasing the degree of truncation. The occurrence of particle ageing with time is reasonable because the particle dispersions were not stored in the dark. One of the main reactions that can occur with light activation [106] is the decomposition of the oleic acid through oxidation of its double bond possibly even up to disruption, resulting in a lower surface coverage of the nanoparticles. If iron atoms are dissolved from the nanocrystal, they are expected to stay in solution as oleates or coordinated by organic side products of the oleic acid decomposition.

This result of a rhombohedral stacking of the truncated cubes illustrates again the high sensitivity of the mesocrystal structure to the nanoparticle shape. As observed here, just a small change in the degree of truncation shifts the stacking preference from a *bct* structure to the rhombohedral arrangement similar to that found for spherical particles. With increasing degree of truncation the nanocubes resemble spherical particles, in particular if the ligand shell is taken into account. Consequently, a change of the mesocrystal structure towards the nanospheres mesocrystal structure is generally expected. However, the higher truncation of the nanocubes under study is still regular enough to differentiate them from spheres, and assembly in an oriented superlattice is likely. This is documented by the occurrence of a superstructure that was observed uniquely in arrangements of the nanocubes and will be discussed in the following section. For this reason it can be assumed that the first nanoparticle layer is determined by interactions of the larger (111) facets with the substrate. From the structural dependence of the mesocrystal structure on the first nanoparticle layer, a layer-wise growth mechanism of the mesocrystals is furthermore inferred.

Because the considerable influence of particle-substrate interactions is not covered by the van der Waals model, the found mesocrystal structure can not be discussed in this framework.

Superstructure Besides the already indexed reflections, the GISAXS pattern of the rhombohedrally packed nanocubes in Figure 5.4.19 exhibits further reflections, especially in the low Q_y range. These are commensurate superstructure reflections, *i.e.* they can be indexed as a combination of the basic reflections with a specific propagation vector.

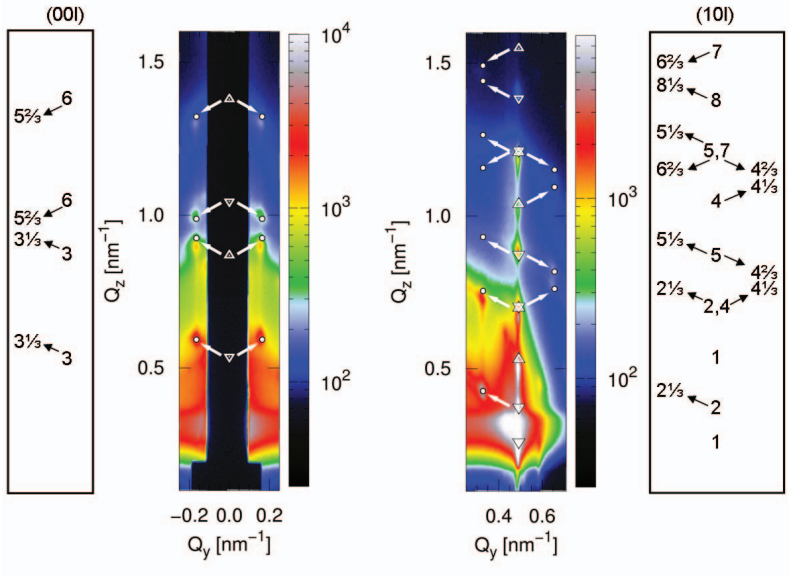

Figure 5.4.21.: Indexing of the superstructure reflections propagating from (00l) reflections (left) and (10l) reflections (right) of the rhombohedral arrangement of nanocubes. The corresponding l indices are given on both sides. For the (10l) reflections, all possible propagation vectors $\mp(\frac{1}{3}0\frac{1}{3})$ (↙, ↗) and $\mp(0\frac{1}{3}-\frac{1}{3})$ (↖, ↘) are observed corresponding to the extinction rules.

Figure 5.4.21 shows indexing of the superstructure reflections around the (00l) and (10l) basic reflections. The indexed superstructure reflections (Table 5.4.3) obey the rhombohedral symmetry by following the propagation vectors $\pm\,(\frac{1}{3}\,0\,\frac{1}{3})$ for (10l) reflections and $\pm\,(0\,\frac{1}{3}\,-\frac{1}{3})$ for (01l) reflections, respectively. For (hhl) reflections, the propagation vectors $(\frac{1}{3}\,0\,-\frac{1}{3})$ and $(\frac{1}{3}\,0\,\frac{1}{3})$ were observed for h + l = 2n and h + l = 2n + 1, respectively. Although (hkl) and (khl) reflections can not be distinguished for a 2 D powder, the found preference of the propagation vectors supports the rhombohedral extinction rules for the basic structure. While *e.g.* the (105) and (015) reflections can not be distinguished by GISAXS, the selective observation of $(0\,\frac{2}{3}\,5\frac{1}{3})$, but not $(0\,\frac{2}{3}\,4\frac{2}{3})$ allows indirectly for differentiation. Combining all observed propagation vectors, the entire superstructure can be described by a larger supercell in all three dimensions with A = 3 x a, B = 3 x b, and C = 3 x c. This supercell need not necessarily be the preferential setting as there might be a smaller unit cell of a different crystal class representing the superstructure better.

Table 5.4.3.: Superstructural reflections indexed in $R\bar{3}$ arranged iron oxide nanocubes (Figure 5.4.21).

(0 0 3)	$\rightarrow$ $(\frac{1}{3}\,0\,3\frac{1}{3})$
(0 0 6)	$\rightarrow$ $(\frac{1}{3}\,0\,5\frac{2}{3})$
(0 1 2)	$\rightarrow$ $(0\,\frac{2}{3}\,2\frac{1}{3})$
(0 1 5)	$\rightarrow$ $(0\,\frac{2}{3}\,5\frac{1}{3})$
(0 1 8)	$\rightarrow$ $(0\,\frac{2}{3}\,8\frac{1}{3})$
(1 0 4)	$\rightarrow$ $(\frac{4}{3}\,0\,4\frac{1}{3})$
(1 0 7)	$\rightarrow$ $(\frac{2}{3}\,0\,6\frac{2}{3})$
(0 1 5)	$\rightarrow$ $(0\,\frac{4}{3}\,4\frac{2}{3})$

Laterally, this larger unit cell can be understood by linear dislocations of the mesocrystal structure as observed by SEM and presented in Figure 5.4.22. These dislocations have the appearance of 1 D nanoparticle rods that are regular over a wide size range and are ordered with a period three times larger than the lateral lattice constant, leading to reflections with a Q_y three times smaller than Q_y(10l). Dislocations have been observed in many mesocrystals of all investigated samples. In one sample (Figure 5.4.22, top right), much broader, more irregular dislocations were observed that are arranged with an even larger period. These larger dislocations are expected to lead to further superstructure reflections. As these will follow an even shorter propagation vector they are located too close to the main reflections to be observable by GISAXS with the chosen incident wavelength and detector distance.

The observed dislocations are certainly not a surface effect of a single layer, but range deep into the bulk of the mesocrystals as is revealed by the $l = \pm\frac{1}{3}$ component of the propagation vector. As the projection of the propagation vector perpendicular to the substrate is equal to the lateral component, a lateral shift of the observed dislocations with each particle layer can be imagined.

Rhombohedral structures have in many cases been revealed to be pseudo-rhombohedral settings of monoclinic structures. Here, the observed reflections including the superstructure reflections follow the extinction rule -h + k + l = 9n for the supercell, which is even exceeding the rhombohedral extinction rule of -h + k + l = 3n. However, the dislocations presented in Figure 5.4.22 do not exhibit the three fold rotational symmetry of a rhombohedral structure. For this reason, it is concluded that the observed rhombo-

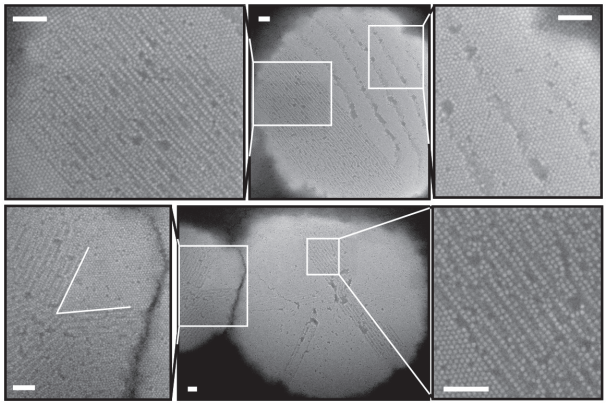

Figure 5.4.22.: SEM images of rhombohedrally arranged iron oxide nanocubes. Scale bars represent 100 nm.

hedral reflection conditions originate in a pseudo-rhombohedral structure that results from twinning of a structure with lower symmetry. An example for twinning of the superstructure within one mesocrystal is given in Figure 5.4.22 (bottom left) with several domains of 1D dislocations oriented at angles of 60° and ~140°. Since maximal a two fold rotation symmetry can be generated by the observed 1D dislocations, twinning of either monoclinic or orthorhombic systems is likely. However, since the GISAXS scattering geometry is pinned to the substrate, the determination of a symmetry with lattice constants that are not parallel to the substrate is challenging. However, because the observed superstructure did not appear in any of the nanospheres mesocrystals, it is assumed that the truncation of the nanocubes is still regular and the particle shape plays an important role during crystal growth.

A closer look at the 1D nanoparticle rods in Figure 5.4.22 reveals a surface-to-surface arrangement of the nanocubes via the (100) facets. Inside the larger dislocations in Figure 5.4.22 some small domains of square lateral order appear. This observation suggests that a rotation of the nanocubes is involved in the transition from the basic rhombohedral structure to the superstructure. The coexistence of rhombohedrally and square ordered domains within the mesocrystals serves as a further indication of the shape sensitivity of the mesocrystal structure. Apparently, the stabilities of *bct* and rhombohedrally packed arrangements are close to equilibrium for the current degree of truncation.

Tetragonal structure A further structure appeared only in mixtures with the rhombohedrally packed nanocube mesocrystals. A sample with this square lateral symmetry

as major phase was prepared by evaporation of the nanoparticle dispersion in a weaker magnetic field, achieved by positioning the substrate shifted out of the homogeneous field of a U-shaped magnet. Indexing of the Yoneda line in Figure 5.4.18 (blue) revealed the lattice constant of a = 14.6(1) nm for the square plane group *p4mm*. The GISAXS pattern of this sample with indexed reflections is presented in Figure 5.4.23.

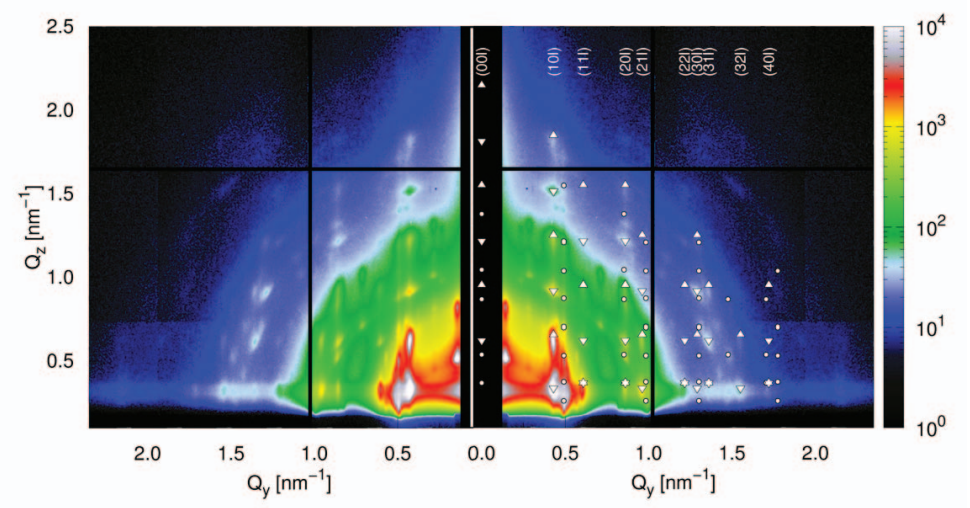

Figure 5.4.23.: GISAXS pattern of tetragonally packed iron oxide nanocubes (α_i = 0.30°). Reflections are indexedm plane both reflections with (△) and without (▽) total reflection of the scattered beam are shown. Reflections of the minor phase of the rhombohedral structure are marked as white points. The intensities observed in the Yoneda line at Q_z = 0.34 nm^{-1} are shown as blue line in Figure 5.4.18. The overlap regions of different detector elements are masked by black lines and the left hemisphere was produced by mirroring of the right hemisphere without indexing.

Indexing of the Q_z positions of the observed reflections resulted in a lattice constant of c = 21.0(1) nm perpendicular to the substrate. The observed extinction rule h + k + l = 2 n determines the space group *I4/mmm*, same as for the *bct* packed nanocubes discussed in section 5.4.3.2. As compared to the *bct* structure type observed before, the lattice constants are elongated by 11 % parallel and by 18 % perpendicular to the substrate. Generally, an increase of the unit cell suggests larger nanoparticle building blocks. If the ageing process suggested for the truncated nanocubes is considered, however, the particles are expected to decrease in volume but maintain the edge length. The larger *bct* unit cell found here can thus not be explained by particle ageing.

In Figure 5.4.23, further superstructure reflections are observed in the low Q_y range, which are not attributed to the superstructure of the minor rhombohedral phase in this sample. The origin of these superstructure reflections remains to be evaluated.

For the shape dependence of the mesocrystal growth it can be concluded, that the obtained mesocrystal structure depends strongly on the degree of truncation of the nanocube corners. For a relatively low degree of truncation, the *bct* arrangement was observed reproducibly. After about one year of ageing, which is suggested to enhance the truncation, the degree of truncation appears to be in a range where *bct* and rhombohedral packing are close to equilibrium. As a consequence of a probably wider distribution of the degree of truncation in the aged dispersion, the nanocrystals with different degrees of truncation self-segregate into the more stable mesocrystal structures. This can be understood as for the oriented assembly of faceted nanocrystals the interaction energy via the facing surfaces is maximized. Because the surface area of the facets scales the interaction energy, those facets with a larger surface area will have a stronger affinity to be oriented surface-to surface to the nearest neighbor particle. Thus, for a large degree of truncation, corresponding to truncated octahedra rather than truncated cubes, preferential formation of the rhombohedrally packed arrangement is expected and has been reported for the case of Ag nanocrystals [167].

5.4.3.5. Routes to a long range ordered nanoparticle monolayer

For preparation of a highly ordered monolayer of nanocubes, the deposition technique should be similar to that for preparation of large mesocrystals, yielding a magnetically induced long range lateral order. On the other hand, formation of large crystals into the third dimension has to be prevented. For this reason, the influence of the orientation of the substrate during evaporation was investigated.

Deposition of nanoparticle dispersion on a substrate tilted out of plane by ~ 10° yielded a substrate with two regions of different sample thickness. The part of the sample that was positioned lower during evaporation contains more material and was expected to contain large mesocrystals as well. The part that was elevated during evaporation is covered with less material and was investigated with GISAXS.

The GISAXS pattern presented in Figure 5.4.24 shows long Bragg rods that suggest this part of the sample to be close to a monolayer or bilayer. The observed degree of lateral order allows for indexing of the Yoneda line, leading to a square plane group with lattice constant a = 14.0(1) nm and a lateral correlation length of 56(2) nm. The lateral correlation length is not as high as observed for the 3D arranged samples, but was

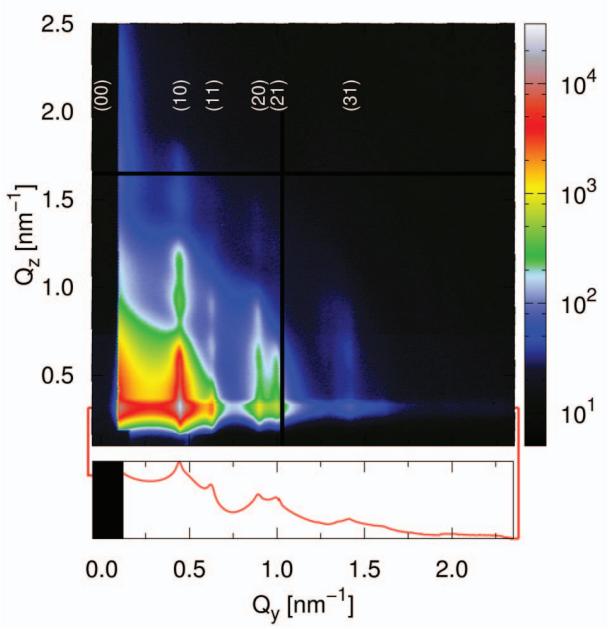

Figure 5.4.24.: GISAXS pattern of a square superlattice of iron oxide nanocubes (α_i = 0.30°). Appearing Bragg rods are indexed according to the discussed square plane group *p4mm*. The intensities observed in the Yoneda line at Q_z = 0.34 nm^{-1} are shown on a logarithmic scale as red line in the bottom.

sufficient to determine the lattice constant by GISAXS. The determined lattice constant is in between those found for the different *bct* mesocrystal types, and shorter than the one observed for *bct* mesocrystals prepared at the same time. It remains unclear whether this deviation may be due to the deposition technique.

SEM images obtained from the different regions of the sample and presented in Figure 5.4.25 show that there are indeed mesocrystals in the lower part of the sample that contained liquid nanoparticle dispersion for a longer time. These mesocrystals exhibit a hexagonal lateral symmetry and are assumed to be rhombohedrally packed as observed in section 5.4.3.4. 1D dislocations are observed as discussed before. The square lateral order observed with GISAXS for the other part of the sample is supported by SEM.

In order to obtain a monolayer with much higher long range order, the correct proportion between an extended evaporation time - yielding higher lateral order - and a tilted substrate - preventing growth out of plane but also shortening the evaporation time - should be determined. This may be accomplished by investigation of the correct tilt angle of the substrate during evaporation. Further development of the procedure

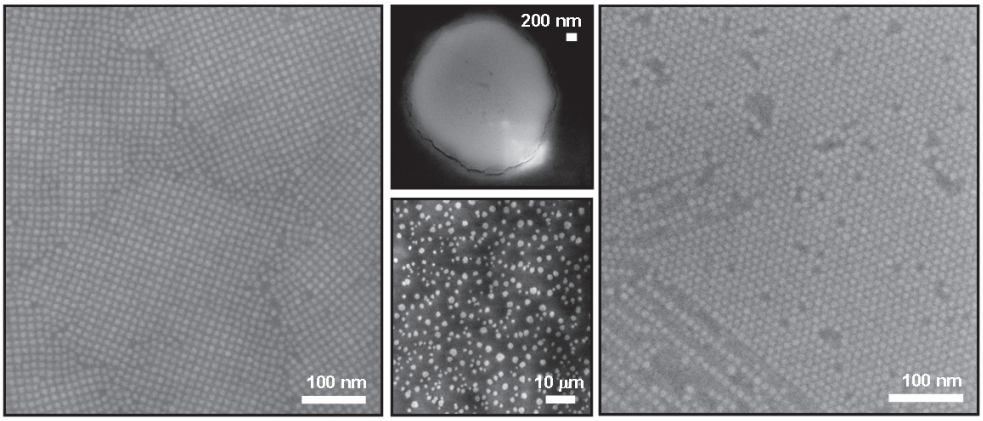

Figure 5.4.25.: SEM images of a nearly monolayer of iron oxide nanocubes. The region of the nearly monolayer with square symmetry is shown (left image). In the part of the sample containing more material, nanocubes are arranged in many, rhombohedrally ordered mesocrystals (right three images).

might include the Langmuir - Blodgett technique, where the substrate is drawn out of the nanoparticle dispersion at a constant angle and with a constant velocity. If the velocity is chosen low enough (which is probably in the velocity range applied for top seeded solution growth (TSSG) of single crystals) to allow for ordering of the nanoparticles in the applied magnetic field, fine tuning of the substrate angle might lead to the desired highly ordered monolayers of magnetic nanoparticles.

5.4.3.6. Magnetization measurements

In order to investigate possible interparticle interactions in the self assembled nanoparticle mesocrystals, field dependent magnetization measurements were performed. In oriented superlattices of nanocrystals the easy axes of the single particles are expected to be aligned and fixed in their orientation to the substrate. Consequently, hysteresis loops measured in different directions with respect to the substrate should exhibit a different behavior. Because the investigated nanocrystal assemblies were found to be 2 D powders of mesocrystals, any measurement parallel to the substrate represents the average of all directions in plane. Magnetic measurements were thus performed parallel as well as perpendicular to the substrate. As only the *bct* arranged nanocube mesocrystals and the nanospheres mesocrystals discussed in sections 5.4.3.2 and 5.4.3.3, respectively, were found to be phase pure, magnetization measurements were performed on these two samples.

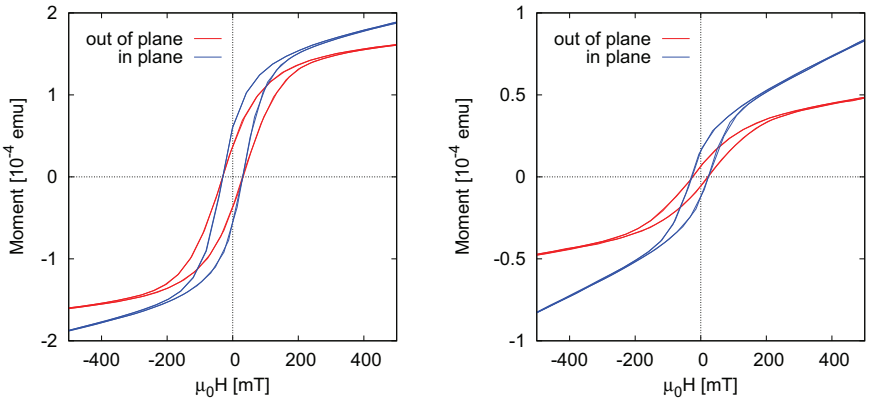

(a) Hysteresis of *bct* arranged nanocubes.

(b) Hysteresis of R$\bar{3}$m arranged nanospheres.

Figure 5.4.26.: Field dependent magnetization measurements of iron oxide superlattices.

The field dependent magnetization measurements presented in Figure 5.4.26 were performed at a temperature of 10 K and corrected for the diamagnetic contributions of substrate and sample holder. For each crystal type, several samples were cut from the same substrate and measured both in and out of plane. As the samples were hand-cut, they varied slightly in size. Because also the substrate coverage with mesocrystals may be different, the exact mass of iron oxide material is unknown, and the measured moment can not be converted to mass magnetization. For the same reason, measurements of different substrate pieces can not be compared quantitatively. For each of the two different mesocrystal structures, field dependent magnetization was measured of several substrate pieces. Those measurements exhibiting the largest moment are supposed to contain the most material and are thus presented in Figure 5.4.26. In plane and out of plane measurements were always performed on the same piece of sample.

For all measured samples, the in plane magnetization curve was observed to be significantly steeper than the out of plane curve. At the same time, the measured coercive field was constant regardless the direction of the measurement. For the *bct* arranged nanocubes and the $R\bar{3}m$ arranged nanospheres, a coercive field at 10 K of H_c = 0.030(3) T and H_c = 0.025(3) T was determined, respectively. In order to compare the slope of the hysteresis curves, the in plane remanent moment was expressed relative to the out of plane remanent moment of the same sample. For the nanocubes, the determined remanence ratio is 1.54 with a variation between 1.4 and 1.65 for all (4) measured samples. For the nanospheres, remanence ratios of 2.0 and 2.33 were observed, with a remanence ratio of 2.33 for the measurement shown in Figure 5.4.26b. Due to the small number of measurements, these values are not precise. Nonetheless, the observation of remanence

ratios larger than 1 is significant for all samples, as is the observation of larger remanence ratios for the nanospheres mesocrystals than for the nanocubes mesocrystals.

While the easy axis of the material can technically be in any direction with respect to the substrate, a remanence ratio larger than 1 (with constant coercive field) indicates that the easy axis has a larger in plane contribution than out of plane. For the nanospheres, this effect is significantly larger than for the nanocubes. Similar to thin magnetic films, the preference of in plane magnetization can also be a result of the demagnetization effect, which has not been corrected here.

As the diamagnetic contribution (determined at 300K) was subtracted from the data, the magnetic moment at magnetic fields higher than the saturation field should technically be constant. The increasing moment in high field can be explained for nanoparticles by a gradual alignment of the surface spins in the particle as discussed for nanoparticle dispersions in section 5.1.3.3 and also observed by polarized SANS in section 5.3.3.1. This increasing moment is observed to be different for in plane and out of plane measurements. For the measurements presented in Figure 5.4.26, the increase is stronger for the in plane measurements. Comparing all performed measurements, however, a statement on the directional preference of this increase can not be made because a stronger increase has also been observed for the out of plane measurement for several samples.

5.4.4. Summary

Within this study, ordered superlattices in three dimensions of iron oxide nanocubes and nanospheres were produced with varying degree of order. By application of a drying mediated approach and inducing dipolar interparticle interactions by a magnetic field, mesocrystals with correlation lengths beyond the resolution limits of the used instruments were obtained.

GISAXS investigations revealed the mesocrystal structures with an accuracy that was not easily achievable by the available SEM methods. The nanocubes were determined to be arranged in a *bct* mesocrystal structure, which could not be distinguished from *sc* by SEM, and the nanospheres stacking type was revealed to be *fcc*, while the distinction between *fcc* and *hcp* was not possible by SEM on the hexagonally packed surface layer.

While the closed packing of the nanospheres can be explained by purely steric interactions, the oriented arrangement of the nanocubes results from increased van der Waals interactions between neighboring particle facets and is thus induced by the anisotropic shape of the nanoparticle building blocks. The shape selectivity was quantified by a free energy calculation performed by Bergström *et al.* on the basis of the determined

bct structure, which justified the preference of *bct* over *sc* due to the truncation of the nanocubes.

Mesocrystals of aged nanocubes revealed an even more sensitive shape dependence of the mesocrystal structure. With ageing, the degree of truncation is expected to increase. This larger truncation leads to a transition of the preferential *bct* structure to a rhombohedral stacking of the heavier truncated nanocubes, similar to the nanospheres arrangement. For the investigated degree of truncation both structure types are close to equilibrium as inferred from the simultaneous observation of *bct* and rhombohedrally arranged mesocrystals. This is supported by a superstructure found in both SEM and GISAXS which can be interpreted as a structural transition from rhombohedral to *bct* structures, *i. e.* from oriented attachment of the (111) to the (100) facets.

As a result, the "structural phase diagram" of truncated nanocubes has been found to reach from a *sc* arrangement for untruncated nanocubes via the *bct* arrangement for an intermediate truncation to a rhombohedral stacking equivalent to a *fcc* arrangement for heavily truncated nanocubes, which is strongly influenced by interaction with the substrate. A layer-wise growth of the mesocrystals is thus suggested.

For investigation of the magnetic interparticle interactions, a monolayer of highly ordered nanoparticles is desirable. Within this study, a thin layer of nanocubes with square symmetry and intermediate correlation lengths was prepared by tilting the substrate during deposition. Further development of this technique, including *e. g.* the Langmuir Blodgett technique for a more controlled tilt angle and evaporation rate, represents a promising route for the preparation of long range ordered monolayers of superparamagnetic nanocubes.

6. Not So Small Angle Neutron Scattering with Polarization Analysis

6.1. Introduction

Neutron scattering with polarization analysis is primarily used for separation of magnetic, coherent, and incoherent scattering contributions. The purely magnetic scattering is of interest for determination of magnetic structures and magnetization densities. With small-angle scattering, the pure magnetic form factor of magnetic nanoparticles can thus in principle be separated using polarization analysis in xyz directions. In contrast, polarized SANS without polarization analysis, *i. e.* a so called half-polarized measurement, as discussed in section 5.3 yields a cross term of nuclear and magnetic scattering contributions. In this case, a precise knowledge of the nuclear scattering contribution is required in order to determine the magnetic form factor.

The primary reason to perform polarized SANS with polarization analysis on cobalt nanoparticle dispersions was the high scattering background found in non-polarized SANS measurements at KWS 2. As discussed in detail in section 4.3.1.7, the reduction agent $NaEt_3BH$, which cannot be purchased in deuterated form, is responsible for a significant incoherent scattering contribution. Since this incoherent scattering background shadows any existing form factor minima, a precise determination of the cobalt nanoparticle core shell structure including the particle size distribution has not been obtained. Polarization analysis is thus required to separate the incoherent and coherent scattering contributions and reveal the cobalt nanoparticle form factor.

There are several neutron scattering instruments that allow for polarization analysis. For example, diffraction experiments can be performed at DNS at JCNS or D7 at ILL, and polarization analysis at small-angle scattering instruments is available at D22 at ILL and is planned at KWS 1 and MARIA, both at JCNS, and V4 at HZB. However, the very small cobalt nanoparticles require polarization analysis in the intermediate momentum transfer range of $0.1\ \text{Å}^{-1} \leq Q \leq 0.7\ \text{Å}^{-1}$, which is not covered by either instrument. Diffraction instruments are usually resolution optimized for investigation of atomic distances, *i. e.* for momentum transfers beyond $0.6\ \text{Å}^{-1}$. Small-angle scattering instruments, on the other hand, reach maximum momentum transfers up to 0.2-0.3 Å^{-1}, which are restricted to an even lower Q range if polarization analysis is required.

The focus of this chapter is thus the configuration of several polarized instruments in order to perform Not So Small-Angle Neutron Scattering with polarization analysis. This requires a reasonable Q resolution in the desired momentum transfer range as well as a high degree of polarization allowing for separation of the coherent and incoherent scattering contributions.

6.2. Methods

6.2.1. Sample preparation and data treatment

6.2.1.1. DNS

The cobalt nanoparticle sample Co A18 (see Table 4.2.1) with a cobalt concentration of 0.05 M in d_8-toluene was prepared according to the standard synthesis route described in section 4.2.1.2. The scattering from the sample, as well as from reference samples of d_8-toluene and a NiCr standard, was measured with polarized neutrons and xyz polarization analysis. The sample holder was an aluminum can with 2 mm sample thickness for the liquid samples. An incoming neutron wavelength of 4.75 Å was chosen. The apetures of the first three detectors in the low Q range were reduced as described more detailed in section 6.3.1. Vanadium was measured as reference for an almost pure spin-incoherent scatterer and for calibration of the detector efficiency. Separation of the measured data was performed using the DNS polarization analysis algorithm, which also accounts for the non-perfect polarization in dependence of Q [181].

6.2.1.2. J-NSE

The samples investigated at the J-NSE instrument comprise iron oxide nanospheres (Bs 10) as well as cobalt nanoparticles. The cobalt nanoparticle dispersion was prepared with a cobalt concentration of 0.045 M by the standard synthesis route described in detail in section 4.2.1.2 using d_8-toluene. For the iron oxide nanospheres the sample also measured at KWS 2 and discussed in section 5.1.3.2 was used. Measurements were performed using Hellma quartz cuvettes with a sample thickness of 1 mm as sample holders. The samples as well as references of an empty sample holder, d_8-toluene, and NiCr were measured with polarized neutrons and polarization analysis in a momentum transfer range of 0.08 $Å^{-1} \leq Q \leq 0.8$ $Å^{-1}$ using an incident wavelength of 5.027 Å. The detector efficiency was calibrated by measurement of a vanadium reference with a detector position at 0.8 $Å^{-1}$ in order to avoid the direct beam. The measured detector images were read out pixel-wise in order to enhance the Q resolution.

6.2.1.3. IN12

The cobalt nanoparticle dispersion Co A19 was prepared according to the standard synthesis route using d_8-toluene. An aluminum sample holder with 2 mm sample thickness was used for measurements of the cobalt nanoparticle dispersion as well as references of H_2O and the empty sample holder. An incident wavelength of 3.49 Å was chosen, and

the small-angle scattering was measured with xyz polarization analysis in a momentum transfer range of 0.05 Å^{-1} ≤ Q ≤ 0.8 Å^{-1}.

6.2.2. Correction of imperfect polarization

For a very high degree of polarization well above 0.9, separation rules can be applied to the observed spin-flip (SF) and non-spin-flip (NSF) intensities without further correction. In case of a significantly lower degree of polarization, however, the observed SF and NSF intensities have to be corrected by the degree of polarization in order to obtain the real SF and NSF intensities that can be used for separation of the different scattering contributions. Figure 6.2.1 illustrates the dependence of the observed flipping ratio $\frac{\mathrm{NSF_{obs}}(\uparrow)}{\mathrm{SF_{obs}}(\downarrow)}$ on the degree of polarization of the incident neutron beam and the real flipping ratio $\frac{\mathrm{NSF_{real}}}{\mathrm{SF_{real}}}$.

In what follows the important simplification is made that the flipping ratio FR is equal for spin-up and spin-down incident neutron polarization

$$FR(\uparrow) = FR(\downarrow) \tag{6.2.1}$$

The observed flipping ratio may be sensitive to spin-up or spin-down incident polarization under certain conditions, including reflection on supermirrors and scattering by Heusler alloys or complex magnetic materials with chiral correlations. Similar to Heusler alloys, also the (111) Bragg reflection in magnetite depends strongly on the incident polarization, and supermirrors and Heusler alloys are even used as polarizer and analyzer materials. Furthermore, magnetic scattering depends on the relative orientation of the neutron spin and the spins in the sample, and for an oriented sample the flipping ratio is thus different for spin-up and spin-down incident polarization.

In the study presented in this section, none of these conditions applies. The studied momentum transfer range is far from the (111) reflection of magnetite ($Q_{(111)}$ = 1.3 Å^{-1}). More importantly, the studied samples are not magnetically oriented, *i. e.* the applied magnetic guide fields at the sample position are significantly lower than the saturation fields ($\mu_0 H_{sat} \approx$ 300mT in case of the iron oxide nanoparticles). The observed flipping ratio will thus be independent on the spin-up or spin-down incident polarization, and the simplification in equation (6.2.1) applies in this case.

In Figure 6.2.1, spin-up polarization was chosen for the incident neutron beam, and the observed NSF fraction of the total scattering is thus the spin-up fraction of the scattered intensity, while the observed SF fraction is the spin-down fraction of the total scat-

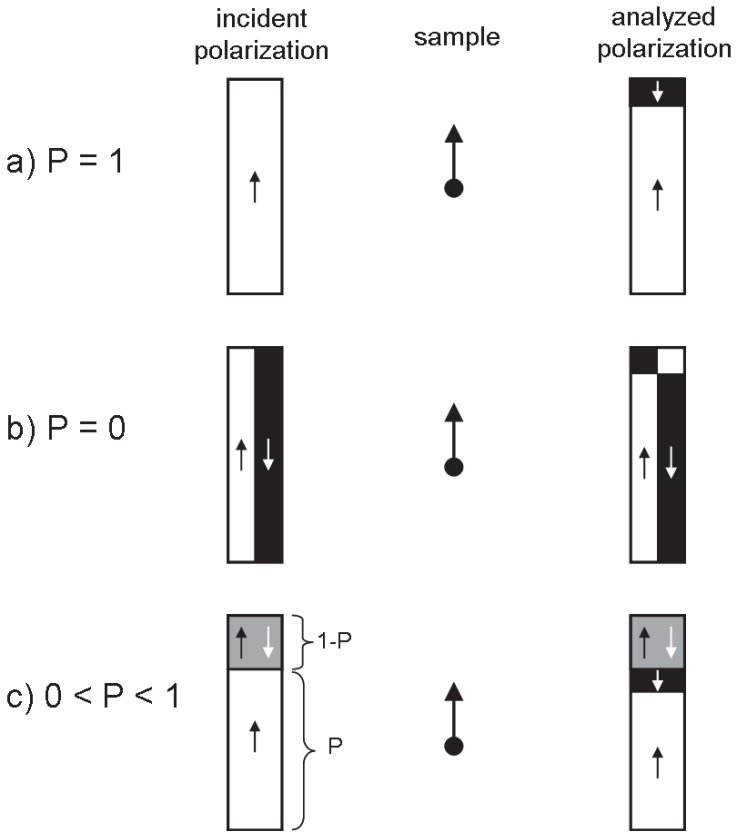

Figure 6.2.1.: Correction for imperfect polarization. Each rectangle represents the total of incident/analyzed neutrons. Fractions of spin-up (↑) and spin-down (↓) polarized neutrons before and after the scattering event are illustrated for a) perfect polarization, b) a non-polarized incident beam, and c) a realistic degree of polarization. Note that the sample is not magnetically oriented and the presentation as an arrow is meant for illustration only.

tered intensity. The real flipping ratio $\frac{\mathrm{NSF_{real}}}{\mathrm{SF_{real}}}$ is defined as the flipping ratio observed in case of a perfect polarization of P = 1, as depicted in Figure 6.2.1a.

$$FR_{\mathrm{obs}} = \frac{\mathrm{NSF_{obs}}(\uparrow)}{\mathrm{SF_{obs}}(\downarrow)} = \frac{\mathrm{NSF_{real}}}{\mathrm{SF_{real}}} = FR_{\mathrm{real}} \tag{6.2.2}$$

For a non-polarized incident neutron beam consisting of 50 % each of spin-up and spin-down neutrons scattered at the sample, an observed flipping ratio of 1 is obtained regardless the real flipping ratio

$$FR_{\mathrm{obs}} = \frac{\mathrm{NSF_{obs}}(\uparrow)}{\mathrm{SF_{obs}}(\downarrow)} = \frac{\frac{1}{2}\,\mathrm{NSF_{real}} + \frac{1}{2}\,\mathrm{SF_{real}}}{\frac{1}{2}\,\mathrm{SF_{real}} + \frac{1}{2}\,\mathrm{NSF_{real}}} = 1 \tag{6.2.3}$$

Consequently, a non-polarized incident neutron beam will not become polarized in the scattering event (except for the conditions mentioned above, which don't apply in the studied case). For the realistic case of a non-perfect polarization of 0 < P < 1, the observed NSF(↑) and SF(↓) fractions of the total scattering intensity are derived as a combination of a perfectly polarized and a non-polarized proportion.

$$FR_{\mathrm{obs}} = \frac{\mathrm{NSF_{obs}}(\uparrow)}{\mathrm{SF_{obs}}(\downarrow)} = \frac{P \cdot \mathrm{NSF_{real}} + (1-P)\,\frac{1}{2}}{P \cdot \mathrm{SF_{real}} + (1-P)\,\frac{1}{2}} \tag{6.2.4}$$

Note that the SF and NSF intensities in the equations above are given in fractions of the total intensity

$$\mathrm{NSF} = \frac{\mathrm{I_{NSF}}}{\mathrm{I_{total}}} \tag{6.2.5}$$

$$\mathrm{NSF} + \mathrm{SF} = 1 \tag{6.2.6}$$

By combination of equations 6.2.4 and 6.2.6, the real SF and NSF intensity fractions are determined with the observed SF and NSF intensities and the degree of polarization P.

$$\mathrm{NSF_{real}} = \frac{FR_{\mathrm{obs}} + \frac{1-P}{2P}\,[FR_{\mathrm{obs}} - 1]}{1 + FR_{\mathrm{obs}}} \tag{6.2.7}$$

$$\mathrm{SF_{real}} = \frac{1 + \frac{1-P}{2P}\,[1 - FR_{\mathrm{obs}}]}{1 + FR_{\mathrm{obs}}} \tag{6.2.8}$$

With equations 6.2.7 and 6.2.8, the observed scattering intensities can be converted into the real SF and NSF intensities, which in turn are used for separation of coherent,

incoherent, and magnetic scattering contributions. Applicability of these relations is restricted to

$$\mathrm{NSF_{real}} < 1 \tag{6.2.9}$$

which requires

$$FR_{\mathrm{obs}} < \frac{1+P}{1-P} \tag{6.2.10}$$

Non-fulfillment of equation (6.2.10) implies that the observed flipping ratio corresponds or exceeds the flipping ratio expected for a 100% coherent scatterer. Thus, a $\mathrm{NSF_{real}}$ determined larger than 1 indicates either an incorrect measurement of the $\mathrm{SF_{obs}}$ and $\mathrm{NSF_{obs}}$ intensities or that the estimation of the degree of polarization is too low.

6.2.3. Multiple scattering correction

For investigation of highly concentrated nanoparticle dispersions by neutron scattering, multiple scattering has to be taken into account. Concerning polarized neutron scattering, multiple scattering affects the observed flipping ratio FR_{obs}, and a correction has to be performed in order to obtain the real flipping ratio. The influence of multiple scattering on primarily SF and NSF scattered intensities is illustrated in Figure 6.2.2.

The first scattering event leads to $\mathrm{SF_1}$ and $\mathrm{NSF_1}$ scattered intensity, which may be used for separation of the coherent, incoherent, and magnetic scattering contributions. In case of a multiple scattering probability of α, (1-α) of the neutrons is scattered once, while α of the neutrons are scattered at least twice, and α^n of the neutrons are scattered at least n+1 times. The aim of this section is the determination of the $\mathrm{SF_1}$ and $\mathrm{NSF_1}$ intensities from the resulting multiple scattering intensities $\mathrm{SF_{mult}}$ and $\mathrm{NSF_{mult}}$.

In the following, only the first scattering event is assumed to consist of incoherent, coherent, and magnetic scattering contributions, while the multiple scattering is assumed to be purely incoherent scattering, *e. g.* $\frac{1}{3}$ NSF and $\frac{2}{3}$ SF. In general, the individual scattering probabilities are independent on the number of scattering events, and a loss of Q information due to coherent and magnetic multiple scattering should be considered. However, in the highly concentrated cobalt nanoparticle dispersions under study the incoherent scattering contribution is highly dominant due to the large amount of non-deuterated solvent required by the synthesis conditions. For this reason, the multiple scattering is assumed to be purely incoherent, an assumption which further allows for an analytic treatment of the multiple scattering correction.

Incoherent multiple scattering induces the change in SF and NSF intensities illustrated in Figure 6.2.2, and is independent on the momentum transfer. In contrast, a

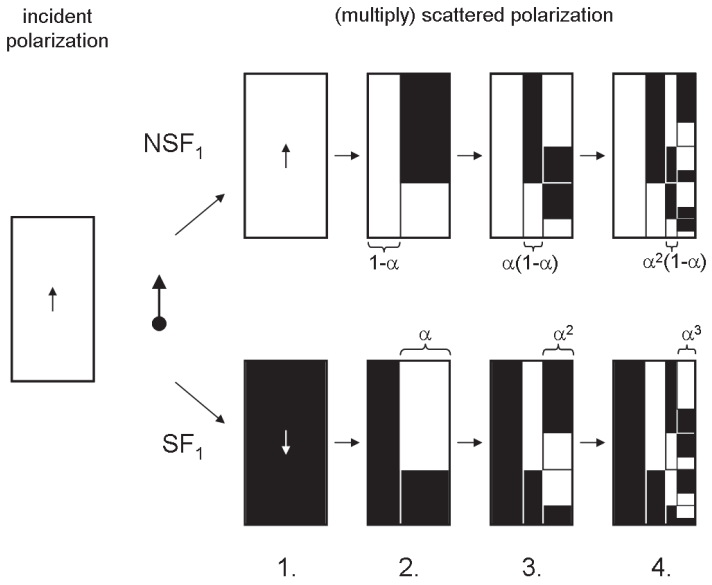

Figure 6.2.2.: Illustration of multiple scattering events. Each rectangle represents the total of primarily SF/NSF scattered neutrons. A probability of multiple scattering of α is assumed. Fractions of spin-up (↑) and spin-down (↓) polarized neutrons after up to four scattering events are illustrated as white and black areas, respectively.

dominant contribution of coherent scattering would result in deviations of the Q dependence of the measured scattering intensity, but would leave the SF and NSF intensities unchanged due to the purely NSF nature of coherent scattering.

The observed NSF scattering is displayed as the white area in Figure 6.2.2, and consists of fractions of both the primary spin-flip channels SF_1 and NSF_1. Similarly, the observed SF scattering is displayed in black and consists of the same fractions of the opposite spin-flip channels.

$$\mathrm{NSF_{mult}} = \mathrm{NSF_1} \cdot A + \mathrm{SF_1} \cdot B \tag{6.2.11}$$

$$\mathrm{SF_{mult}} = \mathrm{NSF_1} \cdot B + \mathrm{SF_1} \cdot A \tag{6.2.12}$$

The fractions A and B depend on the multiple scattering probability α and follow a series expansion

$$\begin{aligned} A &= (1-\alpha) + (1-\alpha)\alpha\tfrac{1}{3} + (1-\alpha)\alpha^2(\tfrac{1}{9}+\tfrac{4}{9}) + (1-\alpha)\alpha^3(\tfrac{1}{27}+\tfrac{4}{27}+\tfrac{4}{27}+\tfrac{4}{27}) + \ldots \\ &= (1-\alpha)[A_1 + A_2 + A_3 + A_4 + \ldots] \end{aligned} \tag{6.2.13}$$

$$\begin{aligned} B &= 0 + (1-\alpha)\alpha\tfrac{2}{3} + (1-\alpha)\alpha^2(\tfrac{2}{9}+\tfrac{2}{9}) + (1-\alpha)\alpha^3(\tfrac{2}{27}+\tfrac{2}{27}+\tfrac{2}{27}+\tfrac{8}{27}) + \ldots \\ &= (1-\alpha)[B_1 + B_2 + B_3 + B_4 + \ldots] \end{aligned} \tag{6.2.14}$$

with the coefficients A_n and B_n determined by recursion

$$\begin{aligned} A_n &= (\frac{1}{3}A_{n-1} + \frac{2}{3}B_{n-1})\alpha \\ B_n &= (\frac{1}{3}B_{n-1} + \frac{2}{3}A_{n-1})\alpha \\ \text{with} \quad A_1 &= 1 \\ B_1 &= 0 \end{aligned} \tag{6.2.15}$$

The fractions A and B given in equations (6.2.13) and (6.2.14) are then derived in dependence of the number of scattering events n as

$$\begin{aligned} A(n) &= A(n-1) + A_n(1-\alpha) \\ B(n) &= B(n-1) + B_n(1-\alpha) \\ \text{with} \quad A(0) &= B(0) = 0 \end{aligned} \tag{6.2.16}$$

For an increasing number of scattering events, the fractions $A(n)$ and $B(n)$ converge towards the coefficients A and B required for equations (6.2.11) and (6.2.12), fulfilling

$A + B = 1$. Convergence may be achieved after less than 10 scattering events, depending on the multiple scattering probability. Figure 6.2.3a presents the convergence of the $A(n)$ and $B(n)$ coefficients for a multiple scattering probability of $\alpha = 0.5$. The depen-

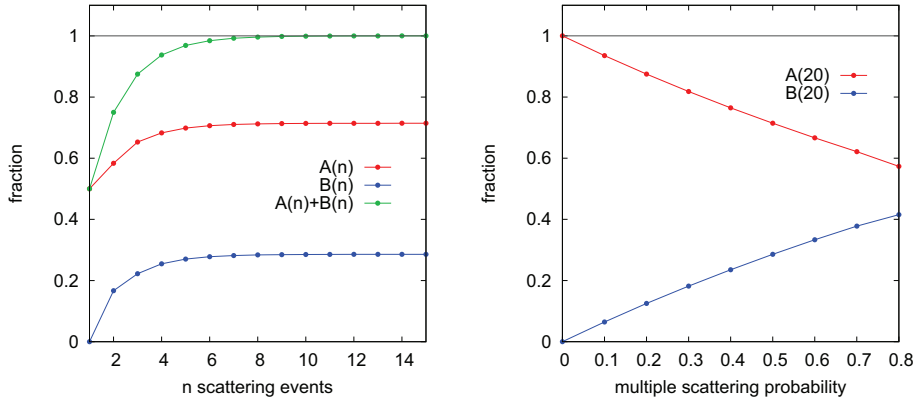

(a) Convergence of the correction coefficients for a multiple scattering probability of $\alpha = 0.5$.

(b) Correction coefficients in dependence of the multiple scattering probability.

Figure 6.2.3.: Multiple scattering correction.

dence of the correction coefficients on the multiple scattering probability is presented in Figure 6.2.3b.

In order to perform multiple scattering correction on experimental data, the multiple scattering probability has to be determined first from the elemental sample composition and the involved coherent and incoherent scattering cross sections (as tabulated in [12]). The correction coefficients A and B are obtained by equations (6.2.16) for a sufficiently high number of scattering events n. With the determined correction coefficients A and B for equations (6.2.11) and (6.2.12), the SF and NSF intensities for a single scattering event are derived from the observed multiple scattering SF and NSF intensities.

$$\mathrm{NSF}_1 = \frac{A \cdot \mathrm{NSF}_{\mathrm{mult}} - B \cdot \mathrm{SF}_{\mathrm{mult}}}{A^2 - B^2} \tag{6.2.17}$$

$$\mathrm{SF}_1 = \frac{A \cdot \mathrm{SF}_{\mathrm{mult}} - B \cdot \mathrm{NSF}_{\mathrm{mult}}}{A^2 - B^2} \tag{6.2.18}$$

The SF_1 and NSF_1 derived by this approach can then be used for subsequent separation of the coherent, incoherent, and magnetic scattering contributions according to the separation rules for polarized neutron scattering (section 2.2.4.2).

6.3. Results and Discussion

6.3.1. DNS

The DNS instrument at JCNS (3.5.1) is designed for polarization analysis in all three cartesian directions and provides reliably high flipping ratios well above 20, corresponding to a degree of polarization > 90%. For this reason, DNS was chosen for separation of the coherent and incoherent scattering contributions in the SANS by cobalt nanoparticles. While the DNS instrument is resolution optimized for a medium Q range suitable for powder diffraction or reciprocal space mapping of single crystals, the small-angle scattering of the cobalt nanoparticles, with form factor minima expected in the range of 0.2 - 0.5 $Å^{-1}$, is at the lower limit of the available Q range.

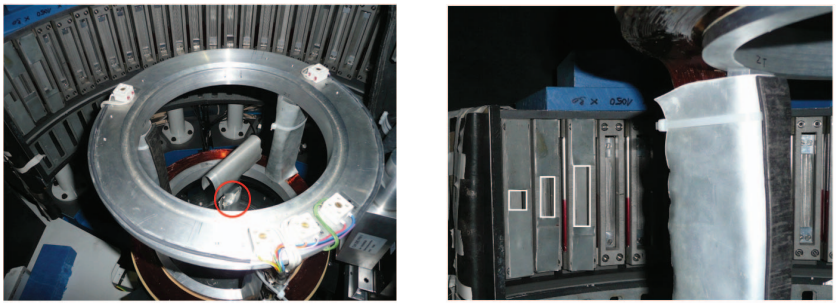

(a) View of the sample position. The aluminum cuvette holding the sample (red circle) is visible within the set of induction coils generating the magnetic field at the sample position. In the background the detector bank of 24 tubes with analyzers is visible. The first three detectors at the left side are partially covered in order to enhance the Q resolution, see (b).

(b) Detailed view of the first detectors. The sensitive area of the partially covered detectors is marked by white rectangles.

Figure 6.3.1.: Experimental setup at DNS.

Because the small-angle scattering is isotropic, but the detectors are tubes of 15 cm height, the first detectors cover a significantly larger Q range in height than horizontally, resulting in a low Q resolution in the small-angle range. In order to increase the resolution in the desired Q range and allow for measurement of the small-angle scattering, the first three detectors were covered by additional cadmium slits, as shown in Figure 6.3.1.

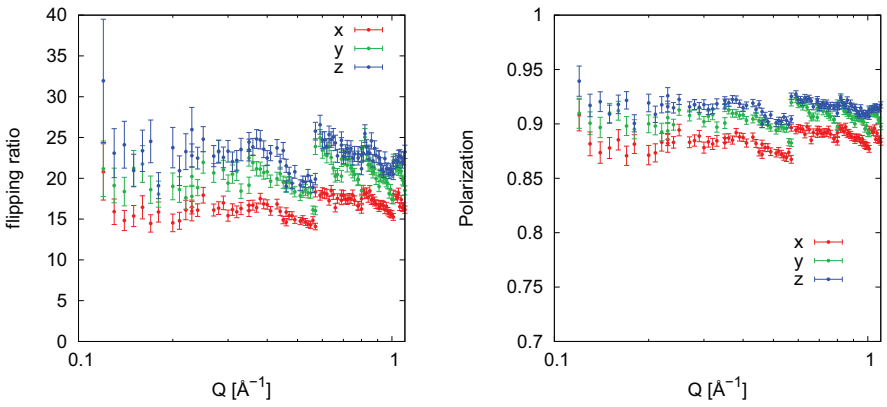

(a) Flipping ratio.

(b) Degree of polarization.

Figure 6.3.2.: Polarized neutrons at DNS.

A reference sample of a NiCr alloy containing 11.4 at-% of Cr was measured for determination of the flipping ratio and thus the degree of polarization in all three polarization directions. The specific composition of the NiCr standard leads to a loss of magnetic moment of the alloy, resulting in purely isotope incoherent and spin coherent scattering (100% non-spin-flip) [182].

The determined flipping ratios and degree of polarization are presented in Figure 6.3.2. The measured degree of polarization is in the range of $0.88 \leq P \leq 0.92$ for the entire momentum transfer range. This non-perfect degree of polarization is considered for separation of the different scattering contributions using the DNS polarization analysis algorithm [181].

Figure 6.3.3a presents the different scattering contributions as separated from SANS by cobalt nanoparticles in d_8-toluene dispersion. A derivation of the separation rules is given in section 2.2.4.2. The nearly constant intensity of the incoherent scattering contribution indicates a successful separation. There is no evidence of magnetic scattering in the performed measurement. Because the magnetic form factor may be several orders of magnitude lower in intensity than the total scattering, statistics might have been insufficient. However, as found repeatedly by magnetization measurements, oxidation of the nanoparticles is also likely.

Separation of the coherent scattering contribution was achieved by 1.5 orders of magnitude as compared to the total scattering intensity. The coherent scattering curve exhibits two steps at 0.24(2) Å^{-1} and 0.50(2) Å^{-1} that may be attributed to form factor minima. For presentation in Figure 6.3.3b a constant background attributed to incoherent

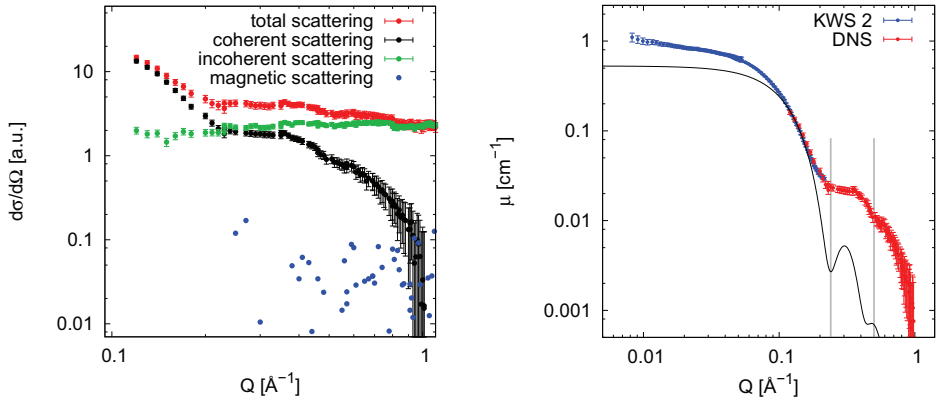

(a) Separation results of the cobalt nanoparticle dispersion.

(b) Comparison of the separated coherent scattering contribution with the SANS measured at KWS 2 and simulation of a core shell form factor. The observed form factor minima are indicated by grey lines.

Figure 6.3.3.: SANS with polarization analysis at DNS.

scattering has been subtracted from the SANS data measured at KWS 2. The separated coherent scattering contribution measured at DNS has been scaled to overlap with the resulting KWS 2 data. In order to estimate the nanoparticle core shell structure, a form factor was simulated to match the KWS 2 data and the Q positions of the separated form factor minima. The slope of the DNS data before the first form factor minimum and the Q position of the first minimum are represented by a simulation of a core shell form factor with a core radius of 10 Å and a shell thickness of 7.7 Å, which is in rough agreement with typical particle sizes determined with SAXS in section 4.3.1.4. However, the Guinier range of the KWS 2 data and the Q position of the second form factor step cannot be matched at the same time by variation of the particle core size or shell thickness. As the KWS 2 measurement was performed on a different sample and the reproducibility of the particle size fluctuates (as discussed in section 4.3.1), a difference in particle size for the two experiments is possible. Moreover, penetration of the ligand shell by the solvent is likely, resulting in a radial decrease of the shell contrast, which may shift the relative positions of the form factor minima. The large intensity difference between the data and the simulated form factor at high Q may result from byproducts of the nanoparticle synthesis, such as excess surfactant micelles, as was discussed for cobalt nanoparticles in section 4.3.1.7 and for iron oxide nanoparticles in section 5.1.3.2. The intensity of the DNS data, however, decreases drastically at $Q \approx 0.9$ Å^{-1}. Assuming this to indicate a form factor minimum of the synthesis byproducts, a micelle diameter

of 7 Å is estimated. The micelle size of NaAOT is twice as large as indicated by the SAXS curve presented in Figure 4.3.10.

Despite the additional slits in front of the first detectors, the resolution in the lower Q range of the DNS measurement is admittedly too low. This may be related to the relatively large sensitive area of the first detector despite the additional detector aperture of 25 x 25 mm. Considering the sample detector distance of 800 mm, a contribution to the angular divergence of 36 mrad is estimated. A slightly better resolution in the higher Q range is indicated by the clearly visible second form factor step at Q = 0.50(2) $Å^{-1}$.

Furthermore, the size distribution of the prepared cobalt nanoparticles is likely narrow, as indicated by several characterization results discussed in section 4.3.1, such as a narrow blocking temperature peak in ZFC magnetization measurements or the clear dispersion colors resulting from surface plasmon resonances discussed in section 4.3.2. An assumptive particle size distribution of 0.15 is implemented for simulation of the core shell form factor in Figure 6.3.3b, along with the Q resolution parameters of the KWS 2 instrument. While the sharpness of the second form factor minimum is comparable to the data, the first minimum is smeared out significantly. However, a particle size distribution of 0.15 or less seems realistic for the cobalt nanoparticles as estimated from characterization results in section 4.3.1.

Thus, xyz polarization analysis has been performed successfully at DNS leading to well separated coherent and incoherent scattering contributions, but the Q resolution is not sufficient for a precise determination of the particle size distribution. A magnetic scattering contribution was not detected.

6.3.2. J-NSE

In order to obtain the coherent scattering contribution with better Q resolution in a Q range of 0.1 - 0.7 $Å^{-1}$, polarized small-angle neutron scattering has been performed at the neutron spin-echo instrument J-NSE at JCNS (3.5.2). Polarized neutrons are generated by a polarized supermirror section inside the neutron guide. For general operation of the spin-echo technique, the polarization direction of the incoming neutrons is rotated by 90° using a $\pi/2$ flipper at the entrance of the first solenoid, thus inducing precession of the neutron spin in a weak magnetic guide field. Close to the sample position, the precession direction is reversed by a rotation of the neutron spin by 180° using a π flipper. After the second solenoid the neutron spin is rotated back into the initial polarization direction by another 90° rotation using a $\pi/2$ flipper. Inelastic or quasielastic scattering events lead to a change of the neutron velocity at the sample position while

the precession frequency is unchanged, resulting finally in a loss of polarization, which is measured by polarization analysis.

In order to perform polarized small-angle scattering, information on inelastic scattering processes as could be obtained by the spin-echo is not necessary. Thus, the $\pi/2$ flippers were not used, and the π flipper was moved to the entrance of the first solenoid in order to provide either spin up or spin down direction of the polarization. The guide field inside the solenoids was set stronger than for spin-echo experiments, to 7 mT. At the sample position three magnetic coils were installed in order to provide an adiabatic rotation of the polarization direction into the x, y, and z direction at the sample and back into its original direction. The x direction was defined to be parallel to the incoming beam, z was defined perpendicular to both Q and the incoming beam, and y perpendicular to both x and z. Note that the magnetic field directions were kept fixed, independently of the detector position. For conventional spin echo experiments, the magnetic field at the sample position is usually rotated by θ in order to maintain y parallel to Q. For enhancement of the Q resolution, however, the detector was used as a multidetector and read out pixel-wise, which requires a fixed direction of the magnetic field independent on Q.

In order to measure the achieved Q resolution, the Bs 10 iron oxide nanospheres were measured at J-NSE in the described configuration. The sample has been investigated in detail in chapter 5, and the core shell structure is well known. The total scattering cross section as measured at J-NSE is presented in Figure 6.3.4 and compared to the SANS curve measured by the same sample at the KWS 2 and D22 instruments. The SANS measurement performed at J-NSE exhibits a better Q resolution than the KWS 2 measurement, which can mainly be attributed to the different wavelength distribution of 10% at J-NSE as compared to 20% at KWS 2. As a dedicated SANS instrument with a wavelength spread of 10 %, D22 is resolution optimized in the required Q range, and the D22 measurement consequently exhibits the best Q resolution for non-polarized SANS.

The J-NSE data set was refined with a core shell form factor of the same structural parameters derived for the Bs10 sample in section 5.1. The known incident wavelength and wavelength spread of J-NSE of 5.027 Å and 10 %, respectively, were applied, and the only fit parameters were the angular divergence parameter, the particle number densities of iron oxide nanospheres as well as excess oleic acid micelles, and a constant background. The refined angular divergence of 8.2 (4) mrad is close to the angular divergence values obtained for the KWS 2 instrument in section 5.1. The fit is in good agreement with the data in a momentum transfer range of 0.05 $Å^{-1} \leq Q \leq 0.2$ $Å^{-1}$.

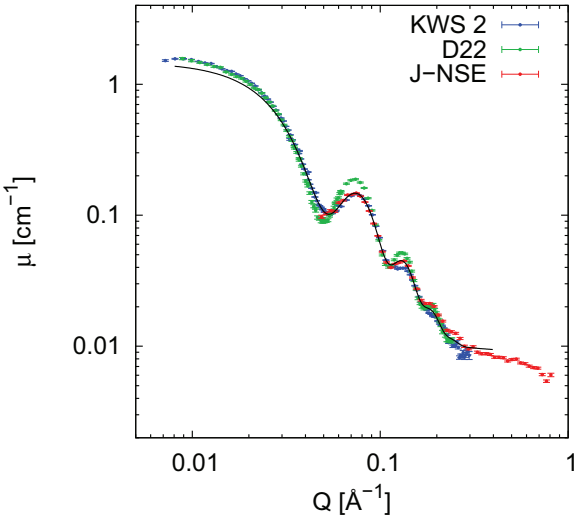

Figure 6.3.4.: SANS by iron oxide nanospheres (Bs 10) at J-NSE as compared to KWS 2. The J-NSE data were fit with the known core shell structure (black line).

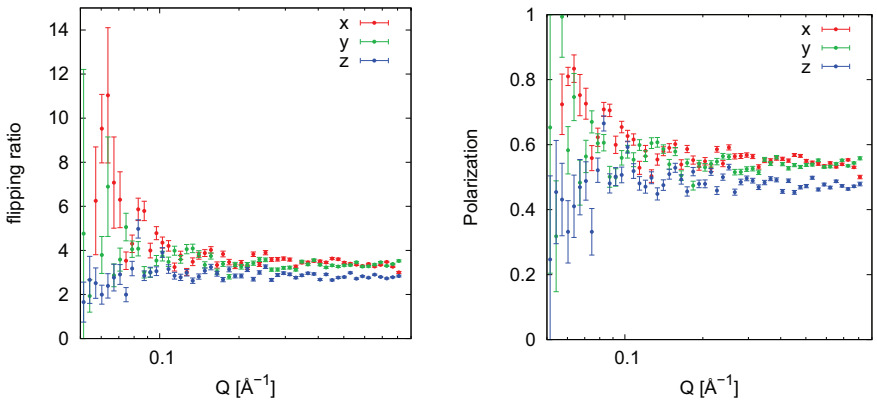

(a) Flipping ratio.

(b) Degree of polarization.

Figure 6.3.5.: Polarized neutrons at J-NSE.

For polarized SANS, the same NiCr and vanadium reference samples used for the DNS experiment were measured in order to determine the polarization of the incoming neutron beam and to calibrate the detector efficiency. The determined flipping ratios and the resulting degree of polarization are presented in Figure 6.3.5. The flipping ratios are in the range of $3 \leq FR \leq 4$, corresponding to a degree of polarization below 0.6 in the major part of the investigated Q range. This low degree of polarization has to be considered before separation of magnetic, coherent, and incoherent scattering contributions, and the real SF and NSF intensities first have to be derived for all directions. As the polarization is not constant in the three directions of the applied magnetic field nor in Q, the measured polarization values for each point were implemented into the correction of SF and NSF intensities. A derivation of the correction procedure is given in section 6.2.2, and the applied separation rules are given in section 2.2.4.2.

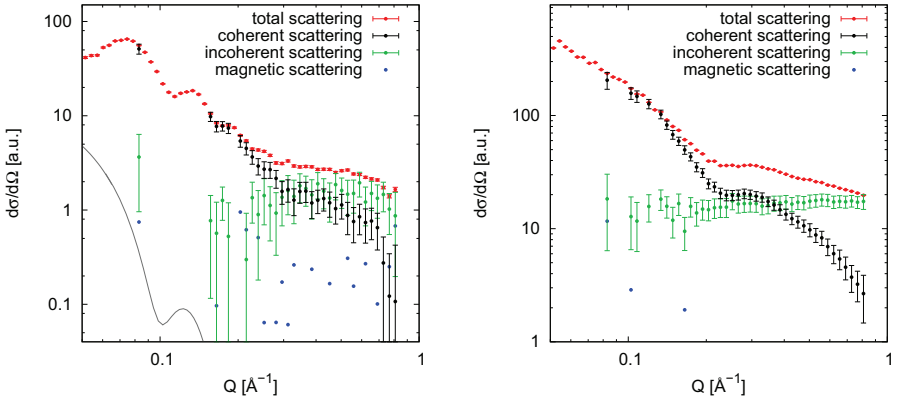

(a) Bs 10 iron oxide nanospheres. The magnetic form factor determined in section 5.3.3.1 is given as a grey line.

(b) Cobalt nanoparticles.

Figure 6.3.6.: Separation results of the polarized SANS at J-NSE. Only points fulfilling equation (6.2.10) were separated into their coherent, incoherent, and magnetic scattering contributions.

Figure 6.3.6 presents the different scattering contributions as separated from SANS by iron oxide as well as cobalt nanoparticles dispersed in d_8-toluene. The constant incoherent scattering contribution observed for both samples indicates a successful separation. However, there is no evidence for magnetic scattering in the cobalt nanoparticle dispersion, and also the magnetic contribution separated from the iron oxide nanospheres measurement is negligible. The expected magnetic scattering contribution as obtained from the half-polarized measurements in section 5.3.3.1 is shown as a grey line in Figure 6.3.6a. In the higher Q range this expected intensity is clearly below the noise level of the

separated magnetic scattering contribution, indicating that the statistics are insufficient for a separation of the magnetic scattering. In the lower Q range, the expected magnetic scattering intensity is larger and a successful separation in this Q range should reveal a significant magnetic scattering contribution. However, in the momentum transfer range below 0.17 $Å^{-1}$ (Bs 10) and 0.10 $Å^{-1}$ (Cobalt), the condition for correction of the imperfect polarization given in section 6.2.2 is not fulfilled. This indicates either an inaccurate determination of the polarization in this Q range or incorrect SF and NSF intensities as might result from multiple scattering. Nonetheless, it may be assumed that the incoherent scattering contributions in this Q range are at the same intensity level as in the higher Q range, and that consequently the coherent scattering contributions are equal to the total scattering intensity within its uncertainty bounds. Separation of the coherent scattering contribution at high Q was thus achieved up to approximately one order of magnitude as compared to the total scattering cross section for the cobalt nanoparticle dispersion.

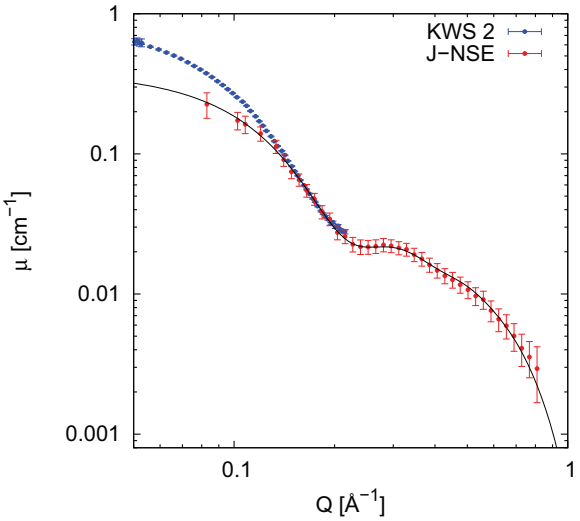

Figure 6.3.7.: Comparison of the coherent scattering contribution of the cobalt nanoparticle dispersion as separated at J-NSE with SANS measured at KWS 2.

In Figure 6.3.7, the separated coherent scattering contribution of the cobalt nanoparticle dispersion is matched to the SANS curve measured at KWS 2. An assumed incoherent scattering contribution of 0.0655 cm^{-1} has been subtracted from the KWS 2 data. The two data sets are matched at 0.15 $Å^{-1} \leq Q \leq 0.2$ $Å^{-1}$, but the different slope at lower Q suggests a different core shell structure for the two samples. For this reason, only the

separated coherent scattering contribution was refined. A first form factor minimum is visible in the coherent scattering contribution at Q ~ 0.24 $Å^{-1}$, and a second form factor minimum can be estimated as a step at Q ~ 0.4 $Å^{-1}$. The refinement of a core shell form factor is presented as a black line in Figure 6.3.7. In order to represent the entire data set, a phenomenological spherical form factor was implemented to account for even smaller aggregates giving rise to the high intensity at Q ≥ 0.4 $Å^{-1}$. Since only the first form factor minimum is significant and the second form factor minimum is rather estimated, it is not possible to refine both the particle core radius and the shell thickness. With the particle core radius set to 10 Å, a shell thickness of 7.7 (2) Å was refined. This shell thickness is reasonable for the AOT molecule, if a certain degree of interpenetration of toluene into the particle shell is considered.

In order to determine the particle size distribution, the angular divergence contribution to the Q resolution as refined from the iron oxide nanospheres sample was implemented, and a lognormal size distribution of 9.5 ± 4.3 % was refined. The large uncertainty of this value results in the large contribution of smaller excess scattering objects shadowing the cobalt form factor minima.

The radius of the additional spherical form factor was refined as 3.94 (3) Å. This radius is too small to account for excess NaAOT micelles, which usually have a radius of ~ 6 Å. The small radius determined here is in the size range of single molecules rather than nanosized particles. Since these molecules certainly have a different density distribution than spherical nanoparticles, the form factor of a solid sphere may not be correct. This model is thus rather a phenomenological description of the form factor plateau observed in the higher Q range.

In summary, the resolution at J-NSE has been shown to be sufficient for small-angle scattering experiments with an angular divergence close to that determined for the KWS-2 instrument. The degree of polarization is rather low, in the range of 0.42 to 0.58, and should be improved in order to perform a successful separation of polarized SANS also in the lower momentum transfer range.

However, the separation of coherent and incoherent scattering contributions in the larger Q range was performed successfully, and a core shell structure of the cobalt nanoparticles was simulated. The particle size distribution of cobalt nanoparticles, which was not accessible by SAXS, was refined for the first time, and a lognormal size distribution of 10 (4) % was obtained.

6.3.3. IN12

As a further instrument with reliably high polarization, the cold neutron triple axis spectrometer IN12 at ILL was utilized for investigation of the small-angle neutron scattering by cobalt nanoparticle dispersions with polarization analysis. The minimum momentum transfer achieved at IN12 depends on the angular resolution obtained for the direct beam. In order to enhance the resolution of the momentum transfer, the divergence of the primary beam was thus optimized.

First, the distances between monochromator and sample position as well as between sample position and analyzer were increased to 1.96 m and 1.31 m, respectively. Collimators with 60′ horizontal divergence were installed between polarizer and sample as well as between sample and analyzer. The vertical divergence was improved by additional slits of 18 x 25 mm^2 placed at the exit of the polarizer as well as in front of the sample and of the analyzer with 1 m distances in between the slits. These slits result in a vertical angular divergence of 25 mrad (≡ 85′). The Heusler crystal utilized for polarization analysis contributes to further enhancement of the angular resolution in the secondary spectrometer because only neutrons fulfilling the Bragg equation are analyzed.

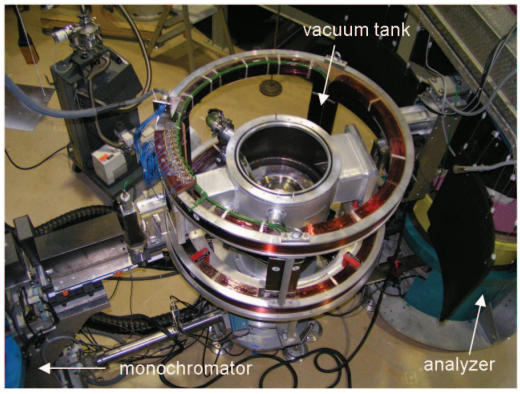

Figure 6.3.8.: Setup of the IN12 instrument. The vacuum tank is shown within the magnetic coils at the sample position. The incident beam enters from the left side.

In order to reduce the broadening of the primary beam by air scattering, a vacuum tank was installed at the sample position, which covered the entire flight path in between the collimators. The magnetic field required at the sample position for xyz polarization analysis was provided by a large set of Helmholtz coils outside the vacuum tank. A view of the full setup is presented in Figure 6.3.8. The degree of polarization for this

configuration was determined by measurement of the flipping ratio of graphite. The found polarization of > 0.95 was considered large enough to neglect any contributions due to imperfect polarization.

The cobalt nanoparticle dispersion was prepared according to the standard synthesis route discussed in section 4.2.1.2. However, in order to enhance the scattering statistics, a much higher cobalt concentration of 0.33 M was chosen. Since a higher reduction temperature was found to minimize the scattering background observed by SAXS (see section 4.3.2.2), the sample under study was prepared at a reduction temperature of 40°C. The higher concentration of cobalt requires also a higher concentration of the reducing agent, which is only available as non-deuterated compound and dispersed in non-deuterated toluene. Due to the high cobalt concentration of 0.33 M and the large amount of reducing agent needed, only one third of the final nanoparticle dispersion consists of d_8-toluene, while the remaining solvent, introduced with the reduction agent, is not deuterated. The incoherent scattering probability calculated from the sample composition is 34%, with a total scattering probability of 37%. The high probability of multiple incoherent scattering was thus considered before separation of the coherent and incoherent scattering contributions, as discussed more detailed in section 6.2.3.

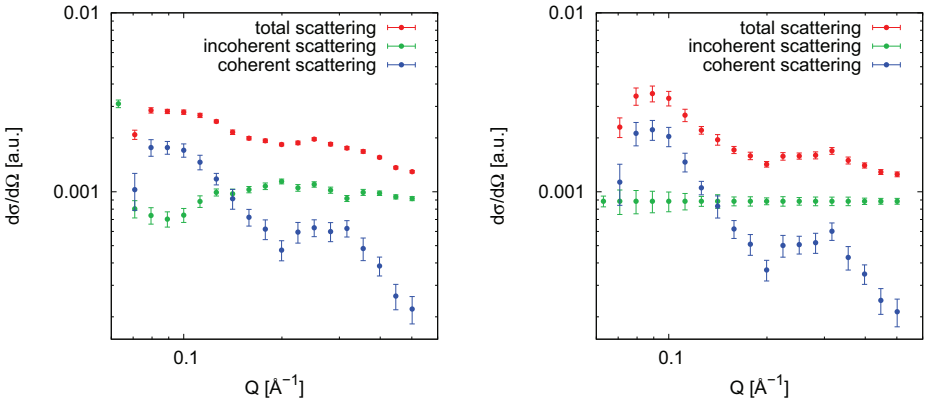

(a) Separation results after background subtraction.

(b) Calibration to the incoherent scattering contribution.

Figure 6.3.9.: Separation results of the polarized SANS at IN12.

The sample under study as well as a reference sample of H_2O and an empty sample holder were measured with xyz polarization analysis in an extended momentum transfer range of 0.05 Å^{-1} ≤ Q ≤ 0.8 Å^{-1}. The multiple scattering correction was applied as derived in section 6.2.3 and separation was performed according to the separation rules given in section 2.2.4.2. Despite a successful separation of the H_2O reference data set, a

calibration of the separated cobalt scattering contributions to the incoherent scattering contribution of the H_2O reference results in increased deviations from a constant incoherent scattering contribution. For this reason, the obtained scattering contributions as presented in Figure 6.3.9a have not been corrected to any incoherent scattering reference. However, the separated incoherent scattering contribution is almost constant at higher momentum transfer. In order to correct for any Q dependent intensity fluctuations of instrumental origin, the incoherent scattering contribution was postulated constant, and all separated scattering contributions were calibrated by the incoherent scattering contribution. The resulting scattering curves are presented in Figure 6.3.9b. The decreasing coherent and total scattering intensities at $Q < 0.08$ Å^{-1} may result from the primary beam that was not corrected perfectly by the measurement of the empty sample holder. A momentum transfer of $Q = 0.09$ Å^{-1} is thus considered a reliable minimal Q. In both Figures 6.3.9 and 6.3.9b, a form factor minimum is clearly visible at $Q = 0.2$ Å^{-1}.

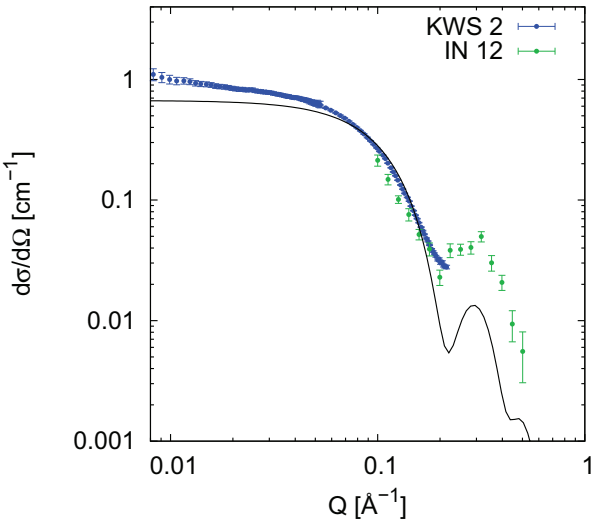

Figure 6.3.10.: Simulation of the core shell form factor with parameters obtained from the DNS and J-NSE measurements in comparison with the coherent scattering contribution as obtained at IN12.

In Figure 6.3.10 the separated coherent scattering contribution is matched to the SANS measurement performed at KWS 2 and compared to a form factor of the core shell structure obtained with the DNS and J-NSE experiments. The coherent scattering contribution obtained at IN12 has been scaled to overlap with the KWS 2 data. A constant back-

ground has been subtracted in order to account for the excess scattering contribution found by the J-NSE experiment, a contribution which is almost constant in the momentum transfer range below 0.5 $Å^{-1}$. The simulation confirms that the Q position of the form factor minimum is in agreement with the results obtained at DNS and J-NSE.

6.3.4. Comparison of the results

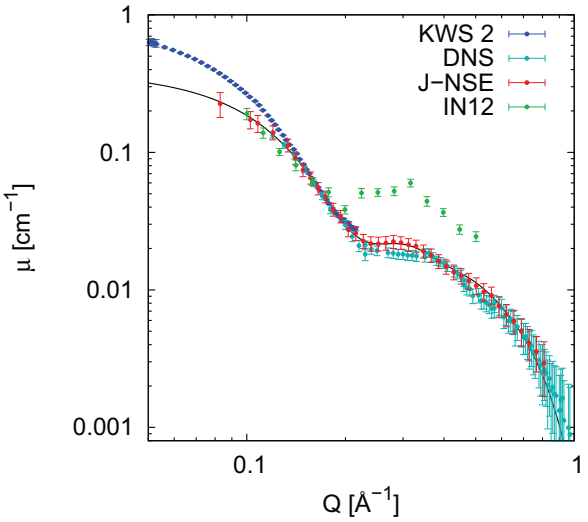

Figure 6.3.11.: Comparison of the SANS results with polarization analysis. The fit of the J-NSE data is shown as a black line.

Figure 6.3.11 compares the results of all three experiments of Not So Small-Angle Neutron Scattering with polarization analysis on cobalt nanoparticles. For all measurements, form factor minima are observed at Q ~ 0.20-0.24 $Å^{-1}$ and Q ~ 0.4-0.5 $Å^{-1}$. Small deviations in the Q position are reasonable because the experiments were performed using three different samples, and the reproducibility of the particle size fluctuates as discussed in section 4.3.1. However, the variation of the form factor minimum position corresponds to fluctuations in the particle size of less than 10 %. The clearest form factor minimum is visible in the IN12 data. This may be due to the much higher cobalt concentration, as well as the slightly larger particle size as indicated by the form factor minimum, resulting in a better signal-to-noise ratio. However, this measurement suggests a significantly higher background level as well. The coherent scattering background of the DNS and J-NSE experiments is in good agreement and can be described

by the plateau of a spherical form factor with a particle radius of R ~ 4 Å. A refinement of the core shell nanoparticle structure including the particle size distribution is possible only for the data obtained at J-NSE. For this instrument configuration the angular resolution could be determined by refinement of the SANS by iron oxide nanospheres with a known particle size distribution. A lognormal particle size distribution of 10(4) % was found for the cobalt nanoparticle dispersion.

6.4. Summary

Not So Small-Angle Neutron Scattering with Polarization Analysis was performed successfully at the DNS, J-NSE, and IN12 instruments. By improvements of the angular resolution in the low Q range, the reliably high degree of polarization at the DNS and IN12 instruments was used for separation of incoherent and coherent scattering contributions of cobalt nanoparticle dispersions. For the IN12 experiment, a significant multiple scattering rate of 0.34 was corrected. However, this measurement exhibits a significantly higher background level, which may originate in either a higher amount of excess coherent scattering or incomplete separation of the incoherent scattering contribution. The J-NSE instrument provides a sufficient angular resolution in the not so small angle range of 0.1 $Å^{-1} \leq Q \leq 0.9$ $Å^{-1}$ with a significantly lower degree of polarization. However, a correction for the non-perfect polarization was introduced, which allowed for successful separation of the different scattering contributions.

These investigations consistently reveal form factor minima for the cobalt nanoparticles, a structural detail which has not been accessible by SAXS nor non-polarized SANS. The angular resolution of the J-NSE instrument is high enough to allow for refinement of the core shell structure with a cobalt core and an AOT ligand shell. By calibration of the instrumental resolution to an iron oxide nanoparticle sample of known particle size distribution, the particle size distribution of the cobalt nanoparticles was determined for the first time. A lognormal particle size distribution of 10 (4) % was found. The large uncertainty can be traced back to the separation involving a low degree of polarization of ~ 0.6. A higher degree of polarization will allow for a more precise determination of the core shell structure and particle size distribution.

The absence of a magnetic scattering signal in both iron oxide and cobalt nanoparticles may also be explained by the relatively low degree of polarization obtained at J-NSE. A higher degree of polarization might reveal the pure magnetic form factor of the iron oxide nanoparticles. Concerning the cobalt nanoparticles, oxidation of the particles is possible and may diminish the magnetic scattering intensity, which is expected

to be significantly lower than the iron oxide magnetic scattering intensity even without oxidation.

A higher degree of polarization at the J-NSE instrument is desired and may be achieved by further improvements on the adiabatic rotation of the polarization direction, the flipper efficiency, and the guide fields. Next to separation of a possible magnetic form factor, the higher polarization will allow for separation of the incoherent and coherent scattering contributions with a lower uncertainty and in an even lower momentum transfer range, providing a larger overlap with dedicated small-angle scattering instruments. Thus, the J-NSE instrument covers the gap in momentum transfer between traditional small-angle scattering instruments and polarized diffraction instruments. In the near future, the JCNS instrument MARIA at FRM II will allow for reflectomety and small-angle neutron scattering experiments with polarization analysis in the required momentum transfer range.

The beamtime required to perform the presented experiments differs from two days at DNS to four days at J-NSE and five days at IN12. Four full days for the measurement of only two samples including the required references seems long if compared to the few hours required for this experiment at a dedicated small-angle scattering instrument (in the small-angle Q range). Nonetheless, due to the good Q resolution and large optimization potential of the degree of polarization, further development of this scattering technique at the J-NSE instrument is promising in order to perform Not So Small Angle Neutron Scattering with Polarization Analysis with high reliability.

7. Conclusive Remarks

Within the scope of this work, an interdisciplinary approach has been applied to magnetic nanoparticles, comprising nanoparticle synthesis and primary characterization as well as detailed investigations of structural and magnetic intra- and interparticle correlations by advanced scattering methods.

Synthesis The goals of the cobalt nanoparticle synthesis were both a precise structural characterization of nanoparticles prepared by a previously developed synthesis technique as well as further optimization of the synthesis route towards a defined variation of the particle size and particle dispersions suitable for subsequent neutron scattering investigations.

Nanoparticle dispersions in toluene were prepared according to a micellar synthesis technique, by reduction of cobalt bis(2-ethylhexyl) sulfosuccinate ($Co(AOT)_2$) reverse micelles in toluene with sodium triethyl borohydride ($NaEt_3BH$). Obtained nanoparticles have particle diameters below 3 nm and exhibit superparamagnetic blocking temperatures significantly below 10 K. Due to these very small nanoparticle sizes the primary characterization is challenging in every respect. For determination of blocking temperatures below 10 K, a precise control of the heating rates of the used magnetometer in this temperature range is crucial. As small nanoparticles with a consequently small integral particle moment are sensitive to very small magnetic fields, the condition of a reliable zero cooling field has furthermore to be fulfilled with a lower tolerance than for ZFC measurements of larger nanoparticles. The characterization of very small nanoparticles with small-angle scattering techniques is impeded because the scattering intensity is low (as it scales linearly with the particle volume) and because the first form factor minimum is located in a Q range where it is easily superposed by scattering contributions of reaction byproducts. Extraction by conventional centrifugation fails due to the low sedimentation of such small nanoparticles. Alternative approaches using ligand exchanges were observed to alter the particle size and size distribution. ASAXS experiments aiming at a separation of the pure cobalt contributions to the small-angle scattering failed for technical reasons. Small magnetic nanoparticles furthermore tend to aggregate, which inhibits the particle size determination by the Guinier approach.

An additional obstacle in nanoparticle synthesis and characterization is a low reproducibility of the particle size, which is likely related to the strong affinity to oxidation. A varying degree of oxidation has been observed, and the coexistence of a defined amount of cobalt and cobalt oxide within the particles with a gradually changing fraction of cobalt oxide was revealed by X-ray absorption spectroscopy. Deliberate oxidation was furthermore observed to impact the particle size as estimated from SAXS.

Particle size distribution and ligand shell thickness were finally determined for one sample by Not So Small Angle Neutron Scattering with polarization analysis at the J-NSE instrument. A reasonable ligand shell thickness of 7.7 (2) Å was determined for a cobalt nanoparticle core of 2 nm in diameter and a lognormal size distribution of 10 (4) %.

Considering the encountered obstacles of poor reliability and applicability of the available characterization methods and the apparently low reproducibility of the synthesis technique including oxidation issues, it is remarkable that a clear variation of the particle size was achieved by several approaches. Note that a variation of the particle size was only detectable as a relative parameter for an entire experimental series, which requires the reliable performance of the used characterization method, a comparable degree of oxidation, and a continuous variation of the particle size for the entire sample series. A significant increase in particle size was obtained by lowering of the cobalt concentration per micelle, achieved by either addition of nonionic surfactants or the ionic liquid ethyl ammonium nitrate (EAN) as polar phase. In case of incomplete or stepwise cobalt reduction, an obtained increase of particle size was accompanied by variation of the dispersion color due to surface plasmon resonance excitation in the visible energy range. The brilliance of the dispersion colors that are easily distinguishable by eye indicates a narrow particle size distribution.

For further development of the cobalt nanoparticle synthesis, the stepwise reduction of $Co(AOT)_2$ micellar solutions is the most promising route to larger nanoparticles in sufficient concentrations for further characterization. By this approach, nanoparticle nucleation and growth may be separated by a more gradual reduction, and as long as the reduction remains incomplete, more starting material might be added, promising much larger particle sizes. In any case, a significant improvement of both inert synthesis conditions and the primary characterization methods is strongly recommended for a successful synthesis development.

For investigations on fundamental physical properties, the particle size is again important. Very small nanoparticles are an interesting case because surface dependent phenomena are enhanced. On the other hand, most neutron scattering instruments are not adapted for investigations of length scales in between the nanoparticle and atomic size level, as required for nanoparticle diameters below 5 nm. Moreover, a good crystallinity of the nanoparticles is desired. This is more likely to be achieved for nanoparticles prepared by high temperature synthesis methods such as thermolytic approaches.

Intraparticle correlations Iron oxide nanoparticles were chosen as model system for investigations on structural and magnetic intra- and interparticle correlations, and a

range of different particle sizes from 5 to 25 nm in diameter and different particle shapes including spheres and cubes were obtained through collaborations. A precise determination of the particle size with small-angle scattering techniques confirms narrow lognormal size distributions between 5 and 7 % for most samples and the good quality of the dispersions in toluene as required for form factor measurements. The cubic nanoparticle shape is not distinguishable from spheres by small-angle scattering due to the orientational average in dispersion and a considerable truncation of the cubes' corners.

The atomic structure of the nanoparticles is confirmed to be the cubic magnetite/-maghemite structure type by X-ray diffraction and analysis of the atomic pair distribution function (PDF). Two different structural aspects are observed in dependence of the particle size. In the long range structure, a transition from near magnetite to near maghemite nanoparticles with decreasing particle size is concluded from decreasing lattice parameters and Fe_o occupancies, which is in agreement with a variation of the Fe valence determined by X-ray absorption spectroscopy. A core shell structure consisting of a magnetite core and a maghemite shell is suggested. For confirmation of an intraparticle variation of both lattice constant and Fe occupancy, PDF measurements with a better instrumental Q resolution, leading to a larger accessible r range in the PDF, are required. Local structural distortions are observed by analysis of the PDF nearest neighbor distances and are assigned to displacements of the Fe_o site by analysis of the nearest neighbor contributions by EXAFS. Due to their particle size dependence, the displacements are suggested to originate in the particle surface, and induction of lattice strain reaching into the nanoparticle core may be assumed.

The spatial magnetization distribution within the nanoparticles was investigated using polarized SANS. The obtained magnetization profile of the nanoparticles indicates a constant magnetization density in the nanoparticle core, which decreases towards the nanoparticle surface inside a surface shell of ~ 3-5 Å thickness. The magnetic shell thickness is in agreement with the magnetic volume determined by macroscopic magnetization measurements. However, the core magnetization of ~ 0.75 μ_B is found significantly lower than the magnetization bulk magnetite or maghemite, which is expected ~ 1.1 μ_B. Considering the local structural dislocations found by PDF and EXAFS, a correlation of magnetization density and lattice distortions is suggested. The thickness of the found iron oxide shell of lower magnetization is in the length scale of the first three nearest neighbor correlation peaks that reveal strong distortions. Furthermore, lattice strain was assumed to reach into the nanoparticle core, which may result in lower magnetic moments or canted Fe spins even inside the magnetic nanoparticle core.

A deeper insight into the magnetic nanoparticle structure can be gained by SANS

with polarization analysis. While the half polarized experiment performed in this work solely measures the magnetization density in direction of the applied magnetic field, linear polarization analysis gives access to the spatial distribution of the magnetization component perpendicular to the applied field. By this approach a possible spin canting due to disorder close to the nanoparticle surface will be detectable as an increased magnetization density contribution perpendicular to the applied magnetic field. A possible non-zero core magnetization perpendicular to the applied magnetic field will furthermore indicate magnetic disorder in the nanoparticle core. Such a disorder might explain the low core magnetization found parallel to the magnetic field.

Interparticle correlations Interparticle correlations of iron oxide nanoparticles were investigated in dependence of the nanoparticle shape using two different approaches. First, highly concentrated nanoparticle dispersions were investigated by SANS in an applied magnetic field. Secondly, long range ordered mesocrystals of different crystal structures were prepared and investigated by grazing incidence X-ray scattering methods.

Field dependent SANS measurements reveal a variation of interparticle order with the nanoparticle shape. Concentrated dispersions of nanospheres exhibit a spatially disordered, short range ordered hard spheres interaction potential that is nearly field independent. In contrast, nanocubes dispersions of a comparable particle size and concentration reveal a more pronounced interparticle interaction with formation of chain-like aggregates even without application of a magnetic field. With increasing magnetic field, these linear aggregates stiffen and are oriented into the field direction. Additionally, the nanoparticle distance inside the chains decreases from 13.1 (1) nm to 12.5 (1) nm. The increased degree of order of the linear aggregates in an applied magnetic field can be understood as oriented face to face attachment of the nanocubes with the nanoparticle moments oriented in a ferromagnetic chain parallel to the applied field. While hard spheres interaction potential and dipolar interaction are of comparable magnitude for the nanospheres and nanocubes dispersions, the difference in interaction energy can arise from either van der Waals attraction or a different magnetic shape anisotropy. Thus, the defined degree of order is induced by the faceted shape of the nanocubes. This is in agreement with the higher tendency of the nanocubes to reveal a structure factor even in lower concentrations as compared to a nanocubes sample with larger degree of truncation and the nanospheres.

A similar shape dependent ordering behavior is found for long range ordered arrangements of nanoparticles. 3D mesocrystals are obtained by application of a magnetic field during deposition of the nanoparticle dispersions onto a substrate. Characteriza-

tion using GISAXS reveals internally structurally coherent mesocrystals with in plane correlation lengths beyond the instrumental resolution limit of 65 nm, mesocrystals which are oriented on the substrates forming a 2D powder. For nanospheres mesocrystals, a closed packing is obtained which is explained by purely steric interactions. GISAXS reveals a rhombohedral mesocrystal structure, corresponding to a preferential *fcc* stacking type instead of *hcp*. In contrast to the nanospheres, truncated nanocubes exhibit (100) orientation in the mesocrystal arrangements, again resulting from increased van der Waals interactions between neighboring particle facets. A *bct* mesocrystal structure is determined by GISAXS, which is opposed to the *sc* structure expected *a priori* for a closed packed arrangement of nanocubes. As supported by a free energy calculation performed by Bergström *et al.*, the observed preference of *bct* over *sc* originates in the truncation of the nanocubes and the consequently increasing van der Waals interaction between the truncated (111) facets.

An even more sensitive shape dependence is found for aged nanocubes, which are supposed to have a larger degree of truncation. Here, a rhombohedral mesocrystal structure is found, which is isotypic to the nanospheres mesocrystal structure. However, the heavily truncated nanocubes are still arranged in (111) oriented assemblies, as is inferred from commensurate superstructure reflections observed exclusively for the truncated nanocubes. The found superstructure is interpreted as originating from a structural phase boundary between the rhombohedral structure with an (111) oriented arrangement and the *bct* structure with preferential arrangement of the (100) facets. This is supported by the simultaneous appearance of both structure types in most samples and the observation of dislocations corresponding to the superstructure by SEM, where both square and hexagonal lateral order appear.

Both investigated approaches, *e. g.* the formation of long range ordered mesocrystals and the structure factors revealed by highly concentrated nanoparticle dispersions, illustrate how oriented arrangements of magnetic nanoparticles can be induced by application of a magnetic field. Alignment of the easy axes in the applied magnetic field is likely. Nonetheless, in both experiments a significant influence of the anisotropic nanoparticle shape on the formed nanoparticle arrangement is found. Thus, the formation of ordered nanoparticle arrangements as observed here depends on the interplay of both dipolar and shape dependent van der Waals interactions.

In the future, both SANS by highly concentrated nanoparticle dispersions and GISANS by long range ordered mesocrystals with polarization analysis are promising experiments for investigation of the magnetic interparticle interactions. Whereas SANS provides information on the linear arrangement of nanoparticles, GISANS by 3D mesocrys-

tals may give access to the magnetic interparticle interactions in correlation with the crystallographic directions of the nanoparticle (and also the mesocrystal). A further model system for investigation of magnetic interparticle interactions is a long range ordered monolayer of nanoparticles. Possible approaches for formation of such a monolayer are indicated by observation of a near monolayer of square symmetry by deposition on a tilted substrate.

Method development Several methodological improvements of nanoparticle characterization with scattering methods were achieved in this work. This includes the development of a form factor for small-angle scattering of truncated nanocubes and its combination with both spherical and truncated cubic shells into core shell form factors. For structural and magnetic characterization of very small nanoparticles, Not So Small Angle Neutron Scattering with polarization analysis was developed in order to bridge the gap in momentum transfer between conventional SANS and diffraction instruments with polarization analysis. Development of this technique involved major instrumental effort, and a typical experiment requires too much time to be considered as a primary characterization technique. However, if the degree of polarization is further improved and the Q resolution is determined more accurately, a more precise determination of the particle size distribution and the separation of the magnetic scattering contribution in an enhanced Q range seem within reach on J-NSE. In the framework of this technique, a correction for a non-perfect degree of polarization is derived. Furthermore, an analytic approach for correction of multiple scattering is given.

Summary This work gives a comprehensive overview of magnetic nanoparticle investigations, including a synthesis approach for very small cobalt nanoparticles and an extensive structural and magnetic characterization of iron oxide nanoparticles in all length scales. In particular the correlation of the local atomic structure and the spatial magnetization distribution within nanoparticles may contribute to a better understanding of fundamental nanoparticle properties such as a possible spin canting close to the nanoparticle surface. The strong nanoparticle shape dependence of the observed mesocrystal structure types illustrates the sensitivity of the interparticle interactions on nanoparticle shape anisotropy. With the structure-directing influence of the anisotropic nanoparticle shape as opposed to the spherical atoms in conventional crystal structures, a new dimension of crystallography has been established.

Appendices

A. Abbreviations & Physical Constants

6-ID-D	high energy synchrotron diffraction beamline at APS (see section 3.3.1)
α_c	critical angle
α_f	scattered wave angle
α_i	incident wave angle
λ	radiation wavelength
μ_B	Bohr magneton
2θ	scattering angle
AFM	atomic force microscopy
ASAXS	anomalous small-angle X-ray scattering
D22	small-angle neutron scattering instrument at ILL (see section 3.1.5)
DNS	diffuse neutron scattering instrument at FRM II (see section 3.5.1)
EAN	ethyl ammonium nitrate
EXAFS	extended X-ray absorption fine structure
FC	field cooled
FWHM	full width at half maximum
GISAXS	grazing incidence small-angle X-ray scattering
HWHM	half width at half maximum
ID01	small-angle X-ray scattering beamline at ESRF (see section 3.1.3)
IN12	triple-axis spectrometer at ILL (see section 3.5.3)
J-NSE	neutron spin echo instrument at FRM II (see section 3.5.2)
JUSIFA	small-angle X-ray scattering beamline at HASYLAB (see section 3.1.1)
k_B	Boltzmann constant
$\vec{k}_f$	forthcoming wave vector
$\vec{k}_i$	incident wave vector
KWS 2	small-angle neutron scattering instrument at FRM II (see section 3.1.4)
NSF	non spin-flip
OA	oleic acid
PDF	pair distribution function
Q	momentum transfer
$\vec{Q}$	scattering vector
SAMBA	X-ray absorption spectroscopy beamline at synchrotron Soleil (see section 3.4.1)
SANS	small-angle neutron scattering

SAXS	small-angle X-ray scattering
SEM	scanning electron microscopy
SF	spin-flip
SLD	scattering length density
SWING	small-angle X-ray scattering beamline at Synchrotron Soleil (see section 3.1.2)
T_B	blocking temperature
TREFF	neutron reflectometer at FRM II (see section 3.2.1)
XANES	X-ray absorption near edge structure
XAS	X-ray absorption spectroscopy
XRD	X-ray diffraction
ZFC	zero-field cooled

B. Chemical reagents

A comprehensive list of all chemical reagents used for synthesis of cobalt nanoparticles is given below.

Table B.0.1.: List of chemical reagents.

Reagent	Mol. formula	M [g/mol]	Supplier	Purity
NaAOT	$NaC_{20}H_{37}SO_7$	444.55	Fluka	
Dowex 50 W				
HCl	HCl			1M
Ethanol	C_2H_6O	46.07	KMF	abs.
Amberlit IRC-76			Supelco	
$Co(OAc)_2 \cdot 4\,H_2O$	$CoC_4H_{14}O_8$	249.07	Alfa Aesar	
Cyclohexane	C_6H_{12}	84.16	Merck	
n-Propanol	C_3H_8O	60.1		
2,7-Dichlorofluorescein	$C_{20}H_{10}Cl_2O$	401.2	Fluka	
Toluene	C_7H_8	92.14	Alfa Aesar	anhydrous, 99.8%
Toluene-d_8	C_7D_8	100.19	Aldrich	99.6 atom %
$NaEt_3BH$	$NaC_6H_{16}B$	121.99	Aldrich	1M in toluene
$P(oct)_3$	$PC_{24}H_{51}$	370.64		
Formamide	CH_3NO	45.04	Fluka	
Igepal CO 520	$C_{25}H_{44}O_6$	440.0	Aldrich	
$C_{12}E_5$	$C_{22}H_{46}O_6$	406.0	Aldrich	
EAN	$C_2H_8N_2O_3$	108.1	obtained through collaboration	
Hydrazine	N_2H_4	32.05	Sigma-Aldrich	anhydr., 1M in THF
Dicobalt octacarbonyl	CoC_8O_8	341.95	Alfa Aesar	

C. Sample holders

C.1. PPMS sample holder

A technical drawing of the sample holder designed specifically for magnetization measurements of liquid samples using the VSM option of the PPMS is given in Figure C.1.1. A detailed description of the characteristics is given in section 4.2.2.1.

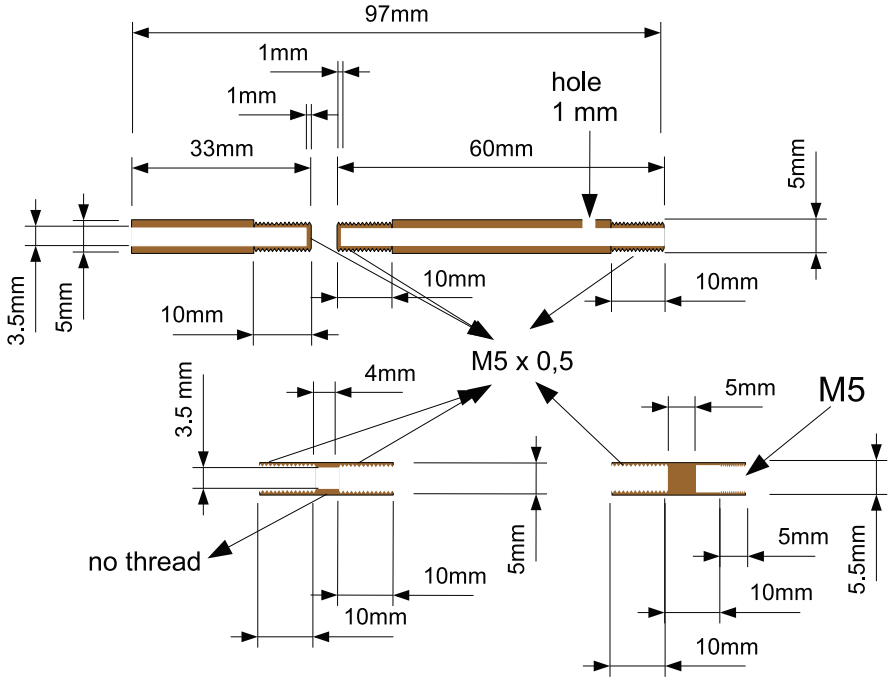

Figure C.1.1.: Technical drawing of the PPMS sample holder made of Vespel® polyimide.

C.2. MPMS sample holder

A technical drawing of the sample holder designed specifically for magnetization measurements of liquid samples on the MPMS is given in Figure C.2.1. A detailed description of the characteristics is given in section 5.1.2.1.

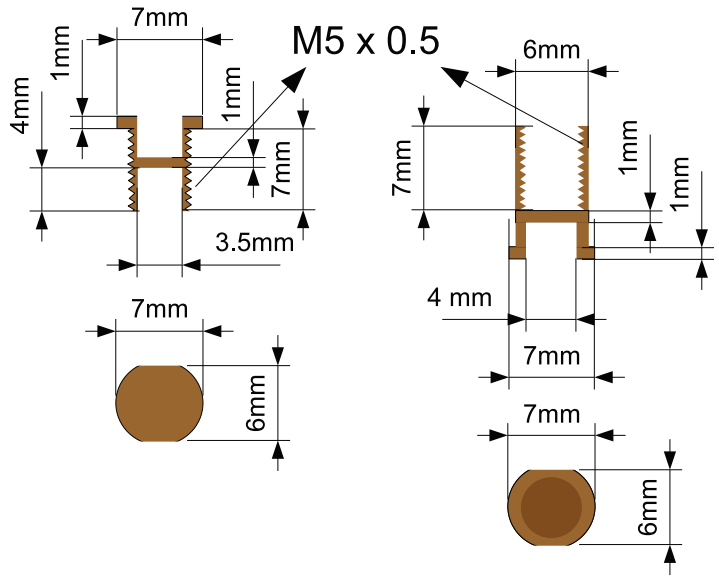

Figure C.2.1.: Technical drawing of the MPMS sample holder made of Vespel® polyimide.

D. Form factors used for small-angle scattering

D.1. Truncated cube

The code for the truncated cubic form factor was written by Denis Korolkov, JCNS, Garching, Germany. The form factor is defined in section 5.1.2.3. It was used for refinement of SAXS by iron oxide nanocubes in section 5.1.3.1 and is implemented in the truncated cubic core shell form factors in D.2 and D.3.

```
1  /*
2   * fftrunccube.cpp
3   *
4   *  Created on: Dec 31, 2009
5   *      Author: denis
6   */
7
8  #include "fftrunccube.h"
9
10 FFTruncCube::FFTruncCube(double a0, double a0sigma, double
       tau, double rhoc, double rho0, int irotpoints, int
       iavpoints) :
11       FunctionoidD(),FormFactor(),_a0(a0),_a0sigma(a0sigma),
             _tau(tau),_rhoc(rhoc),_rho0(rho0) {
12    glav=new GaussLQ<>(iavpoints);
13    glrot=new GaussLQ<>(irotpoints);
14
15 }
16
17
18 FFTruncCube::~FFTruncCube(){
19    delete glav;
20    delete glrot;
21 }
22
23
24 double FFTruncCube::operator()(double alpha, double beta) {
25      double qx = _q * sin(alpha) * sin(beta);
26      double qy = _q * sin(alpha) * cos(beta);
27      double qz = _q * cos(alpha);
```

```
28      double ff = norm(amplitude(qx,qy,qz,_a,_b))*sin(alpha);
29      return ff;
30  }
31
32
33  double FFTruncCube::operator ()(double a){
34    _a=a;
35    _b=_tau*a;
36    double lognorm=1.0/(SQRT_2PI*a*_a0sigma)*exp(-pow((log(a/
        _a0)),2.0)/(2.0*_a0sigma*_a0sigma));
37    return  glrot->calcIntegral(*this, 0.0, 3.1416/2.0, 0.0,
        3.1416/2.0)*lognorm;
38  }
39
40
41  double FFTruncCube::crossSection(double q){
42    _q=q;
43    double std=sqrt(exp(2.0*log(_a0)+_a0sigma*_a0sigma)*(exp(
        _a0sigma*_a0sigma)-1.0));
44    double rd=(_rhoc-_rho0);
45    double intens = glav->calcIntegral(*this, _a0-3.0*std, _a0
        +3.0*std )*rd*rd;
46    return intens;
47  }
48
49  dcplx FFTruncCube::F0(double qx, double qy, double qz,
      double b) {
50      dcplx A = exp(cplxI * b * qx) / (qx * (qx - qy) * (qx -
          qz));
51      dcplx B = exp(cplxI * b * qy) / (qy * (qy - qx) * (qy -
          qz));
52      dcplx C = exp(cplxI * b * qz) / (qz * (qz - qx) * (qz -
          qy));
53      double D = 1.0 / (qx * qy * qz);
54      return cplxI * (A + B + C - D);
55  }
56
57  dcplx FFTruncCube::amplitude(double qx, double qy, double qz
      , double a, double b) {
58      double aa = a / 2.0;
59      double Fc = a*a*a*sinc(aa * qx) * sinc(aa * qy) * sinc(
          aa * qz);
60      dcplx F8 = F0(qx, qy, qz,b) * exp(-cplxI * aa * (qx + qy
           + qz)) + F0(-qx,
```

```
61                  -qy, -qz,b) * exp(-cplxI * aa * (-qx - qy - qz
                       )) + F0(-qx, qy,
62                  qz,b) * exp(-cplxI * aa * (-qx + qy + qz)) +
                       F0(qx, -qy, -qz,b)
63                  * exp(-cplxI * aa * (qx - qy - qz)) + F0(qx, -
                       qy, qz,b) * exp(
64                  -cplxI * aa * (qx - qy + qz)) + F0(-qx, qy, -
                       qz,b) * exp(-cplxI
65                  * aa * (-qx + qy - qz)) + F0(qx, qy, -qz,b) *
                       exp(-cplxI * aa
66                  * (qx + qy - qz)) + F0(-qx, -qy, qz,b) * exp(-
                       cplxI * aa * (-qx
67                  - qy + qz));
68      return Fc-F8;
69  }
```

D.2. Truncated cube with truncated cubic shell

The code for the core shell form factor of a truncated cubic core with a truncated cubic shell was written by Denis Korolkov, JCNS, Garching, Germany. The form factor is defined in section 5.1.2.3 and was used for refinement of SANS by iron oxide nanocubes in section 5.1.3.2.

```
1  /*
2   * fftrunccubecoreshell.cpp
3   *
4   *  Created on: Dec 31, 2009
5   *      Author: denis
6   */
7
8  #include "fftrunccubecoreshell.h"
9
10    FFTruncCubeCoreShell::FFTruncCubeCoreShell(double acore,
         double acore_sigma, double tau,double wshell, double
         rhoc, double rhos, double rho0, int irotpoints, int
         iavpoints) :
11       FFTruncCube(acore, acore_sigma, tau, rhoc, rho0,
            irotpoints,iavpoints), _wshell(wshell), _rhos(rhos){
12
13    }
14
15    FFTruncCubeCoreShell::~FFTruncCubeCoreShell(){
16    }
```

```
17
18    double FFTruncCubeCoreShell::operator()(double alpha,
          double beta) {
19      double qx = _q * sin(alpha) * sin(beta);
20      double qy = _q * sin(alpha) * cos(beta);
21      double qz = _q * cos(alpha);
22      dcplx ampl=(_rhoc-_rhos)*amplitude(qx,qy,qz,_ac,_bc)+(
            _rhos-_rho0)*amplitude(qx,qy,qz,_as,_bs);
23      double ff = norm(ampl)*sin(alpha);
24      return ff;
25    }
26
27    double FFTruncCubeCoreShell::operator()(double a){
28          _ac=a;
29          _as=_ac+2.0*_wshell;
30          _bc=_tau*_ac;
31          _bs=_tau*_as;
32          double lognorm=1.0/(SQRT_2PI*_ac*_a0sigma)*exp(-pow
                ((log(_ac/_a0)),2.0)/(2.0*_a0sigma*_a0sigma));
33          return  glrot->calcIntegral(*this, 0.0, 3.1416/2.0,
                0.0, 3.1416/2.0)*lognorm;
34    }
35
36    double FFTruncCubeCoreShell::crossSection(double q){
37      _q=q;
38      double std=sqrt(exp(2.0*log(_a0)+_a0sigma*_a0sigma)*(exp
            (_a0sigma*_a0sigma)-1.0));
39      double intens = glav->calcIntegral(*this, _a0-3.0*std,
            _a0+3.0*std );
40      return intens;
41    }
```

D.3. Truncated cube with spherical shell

The code for the core shell form factor of a truncated cubic core with a spherical shell was written by Denis Korolkov, JCNS, Garching, Germany. The form factor is defined in section 5.1.2.3 and was used for refinement of SANS by iron oxide nanocubes in section 5.1.3.2.

```
1  /*
2   * fftrcubecoresphereshell.cpp
3   *
4   *  Created on: Dec 31, 2009
```

```
5   *       Author: denis
6   */
7
8  #include "fftrunccubecoresphereshell.h"
9  #include "ffsphere.h"
10
11    FFTruncCubeCoreSphereShell::FFTruncCubeCoreSphereShell(
          double acore, double acore_sigma, double tau, double
          rshell, double rhoc, double rhos, double rho0, int
          irotpoints, int iavpoints) :
12        FFTruncCube(acore, acore_sigma, tau, rhoc, rho0,
              irotpoints,iavpoints), _rshell(rshell), _rhos(rhos){
13
14    }
15
16    FFTruncCubeCoreSphereShell::~FFTruncCubeCoreSphereShell(){
17
18
19    }
20
21    double FFTruncCubeCoreSphereShell::operator()(double alpha
          , double beta) {
22        double qx = _q * sin(alpha) * sin(beta);
23        double qy = _q * sin(alpha) * cos(beta);
24        double qz = _q * cos(alpha);
25        dcplx ampl=(_rhoc-_rhos)*amplitude(qx,qy,qz,_ac,_bc)+
              shell_ampl;
26        double ff = norm(ampl)*sin(alpha);
27        return ff;
28    }
29
30    double FFTruncCubeCoreSphereShell::operator()(double a){
31            _ac=a;
32            _bc=_tau*_ac;
33            double lognorm=1.0/(SQRT_2PI*_ac*_a0sigma)*exp(-pow
                  ((log(_ac/_a0)),2.0)/(2.0*_a0sigma*_a0sigma));
34            return  glrot->calcIntegral(*this, 0.0, 3.1416/2.0,
                  0.0, 3.1416/2.0)*lognorm;
35    }
36
37
38    double FFTruncCubeCoreSphereShell::crossSection(double q){
39        _q=q;
40        double std=sqrt(exp(2.0*log(_a0)+_a0sigma*_a0sigma)*(exp
              (_a0sigma*_a0sigma)-1.0));
```

```
41      shell_ampl=(_rhos-_rho0)*FFSphere::amplitude(_q,_rshell)
            ;
42      double intens = glav->calcIntegral(*this, _a0-3.0*std,
            _a0+3.0*std );
43      return intens;
44    }
```

D.4. Magnetic contrast variation

The scattering cross sections for polarized small angle neutron scattering with magnetic contrast variation are calculated according to equation 5.3.11. The nuclear and magnetic form factor amplitudes are defined in section 5.3.2.2, and the resulting model was used for refinement of polarized SANS by iron oxide nanoparticles in section 5.3.3.1.

```
1  #include <stdio.h>
2  #include <stdlib.h>
3  #include <string.h>
4  #include <math.h>
5  #include <time.h>
6  #include "linalg.h"
7  #include <complex>
8
9  double D(double, double,double) ;
10
11 double Std(double,double) ;
12
13 double Qres(double ,double ,double,double ,double);
14
15 double sq(double, double, double, double);
16
17 double Fsph(double, double) ;
18
19 double Flin(double, double) ;
20
21 double FM(double, double, double, double, double);
22
23 double K(double, double, double) ;
24
25 double FN(double,double,double,double,double);
26
27 double FF(double, double, double, double, double, double,
       double, double, double, double);
28
```

```
29 double FF1(double, double, double, double, double, double,
      double, double, double, double, double);
30
31 double FF2(double, double, double, double, double, double,
      double, double, double, double, double, double);
32
33
34
35 int main (int argc, char* argv[])
36   {
37
38
39   int i,h;
40   double f,qp,qpi,qpf,hsteps,dqp,SAXSINT,s,b,x;
41   vector a;
42
43
44   a.clean(argc-1);
45
46
47 // Initialize parameter vector
48   for(i=1;i<argc-1;i++)
49     {
50     a.cp[i]=atof(argv[i+1]);
51     }
52   x=atof(argv[1]);
53
54        hsteps =10;
55       qpi=x-3*sq(real(a.cp[14]),real(a.cp[15]),x,real(a.cp
           [16]));
56       qpf=x+3*sq(real(a.cp[14]),real(a.cp[15]),x,real(a.cp
           [16]));
57       dqp=(qpf-qpi)/hsteps;
58
59
60      SAXSINT=0.;
61       for (int h = 1; h < hsteps+1; h++)
62    {
63             qp=qpi+h*dqp;
64           SAXSINT=SAXSINT+Qres(x,qp,real(a.cp[14]),real(a.cp
               [15]),real(a.cp[16]))*FF2(qp,real(a.cp[3]),real
               (a.cp[4]),real(a.cp[5]),real(a.cp[6]),real(a.cp
               [7]),real(a.cp[8]),real(a.cp[9]),real(a.cp[10])
               ,real(a.cp[11]),real(a.cp[12]),real(a.cp[13]))*
               dqp;
```

```
65              }
66
67          f=real(a.cp[1]*a.cp[18]*a.cp[19])*SAXSINT+real(a.cp
                [2]*a.cp[17]);
68
69
70      printf("%14.8f\n",f);
71      return 1;
72          }
73
74
75
76  double Qres(double q,double qp,double dtheta, double dlambda
        , double lambda)
77  {
78  return  1/(sqrt(2*M_PI)*sq(dtheta,dlambda,q,lambda))*exp(-
        pow((qp-q),2)/(2*sq(dtheta,dlambda,q,lambda)*sq(dtheta,
        dlambda,q,lambda)));
79  }
80
81
82  double sq(double dtheta, double dlambda, double q, double
        lambda)
83  {
84  return  sqrt(4./5.52*M_PI*M_PI/lambda*((dtheta)*(dtheta)+(q*
        dlambda*lambda/(4*M_PI))*(q*dlambda*lambda/(4*M_PI))));
85  }
86
87
88  double FF2(double q, double r, double dr, double ns, double
        nc, double R1, double R2, double n1, double n2, double p,
         double sigma1, double sigma2)
89  {
90          double nsteps,bi,bf,db,INT,c;
91
92          nsteps =10;
93      bi=R1-3.*Std(R1,sigma2);
94      bf=R1+3.*Std(R1,sigma2);
95      db=(bf-bi)/nsteps;
96
97
98          INT=0.;
99           for (int n = 1; n < nsteps+1; n++)
100      {
101             c=bi+n*db;
```

```
102             INT=INT+(FF1(q,r,dr,ns,nc,c,R2,n1,n2,p,sigma1))*D(
                    c,R1,sigma2);
103     }
104 return db*INT;
105 }
106
107
108 double FF1(double q, double r, double dr, double ns, double
      nc, double R1, double R2, double n1, double n2, double p,
       double sigma1)
109 {
110         double lsteps,ai,af,da,INT,c;
111
112         lsteps =10;
113    ai=r-3.*Std(r,sigma1);
114    af=r+3.*Std(r,sigma1);
115    da=(af-ai)/lsteps;
116
117
118        INT=0.;
119         for (int l = 1; l < lsteps+1; l++)
120     {
121             c=ai+l*da;
122             INT=INT+(FF(q,c,dr,ns,nc,R1,R2,n1,n2,p))*D(c,r,
                    sigma1);
123
124     }
125 return da*INT;
126 }
127
128
129 double FF(double q, double r, double dr, double ns, double
      nc, double R1, double R2, double n1, double n2, double p)
        // with p = -1. for I(+) and p = 0.99 (flipper
      efficiency) for I(-)
130 {
131         double P,sin2a;
132
133         P = 0.89; // Polarisation
134         sin2a = 0.9974; // a: angle betw. Q and H
135
136 return (FN(q,r,dr,ns,nc)*FN(q,r,dr,ns,nc) + (FM(q,R1,R2,n1,
      n2)*FM(q,R1,R2,n1,n2) + p *2.*P*FN(q,r,dr,ns,nc)*FM(q,R1,
      R2,n1,n2))*sin2a);
137 }
```

```
138
139
140 double FM(double q, double R1, double R2, double n1, double
      n2)
141 {
142         double m,n0,n3;
143
144         m  = (n1-n2)/(R1-R2);
145         n0 = n1-(n1-n2)/(R1-R2)*R1;
146         n3 = 0.;
147
148 return ((n0-n3)*Fsph(q,R2)+m*Flin(q,R2)-m*Flin(q,R1)-(n0-n1)
      *Fsph(q,R1));
149 }
150
151
152 double Fsph(double q, double r)
153 {
154 return (4. * M_PI*pow(r,3)*(sin(q*r)-q*r*cos(q*r))/pow((q*r)
      ,3.));
155 }
156
157
158 double Flin(double q, double r)
159 {
160 return (4. * M_PI*pow(r,4)*(2.*cos(q*r)+2.*q*r*sin(q*r)-q*q*
      r*r*cos(q*r))/pow((q*r),4.));
161 }
162
163
164 double FN(double q, double r, double dr, double ns, double
      nc)
165 {
166 return (K(q,(r+dr),ns)-K(q,r,(ns-nc)));
167 }
168
169
170 double K(double q, double c, double n)
171 {
172 return (4./3. * M_PI*pow(c,3)*n*3.*(sin(q*c)-q*c*cos(q*c))*
      pow((q*c), -3.));
173 }
174
175
176 double D(double c, double ro,double sigma)
```

```
177 {
178 return 1/(sqrt(2*M_PI)*sigma*c)*exp(-pow((log(c/ro)),2)/(2*
      sigma*sigma));
179 }
180
181
182 double Std(double ro,double sigma)
183 {
184 return sqrt(exp(2*log(ro)+sigma*sigma)*(exp(sigma*sigma)-1))
      ;
185 }
```

D.5. Magnetic-nuclear cross term

The magnetic-nuclear cross term of the polarized small angle neutron scattering cross sections with magnetic contrast variation are calculated according to equation 5.3.12. The nuclear and magnetic form factor amplitudes are defined in section 5.3.2.2, and the resulting model was used for refinement of polarized SANS by iron oxide nanoparticles in section 5.3.3.1.

```
 1 #include <stdio.h>
 2 #include <stdlib.h>
 3 #include <string.h>
 4 #include <math.h>
 5 #include <time.h>
 6 #include "linalg.h"
 7 #include <complex>
 8
 9 double D(double, double,double) ;
10
11 double Std(double,double) ;
12
13 double Qres(double ,double ,double,double ,double);
14
15 double sq(double, double, double, double);
16
17 double Fsph(double, double) ;
18
19 double Flin(double, double) ;
20
21 double FM(double, double, double, double, double);
22
23 double K(double, double, double) ;
```

```
24
25 double FN(double,double,double,double,double);
26
27 double FF(double, double, double, double, double, double,
     double, double, double);
28
29 double FF1(double, double, double, double, double, double,
     double, double, double, double);
30
31 double FF2(double, double, double, double, double, double,
     double, double, double, double, double);
32
33
34
35 int main (int argc, char* argv[])
36   {
37
38
39   int i,h;
40   double f,qp,qpi,qpf,hsteps,dqp,SAXSINT,s,b,x;
41   vector a;
42
43
44   a.clean(argc-1);
45
46
47 // Initialize parameter vector
48   for(i=1;i<argc-1;i++)
49     {
50
51     a.cp[i]=atof(argv[i+1]);
52     }
53   x=atof(argv[1]);
54
55        hsteps =10;
56       qpi=x-3*sq(real(a.cp[13]),real(a.cp[14]),x,real(a.cp
           [15]));
57       qpf=x+3*sq(real(a.cp[13]),real(a.cp[14]),x,real(a.cp
           [15]));
58       dqp=(qpf-qpi)/hsteps;
59
60
61      SAXSINT=0.;
62       for (int h = 1; h < hsteps+1; h++)
63    {
```

```
64                qp=qpi+h*dqp;
65              SAXSINT=SAXSINT+Qres(x,qp,real(a.cp[13]),real(a.cp
                    [14]),real(a.cp[15]))*FF2(qp,real(a.cp[3]),real
                    (a.cp[4]),real(a.cp[5]),real(a.cp[6]),real(a.cp
                    [7]),real(a.cp[8]),real(a.cp[9]),real(a.cp[10])
                    ,real(a.cp[11]),real(a.cp[12]))*dqp;
66            }
67
68          f=real(a.cp[1]*a.cp[17]*a.cp[18])*SAXSINT+real(a.cp
                [2]*a.cp[16]);
69
70
71     printf("%14.8f\n",f);
72     return 1;
73          }
74
75
76  double Qres(double q,double qp,double dtheta, double dlambda
       , double lambda)
77  {
78  return   1/(sqrt(2*M_PI)*sq(dtheta,dlambda,q,lambda))*exp(-
       pow((qp-q),2)/(2*sq(dtheta,dlambda,q,lambda)*sq(dtheta,
       dlambda,q,lambda)));
79  }
80
81
82  double sq(double dtheta, double dlambda, double q, double
       lambda)
83  {
84  return   sqrt(4./5.52*M_PI*M_PI/lambda*((dtheta)*(dtheta)+(q*
       dlambda*lambda/(4*M_PI))*(q*dlambda*lambda/(4*M_PI))));
85  }
86
87  double FF2(double q, double r, double dr, double ns, double
       nc, double R1, double R2, double n1, double n2, double
       sigma1, double sigma2)
88  {
89          double nsteps,bi,bf,db,INT,c;
90
91          nsteps =10;
92     bi=R1-3.*Std(R1,sigma2);
93     bf=R1+3.*Std(R1,sigma2);
94     db=(bf-bi)/nsteps;
95
96
```

```
97        INT=0.;
98          for (int n = 1; n < nsteps+1; n++)
99      {
100             c=bi+n*db;
101             INT=INT+(FF1(q,r,dr,ns,nc,c,R2,n1,n2,sigma1))*D(c,
                    R1,sigma2);
102
103     }
104 return db*INT;
105 }
106
107
108 double FF1(double q, double r, double dr, double ns, double
      nc, double R1, double R2, double n1, double n2, double
      sigma1)
109 {
110         double lsteps,ai,af,da,INT,c;
111
112         lsteps =10;
113     ai=r-3.*Std(r,sigma1);
114     af=r+3.*Std(r,sigma1);
115     da=(af-ai)/lsteps;
116
117
118       INT=0.;
119         for (int l = 1; l < lsteps+1; l++)
120     {
121             c=ai+l*da;
122             INT=INT+(FF(q,c,dr,ns,nc,R1,R2,n1,n2))*D(c,r,
                    sigma1);
123
124     }
125 return da*INT;
126 }
127
128
129 double FF(double q, double r, double dr, double ns, double
      nc, double R1, double R2, double n1, double n2)
130 {
131         double P,sin2a,e;
132
133         P = 0.89;    // Polarization
134         sin2a = 0.9974;    // correction term for 10 deg
              section, a: angle betw. Q and H
135         e = 0.99;    // flipper efficiency
```

```
136
137 return (sin2a*2.*P*(1.+e)*FN(q,r,dr,ns,nc)*FM(q,R1,R2,n1,n2)
    );
138 }
139
140
141 double FM(double q, double R1, double R2, double n1, double
    n2)
142 {
143         double m,n0,n3;
144
145         m  = (n1-n2)/(R1-R2);
146         n0 = n1-(n1-n2)/(R1-R2)*R1;
147         n3 = 0.;
148
149 return ((n0-n3)*Fsph(q,R2)+m*Flin(q,R2)-m*Flin(q,R1)-(n0-n1)
    *Fsph(q,R1));
150 }
151
152
153 double Fsph(double q, double r)
154 {
155 return (4. * M_PI*pow(r,3)*(sin(q*r)-q*r*cos(q*r))/pow((q*r)
    ,3.));
156 }
157
158
159 double Flin(double q, double r)
160 {
161 return (4. * M_PI*pow(r,4)*(2.*cos(q*r)+2.*q*r*sin(q*r)-q*q*
    r*r*cos(q*r))/pow((q*r),4.));
162 }
163
164
165 double FN(double q, double r, double dr, double ns, double
    nc)
166 {
167 return (K(q,(r+dr),ns)-K(q,r,(ns-nc)));
168 }
169
170
171 double K(double q, double c, double n)
172 {
173 return (4./3. * M_PI*pow(c,3)*n*3.*(sin(q*c)-q*c*cos(q*c))*
    pow((q*c), -3.));
```

```
174 }
175
176
177 double D(double c, double ro,double sigma)
178 {
179 return 1/(sqrt(2*M_PI)*sigma*c)*exp(-pow((log(c/ro)),2)/(2*
      sigma*sigma));
180 }
181
182
183 double Std(double ro,double sigma)
184 {
185 return sqrt(exp(2*log(ro)+sigma*sigma)*(exp(sigma*sigma)-1))
      ;
186 }
```

E. Refinement parameters

E.1. Diffraction

Tables E.1.1 and E.1.2 list the parameters obtained from diffraction data by Rietveld refinement of the bulk magnetite reference and constrained Le Bail fits of all investigated samples, respectively. The applied profile function is a modified pseudo-Voigt [125]. The Gaussian broadening is comprised of the instrumental broadening parameters U, V, W, and a particle size broadening parameter GP. The Lorentzian broadening is given by particle size broadening (LX) and strain broadening (LY) contributions.

Table E.1.1.: Rietveld refinement results of bulk magnetite powder. Data were refined in a Q range of $1.1 \leq Q \leq 5.3$ Å^{-1}. Refined parameters are given including uncertainties.

space group		F d$\bar{3}$m (No. 227)				
a	[Å]	8.39348 (8)				
atom	Wyckhoff position	x	y	z	frac	U_{iso}
Fe_t	8a	0.125	0.125	0.125	0.939 (3)	0.0020 (2)[a]
Fe_o	16d	0.5	0.5	0.5	0.933 (3)	0.0020 (2)[a]
O	32e	0.25478 (9)	0.25478 (9)	0.25478 (9)	1.0	0.0081 (6)
profile function		modified pesudo-Voigt [125]				
U,V,W	[0.01°]	0.	-1.9 (2)	0.651 (5)		
LX,LY	[0.01°]	0.	14.8 (1)			
zero	[0.01°]	-0.153 (3)				
background function		shifted Chebyshev polynomial (12 refined parameters)				
# parameters		23				
wRp		0.0221				
R(F^2)		0.0117				

[a] the thermal parameters for the Fe sites were constrained

Table E.1.2.: Le Bail fit results of simultaneously refined nanoparticle samples and magnetite reference. The A and B reflection sets comprise the (400), (440) and the (220), (511) reflections, respectively. Data were refined in Q ranges of $2.85 \leq Q_{(400)} \leq 3.2$ Å^{-1}, $4.05 \leq Q_{(440)} \leq 4.4$ Å^{-1}, $1.95 \leq Q_{(220)} \leq 2.3$ Å^{-1}, and $3.75 \leq Q_{(511)} \leq 4.05$ Å^{-1}. Refined parameters are given including uncertainties.

		Bc 9		Bc 14		Bo 22		Fe_3O_4	
		A	B	A	B	A	B	A	B
space group		F d$\bar{3}$m (No. 227)							
a	[Å]	8.3555 (3)		8.3740 (6)		8.3871 (2)		8.39443 (7)	
U	[0.01°]	0.							
V	[0.01°]	-2.8 (7)							
W	[0.01°]	0.72 (2)							
LX	[0.01°]	0.							
LY	[0.01°]	27 (2)	58 (5)	47 (3)	116 (8)	78.5 (9)	129 (4)	12.2 (4)	13.0 (4)
GP	[0.01°]	8.3 (2)	15.8 (6)	3.9 (3)	5.5 (6)	1.57 (6)	5.4 (2)	0.	0.
background fct.		shifted Chebyshev polynomial (6 parameters each)							
wRp		0.0114	0.0136	0.0192	0.0292	0.0648	0.0490	0.0277	0.0378

E.2. PDF

Parameters obtained by global PDF refinements performed in a fitting range of 0.7 Å ≤ R ≤ 50 Å are given in Table E.2.1. The instrumental resolution parameter was determined by refinement of a nickel reference sample as $Q_{damp} = 0.050813$. The used $Fd\bar{3}m$ structure model is the same as for the diffraction data. Refined parameters include the lattice constant a, the linear correlation motion coefficient δ, the particle diameter, and structural parameters such as the O site, atomic displacement parameters (adp), and occupancies (occ). Absolute uncertainties were not obtained by PDFgui because the PDF was generated from image plate data without intensity error bars. Uncertainties given in the Table have been estimated from the significance of slight parameter variations to the fit.

E.3. EXAFS

The parameters obtained for the first nearest neighbor correlations in magnetite as well as Bc 9 nanoparticles are listed in Table E.3.1. The data was refined in R space in a fitting range of 1 Å ≤ R ≤ 3.7 Å.

Table E.2.1.: Results of the global PDF refinements of the investigated nanoparticle samples and bulk magnetite. Refined parameters are given including uncertainties.

		Bc 9	Bc 14	Bo 22	Fe_3O_4
a	[Å]	8.364 (2)	8.388 (2)	8.392 (2)	8.400 (2)
δ	[$Å^{-1}$]	1.34 (1)	1.32 (1)	1.28 (1)	0.77 (1)
diameter	[Å]	112 (3)	135 (3)	138 (3)	-
O_x (= O_y = O_z)		0.2549 (5)	0.2547 (5)	0.2542 (5)	0.2552 (5)
$U_{iso}(Fe_t)$		0.0103 (5)	0.0093 (5)	0.0084 (5)	0.0049 (5)
$U_{iso}(Fe_o)$		0.0118 (5)	0.0104 (5)	0.0104 (5)	0.0067 (5)
U_{iso}(O)		0.0191 (3)	0.017 (1)	0.016 (1)	0.014 (1)
occ(Fe_t)		0.97 (2)	1.02 (2)	0.98 (2)	1.
occ(Fe_o)		0.76 (2)	0.89 (2)	0.95 (2)	1.03 (2)
occ(O)		1.	1.	1.	1.
Rw		0.190	0.156	0.169	0.119

Table E.3.1.: Results of the EXAFS refinements of bulk magnetite and Bc 9 nanoparticles. For each of the paths, degeneracy (N), the atomic pair distance (R), and mean square displacement of R (σ^2) are given.

		Fe_3O_4		Bc 9	
path	N	R [Å]	σ^2	R [Å]	σ^2
Fe_t-O	4	1.87 (5)	0.009 (3)	1.932 (7)	0.0102 (5)
Fe_o-O	6	2.02 (1)	0.009 (3)	1.932 (7)	0.0102 (5)
Fe_o-Fe_o	6	2.97 (1)	0.010 (1)	2.98 (1)	0.014 (1)
Fe_t-Fe_o	12	3.47 (1)	0.0072 (6)	3.43 (1)	0.0098 (5)
Fe_t-Fe_t	4	3.63 (1)	0.0072 (6)	3.59 (1)	0.0098 (5)
E_0		-1.4 (1.3)		-3 (1)	
χ^2		3457		13	
χ^2_{red}		996		3	
R		0.0045		0.0026	

F. Neutron PDF

Wide angle neutron scattering measurements of the Hs iron oxide nanoparticle samples were carried out at the NPDF instrument at LANSCE, USA. As impurity phase reflections were observed for all Hs samples, these samples were not considered for evaluation of the wide angle scattering. However, the data will be presented briefly in order to illustrate both the limitations and the gain in information related to neutron PDF.

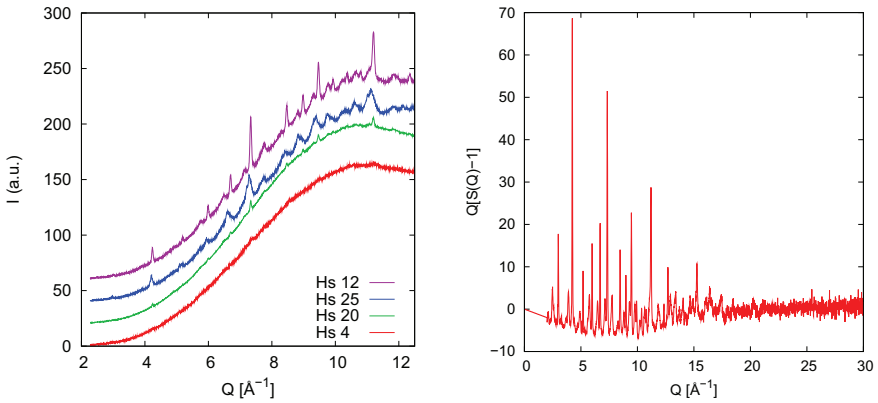

(a) Neutron diffraction. Data have been scaled and offset for display.

(b) Reduced total scattering structure function of the Hs 12 nanoparticle sample as obtained after *ad hoc* correction and normalization.

Figure F.0.1.: Wide angle neutron scattering by iron oxide nanoparticles.

The neutron diffraction data of the studied samples presented in Figure F.0.1a reveals a large scattering background consisting of an incoherent scattering contribution as well as a large scattering intensity in the higher Q range. Both contributions may result from the large amount of oleic acid in the samples, namely the incoherent scattering due to the large amount of hydrogen in the sample, and the higher intensity at high Q due to inelastic scattering of the flexible oleic acid molecules.

Due to these dominant backgrounds treatment of the data with the usually applied programs for generation of the PDF [183] is not sufficient. An *ad hoc* correction and normalization procedure was thus developed to extract the PDF after subtraction of the sample scattering background. This procedure includes the estimation of a realistic sample composition before normalization, the manual subtraction of the inelastic scattering background, and the subsequent introduction of an artificial Debye-Waller factor

which had been overcorrected due to the manual background subtraction. An absolute intensity calibration is not possible with this procedure. However, the reduced total scattering structure function obtained by this approach (and presented in Figure F.0.1b for Hs 12) allows for generation of the PDF and qualitative PDF analysis.

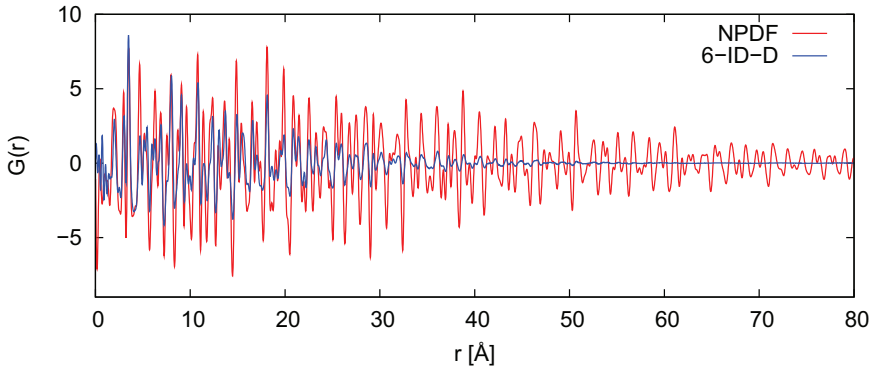

Figure F.0.2.: PDF of the Hs 12 nanoparticles as obtained from X-ray (6-ID-D) and neutron (NPDF) data.

In Figure F.0.2 the finally obtained neutron PDF of the Hs 12 sample is compared with the PDF obtained from synchrotron diffraction data. The peak positions in the lower r range are comparable for both data sets. The instrumental decrease of the PDF signal is much stronger for the synchrotron PDF with a vanishing signal beyond r = 50 AA. In contrast, neutron PDF can be evaluated in a much wider r range. This is also illustrated by the different instrumental damping parameters of Q_{damp} = 0.050813 for the synchrotron data and Q_{damp} = 0.00623 for the neutron data.

Thus, neutron PDF can give additional information by providing a larger r range, which is useful for r dependent refinements of the lattice constant or occupancy parameters as discussed in section 5.2. However, the observed incoherent and inelastic scattering contributions should be reduced significantly, *e. g.* by reduction of the used amount of oleic acid.

Bibliography

[1] Coey, J. M. D. *J. Magn. Magn. Mat.* **2001,** *226,* 2107-2112.

[2] Binasch, G.; Grünberg, P.; Saurenbach, F.; Zinn, W. *Phys. Rev. B* **1989,** *39,* 4828-4830.

[3] Baibich, M. N.; Broto, J. M.; Fert, A.; Nguyen Van Dau, F.; Petroff, F. *Phys. Rev. Lett.* **1988,** *61,* 2472-2475.

[4] Pankhurst, Q. A.; Connolly, J.; Jones, S. K.; Dobson, J. *J. Phys. D: Appl. Phys.* **2003,** *36,* R167-R181.

[5] Gossuin, Y.; Hocq, A.; Vuong, Q. L.; Disch, S.; Hermann, R. P.; Gillis, P. *Nanotechnology* **2008,** *19,* 475102.

[6] Gossuin, Y.; Disch, S.; Vuong, Q. L.; Gillis, P.; Hermann, R. P.; Park, J. H.; Sailor, M. *Contrast Media Mol. Imaging* **2010,** *5,* 318-322.

[7] Feygenson, M. *Magnetic and structural properties of thin films and nanoparticles studied by scattering methods,* Thesis, Forschungszentrum Jülich, 2007.

[8] 36th IFF Spring School 2005, *Magnetism goes Nano;* Forschungszentrum Jülich: 2005.

[9] Blundell, S. *Magnetism in Condensed Matter;* Oxford University Press, New York: 2001.

[10] 38th IFF Spring School 2007, *Probing the Nanoworld;* Forschungszentrum Jülich: 2007.

[11] Brückel, T.; Heger, G.; Richter, D.; Zorn, R., Eds.; *Laboratory Course Neutron Scattering;* volume 38 Forschungszentrum Jülich: 2007.

[12] *Neutron Data Booklet;* Institut Laue-Langevin: 2003.

[13] Egami, T.; Billinge, S. *Underneath the Bragg peaks - Structural Analysis of Complex Materials;* Pergamon, Amsterdam: 2003.

[14] Larson, A.; Von Dreele, R. "General Structure Analysis System (GSAS)", Los Alamos Laboratory Report LAUR 86-748, 2004.

[15] Kodre, A.; Arčon, I.; Padežnik Gomilšek, J. *Acta Chim. Slov.* **2004,** *51,* 1-10.

[16] Rehr, J. J.; Albers, R. C. *Rev. Mod. Phys.* **2000,** *72,* 621-654.

[17] Ankudinov, A. L.; Ravel, B.; Rehr, J. J.; Conradson, S. D. *Phys. Rev. B* **1998,** *58,* 7565-7576.

[18] Pedersen, J. S. *Adv. Colloid Interface Sci.* **1997,** *70,* 171–210.

[19] Kohlbrecher, J. "User guide for the SASfit software package", Paul Scherrer Institute, CH-5232 Villigen PSI.

[20] Yarnell, J. L.; Katz, M. J.; Wenzel, R. G.; Koenig, S. H. *Phys. Rev. A* **1973,** *7,* 2130–2144.

[21] Percus, J. K.; Yevick, G. J. *Phys. Rev.* **1958,** *110,* 1.

[22] Baxter, R. J. *J. Chem. Phys.* **1968,** *49,* 2770-2774.

[23] 39th IFF Spring School 2007, *Soft Matter: From Synthetic to Biological Materials;* Forschungszentrum Jülich: 2008.

[24] Chen, S.; Teixeira, J. *Phys. Rev. Lett.* **1986,** *57,* 2583.

[25] Kotlarchyk, M.; Chen, S. H. *The Journal of Chemical Physics* **1983,** *79,* 2461–2469.

[26] Pedersen, J. S. *J. Appl. Cryst.* **1994,** *27,* 595–608.

[27] Pedersen, J.; Posselt, D.; Mortensen, K. *J. Appl. Cryst.* **1990,** *23,* 321.

[28] Guinier, A.; Fournet, G. *Small Angle Scattering of X-rays;* Wiley Interscience, New York: 1955.

[29] Mittelbach, P. *Acta Phys. Austriaca* **1964,** *19,* 53-102.

[30] Beaucage, G. *J. Appl. Cryst.* **1995,** *28,* 717-728.

[31] Goerigk, G.; Schweins, R.; Huber, K.; Ballauff, M. *Europhys. Lett.* **2004,** *66,* 331-337.

[32] Braun, C. "Parratt32, v 1.5".

[33] Paratt, L. G. *Phys. Rev.* **1954,** *95,* 359.

[34] Korolkov, D. *Structural analysis of diblock copolymer nanotemplates using grazing incidence scattering,* Thesis, Forschungszentrum Jülich, 2008.

[35] Yoneda, Y. *Phys. Rev.* **1963,** *131,* 2010–2013.

[36] Busch, P.; Rauscher, M.; Smilgies, D. M.; Posselt, D.; Papadakis, C. M. *J. Appl. Cryst.* **2006,** *39,* 433-442.

[37] Blume, M. *Phys. Rev.* **1963,** *130,* 1670–1676.

[38] Blume, M. *Phys. Rev.* **1964,** *133,* A1366–A1369.

[39] Maleev, S. *Soviet Phys. JETP* **1958,** *7,* 89-90.

[40] Maleev, S. V. *Soviet Phys. JETP* **1961,** *13,* 860-862.

[41] Moon, R. M.; Riste, T.; Koehler, W. C. *Phys. Rev.* **1969,** *181,* 920–931.

[42] Shirane, G.; Uemura, Y. J.; Wicksted, J. P.; Endoh, Y.; Ishikawa, Y. *Phys. Rev. B* **1985,** *31,* 1227–1232.

[43] Brückel, T. *Magnetische Fehlordnung in dem Mischgranatsystem* $(Fe_xCr_{1-x})_2Ca_3(GeO_4)_3$, Thesis, Tübingen, 1988.

[44] Schärpf, O.; Capellmann, H. *Phys. Stat. Sol. (a)* **1993,** *135,* 359-379.

[45] Kohlbrecher, J.; Wiedenmann, A. *Physica B* **1998,** *241-243,* 591-593.

[46] Wiedenmann, A. *Physica B* **2001,** *297,* 226-233.

[47] Wiedenmann, A. *Physica B* **2005,** *356,* 246-253.

[48] http://hasylab.desy.de/facilities/doris_iii/beamlines/b1/index_eng.html.

[49] http://www.synchrotron-soleil.fr/portal/page/portal/Recherche/LignesLumiere/SWING.

[50] http://www.esrf.eu/UsersAndScience/Experiments/StructMaterials/ID01.

[51] http://www.jcns.info/jcns_kws2.

[52] http://www.ill.eu/instruments-support/instruments-groups/instruments/d22/characteristics/.

[53] http://6id.xor.aps.anl.gov/mucat/index.html.

[54] http://www.synchrotron-soleil.fr/portal/page/portal/Recherche/LignesLumiere/SAMBA.

[55] http://www.jcns.info/jcns_dns/.

[56] http://www.jcns.info/phps/nsewiki.php?index=34&print=0&portal=0.

[57] http://www.ill.eu/instruments-support/instruments-groups/instruments/in12/characteristics/.

[58] Cushing, B. L.; Kolesnichenko, V. L.; O´Connor, C. J. *Chem. Rev.* **2004,** *104,* 3893-3946.

[59] Bönnemann, H.; Richards, R. M. *Eur. J. Inorg. Chem.* **2001,** 2455-2480.

[60] Gubin, S. P., Ed.; *Magnetic Nanoparticles;* Wiley-VCH, Weinheim: 2009.

[61] Turkevich, J.; Stevenson, P. S.; Hillier, J. *Discuss. Faraday Soc.* **1951,** *11,* 55.

[62] Sun, S.; Murray, C. B. *J. Appl. Phys.* **1999,** *85,* 4325-4330.

[63] Osuna, J.; de Caro, D.; Amiens, C.; Chaudret, B.; Snoeck, E.; Respaud, M.; Broto, J.-M.; Fert, A. *J. Phys. Chem.* **1996,** *100,* 14571.

[64] Dinega, D. P.; Bawendi, M. G. *Angew. Chem. Int. Ed.* **1999,** *38,* 1788.

[65] Puntes, V. F.; Krishnan, K. M.; Alivisatos, A. M. *Science* **2001,** *291,* 2115.

[66] Puntes, V.; Zanchet, D.; Erdonmez, C.; Alivisatos, A. *J. Am. Chem. Soc.* **2002,** *124,* 12874.

[67] Mee, C. D.; Daniel, E. D., Eds.; *Magnetic Recording;* McGraw-Hill: New York, 1987.

[68] Schabes, M. *J. Magn. Magn. Mat.* **1991,** *95,* 249-288.

[69] Sager, W. F. C. Forschungszentrum Jülich, Germany. Private communication.

[70] Petit, C.; Taleb, A.; Pileni, M. P. *J. Phys. Chem. B* **1999,** *103,* 1805-1810.

[71] Sager, W. Microemulsion Templating. In *Nanostructured Soft Matter*; Springer Verlag: 2007.

[72] Sager, W. *Curr. Op. Coll. Int. Sci.* **1998,** *3,* 276-283.

[73] Lisiecki, I.; Pileni, M. P. *Langmuir* **2003,** *19,* 9486-9489.

[74] Petit, C.; Lixon, P.; Pileni, M. P. *J. Phys. Chem.* **1990,** *94,* 1598-1603.

[75] "Spectral Database for Organic Compounds SDBS", http://riodb01.ibase.aist.go.jp/sdbs/ (National Institute of Advanced Industrial Science and Technology).

[76] Evans, D. F.; Yamauchi, A.; Roman, R.; Casassa, E. Z. *J. Coll. Int. Sci.* **1982,** *88,* 89-96.

[77] Pyckhout-Hintzen, W. Forschungszentrum Jülich, Germany. Private communication.

[78] Lyon, O. "Actionjava, v 1.4".

[79] Evans, G.; Pettifer, R. F. *J. Appl. Cryst.* **2001,** *34,* 82-86.

[80] Pipich, V. "QtiKWS, based on QtiPlot".

[81] Ravel, B.; Newville, M. *J. Synchrotron Rad.* **2005,** *12,* 537-541.

[82] Kahlweit, M.; Busse, G.; Faulhaber, B. *Langmuir* **1994,** *10,* 1134-1139.

[83] Sager, W.; Sun, W.; Eicke, H. *Progr. Colloid Polym. Sci.* **1992,** *89,* 284-287.

[84] Tracy, J. B.; Weiss, D. N.; Dinega, D. P.; Bawendi, M. G. *Phys. Rev. B* **2005,** *72,* 064404.

[85] Bönnemann, H.; Brijoux, W.; Brinkmann, R.; Matoussevitch, N.; Waldöfner, N.; Palina, N.; Modrow, H. *Inorg. Chim. Act.* **2003,** *350,* 617-624.

[86] Margeat, O.; Amiens, C.; Chaudret, B.; Lecante, P.; Benfield, R. E. *Chem. Mater.* **2005,** *17,* 107-111.

[87] Carta, D.; Casula, M. F.; Mountjoy, G.; Corrias, A. *Phys. Chem. Chem. Phys.* **2008,** *10,* 3108-3117.

[88] Cheng, G.; Carter, J. D.; Guo, T. *Chem. Phys. Lett.* **2004,** *400,* 122-127.

[89] Bonini, M.; Fratini, E.; Baglioni, P. *Mat. Sci. Eng. C* **2007,** *27,* 1377-1381.

[90] Bonini, M.; Wiedenmann, A.; Baglioni, P. *J. Appl. Cryst.* **2007,** *40,* s254-s258.

[91] Lalatonne, Y.; Richardi, J.; Pileni, M. P. *Nat. Mat.* **2004,** *3,* 121-125.

[92] Camp, P. J.; Patey, G. N. *Phys. Rev. E* **2000,** *62,* 5403–5408.

[93] Cheng, G.; Shull, R. D.; Hight Walker, A. R. *J. Magn. Magn. Mat.* **2009,** *321,* 1351-1355.

[94] Zhang, J.; Han, B.; Liu, J.; Zhang, X.; He, J.; Liu, Z.; Jiang, T.; Yang, G. *Chem. Eur. J.* **2002,** *8,* 3879-3883.

[95] Bagwe, R. P.; Khilar, K. C. *Langmuir* **2000,** *16,* 905-910.

[96] Sanghamitra, N. J. M.; Mazumdar, S. *Langmuir* **2008,** *24,* 3439-3445.

[97] Du, G. X.; Mori, T.; Suzuki, M.; Saito, S.; Fukuda, H Takahashi, M. *Appl. Phys. Lett.* **2010,** *96,* 081915.

[98] Su, Y. K.; Shen, C. M.; Yang, T. Z.; Yang, H. T.; Gao, H. J.; Li, H. L. *Appl. Phys. A* **2005,** *81,* 569-572.

[99] Park, J.; An, K.; Hwang, Y.; Park, J.; Noh, H.; Kim, J.; Park, J.; Hwang, N.; Hyeon, T. *Nat. Mater.* **2004,** *3,* 891–895.

[100] Chaudret, B. CNRS Toulouse, France. Private communication.

[101] Ahniyaz, A.; Seisenbaeva, G. A.; Häggström, L.; Kamali, S.; Kessler, V. G.; Nordblad, P.; Johansson, C.; Bergström, L. *J. Magn. Magn. Mat.* **2008,** *320,* 781–787.

[102] Hyeon, T.; Lee, S. S.; Park, J.; Chung, Y.; Bin Na, H. *J. Am. Chem. Soc.* **2001,** *123,* 12798-12801.

[103] Rebbouh, L.; Hermann, R. P.; Grandjean, F.; Hyeon, T.; An, K.; Amato, A.; Long, G. J. *Phys. Rev. B* **2007,** *76,* 174422.

[104] An, K. Seoul University, South Korea. Private communication.

[105] Ahniyaz, A.; Sakamoto, Y.; Bergström, L. *Proc. Natl. Acad. Sci. USA* **2007,** *104,* 17570–17574.

[106] Wetterskog, E.; Salazar Alvarez, G.; Bergström, L. Stockholm University, Sweden. Private communication.

[107] Bødker, F.; Mørup, S.; Linderoth, S. *Phys. Rev. Lett.* **1994,** *72,* 282-285.

[108] Shmakov, A. N.; Kryukova, G. N.; Tsybulya, S. V.; Chuvilin, A. L.; Solovyeva, L. P. *J. Appl. Cryst.* **1995,** *28,* 141-145.

[109] Park, J.; Lee, E.; Hwang, N.; Kang, M.; Kim, S. C.; Hwang, Y.; Park, J.; Noh, H.; Kim, J.; Park, J.; Hyeon, T. *Angew. Chem. Int. Ed.* **2005,** *44,* 2872–2877.

[110] Evans, D. F.; Wennerström, H. *The Colloidal Domain: Where Physics, Chemistry, Biology, and Technology Meet;* Wiley-VCH, New York: 1999.

[111] Mittelbach, P.; Porod, G. *Acta Phys. Austriaca* **1961,** *14,* 185.

[112] Hendrick, R. W.; Schelten, J.; Schmatz, W. *Phil. Mag.* **1974,** *30,* 819-837.

[113] Pérez, N.; Guardia, P.; Roca, A. G.; Morales, M. P.; Serna, C. J.; Iglesias, O.; Bartolomé, F.; García, L. M.; Batlle, X.; Labarta, A. *Nanotechnology* **2008,** *19,* 475704.

[114] Hrianca, I.; Caizer, C.; Schlett, Z. *J. Appl. Phys.* **2002,** *92,* 2125-2132.

[115] Frenkel, A. I.; Hills, C. W.; Nuzzo, R. G. *J. Phys. Chem. B* **2001,** *105,* 12689-12703.

[116] Gilbert, B.; Huang, F.; Zhang, H.; Waychunas, G. A.; Banfield, J. F. *Science* **2004,** *651,* 305.

[117] Masadeh, A. S.; Bozin, E. S.; Farrow, C. L.; Paglia, G.; Juhas, P.; Billinge, S. J. L.; Karkamkar, A.; Kanatzidis, G. *Phys. Rev. B* **2007,** *76,* 115413.

[118] Gilbert, B.; Huang, F.; Lin, Z.; Goodell, C.; Zhang, H.; Banfield, J. F. *Nano Lett.* **2006,** *6,* 605-610.

[119] Kodama, R.; Berkowitz, A.; McNiff, E.; Foner, S. *Phys. Rev. Lett.* **1996,** *77,* 394-397.

[120] Morales, M. P.; Veintemillas-Verdaguer, S.; Montero, M. I.; Serna, C. J.; Roig, A.; Casas, L.; Martinez, B.; Sandiumenge, F. *Chem. Mater.* **1999,** *11,* 3058-3064.

[121] Jović, N. G.; Masadeh, A. S.; Kremenović, A. S.; Antić, B. V.; Blanuša, J. L.; Cvjetičanin, N. D.; Goya, G. F.; Antisari, M. V.; Božin, E. *J. Phys. Chem. C* **2009,** *113,* 20559-20567.

[122] Signorini, L.; Pasquini, L.; Savini, L.; Carboni, R.; Boscherini, F.; Bonetti, E.; Giglia, A.; Pedio, M.; Mahne, N.; Nannarone, S. *Phys. Rev. B* **2003,** *68,* 195423.

[123] Hammersley, A. P.; Svensson, S. O.; Hanfland, M.; Fitch, A. N.; Häusermann, D. *High Press. Res.* **1996,** *14,* 235-248.

[124] Howard, C. J. *J. Appl. Cryst.* **1982,** *15,* 615-620.

[125] Thompson, P.; Cox, D. E.; Hastings, J. B. *J. Appl. Cryst.* **1987,** *20,* 79-83.

[126] Rietveld, H. M. *J. Appl. Cryst.* **1969,** *2,* 65.

[127] Le Bail, A.; Duroy, H.; Fourquet, J. L. *Mat. Res. Bull.* **1988,** *23,* 447-452.

[128] Qiu, X.; Thompson, J. W.; Billinge, S. J. L. *J. Appl. Cryst.* **2004,** *37,* 678.

[129] Farrow, C. L.; Juhás, P.; Liu, J. W.; Bryndin, D.; Božin, E. S.; Bloch, J.; Proffen, T.; Billinge, S. J. L. *J. Phys.: Condens. Matter* **2007,** *19,* 335219.

[130] Billinge, S. J. L. *Local Structure From Diffraction;* Plenum, New York: 1998.

[131] Jeong, I. K.; Heffner, R. H.; Graf, M. J.; Billinge, S. J. L. *Phys. Rev. B* **2003,** *67,* 104301.

[132] Newville, M. *J. Synchrotron Rad.* **2001,** *8,* 322-324.

[133] Braun, P. B. *Nature* **1952,** *170,* 1123.

[134] van Oosterhout, G. W.; Rooijmans, C. J. M. *Nature* **1958,** *181,* 44.

[135] Greaves, C. *J. Sol. State Chem.* **1983,** *49,* 325-333.

[136] Morales, M. P.; Serna, C. J.; Bødker, F.; Mørup, S. *J. Phys.: Condens. Matter* **1997,** *9,* 5461-5467.

[137] Curiale, J.; Granada, M.; Troiani, H. E.; Sanchez, R. D.; Leyva, A. G.; Levy, P.; Samwer, K. *Appl. Phys. Lett.* **2009,** *95,* 043106.

[138] Wu, X. W.; Liu, C.; Li, L.; Jones, P.; Chantrell, R. W.; Weller, D. *J. Appl. Phys.* **2004,** *95,* 6810-6812.

[139] Sun, S.; Murray, C.; Weller, D.; Folks, L.; Moser, A. *Science* **2000,** *287,* 1989-1992.

[140] Held, G. A.; Grinstein, G.; Doyle, H.; Sun, S.; Murray, C. B. *Phys. Rev. B* **2001,** *64,* 012408.

[141] Kodama, R. H.; Berkowitz, A. E. *Phys. Rev. B* **1999,** *59,* 6321-6336.

[142] Dey, P.; Nath, T. K.; Banerjee, A. *Appl. Phys. Lett.* **2007,** *91,* 012504.

[143] Restrepo, J.; Labaye, Y.; Greneche, J. M. *Physica B* **2006,** *384,* 221-223.

[144] Mazo-Zuluaga, J.; Restrepo, J.; Mejía-López, *Physica B* **2007,** *398,* 187-190.

[145] Kohlbrecher, J.; Wiedenmann, A.; Wollenberger, H. *Z. Phys.* **1997,** *204,* 1.

[146] Wiedenmann, A.; Hoell, A.; Kammel, M.; Boesecke, P. *Phys. Rev. E* **2003,** *68,* 031203.

[147] Dewhurst, C. "Graphical Reduction and Analysis SANS Program for Matlab", http://www.ill.eu/instruments-support/instruments-groups/groups/lss/grasp/.

[148] Salazar-Alvarez, G.; Qin, J.; Šepelák, V.; Bergmann, I.; Vasilakaki, M.; Trohidou, K. N.; Ardisson, J. D.; Macedo, W. A. A.; Mikhaylova, M.; Muhammed, M.; Baró, M. D.; Nogués, J. *J. Am. Chem. Soc.* **2008,** *130,* 13234-13239.

[149] Kim, T.; Shima, M. *J. Appl. Phys.* **2007,** *101,* 09M516.

[150] De Gennes, P. G.; Pincus, P. A. *Physik der kondensierten Materie* **1970,** *11,* 189.

[151] Klokkenburg, M.; Erné, B. H.; Wiedenmann, A.; Petukhov, A. V.; Philipse, A. P. *Phys. Rev. E* **2007,** *75,* 051408.

[152] Song, Q.; Ding, Y.; Wang, Z. L.; Zhang, Z. J. *J. Phys. Chem. B* **2006,** *110,* 25547-25550.

[153] Krycka, K. L.; Booth, R. A.; Hogg, C. R.; Ijiri, Y.; Borchers, J. A.; Chen, W. C.; Watson, S. M.; Laver, M.; Gentile, T. R.; Dedon, L. R.; Harris, S.; Rhyne, J. J.; Majetich, S. A. *Phys. Rev. Lett.* **2010,** *104,* 207203.

[154] Whitesides, G. M.; Grzybowski, B. *Science* **2002,** *295,* 2418-2421.

[155] Murray, C. B.; Kagan, C. R.; Bawendi, M. G. *Ann. Rev. Mat. Sci.* **2000,** *30,* 545-610.

[156] Alivisatos, A. P. *Science* **1996,** *271,* 933-937.

[157] Perrin, J. *J. Ann. Chim. Phys.* **1909,** *18,* 5-114.

[158] Denkov, N. D.; Velev, O. D.; Kralchevsky, P. A.; Ivanov, I. B.; Yoshimura, H.; Nagayama, K. *Langmuir* **1992,** *8,* 3183-3190.

[159] Bentzon, M. D.; Van Wonterghem, J.; Mørup, S.; Thölén, A. *Phil. Mag. B* **1989,** *60,* 169-178.

[160] Murray, C.; Kagan, C.; Bawendi, M. *Science* **1995,** *270,* 1335-1338.

[161] Rödner, S. C.; Wedin, P.; Bergstrom, L. *Langmuir* **2002,** *18,* 9327-9333.

[162] Narayanan, S.; Wang, J.; Lin, X. M. *Phys. Rev. Lett.* **2004,** *93,* 135503.

[163] Shevchenko, E.; Talapin, D.; Kornowski, A.; Wiekhorst, F.; Kotzler, J.; Haase, M.; Rogach, A.; Weller, H. *Adv. Mat.* **2002,** *14,* 287-290.

[164] Bigioni, T. P.; Lin, X. M.; Nguyen, T. T.; Corwin, E. I.; Witten, T. A.; Jaeger, H. M. *Nat. Mat.* **2006,** *5,* 265-270.

[165] Bishop, K. J. M.; Wilmer, C. E.; Soh, S.; Grzybowski, B. A. *Small* **2009,** *5,* 1600-1630.

[166] Zheng, R.; Gu, H.; Xu, B.; Fung, K. K.; Zhang, X.; Ringer, S. P. *Adv. Mat.* **2006,** *18,* 2418-2421.

[167] Wang, Z. L. *J. Phys. Chem. B* **2000,** *104,* 1153-1175.

[168] Shevchenko, E. V.; Talapin, D. V.; Kotov, N. A.; O'Brien, S.; Murray, C. B. *Nature* **2006,** *439,* 55-59.

[169] Whetten, R. L.; Shafigullin, M. N.; Khoury, J. T.; Schaaff, T. G.; Vezmar, I.; Alvarez, M. M.; Wilkinson, A. *Accounts of Chemical Research* **1999,** *32,* 397–406.

[170] Shevchenko, E. V.; Talapin, D. V.; Murray, C. B.; O'Brien, S. *J. Am. Chem. Soc.* **2006,** *128,* 3620-3637.

[171] Dumestre, F.; Chaudret, B.; Amiens, C.; Renaud, P.; Fejes, P. *Science* **2004,** *303,* 821-823.

[172] Demortière, A.; Launois, P.; Goubet, N.; Albouy, P. A.; Petit, C. *J. Phys. Chem. B* **2008,** *112,* 14583-14592.

[173] Smilgies, D.-M.; Busch, P.; Papadakis, C.; Posselt, D. *Synchr. Rad. News* **2002,** *15,* 35-42.

[174] Lee, B.; Park, I.; Yoon, J.; Park, S.; Kim, J.; Kim, K. W.; Chang, T.; Ree, M. *Macromolecules* **2005,** *38,* 4311-4323.

[175] Stein, G. E.; Kramer, E. J.; Li, X.; Wang, J. *Phys. Rev. Lett.* **2007,** *98,* 086101.

[176] Aleksandrovic, V.; Greshnykh, D.; Randjelovic, I.; Froemsdorf, A.; Kornowski, A.; Roth, S. V.; Klinke, C.; Weller, H. *ACS Nano* **2008,** *2,* 1123-1130.

[177] Constantinides, M. G.; Jaeger, H. M.; Li, X.; Wang, J.; Lin, X.-M. *Z. Krist.* **2007,** *222,* 595-600.

[178] Smith, D. K.; Goodfellow, B.; Smilgies, D. M.; Korgel, B. A. *J. Am. Chem. Soc.* **2009,** *131,* 3281-3290.

[179] Bosworth, J. K.; Paik, M. Y.; Ruiz, R.; Schwartz, E. L.; Huang, J. Q.; Ko, A. W.; Smilgies, D.-M.; Black, C. T.; Ober, C. K. *ACS Nano* **2008,** *2,* 1396-1402.

[180] Dunphy, D.; Fan, H.; Li, X.; Wang, J.; Brinker, C. J. *Langmuir* **2008,** *24,* 10575-10578.

[181] Schweika, W. Forschungszentrum Jülich, Germany. Private communication.

[182] Chiffey, R.; Hicks, T. *Phys. Lett.* **1971,** *34A,* 267-268.

[183] Peterson, P. F.; Gutmann, M.; Proffen, T.; Billinge, S. J. L. *J. Appl. Cryst.* **2000,** *33,* 1192.

Personal Bibliography

Journal Articles

2011 *Quantitative spatial magnetization distribution in iron oxide nanocubes and nanospheres by polarized small-angle neutron scattering* Disch, S.; Wetterskog, E.; Hermann, R.P.; Wiedenmann, A.; Vainio, U.; Salazar-Alvarez, G.; Bergström, L.; Brückel, Th. *Phys. Rev. Lett.* (submitted, Mar 2011).

2011 *Shape induced symmetry in self-assembled mesocrystals of iron oxide nanocubes* Disch, S.; Wetterskog, E.; Hermann, R.P.; Salazar-Alvarez, G.; Busch, P.; Brückel, Th.; Bergström, L.; Kamali, S. *Nano Letters* (accepted, 2011).

12.2010 *NMR relaxation and magnetic properties of superparamagnetic nanoworms* Gossuin, Y.; Disch, S.; Vuong, Q. L.; Gillis, P.; Hermann, R. P.; Park, J. H.; Sailor, M. J. *Contrast Media Mol. Imaging* 5,318 (2010).

11.2008 *Physico-chemical and NMR relaxometric characterization of gadolinium hydroxide and dysprosium oxide nanoparticles* Gossuin, Y.; Hocq, A.; Vuong, Q. L.; Disch, S.; Hermann, R. P.; Gillis, P. *Nanotechnology* 19, 475102 (2008).

02.2008 *Formation of Unsaturated C_3 Hydrocarbons by the Protolysis of Magnesium Sesquicarbide with Ammonium Halides* Disch, S.; Cheetham, A. K.; Ruschewitz, U. *Inorg. Chem.* 47, 969 (2008).

11.2004 *$Ca[Cu(C_2H)_3]\cdot 6\,NH_3$ und $Rb_2[Cu(C_2H)_3]\cdot NH_3$: Zwei Ethinylocuprate mit einem trigonal planaren $[Cu(C_2H)_3]^{2-}$-Anion* Cremer, U.; Disch, S.; Ruschewitz, U. *Z. Anorg. Allg. Chem.* 630, 2304 (2004).

Conference Talks

07.2010 *Polarized SANS by iron oxide nanoparticles* Disch, S.; Wetterskog, E.; Hermann, R. P.; Bergström, L.; Brückel, T. *Polarized Neutrons in Condensed Matter Investigations*, Delft, Netherlands.

03.2009 *Small-angle scattering by magnetic nanoparticles* Disch, S.; Hermann, R. P.; Busch, P.; Sager, W. F. C.; Brückel, T. *DPG Früjahrstagung*, Dresden.

03.2008 *Synthesis and Characterization of Magnetic Nanoparticles* Disch, S.; Sager, W. F. C.; Hermann, R. P.; Goerigk, G.; Brückel, T. *DGK Jahrestagung*, Erlangen.

02.2008 *Synthesis and Characterization of Magnetic Nanoparticles* Disch, S.; Sager, W. F. C.; Hermann, R. P.; Goerigk, G.; Brückel, T. *DPG Frühjahrstagung*, Berlin.

Posters

10.2010 *Spin-wave excitations in magnetic nanoparticles* Disch, S.; Hermann, R. P.; Wetterskog, E.; Bergström, L.; Brückel, T. *JCNS workshop: Trends and Perspectives in Neutron Scattering*, Bernried.

08.2010 *Oriented supercrystals of anisotropic iron oxide nanoparticles* Disch, S.; Wetterskog, E.; Salazar-Alvarez, G.; Hermann, R. P.; Bergström, L.; Brückel, T. *26th European Crystallographic Meeting*, Darmstadt.

02.2010 *Magnetic Scattering by Iron Oxide Nanoparticles* Disch, S.; Hermann, R. P.; Brückel, T. *SNI Conference*, Berlin.

08.2009 *Not so Small Angle Scattering with Polarization Analysis: Towards the Magnetic Form Factor of Nanoparticles* Disch, S.; Hermann, R. P.; Sager, W. F. C.; Brückel, T. *Polarized Neutrons and Synchrotron X-rays for Magnetism*, Bonn.

04.2009 *Scattering by Ordered Iron Oxide Nanostructures* Disch, S.; Hermann, R. P.; Busch, P.; Brückel, T.; Wetterskog, E.; Bergström, L.; Kamali, S. *European Workshop on Self-Organized Nanomagnets* , Aussois, France.

Danksagung

Es gibt viele Personen, die mich im Laufe meiner Doktorandenzeit begleitet haben und auf unterschiedliche Art und Weise zu dieser Arbeit beigetragen haben. Ihnen allen möchte ich an dieser Stelle meinen Dank aussprechen.

Mein besonderer Dank gilt Prof. Dr. Thomas Brückel für die Möglichkeit der Promotion in seiner Arbeitsgruppe, seine Unterstützung sowie sein stetes Interesse an dieser Arbeit. Die Arbeit an einem interdisziplinären Projekt unter exzellenten Forschungsbedingungen und in internationalem Umfeld hat mit darüber hinaus viele Möglichkeiten eröffnet.
Herrn Prof. Dr. Ulrich Simon danke ich für die Übernahme des Korreferats.
Herrn Prof. Dr. Richard Dronskowski danke ich für die Beteiligung an meiner Doktorprüfung.
Herrn Prof. Dr. Raphaël P. Hermann danke ich herzlich für die hervorragende wissenschaftliche Betreuung während meiner Doktorandenzeit sowie die detaillierten Anmerkungen zur vorliegenden Dissertation. Seine vielfältige Unterstützung, sei es in zahlreichen Diskussionen oder während der vielen gemeinsamen Messreisen, hat mir das weite Feld der Streumethoden nähergebracht und mein Interesse für die wissenschaftliche Forschung nachhaltig gefördert.
Dr. Wiebke F. C. Sager danke ich für die Einführung in das Gebiet der weichen Materie und die bereichernden Diskussionen zur Synthese von Cobalt Nanoteilchen.
Dr. Peter Busch danke ich für die Unterstützung auf einigen GISAXS und SANS Messreisen sowie die umfangreiche Einführung in die Kleinwinkelstreuung unter streifendem Einfall.

I would like to sincerely thank Prof. Dr. Lennart Bergström, Erik Wetterskog, and Dr. German Salazar-Alvarez from Stockholm University for the prosperous collaboration we have had during the last few years. The high quality iron oxide nanoparticle samples and the intense discussions on nanoparticle assembly and interparticle interactions are an important contribution to this work.
Furthermore, I would like to thank Prof. Dr. Taeghwan Hyeon and Kwangjin An from Seoul University for providing monodisperse iron oxide nanoparticle samples.
Prof. Dr. Werner Kunz und Oliver Zech von der Universität Regensburg danke ich für die Bereitstellung von ionischen Flüssigkeiten zur Synthese.

I would like to acknowledge all local instrument scientists at the various large-scale facilities who helped to make most of our beamtimes a success. In particular, I would like to thank Dr. Emiliano Fonda for introducing me to EXAFS analysis and Dr. Albrecht Wiedenmann for support in analysis of polarized SANS measurements.

I would like to thank Prof. Dr. Simon J. L. Billinge for his help in correction of the hydrogen contribution in neutron diffraction data for PDF analysis, and also Dr. Ahmad Masadeh for his help in synchrotron PDF data acquisition and reduction.

I would like to thank all colleagues from the institute of scattering methods, JCNS, and the institute of solid state research for helpful scientific discussions and a pleasant working atmosphere.
In particular I would like to thank Dr. Denis Korolkov for help with the development and programming of the truncated cubic form factors as well as numerous discussions on grazing incidence scattering. I would like to thank Dr. Mikhail Feygenson for his initial work on synthesis and characterization of cobalt nanoparticles.
Ich danke Dr. Wim Pyckhout-Hintzen für unzählige SAXS Messungen sowie hilfreiche Diskussionen zur Kleinwinkelstreuung. Dr. Günter Goerigk danke ich für die Einführung in die anomale Kleinwinkelstreuung.
Elke Brauweiler-Reuters (IBN) danke ich für die SEM Aufnahmen von Nanopartikelanordnungen auf Substraten. Für die Hilfe bei AFM Messungen und Fragen zur Programmierung danke ich Artur Glavic.
Berthold Schmitz danke ich für die Unterstützung am PPMS und MPMS.
Den Mitarbeitern des ZCH danke ich für ICP-OES sowie NMR Messungen.

Der Studienstiftung des deutschen Volkes danke ich herzlich für die finanzielle und ideelle Förderung meiner Arbeit.

Ich widme diese Arbeit meiner Familie, die immer für mich da ist und mir Rückhalt gibt. Jens, ich danke Dir für Deine Geduld und Unterstützung in jeder Lebenslage.

Die vorliegende Arbeit wurde im Zeitraum von April 2007 bis Juli 2010 am Institut für Festkörperforschung des Forschungszentrum Jülich in der Arbeitsgruppe von Prof. Dr. Thomas Brückel durchgeführt.

Zur Wahrung der Priorität wurden Teile dieser Arbeit bereits publiziert:

2011 *Shape induced symmetry in self-assembled mesocrystals of iron oxide nanocubes* Disch, S.; Wetterskog, E.; Hermann, R.P.; Salazar-Alvarez, G.; Busch, P.; Brückel, Th.; Bergström, L.; Kamali, S. *Nano Letters* (accepted, 2011).

1. **Soft Matter**
   From Synthetic to Biological Materials
   Lecture manuscripts of the 39th IFF Spring School March 3 – 14, 2008
   Jülich, Germany
   edited by J.K.G. Dhont, G. Gompper, G. Nägele, D. Richter, R.G. Winkler (2008),
   c. 1000 pages
   ISBN: 978-3-89336-517-3

2. **Structural analysis of diblock copolymer nanotemplates using grazing incidence scattering**
   by D. Korolkov (2008), III, 167 pages
   ISBN: 978-3-89336-522-7

3. **Thermal Nonequilibrium**
   Thermal forces in fluid mixtures
   Lecture Notes of the 8th International Meeting on Thermodiffusion,
   9 – 13 June 2008, Bonn, Germany
   edited by S. Wiegand, W. Köhler (2008), 300 pages
   ISBN: 978-3-89336-523-4

4. **Synthesis of CMR manganites and ordering phenomena in complex transition metal oxides**
   by H. Li (2008), IV, 176 pages
   ISBN: 978-3-89336-527-2

5. **Neutron Scattering**
   Lectures of the JCNS Laboratory Course held at the Forschungszentrum Jülich and the research reactor FRM II of TU Munich
   edited by R. Zorn, Th. Brückel, D. Richter (2008), ca. 500 pages
   ISBN: 978-3-89336-532-6

6. **Ultrafast Magnetization Dynamics**
   by S. Woodford (2008), 130 pages
   ISBN: 978-3-89336-536-4

7. **Role of Surface Roughness inTribology: from Atomic to Macroscopic Scale**
   by C. Yang (2008), VII, 166 pages
   ISBN: 978-3-89336-537-1

8. **Strahl- und Spindynamik von Hadronenstrahlen in Mittelenergie-Ringbeschleunigern**
   von A. Lehrach (2008), II, 171 Seiten
   ISBN: 978-3-89336-548-7

9. **Phase Behaviour of Proteins and Colloid-Polymer Mixtures**
   by C. Gögelein (2008), II, 147 pages
   ISBN: 978-3-89336-555-5

10. **Spintronics – From GMR to Quantum Information**
    Lecture Notes of the 40th IFF Spring School March 9 – 20, 2009
    Jülich, Germany
    edited by St. Blügel, D. Bürgler, M. Morgenstern, C. M. Schneider,
    R. Waser (2009), c. 1000 pages
    ISBN: 978-3-89336-559-3

11. **ANKE / PAX Workshop on SPIN Physics**
    JINR, Dubna, Russia / June 22. – 26, 2009
    Org. Committee: A. Kacharava, V. Komarov, A. Kulikov, P. Lenisa, R. Rathmann,
    H. Ströher (2009), CD-ROM
    ISBN: 978-3-89336-586-9

12. **Entwicklung einer Nanotechnologie-Plattform für die Herstellung Crossbar-basierter Speicherarchitekturen**
    von M. Meier (2009), 135 Seiten
    ISBN: 978-3-89336-598-2

13. **Electronic Oxides –**
    Correlation Phenomena, Exotic Phases and Novel Functionalities
    Lecture Notes of the 41st IFF Spring School March 8 – 19, 2010
    Jülich, Germany
    edited by St. Blügel, T. Brückel, R. Waser, C.M. Schneider (2010), ca. 1000 pages
    ISBN: 978-3-89336-609-5

14. **4th Georgian-German School and Workshop in Basic Science**
    Tbilisi, Georgia / May 3 – 7, 2010
    Org. Committee: E. Abrosimova, R. Botchorishvili, A. Kacharava, M. Nioradze,
    A. Prangishvili, H. Ströher (2010); CD-ROM
    ISBN: 978-3-89336-629-3

15. **Neutron Scattering**
    Lectures of the JCNS Laboratory Course held at Forschungszentrum Jülich and the research reactor FRM II of TU Munich
    edited by Th. Brückel, G. Heger, D. Richter, G. Roth and R. Zorn (2010),
    ca 350 pages
    ISBN: 978-3-89336-635-4

16. **Ab *initio* investigations of magnetic properties of ultrathin transition-metal films on *4d* substrates**
    by A. Al-Zubi (2010), II, 143 pages
    ISBN: 978-3-89336-641-5

17. **Investigation of a metal-organic interface realization and understanding of a molecular switch**
    by O. Neucheva (2010), 134 pages
    ISBN: 978-3-89336-650-7

18. **Reine Spinströme in lateralen Spinventilen, *in situ* Erzeugung und Nachweis**
von J. Mennig (2010), V, 95 Seiten
ISBN: 978-3-89336-684-2

19. **Nanoimprint Lithographie als Methode zur chemischen Oberflächenstrukturierung für Anwendungen in der Bioelektronik**
von S. Gilles (2010), II, 169 Seiten
ISBN: 978-3-89336-686-6

20. **Macromolecular Systems in Soft- and Living-Matter**
Lecture Notes of the 42nd IFF Spring School 2011 February 14 – 25, 2011 Jülich, Germany
edited by Jan K.G. Dhont, Gerhard Gompper, Peter R.Lang, Dieter Richter, Marisol Ripoll, Dieter Willbold, Reiner Zorn (2011), ca. 1000 pages
ISBN: 978-3-89336-688-0

21. **The spin structure of magnetic nanoparticles and in magnetic nanostructures**
by S. Disch (2011), V, 342 pages
ISBN: 978-3-89336-704-7

Schlüsseltechnologien / Key Technologies
Band / Volume 21
ISBN 978-3-89336-704-7

JÜLICH
FORSCHUNGSZENTRUM